



NO_x Removal and Effect of Adsorbate-Adsorbate Interactions

Khan, Tuhin Suvra

Publication date:
2013

Document Version
Publisher's PDF, also known as Version of record

[Link back to DTU Orbit](#)

Citation (APA):
Khan, T. S. (2013). NO_x Removal and Effect of Adsorbate-Adsorbate Interactions. Technical University of Denmark.

General rights

Copyright and moral rights for the publications made accessible in the public portal are retained by the authors and/or other copyright owners and it is a condition of accessing publications that users recognise and abide by the legal requirements associated with these rights.

- Users may download and print one copy of any publication from the public portal for the purpose of private study or research.
- You may not further distribute the material or use it for any profit-making activity or commercial gain
- You may freely distribute the URL identifying the publication in the public portal

If you believe that this document breaches copyright please contact us providing details, and we will remove access to the work immediately and investigate your claim.

NO_x Removal and Effect of Adsorbate-Adsorbate Interactions

Dissertation for the Ph. D. degree in Physics

Tuhin Suvra Khan
June 2013

CENTER FOR ATOMIC-SCALE MATERIALS DESIGN
DEPARTMENT OF PHYSICS
TECHNICAL UNIVERSITY OF DENMARK



Technical University of Denmark
Department of Physics
Center for Atomic-scale Materials Design
Building 311, DK-2800 Kongens Lyngby, Denmark
www.camd.dtu.dk

Preface

This thesis is submitted in candidacy for the Ph.D. degree in physics from the Technical University of Denmark (DTU). The work has been carried out from August 2010 to July 2013 at the Center for Atomic-scale Materials Design (CAMD), Department of Physics, DTU. Supervisors have been Associate Professor Thomas Bligaard, now Senior Staff Scientist at the SUNCAT Center for Interface Science and Catalysis at SLAC National Accelerator Laboratory, Menlo Park, California, Professor Søren Dahl, now Project manager at Haldor Topsøe and Associate Professor Jan Rossmeisl. This thesis contains results obtained in collaboration with other researchers at CAMD and SUNCAT.

Lyngby, June 30, 2013
Tuhin Suvra Khan

Abstract in English

Heterogeneous catalysis is immensely important to modern and future society. It forms the foundation of chemical industry, supplying essential chemicals and commodities for transport, food production, and pharmaceuticals, and is also a cornerstone in current and future energy platforms. If the long-standing dream of an environmentally sustainable energy sector is to be fulfilled, heterogeneous catalysts aiding production, storage, and use of energy from sustainable sources, e.g. sunlight, wind, and biomass, are expected to be essential. New catalysts improving the efficiency of existing chemical processes, such as ammonia synthesis and sulphur removal in refining, may also contribute to improving future society at large. However, developing the catalysts of tomorrow presents a wealth of scientific challenges.

Understanding surface science has always been essential for development and improvement of industrial chemical processes, nano-science and nano-technology, in general any process where a solid surface interacts with any surrounding liquid or gas-phase species. Computational approaches play an increasingly important role in modern surface science, and density functional theory (DFT) in particular. Indeed, several recent developments in our understanding of important aspects of heterogeneous catalysis derive from electronic structure calculations based on DFT. However, there are still many challenges and lots of scope for improvement in the density functional approach to surface science. To mention a few, to improve the accuracy of electronic structure calculations, accuracy of the physical model, completeness of kinetic models for chemical reactions, figuring out the exact state of catalysts under reaction conditions, and also reducing the complexity of our physical models.

In this thesis I have analyzed these challenges systematically and have developed some new methods and models to counter those challenges and obtain some general understanding of the catalytic process. I have developed an adsorbate-adsorbate interaction model to include the coverage dependency of the adsorption energy in kinetic models to obtain more accurate catalytic rates than with the commonly used non-interacting

mean field model. I then applied the proposed adsorbate-adsorbate interaction model to three important catalytic reactions, the direct NO decomposition, CO methanation, and steam reforming of methane, and analyzed the effect of adsorbate-adsorbate interactions on their catalytic rates. An alloy screening method has also been developed to screen for the industrially most promising alloy catalysts for any catalytic reaction. I have also studied the structure sensitivity of the rates of catalytic direct NO decomposition on different low-index metal surfaces. Furthermore, I have used DFT calculated adsorption and transition state energies coupled with a microkinetic model to study two industrially important catalytic reactions, NH_3 oxidation and selective catalytic reduction of NO_x , to obtain the catalytic trends and understand the reaction mechanisms.

Resumé på dansk

Heterogen katalyse er en fantastisk vigtig videnskabelig disciplin for nutidens og fremtidens samfund. Katalyse danner grundlaget for den kemiske industri, som producerer vigtige kemikalier og råvarer til transport, fødevareproduktion og lægemidler, og er også en hjørnesteen i nuværende og fremtidige energi-pladformer. Hvis den mangeårige drøm om en miljømæssigt bæredygtig energisektor skal indfries, forventes heterogene katalysatorer til produktion, opbevaring og brug af energi fra bæredygtige kilder, fx sol, vind og biomasse, at få afgørende betydning. Nye katalysatorer som forbedrer effektiviteten af eksisterende kemiske processer, såsom ammoniak-syntese og fjernelse af svovl under raffinering af råolie, kan også bidrage til generel forbedring af forholdene i verden omkring os. Udvikling af morgendagens katalysatorer indebærer dog et væld af videnskabelige udfordringer.

Forståelse af overflade-fysik og -kemi har altid været afgørende for udvikling og forbedring af industrielle kemiske processer, nanovidenskab og nanoteknologi, i almindelighed enhver proces hvor en fast overflade interagerer med en omgivende væske eller gas-fase molekyler. Beregnings-baserede metoder spiller i stigende omfang en vigtig rolle i moderne overfladekemi, tæthedsfunktionalteori i særdeleshed. Faktisk er en betydelig del af det seneste årtis fremskridt i vores forståelse af vigtige aspekter af heterogen katalyse opnået ved elektronstruktur-beregninger baseret på DFT. Der er dog stadig mange udfordringer og masser af muligheder for forbedring af tæthedsfunktional-tilgangen til overfladekemi. For blot at nævne et par stykker, forbedring af nøjagtigheden af elektronstruktur- beregninger, nøjagtigheden af den fysiske model, fuldstændighed af kinetiske modeller for kemiske reaktioner, at forudsige den nøjagtige tilstand af en katalysator under reaktionsbetingelser, og også at reducere kompleksiteten i vores fysiske modeller.

I denne afhandling har jeg analyseret disse udfordringer systematisk, og har udviklet nye metoder og modeller til at imødegå disse udfordringer og opnå en generel forståelse af den katalytiske proces. Jeg har udviklet en adsorbat-adsorbat interaktions-model,

som inkluderer dækningsgrad-afhængighed af adsorptionsenergier i kinetiske modeller, for at få mere præcise katalytiske rater end med standard ikke-interagerende "mean field"modeller. Jeg har derefter anvendt den udviklede adsorbat-adsorbat interaktionsmodel i studier af tre vigtige katalytiske reaktioner, direkte NO dekomponering, CO metanisering og steam reforming af metan, og analyseret effekten af adsorbat-adsorbat interaktioner på de katalytiske rater. En screening-metode er også blevet udviklet til at søge efter de industrielt mest lovende legeringer som kan katalysere en given kemisk reaktion. Jeg har også studeret struktur-følsomheden af raterne for katalytisk direkte NO dekomponering på forskellige lav-indeks metaloverflader. Desuden har jeg brugt DFT-beregnete adsorptions- og overgangstilstands-energier kombineret med en mikrokinetisk model til at studere to industrielt vigtige katalytiske reaktioner, NH_3 oxidation og selektiv katalytisk reduktion af NO_x , for at bestemme de katalytiske trends og forstå reaktionsmekanismerne.

Acknowledgements

Many people at CAMD and SUNCAT should be acknowledged for their contributions to the successful completion of this work. First of all I would like to thank my supervisors Thomas Bligaard, Senior Staff Scientist at the SUNCAT Center for Interface Science and Catalysis at SLAC National Accelerator Laboratory; Søren Dahl, Project manager at Haldor Topsøe and Jan Rossmeisl, Associate Professor at CAMD, DTU for the excellent supervision of my project. It has been a great pleasure working together with such committed and knowledgeable people for the past three years and I could not have wished for a better supervision team. I would like to thank Thomas Bligaard for the constant flow of ideas and for his contagious enthusiasm and for all the pep talks during the difficult times. I would also like to thank Søren Dahl for all the excellent ideas for combining the DFT calculated data with the experimental results. A special thank also goes to Jan Rossmeisl, for agreeing to be my supervisor when Thomas Bligaard and Søren Dahl left DTU. I would also like to thank Professor Jens K. Nørskov for allowing me to come to SUNCAT and work for two years with all the nice people, in the excellent California weather.

I would also like to thank Professor Ib Chorkendorff and Senior Scientific Advisor Debasish Chakraborty for all the valuable informations and excellent ideas on the NH_3 oxidation project.

I would like to thank all my collaborators, Hanne Falsig, Wei Guo, Dmitry E. Doronkin, Keld Lungaard, Yue Xu, Andrew James Medford, Adam Lausche and Simon Hede-gaard Brodersen for the excellent collaboration. Our works together had been absolutely smooth and fruitful. I would furthermore like to thank all other co-authors of the manuscripts included in this thesis for their contributions. Frank Abild-Pedersen, Felix Studt and Aleksandra Vojvodic from SUNCAT are gratefully acknowledged for all the interesting discussion and valuable informations on the heterogeneous catalysis.

A special thank also goes to Jess Wellendorff for kindly providing the Latex template

used for the thesis and helping me writing the abstract in Danish. I also thank Keld Lungaard, Jess Wellendorff, Yue Xu, Andrew James Medford, Adam Lausche, Aleksandra Vojvodic and Simon Hedegaard Brodersen for doing the proof reading of my PhD thesis.

My every-day work for the last three years would have been far less productive without invaluable help by CAMD computer staff Ole Holm Nielsen and Marcin Dułak, and Head of Administration Marianne Ærsøe, who have all made my life much easier. The same thanks goes to Christopher O’Grady, Helle Wellejus, Cheryl Johnson and Amita Gupta, who all made my two years stay in SUNCAT/SLAC smooth and easy.

Finally, I am especially thankful to all my friends here in Denmark and in California, who made my life away from home much easier than I had thought.

Thank you all for some memorable, inspiring and joyful years.

List of Included Papers

Paper I

On the structure sensitivity of direct NO decomposition over low-index transition metal facets

Hanne Falsig, Juan Shen, Tuhin Suvra Khan,

Wei Guo, Glenn Jones, Søren Dahl, and Thomas Bligaard

Topics in Catalysis accepted (2013)

Paper II

Parameterization of a Model for Adsorbate-Adsorbate Interactions

Tuhin Suvra Khan, Hanne Falsig, Shengguang Wang, Wei Guo, Søren Dahl, and Thomas Bligaard

To be submitted (2013)

Paper III

On the Effect of Coverage Dependent Adsorbate-Adsorbate Interactions

for CO Methanation on Transition Metal Surfaces

Adam C. Lausche, Andrew J. Medford, Tuhin Suvra Khan, Yue Xu, Thomas Bligaard, Frank Abild-Pedersen, Jens K. Nørskov, and Felix Studt

submitted (2013)

Paper IV**In silico Search for Novel Methane Steam Reforming Catalysts**

Yue Xu, Adam C. Lausche, Shengguang Wang, Tuhin Suvra Khan,
Frank Abild-Pedersen, Felix Studt, Jens K. Nørskov and Thomas
Bligaard
submitted (2013)

Paper V**Study of the "Fast SCR"-like mechanism
of H₂-assisted SCR of NO_x with ammonia over Ag/Al₂O₃**

Dmitry E. Doronkin, Sebastian Fogel, Stefanie Tamm,
Louise Olsson, Tuhin Suvra Khan, Thomas Bligaard,
Pär Gabrielsson and Søren Dahl
Applied Catalysis B: Environmental **113–114**, 228–236 (2012)

Paper VI**Sulfur poisoning and regeneration of the Ag/ γ -Al₂O₃
catalyst for H₂-assisted SCR of NO_x by ammonia**

Dmitry E. Doronkin, Tuhin Suvra Khan, Thomas Bligaard,
Sebastian Fogel, Pär Gabrielsson and Søren Dahl
Applied Catalysis B: Environmental **117–118**, 49–58 (2012)

Contents

1	Introduction	1
2	Electronic Structure Theory	5
2.1	The Schrödinger Equation	6
2.2	Born–Oppenheimer Approximation	6
2.3	Density Functional Theory	7
2.3.1	Kohn–Sham Theory	8
2.4	Exchange–Correlation Functionals	9
2.4.1	Local Density Approximation (LDA)	10
2.4.2	Generalized Gradient Approximation (GGA)	10
2.4.3	PBE and RPBE Functionals	11
2.5	Implementation of Density Functional Theory	12
2.5.1	DACAPO Code	12
2.6	Summary	14
3	Heterogeneous Catalysis	15
3.1	Catalysis	15
3.2	d-band Model and Trends in Chemisorption Energies	17
3.2.1	Trends in Chemisorption Energies	17
3.3	Surface Structure and Reactivity	18
3.4	Correlation from DFT Calculations	21
3.4.1	Adsorption Energy Scaling	21
3.4.2	Brønsted–Evans–Polanyi Relationship	21
3.4.3	Universal Relationship	21
3.5	Electronic and Geometric Effect	23
3.6	Microkinetic Modeling and Volcano Curves	24

4	Structure Sensitivity of Direct NO Decomposition	27
4.1	DFT Setups	28
4.2	Microkinetic Model	29
4.3	DFT Results	30
4.3.1	Brønsted-Evans-Polanyi and Scaling Relationship	31
4.4	Catalytic Activity	34
4.5	Reaction Rate Sensitivity	38
4.6	Summery	39
5	Adsorbate-Adsorbate Interaction Model	41
5.1	Parameterization of a Model for Adsorbate-Adsorbate Interactions	42
5.1.1	Method	45
5.1.2	DFT Setups	46
5.1.3	Result and Discussion	46
5.1.4	Piecewise Interaction Model	54
5.2	Effect of Adsorbate-Adsorbate Interactions in Catalytic NO Decomposition	59
5.3	Effect of Adsorbate-Adsorbate Interactions on CO Methanation	63
5.3.1	Microkinetic Model	64
5.3.2	Adsorbate-Adsorbate Interaction Model	66
5.3.3	DFT Setups	67
5.3.4	DFT Results	68
5.3.5	Microkinetic Modeling Results	72
5.4	Catalyst Screening for Steam Reforming of Methane using Adsorbate-Adsorbate Interaction Model	77
5.4.1	Microkinetic Model	77
5.4.2	Alloy Screening Method	80
5.4.3	Microkinetic Modeling Results	82
5.4.4	Alloy Screening Results	86
5.5	Summary	87
6	Ammonia Oxidation over Transition Metal Surfaces	91
6.1	Microkinetic model	94
6.2	DFT Setups	99
6.3	DFT Results	99
6.4	Catalytic Activity	104
6.4.1	NH ₃ Oxidation in Absence of H ₂	104
6.4.2	NH ₃ Oxidation in Presence of H ₂	108
6.5	Summary	112
7	H₂ assisted Selective Catalytic Reduction of NO_x using NH₃	115
7.1	Mechanistic Study of the H ₂ -assisted NO _x -SCR by NH ₃	116
7.1.1	Experimental Setups	117
7.1.2	DFT Setups	118

7.1.3	Microkinetic Model	119
7.1.4	Experimental Results	124
7.1.5	DFT and Microkinetic Modeling Results	131
7.2	Study of the Sulphur Poisoning of Ag/Al ₂ O ₃ during the H ₂ -assisted NO _x -SCR by NH ₃	140
7.2.1	Experimental Setups	141
7.2.2	DFT Setups	142
7.2.3	Experimental Results	144
7.2.4	Evaluation of the Proposed Sulfation and Regeneration Mecha- nism by DFT	149
7.3	Summary	151
8	Summary and Outlook	153
A	Appendix	157
A.1	Adsorption Sites of O, N and NO over Low-index Facets.	157
A.2	Interaction Matrix for Rh{111}	159
A.3	CO Methanation	160
A.4	Steam Refoming of Methane	165
A.5	NH ₃ Oxidation over Transition Metal Surfaces	167
A.6	H ₂ assisted NO _x -SCR by NH ₃	173
A.6.1	Ag{211} Adsorption Summary	173
A.6.2	Scaling Summary	174
	Bibliography	181
	Included Papers	195

CHAPTER 1

Introduction

Heterogeneous catalysis forms the foundation of the chemical industry. Catalysis is applied to facilitate the production of many essential chemicals and commodities we use in our common lives. Heterogeneous catalysis is used to produce a wide range of product from petrochemical fuels, fertilizers, and plastics to life saving pharmaceuticals. Heterogeneous catalysts are also used to clean our environments, like cleaning the exhaust gas from cars, power plants, etc. The emergence of heterogeneous catalysis in the 20th century probably has the most significant part in improving the standard of living for the large fraction of population of the world. Probably this is why the nature article chooses a heterogeneous catalysis, the Haber-Bosch process for NH₃ synthesis as the most important invention in the 20th century ahead of the discovery of airplanes, nuclear reactor, space flight, television, computer, Internet and penicillin.¹ Without the discovery of Haber-Bosch process for NH₃ synthesis, we would not have any inorganic fertilizers, and hence no food security and many people would have been without food today. However there is still lot of work to be done in the field of developing new catalyst and also improve our existing catalyst to keep our world clean and beautiful.

As the heterogeneous catalysis happens near the active site and the electronic structure of the active site² not the global electronic structure of the whole catalyst control the catalytic process, it is possible to model it in an atomic scale with only few atoms to few hundred atoms. With the advances in the modern electronic structure theory we can now calculate the adsorption energy of the intermediates and activation barrier of any elementary reaction step with high enough accuracy so that we can successfully model catalytic reaction based on density functional theory calculation

to a first approximation.^{3,4} Due to the underlying correlation between the adsorption energy and activation barriers we have successfully reduced the number of independent parameters to one or two, usually called descriptors. With these scaling based microkinetic model we can obtain catalytic activity in the function of the two descriptors.^{5,6} The rates generally looks like a volcano shaped curve, and the top of the volcano represent position of descriptors where the catalytic rate is maximum. This scaling based microkinetic model form the base of the “*in-silico*” approach for the search of new catalytic material. There are already several examples where this approach has been successfully applied to discover new catalytic materials.⁷⁻¹⁰ Modern DFT methods have contributed much in the development of heterogeneous catalysts through the understanding of the catalytic process, elucidating reaction mechanisms and understanding fundamental trends within the heterogeneous catalysis.

However even with all the recent developments in DFT theory there are still many challenges exist in the DFT approach of the surface science process. Some of the most general and extremely important challenges are accuracy of electronic structure calculation, accuracy of physical models, completeness of the reaction kinetics, figuring out the structure and state of the catalyst under the reaction condition (extremely difficult to probe experimentally) and most importantly reducing the complexity of the model to get a general understanding of the processes but without oversimplifying it.

One of the main limitation of the current approach of using DFT calculations for catalyst screening is the use of model surface like the flat {111} or stepped {211} surface to obtain the catalytic activity. However in the industrial condition the metal catalyst are mainly present in the form of nanoparticles and it can have different surfaces like terrace, steps, corners etc. It is necessary to know the correct structure of the nanoparticles under the reaction condition. Also the catalytic rate of these different surfaces can vary orders of magnitude. For these reasons there is a need for the development of a method for the modeling of a nanoparticle under the reaction condition and calculate the total rate of the of it. This will give us better accuracy of the DFT calculated catalytic rates to the experimentally observed ones.

For the search of new promising catalyst we generally use the DFT calculated adsorption and transition state energies coupled in the microkinetic modeling to obtain catalytic rates. However a major short coming of the current microkinetic models is that it does not include the coverage dependency of adsorption energy. Most of the industrial reactions are operated under high pressure condition and consequently the surface species coverages are also very high under those conditions. Hence the inclusion of coverage dependent adsorption energy into the microkinetic modeling becomes very important for our “*in-silico*” search of novel industrial catalysts.

Outline

In this thesis I have analyzed the challenges I mentioned above. I will go through the chapters here to describe the challenges and their solution in a few words. More details description will be presented in their respective following chapters. In Chapter 2 and 3, brief introductions to the electronic structure theory and heterogeneous catalysis will be given, with main focus on the topics relevant to this thesis.

Chapter 4 describes the structure sensitivity of catalytic reaction over low-index transition metal surfaces. It is well known that different surfaces of a nanoparticle have different activity. In this chapter I have taken direct NO decomposition as an example to show the effect structure sensitivity in the BEP scaling relations and on catalytic activity. In future this work will be extended to obtain the catalytic rate of nanoparticles under the reaction conditions.

In Chapter 5, I will present a new parametrized adsorbate-adsorbate interaction model to include the coverage dependency of adsorption energy into the microkinetic modeling. This model will help us to obtain catalytic rates with much higher accuracy than the commonly used non-interacting mean field model. I will then apply this interaction model to investigate three important catalysis processes, direct NO decomposition, CO methanation and methane steam reforming. The inclusion of adsorbate-adsorbate interaction is crucial if one wants to use the theoretical model to tailor the new catalysts. In this chapter a detail description of alloy screening method based on stability, cost and reactivity will also be presented. The alloy screening method has been developed to find out the industrially promising alloy catalysts.

In Chapter 6 and 7, I will present the studies on two very important environmental catalytic processes, NH_3 oxidation and H_2 assisted selective catalytic reduction of NO_x with NH_3 over transition metal catalysts. In Chapter 6, the oxidation of NH_3 over transition metal catalyst have been studied under different reactant condition to obtain the catalytic trends among the transition metals and find out the optimal catalyst for this reaction. Chapter 7 contains both experimental and theoretical description of the mechanistic study of the H_2 assisted selective catalytic reduction of NO_x with NH_3 . I also have studied the sulfur poisoning of $\text{Ag}/\text{Al}_2\text{O}_3$ in the H_2 assisted NH_3 -SCR condition to find out the optimal catalyst composition also to propose a sulfur poisoning mechanism. Both NH_3 oxidation and H_2 assisted selective catalytic reduction of NO_x with NH_3 are work in progress.

CHAPTER 2

Electronic Structure Theory

Due to the many body problem^{11–13}, solving Schrödinger equation for a system with many electrons is problematic and cannot be done without introducing approximations. The density functional theory (DFT) is one approximation to solve the Schrödinger equation. In this chapter I have presented a brief discussion on the main fundamental theories of quantum mechanics, the Schrödinger equation and Born-Oppenheimer approximation. The foundation of the density functional theory by Kohn and Sham and the origin of the exchange correlation functional have also been discussed. The formulation and differences of the commonly used exchange-correlation functional will also be discussed briefly. We also have presented a brief overview of the implementation of the DFT theory through computational code DACAPO. Some important parameters of the DACAPO DFT code are also discussed. Atomic units have been used throughout the chapter for the equations, $e = \hbar = a_0 = m_e = 1$, where e , \hbar , a_0 , m_e are the unit charge, reduced plank constant, Bohr radius and electron mass respectively.

This chapter is only meant for the brief introduction to the basic theorems and principles of density functional theory. More detailed discussion behind the foundation of DFT can be found in number of good books^{14,15} and review articles.^{16,17}

2.1 The Schrödinger Equation

The central theme of quantum mechanics is the solution of the Schrödinger equation.¹⁸ It is a wave equation, which describes all the quantum properties of a system. The time independent non-relativistic Schrödinger equation can be written as:

$$\hat{H}\hat{\Psi}_n = E_n\hat{\Psi}_n \quad (2.1)$$

where \hat{H} is the Hamiltonian operator, which gives the energy of the system, $\hat{\Psi}_n$ is the eigenfunction and eigenvalue E_n is the solution of the eigenvalue problem. Eigenvalue E_n is associated with the energy of the system. The Hamiltonian \hat{H} of an atom consisting of M nuclei and N electrons can be given by,

$$\begin{aligned} \hat{H} &= -\frac{1}{2} \sum_{i=1}^N \nabla_i^2 - \frac{1}{2} \sum_{A=1}^M \frac{1}{M_A} \nabla_A^2 - \sum_{i=1}^N \sum_{A=1}^M \frac{Z_A}{r_{iA}} + \sum_{i=1}^N \sum_{j>i}^N \frac{1}{r_{ij}} + \sum_{A=1}^M \sum_{B>A}^M \frac{Z_A Z_B}{R_{AB}} \\ &= \hat{T}_e + \hat{T}_N + \hat{V}_{Ne} + \hat{V}_{ee} + \hat{V}_{NN}, \end{aligned} \quad (2.2)$$

where \hat{T}_e and \hat{T}_N are kinetic energy contributions of the electron and nuclei respectively. \hat{V}_{Ne} , \hat{V}_{ee} and \hat{V}_{NN} are the potential energy contribution from the nuclei-electron, electron-electron and nuclei-nuclei interactions.

2.2 Born–Oppenheimer Approximation

As the nucleus is much heavier than electron, it moves much slower than electrons. So one can simplify the Schrödinger equation using the Born-Oppenheimer Approximation.¹⁹ It states that the nuclei can be regarded as stationary compared to the movement of the electrons and thus the interaction between nuclei and electrons can be decoupled. So instead of solving the full Schrödinger equation, only the Schrödinger equation for the electron moving in a static external potential of the "stationary" nuclei is solved.

As the nuclei are considered fixed, their kinetic energy is zero and the potential energy contribution for the nuclei-nuclei interaction is a constant. Using these approximations we can reduce the full Hamiltonian of (2.2) to only the electronic Hamiltonian:

$$\begin{aligned} \hat{H}_{elec} &= -\frac{1}{2} \sum_{i=1}^N \nabla_i^2 - \sum_{i=1}^N \sum_{A=1}^M \frac{Z_A}{r_{iA}} + \sum_{i=1}^N \sum_{j>i}^N \frac{1}{r_{ij}} \\ &= \hat{T}_e + \hat{V}_{Ne} + \hat{V}_{ee}, \end{aligned} \quad (2.3)$$

Here the potential \hat{V}_{Ne} is also called \hat{V}_{ext} , because it is the measure of the nuclei induced external potential the electrons move in.

The eigenfunction of the Schrödinger equation with \hat{H}_{elec} is called $\hat{\Psi}_{elec}$ and the corresponding eigen value is called E_{elec} , represent the electronic energy. $\hat{\Psi}_{elec}$ is a function of the electrons coordinate only. The total energy of the system within the Born-Oppenheimer approximation can be written as,

$$E^{Total} = E_{nuc} + E_{elec}, \quad (2.4)$$

where E_{nuc} and E_{elec} are the energy contribution from the nuclei and electrons respectively.

In the following parts as only the electronic part of the Schrödinger equation is considered; from hereafter \hat{H} will refer to \hat{H}_{elec} .

2.3 Density Functional Theory

Density functional theory^{16,20,21} takes a rather different approach than the wave function based method. Here the electron density rather than the wave functions are the central quantity. The fundamental principle of DFT is that any property of an interacting system of electrons can be viewed as a functional of the ground state electron density $n_0(\mathbf{r})$.

Hohenberg and Kohn in 1964^{20,22} in their pioneering work proved that all the ground and excited state properties of a fully interacting system is determined by the ground state electron density $n_0(\mathbf{r})$. They showed that there is a one to one correspondence between ground state electron density and the external potential. That is for any given ground state electron density there cannot exist more than one external potential. Also that means the ground state electron density of N electrons under some external potential cannot be produced by any other external potential. The total energy functional from Hohenberg-Kohn theorems can be written as,

$$E_{HK}[n(\mathbf{r})] = T[n(\mathbf{r})] + V_{ee}[n(\mathbf{r})] + v_{ext}[n(\mathbf{r})] = T[n(\mathbf{r})] + V_{ee}[n(\mathbf{r})] + \int v_{ext}[n(\mathbf{r})]d\mathbf{r}, \quad (2.5)$$

Where, $T[n(\mathbf{r})]$ is the kinetic energy, $V_{ee}[n(\mathbf{r})]$ is the potential energy from the electron-electron interaction and v_{ext} is the external potential acting on the electrons. We can also rewrite the equation (2.5) as,

$$E_{HK}[n(\mathbf{r})] = F[n(\mathbf{r})] + \int v_{ext}[n(\mathbf{r})]d\mathbf{r} \quad (2.6)$$

Where, $F[n(\mathbf{r})] = T[n(\mathbf{r})] + V_{ee}[n(\mathbf{r})]$.

So Hohenberg-Kohn approach simplified the electronic Hamiltonian to knowing $F[n(\mathbf{r})]$ and the minimizing the total energy in (2.6) with respect to variation in $n(\mathbf{r})$ using the variational principle²³.

Hohenberg-Kohn theorems only proved that there exist a unique $F[n(\mathbf{r})]$ for each system but do not provide any knowledge about the construction of $F[n(\mathbf{r})]$.

2.3.1 Kohn–Sham Theory

To overcome the problem of not knowing the exact form of the $F[n(\mathbf{r})]$ in the Hohenberg-Kohn formalism, Kohn and Sham in 1965^{21,24}, one year after the Hohenberg-Kohn theorem, provided the framework for the construction of an approximate but extremely useful density functional theory for many body electron systems. In order to do this, Kohn and Sham replace the interacting many-body system of Hohenberg-Kohn model with a non-interacting reference (fictitious) system. Kohn-Sham theory is based on the ansatz that the ground state electron density for the reference non-interacting system is equal to the one corresponds to the fully interacting system. Now the Hohenberg-Kohn equation can be reformulated in terms of solvable independent-particle equation and all the non-solvable difficult electronic-electronic interactions are moved to a single exchange-correlational functional. In Kohn-Sham formalism any reference Hamiltonian will do the job as long as it is provided with a correct ground state electron density.

The non-interacting Hamiltonian introduced by Kohn-Sham is given by:

$$\hat{H}_{KS} = -\frac{1}{2} \sum_{i=1}^N \nabla_i^2 + v_s[n], \quad (2.7)$$

where $v_s[n]$ is the effective Kohn-Sham single particle potential ($n = n(\mathbf{r})$) such that the ground state electron density of the \hat{H}_{KS} is equal to the electron density of the real Hamiltonian. The minimization problem of \hat{H}_{KS} is simple if the $v_s[n]$ is known. We can simply solve the Schrödinger equation for each single-electron state $\Phi_i(\mathbf{r})$, with the effective Kohn-Sham single particle potential $v_s[n]$:

$$\left(-\frac{1}{2} \sum_{i=1}^N \nabla_i^2 + v_s[n]\right) \Phi_i(\mathbf{r}) = E_i \Phi_i(\mathbf{r}), \quad (2.8)$$

where E_i is the energy eigenvalue of the electron i . The ground state of (2.7) is a wave function, which is a Slater determinant consist of N lowest eigenstates $\Phi_i(\mathbf{r})$, computed from (2.8) as,

$$\Phi_s = \frac{1}{\sqrt{N!}} \det[\Phi_1, \Phi_2, \dots, \Phi_N]. \quad (2.9)$$

The Kohn-Sham effective potential can be written as,

$$v_s[n] = v_H[n] + v_{\text{ext}}[n] + v_{XC}[n], \quad (2.10)$$

where $v_H[n]$, $v_{\text{ext}}[n]$ and $v_{XC}[n]$ are Hartree potential, external potential and exchange-correlation potential respectively. We can write the Kohn-Sham energy as,

$$E_{KS}[n] = T_S[n] + U_H[n] + \int v_{\text{ext}}[n(\mathbf{r})] d\mathbf{r} + E_{XC}[n], \quad (2.11)$$

The $T_S[n]$ is the kinetic energy of the non-interacting electron and can be obtained from the independent-particle Kohn-Sham orbitals as,

$$T_S[n] = T_S[\Phi_i] = \sum_{i=1}^N \langle \hat{\Phi}_i | -\frac{1}{2} \nabla_i^2 | \hat{\Phi}_i \rangle, \quad (2.12)$$

Comparing the Kohn-Sham energy in (2.11) with the Hohenberg-Kohn energy in (2.5), we get the expression for the exchange-correlation functional:

$$\begin{aligned} E_{XC}[n] &= (E_{KS}[n] - \int v_{\text{ext}}[n(\mathbf{r})] d\mathbf{r}) - (T_S[n] + U_H[n]) \\ &\approx F_{KS}[n] - (T_S[n] + U_H[n]) = (T[n] - T_S[n]) + (E_{\text{int}}[n] - U_H[n]), \end{aligned} \quad (2.13)$$

where $T[n]$ and $E_{\text{int}}[n]$ have to be calculated from a true many body wave function, and these make the formalism of the exchange-correlation energy of a many-body system very complicated. From equation (2.13) we can say that the exchange correlation energy is the sum of the difference in the kinetic and potential energy between the interacting many body electron system and the non-interacting fictitious Kohn-Sham systems, where the real electron-electron interaction has been replaced by the classical Hartree energy. The second term contains both the non-classical exchange and correlation term. The exchange correlation potential is defined as a functional derivative of the $E_{XC}[n]$ with respect to the electron density,

$$v_{XC}[n] = \frac{\delta E_{XC}[n]}{\delta [n(\mathbf{r})]}. \quad (2.14)$$

The Kohn-Sham energy for a system with N electrons with electron density $n(\mathbf{r})$ can be written as,

$$E_{KS}[n] = \sum_{i=1}^N \langle \hat{\Phi}_i | -\frac{1}{2} \nabla_i^2 | \hat{\Phi}_i \rangle + \int v_{\text{ext}}[n(\mathbf{r})] d\mathbf{r} + \frac{1}{2} \int \frac{n(\mathbf{r})n(\mathbf{r}')}{|\mathbf{r} - \mathbf{r}'|} d\mathbf{r} d\mathbf{r}' + E_{XC}[n]. \quad (2.15)$$

The expression for the E_{KS} is exact is if we can find the exact exchange-correlation functional. Unfortunately we do not have any exact formulation of the E_{XC} . So in practice we have to use the approximate representation of the exchange-correlational functional.

2.4 Exchange–Correlation Functionals

Exchange

The electrons are fermions and hence their wavefunctions are anti-symmetric under exchange. That means the electron density do not change when two electrons exchange

their special position. The simplest implementation is the Hartree-Fock approximation²², where the electron-electron interaction energy is called exchange energy.

Correlation

Due to the electron-electron repulsion, the presence of one electron in a given spatial position decreases the probability of finding another electron in the vicinity. In other word there is a strong correlation between the positions of one electron relative to the other electron present in the system and hence the electron gas is not homogeneous. This is the origin of the correlation energy.

2.4.1 Local Density Approximation (LDA)

The construction of the exchange-correlation functional is not simple as has been explained earlier. LDA assumes that the density at a point in space of any many electrons system can be considered a homogeneous electron gas.^{21,22,25} In this way we can obtain the exchange-correlation energy of an inhomogeneous system by doing integration over all the space. The exchange-correlation energy obtained using LDA can be written as,

$$E_{XC}^{LDA} = \int n(\mathbf{r}) \varepsilon_{XC}^{HEG} n(\mathbf{r}) d\mathbf{r}, \quad (2.16)$$

where $\varepsilon_{XC}^{HEG} = \varepsilon_X^{HEG} + \varepsilon_C^{HEG}$, where ε_{XC}^{HEG} , ε_X^{HEG} , ε_C^{HEG} are exchange-correlation functional, exchange functional and correlation functional of the homogeneous electron gas respectively.

LDA performs remarkably well for electronic structure calculation of the periodic solids. The error on the LDA predicted lattice parameters are in the order of only few percent. But LDA performs badly in the field of chemical bonding. LDA generally overestimates the binding energy and underestimates the bond length.²⁶

2.4.2 Generalized Gradient Approximation (GGA)

Generalized Gradient Approximation²⁷⁻³¹ is an improvement over LDA as it also includes the gradient of the electron density into the exchange-correlation energy expression.^{28,30-33}

$$E_{XC}^{GGA} = \int n(\mathbf{r}) \varepsilon_{XC}^{GGA}(n(\mathbf{r}), \nabla n(\mathbf{r})) d\mathbf{r}, \quad (2.17)$$

where,

$$\varepsilon_X^{GGA} = \varepsilon_X^{HEG}[n] \cdot F_x(s(n, \nabla n)), \quad (2.18)$$

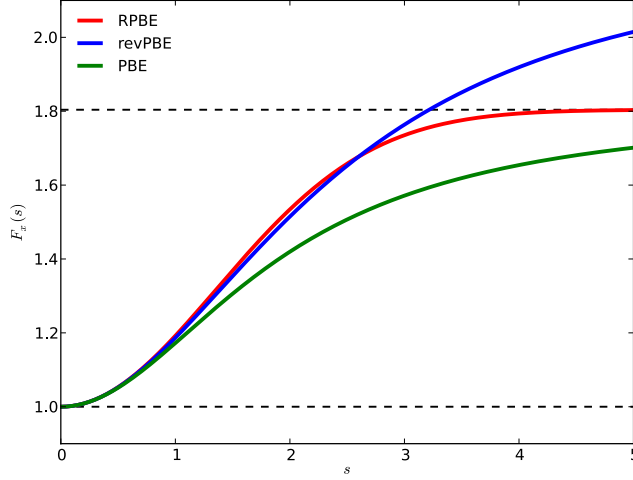


Figure 2.1: Exchange enhancement function of various GGA exchange functional.

where $F_x(s)$ is the exchange enhancement factor, the reduced density gradient $s = \frac{|\nabla n(\mathbf{r})|}{2\kappa_F n} \in [0, \infty]$, where $\kappa_F = (3\pi^2 n(\mathbf{r}))^{\frac{1}{3}}$

2.4.3 PBE and RPBE Functionals

PBE³⁴ exchange correlation functional proposed by Perdew, Burke and Ernzerhof. In case of the PBE functional, the exchange enhancement factor $F_x(s)$ is given by,

$$F_x^{PBE}(s) = 1 + \kappa - \frac{1}{1 + \frac{\mu s^2}{\kappa}} \quad (2.19)$$

where the constant $\mu = 0.21951$ and $\kappa = 0.804$ are chosen to obey the LDA limit $F_x(s=0) = 1$ and Lieb-Oxford lower bound³⁵ $F_x(s) \leq 1.804$.

GGA correlations approximations are more complex and mostly obtained from correction of the LDA correlation. PBE and LYP (Lee-Yang-Parr)³⁶ are the two most commonly used GGA correlation functionals. The PBE exchange correlation functional is a much improved XC functional over the LDA or PW91³⁷ (GGA functional). Though PBE captures most of the solid-state properties and chemical bonding correctly, there is a general trend that the PBE overestimates the binding energy of the adsorbates (atoms and molecules) to a solid surface.

RPBE³⁸ is a revised version of the PBE exchange-correlation functional, developed to correct the over-binding of the adsorbates to the surface. In case of RPBE the

exchange enhancement factor is expressed as,

$$F_x^{RPBE}(s) = 1 + \kappa(1 - \exp(-\frac{\mu s^2}{\kappa})) \quad (2.20)$$

which resembles revPBE³⁹ (same as PBE, but $\kappa = 1.245$) at small reduced density and resembles PBE at larger reduced density as shown in Figure 2.1. As RPBE gives binding energy with higher accuracy than PBE, it has been used for most of the adsorption energy and transition state energy calculations done in this thesis.

2.5 Implementation of Density Functional Theory

We have already seen that in density functional theory the weak link is the unknown exchange correlation term. If we have a good XC functional, we can calculate the ground state energy and electron density by solving the Kohn-Sham equation iteratively using the self-consistent method. However when we consider the implementation of DFT in a computer program, the representation of the Kohn-Sham orbitals poses the main problem. Commonly they are represented using expression in the atom-centered orbital or plane-waves or numerical representation on a real-space grid.

To overcome the rapidly oscillating wave functions in the core region, the frozen core approximation is applied. The core orbitals are not allowed to relax in the SCF(Self Consistent Field) procedure. The physical justification for the frozen core approximation is that the most of the interesting chemical processes takes place in the outer region of the electrons and change in the electronic environment at the core is very small and therefore can be neglected.

2.5.1 DACAPO Code

DACAPO is an open source implementation of DFT developed and maintained at CAMD.⁴⁰ It uses the plane wave basis set for the valence electrons and Vanderbilt ultra-soft pseudopotential for the core electrons. DACAPO code has been used extensively in these thesis and attached papers for the calculation of gas phase energy of the molecules, adsorption energy of surface species and transition state energy of chemical reaction. In this section I have briefly discussed some of the key parameters of the Dacapo code.

Plane wave basis and Cut-off energy

In Dacapo the wave functions of the electrons are expanded in a plane wave basis set. As proposed in the Bloch's theorem, to use the plane wave basis we also require periodic

super cell. Bloch theorem⁴¹ states that, for a periodic system the wave function can be expanded into a plane wave basis set as,

$$\Psi_i(r) = \sum_j C_{i,j} \Phi_j(r) = \sum_G C_{i,k+G} e^{i(k+G)r} \quad (2.21)$$

where $C_{i,k+G}$ are the expansion coefficient, k is the wave vector in the first Brillouin Zone, and G is the wave vector in the reciprocal space. In principle one need infinite number of plane waves to represent the wave function for each k -points. However as the $C_{i,k+G}$ coefficient for large kinetic energies become very small, finite number of plane wave basis are sufficient to obtain approximate wave function and total energy. The plane wave basis set is truncated by introducing certain Cut-off energy, $\frac{1}{2}|k+G|^2 \leq E_{Cut-off}$.

We can also improve the accuracy by using high-energy plane waves for the expansion of electron density rather than the wave functions. We use certain density cut-off energy for this. That means the density cutoff energy is always higher than the energy cutoff. While using DACAPO the most computationally expensive part is the calculation of the wave function and hence increasing the energy cut-off ($E_{Cut-off}$) increases the computational time, whereas increasing the density cut-off do not increase the computational time significantly, it only require larger memory.

As the crystals are periodic, for the bulk metal structure calculation the periodicity is present naturally. However for the gas phase calculation of the single atom and molecule and for the surface slab calculation we need to apply the periodicity forcefully. The common way to do it is to increase the super cell in one or more direction and have enough vacuum in between so that there is no interaction between the gas phase species or the surface slabs of two adjacent super cells in those directions.

***k*-point sampling**

As shown previously in the plane wave basis set formalism, one must evaluate the wave function at each reciprocal lattice vector in the first Brillouin zone and there can be infinite different reciprocal lattice. However the band energies of the two neighboring lattice are almost the same and hence calculating energy at a finite number of lattice vectors is enough. This is called the k -point sampling⁴². k -point sampling should be chosen wisely, as using too few k -points will give erroneous results whereas using too many k -points than required, is a waste of computer power. As the gas phase atoms and molecules have discrete energy levels for these calculations it is enough to do the sampling in the Γ -point.

Pseudopotentials

As discussed before, to reduce the computer calculation time, one can replace the tightly bound core electrons by the pseudopotentials. The pseudopotential is the potential felt by the electron inserted upon them by the nuclei and core electrons. However to represent the rapidly oscillating wave function near the core we still need high energy plane waves and hence a very high $E_{Cut-off}$ is needed and this increases

the required computer time by many folds. This problem is genuine and is encountered in both all electron and pseudopotential approach. The introduction of the ultra-soft pseudopotentials by Vanderbilt⁴³ give us the handle to reduce the number of the plane waves required for the representation of the rapidly oscillating wave functions. To reduce the oscillation in the wave function near the core, in Dacapo the deep potential closed to the core is replaced by the smoother ultra-soft pseudopotential. As using different pseudopotentials will give different total energy, now the absolute value of total energy is meaningless- and only the difference between total energies of two systems obtained using the same pseudopotential is the meaningful quantity.

2.6 Summary

The main fundamental theories of quantum mechanics have been outlined. The Kohn-Sham density functional approach to obtain the ground state electronic properties for many electronic system is discussed. Kohn-Sham DFT theory is an exact theory if the exact exchange-correlation is known, which is not the case and hence one need to approximate the XC functional for the DFT theory. There are few thousands different XC functionals with different approximation. In the field of surface science the most commonly used XC functionals are PW91, PBE, RPBE and B3LYP (hybrid functional)⁴⁴⁻⁴⁶. Due to good accuracy of RPBE in estimation of metal- adsorbate bonding energy, it has been used almost exclusively throughout this PhD thesis. For the implementation of DFT for the electronic structure calculation the ultrasoft pseudopotential based DACAPO DFT code is introduced here. For this PhD thesis the DACAPO method have been used extensively.

CHAPTER 3

Heterogeneous Catalysis

In this chapter we will briefly discuss the heterogeneous catalysis and the factors determining the catalytic reactivity of a catalyst. This chapter is the background of the material discussed in the thesis and also the included papers. I will present a brief discussion on the d-band model and the trends in the chemisorption energies among the transition metals. I will then move on to describe different correlations between the adsorption energies and activation barriers, most notably the Brønsted-Evans-Polanyi (BEP) relation. Then a brief discussion on the electronic and geometric effects and how they can affect the catalytic activity by changing the activation barriers will be presented. Finally I will show how to use these correlations and understanding to calculate a catalytic rate volcano curve and find the catalytic trends.

3.1 Catalysis

Catalysis is the phenomena of increasing in rate of a catalytic reaction through the involvement of a substance known as catalyst. A catalyst only affects the kinetics of a reaction by lowering the activation barrier while the thermodynamics of the reaction remains unaffected. Heterogeneous catalysis in general works in a closely coupled four-step process. First, the catalyst adsorbs the reactants, then it breaks the required bonds between the reactants, next it helps the reactants to react between themselves to form new bonds in the products and finally the products desorb from the surface.

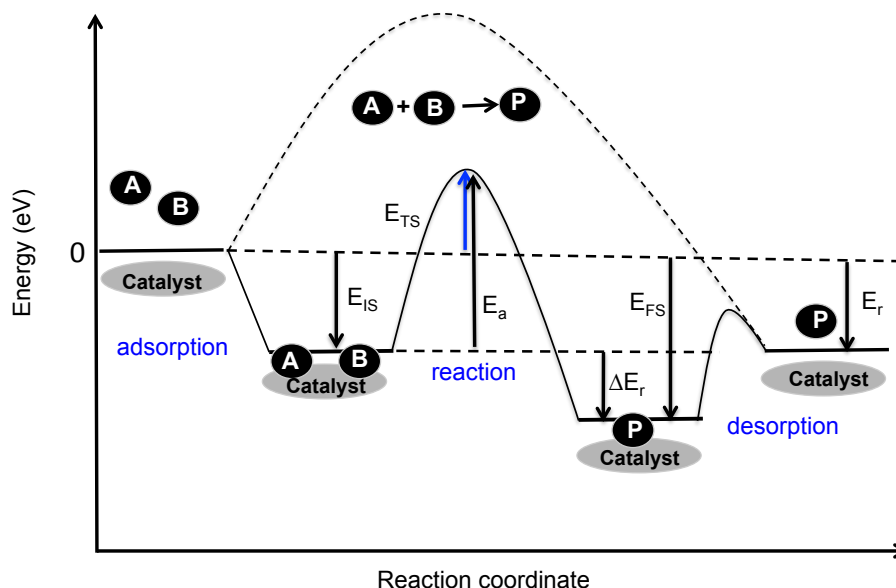


Figure 3.1: Schematic energy diagram for a chemical reaction of reactant A and B reacting on a catalyst surface to give product P is shown along the reaction coordinate of the reaction. The general energy notations used in catalysis, like the initial state energy E_{IS} , final state energy E_{FS} , transition state energy E_{TS} , activation barrier E_a , reaction energy of an elementary step ΔE_r and overall reaction energy of the process E_r are also depicted.

Heterogeneous catalysts are widely used in chemical industry⁴⁷, such as NH_3 synthesis using the Haber-Bosch process, HNO_3 synthesis using the Ostwald process, olefin polymerization using the Ziegler-Natta catalyst, H_2 production using the steam reforming etc.

As discussed earlier, a catalytic reaction generally occurs in a number of elementary steps. We generally describe the whole reaction mechanism with a potential energy diagram shown in Figure 3.1.⁴⁷ The potential energy diagram shows the relative energies of the reactants, products and intermediates with the activation barriers between them for each elementary reaction. The lowest energy configuration of the reactant region and product region are generally depicted as initial state (E_{IS}) and final state (E_{FS}), respectively, whereas the transition state is the local maxima separating the initial and the final states. The energy difference between the transition state and the gas phase species as the transition state energy (E_{TS}) whereas the difference between the transition state and the initial state is referred to as the activation barrier (E_a). The reaction energy, ΔE_r is the energy difference between the initial state and the final state.

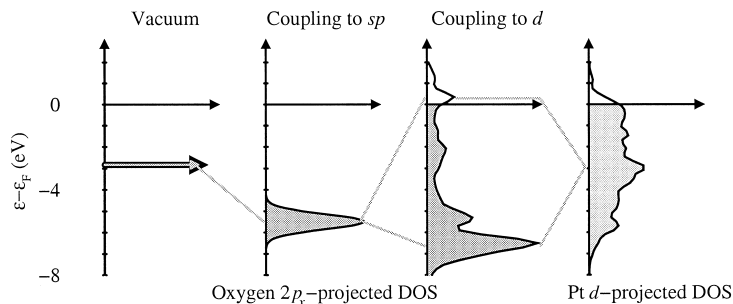


Figure 3.2: Schematic illustration of the change in projected density of states of the oxygen atom upon adsorption on the Pt{111} transition metal surface. Adapted from Ref. 48

3.2 d-band Model and Trends in Chemisorption Energies

The d-band model proposed by Hammer and Nørskov^{48–51} correlates the systematic change in the adsorption energy along a given metal series to the position of the d-band center compared to the Fermi level of the metal surfaces.

During the adsorption process the adsorbate energy level first interacts with the metal *sp* band and gets broadened and shifted. Then this broadened adsorbate band interacts with the narrow metal *d*-band and gets split into bonding and anti-bonding states, as shown in Figure 3.2. All the transition metals have a half-filled broad *s*-band. Hence it has been assumed in the d-band model that the interaction of the adsorbate with the metal *s*-band is independent of the metal in question. Therefore the trends in adsorption energy only depends on the interaction between the metal *d*-state and adsorbate. However it is invalid for the metals where the *d*-band of the metal does not contribute to the adsorption energy.⁴⁹

3.2.1 Trends in Chemisorption Energies

The trends in the chemisorption energy of the different adsorbates over different transition metals have been explained using the d-band model.^{48,49,52} In reference⁴⁸ Hammer et al. used the d-band model to predict the trends in the dissociative chemisorption energy of atomic oxygen, shown in Figure 3.3. Generally a lowering of the d-band center relates to a decrease in the bond strength due to the weakening of the metal-adsorbate bonding. As the metal *d*-band center is downshifted in energy or the *d*-band becomes broadened, the anti-bonding orbitals become more occupied and this results

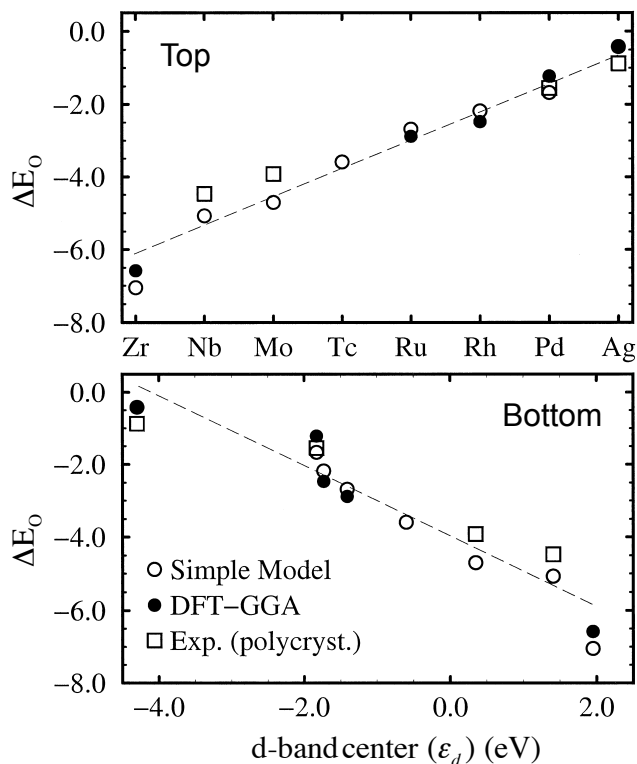


Figure 3.3: (Top) Comparison of DFT-calculated oxygen chemisorption energies (relative to O_2 gas phase), $E(O/surface) - \frac{1}{2}E(O_2) - E(surface)$ (PW91), experimental values, and model estimates of the bond strengths for various close-packed transition and noble metal surfaces. Data represented by open circles were determined by using the Newns-Anderson model.⁴⁹ The experimental values are from Toyoshima and Somorjai. (Bottom) The calculated adsorption energies correlate well with the d band center ϵ_d . Adapted from Ref. 48

in a weaker metal-adsorbate bond.

3.3 Surface Structure and Reactivity

The surface of metal nanoparticles used in industry generally consists of different local structures like terraces, steps and kinks.^{54–57} In Figure 3.6, I have shown the schematic diagram of the $\{111\}$ and $\{100\}$ terrace; $\{110\}$, $\{211\}$ and $\{311\}$ stepped and $\{532\}$ kink surfaces. The terrace, step and kink site have different coordination

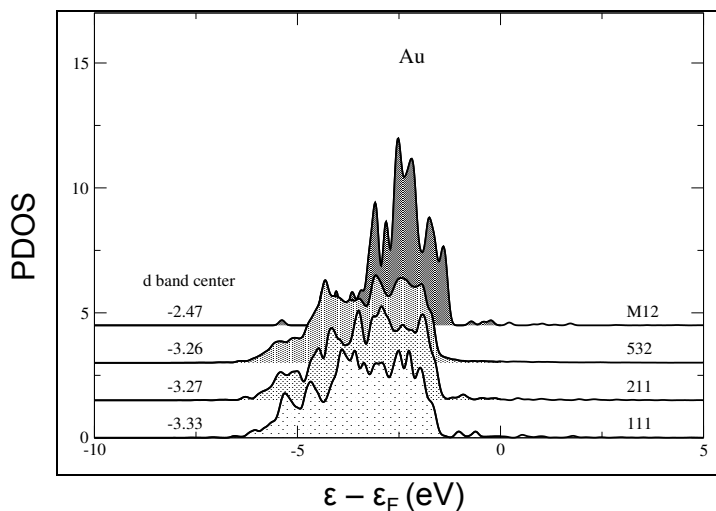


Figure 3.4: Local projected DOS for the lowest coordinated metal atoms on different surface structures of Au metal. Adapted from ref. 53

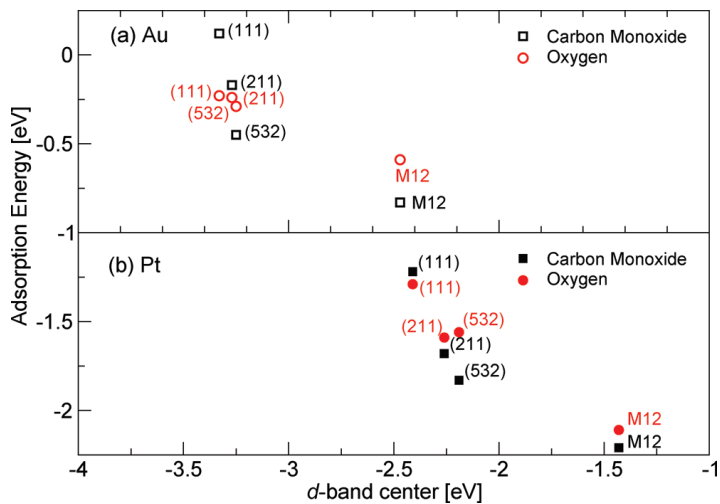


Figure 3.5: Adsorption energy E_{CO} and E_O versus d-band center for {111} surfaces, {211} surfaces, {532} surfaces, and {M12} clusters of (a) Au (open black square, open red circle) and (b) Pt (solid black square, solid red circle). Adapted from ref. 54

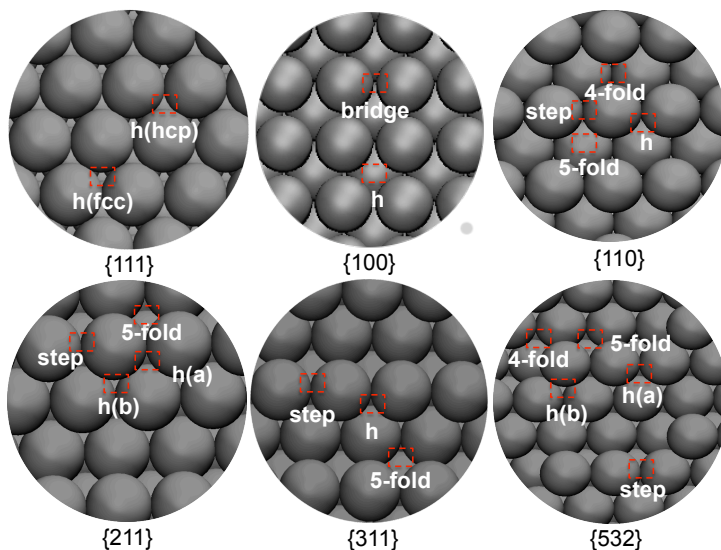


Figure 3.6: Schematics of the surface structure of the $\{111\}$, $\{100\}$, $\{110\}$, $\{211\}$, $\{311\}$ and $\{532\}$ facets. The different active sites present on these facets are also shown.

number. For the terrace atom in $\{111\}$ and $\{100\}$ surfaces, the coordination number is 9 and 8 respectively; for the step atom in stepped $\{110\}$, $\{211\}$ and $\{311\}$ and kink $\{532\}$ surfaces, the coordination number is 7 and for the kink atom in $\{532\}$ surface, the coordination number is 6. The reactivity of a metal site generally increases with decreasing coordination number.

The d-band model also can explain the reactivity of the different surface structures.^{54,58} The corner atom of a 12 metal cluster $\{M12\}$ has coordination number 4. The position of the d-band center of a metal atom on different surface structures depends strongly on the coordination number. The d-band center shifts up in energy as the coordination number of the active site is reduced. The higher the coordination number, the lower the d-band center of the metal for that surface structure, and hence the surface is less reactive. In Figure 3.4, the local projected density of states of the metal d-band center of the different facets $\{111\}$, $\{211\}$, $\{532\}$ and $\{M12\}$ are shown. As described earlier the coordination number increases in the following order $\{M12\} < \{532\} < \{211\} < \{111\}$, and the trend in the position of the d-band center is $\{M12\} > \{532\} > \{211\} > \{111\}$. Therefore, the reactivity of the metal surfaces follows the trend $\{M12\} > \{532\} > \{211\} > \{111\}$ and is linearly correlated to the position of the d-band center of the metal surfaces, shown in Figure 3.5.

3.4 Correlation from DFT Calculations

I already have shown that the adsorption are governed by some fundamental properties of the surfaces and adsorbates. It has been shown by Nørskov et. al. that the transition states energies also governed by the same fundamental properties.^{48,49} Therefore, one should presume that the adsorption energies and the transition state energies for different adsorbates and transition states should also be correlated.^{49,58,59} These underlying correlations are very important for understanding the factors affecting the catalytic activity in heterogeneous catalysis.

3.4.1 Adsorption Energy Scaling

Due to the same underlying electronic factors the adsorption energies of different atoms and molecules are correlated with each other following linear scaling between them, known as adsorption energy scaling. Due to the adsorption energy scaling, one can express the adsorption energies of all the reaction intermediates, even for a very complex reaction, using one or two parameters, usually the binding energy of carbon, oxygen and nitrogen atom. These parameters are usually called the descriptors of the catalytic reaction. Also using the adsorption energy scaling one can get an approximate binding energy of an adsorbate over any transition metal without doing the DFT calculation.^{3,49,60}

3.4.2 Brønsted-Evans-Polanyi Relationship

The linear correlation between the reaction activation barriers and the reaction energies is known as the Brønsted-Evans-Polanyi relationship,^{61,62} as is given as, $E_a = \alpha \Delta E + \beta$, where E_a is the activation barrier and ΔE is the reaction energy for the surface reaction. The constants α (slope of the linear scaling) and β (intercept of the linear scaling) are called scaling parameters. The BEP relations are really important, as they provide a simple tool to understand the activity of different metal surfaces.⁶³⁻⁶⁹ The BEP relations can be used as a tool to obtain an estimated activation barrier from the adsorption energies. A slope close to 1, i.e $\alpha = 1$, as mainly seen in the case of dissociation for the diatomic molecules implies that the transition state is final state like. The electronic and geometric effect on the BEP scaling relation will be discussed briefly in the next section 3.5.

3.4.3 Universal Relationship

It has been found that for similar type of reactions the BEP scaling relation is universal, or in other words for dissociation of a number of similar molecules, the scaling relations

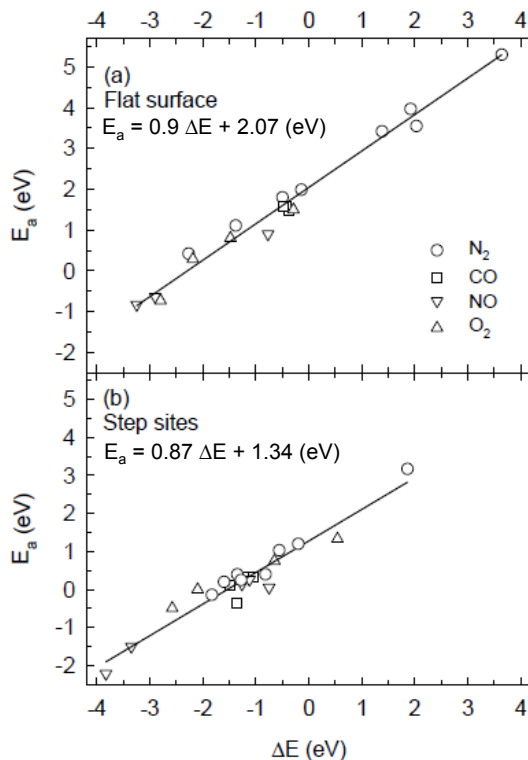


Figure 3.7: The universal BEP-relations for dissociative chemisorption of diatomic molecules on (a) close-packed surfaces and (b) stepped surfaces. Adapted from Ref. 6

between the transition state energy and reaction energy are very similar. This is referred to as the universality of BEP relations.^{6,70–72} In Figure 3.7 the universal BEP scaling relations has been shown for dissociative chemisorption of diatomic molecules over both close-packed $\{111\}$ and stepped $\{211\}$ transition metal surfaces. For the close-packed surfaces the universal BEP relation is, $E_a = 0.90 \Delta E + 2.07 \text{ eV}$. Whereas for the stepped surfaces the universal BEP relation is, $E_a = 0.87 \Delta E + 1.34 \text{ eV}$. As the electronic structures of the transition states resemble each other very strongly, the correlation between the transition state energy and the dissociative chemisorption energy of the different diatomic molecules turns out to be the same over same kind of surface structure.

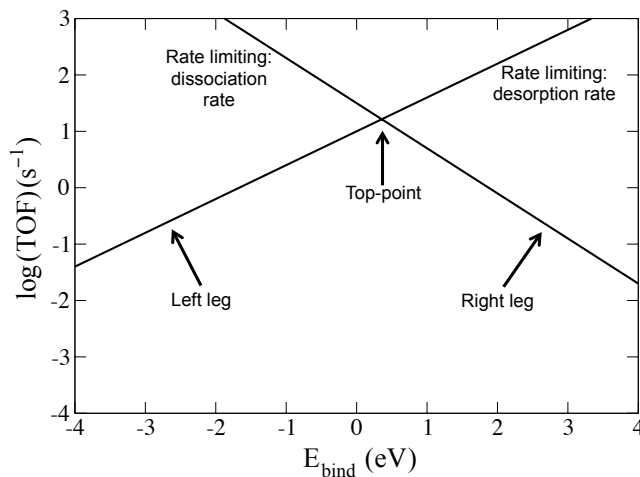


Figure 3.8: The catalytic activity versus the binding energy of the descriptor (E_{bind}). A more negative reaction energy (left) means that the adsorption reaction is more exothermic. The top-point refers to the point with highest catalytic rate.

3.5 Electronic and Geometric Effect

The origin of the electronic effect is due to the changes in the d-band center. The electronic effect shifts the transition state energy (ΔE_{TS}) and the reaction energy (ΔE) in the same way, and thus the individual points move along the same BEP line. For a given surface structure, more reactive metal surfaces have both a lower transition state energy and a lower reaction energy than a less reactive metal surface.

The shift of the BEP line along the y-axis for different surface structures is purely due to the difference in “geometric stabilization” of the transition states, is referred to as the geometric effect. For example, in Figure 3.7 the BEP line for dissociation of diatomic molecules over the stepped $\{211\}$ surface is ~ 0.8 eV lower than the flat close-packed $\{111\}$ surface due to the geometric effect. On a $\{111\}$ surface, the transition state is stabilized by 4 metal atoms and one metal atom is shared between the two adsorbate atoms giving rise to the destabilization of the transition state. Whereas for the $\{211\}$ surface the transition state generally occurs at the ‘B5-site’, where it is stabilized by 5 metal atoms and none of the metal atoms are shared between the adsorbate atoms. Hence, the transition state is more stabilized than the $\{111\}$ surface and thus gives rise to the lower lying BEP line for the $\{211\}$ facet.^{49,56,59,70,73}

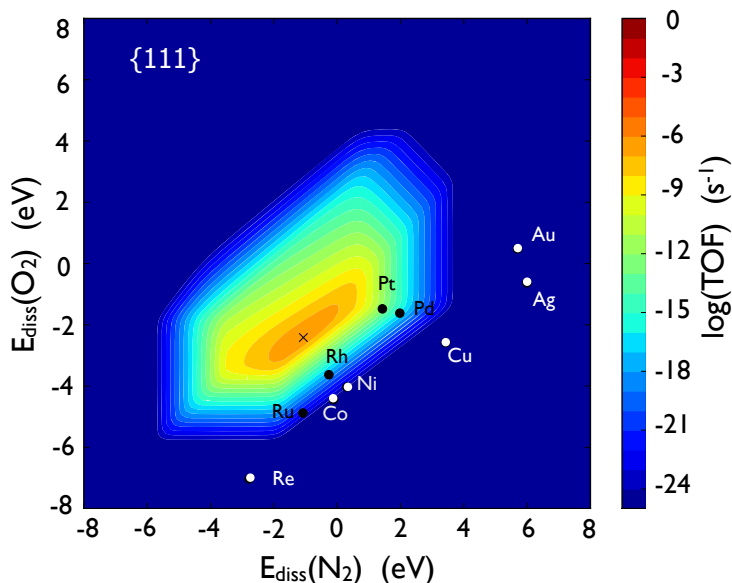


Figure 3.9: A two dimensional contour plot of the catalytic activity of direct NO decomposition over the $\{111\}$ transition metal surfaces versus the dissociative chemisorption energy of the two descriptors, here N and O. Top-point with highest catalytic rate is shown as the black cross. The reaction considered here is $2 \text{NO(g)} \leftrightarrow \text{N}_2\text{(g)} + \text{O}_2\text{(g)}$, reaction condition $p_{\text{NO}} = 0.001$ bar, $p_{\text{O}_2} = 0.1$ bar, $p_{\text{N}_2} = 0.7$ bar and $p_{\text{total}} = 1$ bar, $T = 700\text{K}$.

3.6 Microkinetic Modeling and Volcano Curves

Microkinetic modeling is a method to obtain the steady state kinetics, given that we provide the necessary input parameters (reaction conditions, gas-phase energies, adsorption energies and transition state energies of the species involved),^{6,49,73–76} Microkinetic modeling does not need to assume any elementary steps as the rate-determining step. If one is sure about the rate-determining step for the whole reaction scheme, it is usually a good idea to solve the kinetics for that reaction analytically. However, in most of the catalytic reactions we do not have good information about the rate-determining step before-hand, and hence it is often better to use the steady-state microkinetic model to obtain the catalytic reactivity and then from the kinetic output determine the rate-determining step (if one exist). Microkinetic modeling also has the potential to provide us many important information about the kinetics like “degree of rate control”, “order of the reaction” etc.

A reaction scheme usually consists of a number of elementary steps. As discussed before the adsorption energies of the intermediates and the transition state energies of

the elementary steps are scaled against binding energies of most relevant intermediates, usually carbon, oxygen or nitrogen. These binding energies are called as descriptors in microkinetic modeling. Using these scaling parameters one can obtain the adsorption energies and transition state energies for any value in the descriptor space. The forward and backward rate constant for each elementary steps are obtained using the activation free energy barriers. Then the differential equations for each elementary steps is constructed based on the microkinetic model. The differential equations consist of the surface coverages of the species, forward and backward rate constants and concentration of the species (e.g. partial pressure for gas-phase species). For a given simulation we need to assume some realistic initial reaction condition and initial coverage, and then solve the coupled differential equations self-consistently until a steady state solution is obtained.

As we already have stated due to the underlying correlation between the adsorption energies and transition state energies we can describe the catalytic activity trend of a catalytic reaction, just using one or two descriptors, usually known as one dimensional (shown in Figure 3.8) and two-dimensional volcano curve (shown in Figure 3.9). As shown in Figure 3.8, for the reactive metals (left to the top of the volcano, higher ΔE), the removal of the dissociated product from the surface to the gas phase is the rate limiting step, whereas for the less reactive metals (right to the top of the volcano, lower ΔE), the activation energy barrier for the dissociation process is high and hence the activation of the key reactant is the rate limiting step. The optimal catalyst with the highest catalytic rate sits at the top of the volcano curve, known as the top-point of the volcano. It can be seen the catalyst-adsorbate interaction is “just right” for the optimal catalyst as predicted by P. Sabatier, neither too weak for activating the dissociation of chemical bond nor too strong that the surface become blocked due to low desorption rate.^{47,77} We will see more of the two dimensional volcano curves in the following chapters.

CHAPTER 4

Structure Sensitivity of Direct NO Decomposition

Nitrogen oxides (NO_x) are harmful pollutants and their removal is also very challenging. Hence the NO_x emission requirements in Europe and USA are very stringent. With increasing use of hi-duty diesel engine, known to form more NO_x than other conventional engines, we need a better NO_x removal technology, effective under the lean burn condition to meet the stringent NO_x emission requirement.^{78,79} Various sophisticated technologies like fuel injection, exhaust gas recirculation, NO_x traps and selective catalytic reduction are presently available.^{78–81} However it would be preferable to have a simple process for NO_x removal, if one can directly decompose the NO_x in the exhaust gas over a metal catalyst to form N_2 and O_2 .^{74,75}

In heterogeneous catalysis, transition metals are commonly used as nanoparticles to maximize the metal surface area. As we have discussed in the previous chapter the surface of the metal nanoparticle can have different local surface structure like terrace, steps and kinks, edges and corners.^{54,55,57,73,82} It is well known from the experiments and theoretical studies that the catalytic activity for the different facet can vary by several orders of magnitude and hence the catalytic activity of a nanoparticle will also depend on the area different facets present in the nanoparticle in the reaction condition.^{2,56,58,83,84}

In this chapter, I will analyse the structure sensitivity of the BEP^{61,62} through a systematic study on the change in the BEP relationship over different transition metal facets; {111}, {100}, {110}, {211}, {311} and {532}.^{63–69} I will also discuss the cause

Table 4.1: Computational details.

Surface	k-mesh	unitcell	#atoms
{111}	$8 \times 8 \times 1$	2×2	16
{100}	$8 \times 8 \times 1$	2×2	16
{110}	$8 \times 6 \times 1$	2×2	28
{211}	$8 \times 6 \times 1$	2×1	24
{311}	$8 \times 6 \times 1$	2×2	24
{532}	$6 \times 6 \times 1$	1×1	24

of structure sensitivity of the BEP in terms of electronic and geometric effect. I also have studied the microkinetic model based on the adsorption energy and BEP scalings to obtain the catalytic rates for the different surfaces. From the catalytic rate volcano for the different metal surfaces I will discuss the structure sensitivity of the catalytic activity and trends. In the end I will present a sensitivity study of the catalytic rate by varying the number of microkinetic model descriptors.

4.1 DFT Setups

Adsorption, transition state, and gas-phase energies were obtained from using the plane wave density functional theory DACAPO code.⁴⁰ The exchange-correlation (xc)-energy was described by employing the RPBE generalized gradient correction self-consistently.³⁸ Vanderbilt nonlocal ultrasoft pseudopotentials are used to describe the core electrons.⁸⁵ Kohn-Sham one-electron valence states were expanded in a basis of plane waves, which were truncated at a energy cutoff of 340 eV and a density cutoff of 680 eV. The Fermi population of the Kohn-Sham state was calculated at electronic temperature of $k_B T = 0.1$ eV, and all energies have been extrapolated to $T = 0$ K. The surface Brillouin zone was sampled using a Monkhorst-Pack grid.⁸⁶ The surface model and k-point sampling are shown in Table 4.1.

The {111}, {100}, and {110} surfaces were modeled with a slab thickness of four layers and the two topmost layers were allowed to relax. For the {211}, {311} and {532} surfaces the upper half of the atoms in the unit cell were allowed to relax. An inter slab vacuum separation of at least 10 Å were used for all surfaces. Transition state energies were calculated by increasing the bond length of the diatomic molecule in small steps until a saddle point was reached. The {111} and {100} surfaces were modeled with a slab thickness of four layers and the two topmost layers were allowed to relax. The {110} surfaces were modeled with a seven layer slab and the four topmost layers were allowed to relax. For the {211}, {311} and {532} surfaces the upper half of the atoms in the unit cell were allowed to relax. A vacuum of more than 10 Å separated the successive slabs. Transition state energies were calculated using the fixed bond length (FBL) method.

4.2 Microkinetic Model

We here describe the microkinetic model used to obtain the catalytic activity of direct NO decomposition based on the calculated adsorption energies and activation energies from DFT. The microkinetic model employed here is built on the assumption that the reaction has reached steady state.

The direct NO decomposition is assumed to take place via the following reaction steps:

1. $\text{NO(g)} + * \leftrightarrow \text{NO}^*$
2. $\text{NO}^* + * \leftrightarrow \text{N}^* + \text{O}^*$
3. $2 \text{O}^* \leftrightarrow \text{O}_2(\text{g}) + 2^*$
4. $2 \text{N}^* \leftrightarrow \text{N}_2(\text{g}) + 2^*$

At steady state the reaction rate for all the elementary step is equal, hence the overall NO decomposition reaction rate $R = R_1 = R_2 = 2R_3 = 2R_4$, where the rate for each elementary step is given by:

1. $R_1 = p_{\text{NO}}\theta_*k_1 - \theta_{\text{NO}}k_{-1}$
2. $R_2 = \theta_{\text{NO}}\theta_*k_2 - \theta_{\text{N}}\theta_{\text{O}}k_{-2}$
3. $R_3 = \theta_{\text{NO}}\theta_*k_2 - \theta_{\text{N}}\theta_{\text{O}}k_{-2}$
4. $R_4 = \theta_{\text{N}}^2k_4 - p_{\text{N}_2}\theta_*^2k_{-4}$

θ_{O} , θ_{N} , θ_{NO} and θ_* are the coverages of O, N, NO and free sites respectively. The forward rate constant is given by,

$$k_i = v_i \exp\left(\frac{-(E_{a_i} - T\Delta S_{a_i} + \Delta \text{ZPE}_{a_i})}{k_B T}\right) \quad (4.1)$$

,where v_i is the prefactor, E_{a_i} is the activation energy, ΔZPE_{a_i} is change in zero point energy, ΔS_{a_i} is the change in entropy, T is the temperature, k_B is the Boltzmann's constant. We obtain the backward rate constant from $k_{-i} = \frac{k_i}{K_i}$, where K_i the equilibrium constant. The prefactor is considered metal independent and given by $v_i = \frac{k_B T}{h}$. The activation energy $E_{a_i} = E_{\text{TS}} - E_{\text{IS}}$, the activation entropy $\Delta S_{a_i} = S_{\text{TS}} - S_{\text{IS}}$, activation zero point energy $\Delta \text{ZPE}_{a_i} = \text{ZPE}_{\text{TS}} - \text{ZPE}_{\text{IS}}$, where,
 E_{TS} = transition state energy,
 E_{IS} = initial state energy,
 S_{TS} = transition state entropy,
 S_{IS} = initial state entropy,
 ZPE_{TS} = transition state zero point energy and

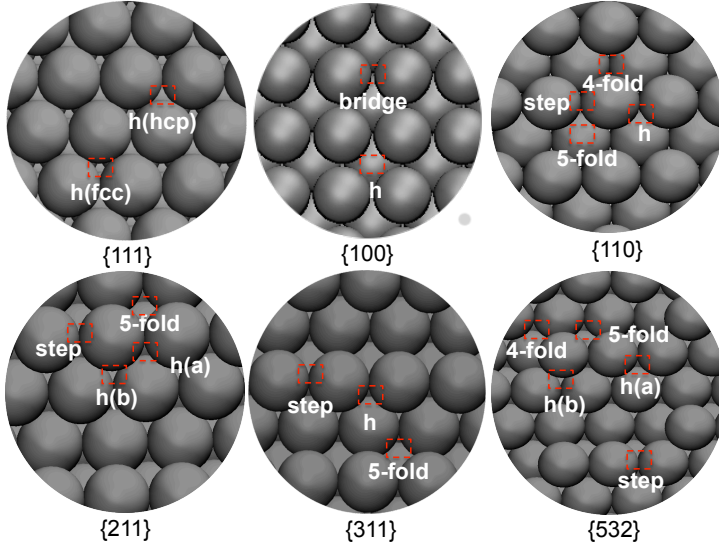


Figure 4.1: Schematics of the surface structure of $\{111\}$, $\{100\}$, $\{110\}$, $\{211\}$, $\{311\}$ and $\{532\}$ facets. The different active sites present on these facets are also shown.

ZPE_{IS} = initial state zero point energy.

We further assume that the entropies of the adsorbed species do not change appreciably for different metals and metal facets. Entropy of the adsorbed and transition state species are calculated on Rh $\{111\}$ surface, are used for all the metals and different metal facets. Gas-phase entropies are taken from ref. 87.

4.3 DFT Results

For a number of transition metals, Ag, Au, Co, Cu, Ni, Pd, Pt, Re, Rh and Ru; and the following metal facets, $\{111\}$, $\{100\}$, $\{110\}$, $\{211\}$, $\{311\}$ and $\{532\}$, we have calculated the adsorption energies of N, O and NO, together with the transition state energies for the dissociations of NO, O₂ and N₂. The different surface structures are shown in Figure 4.1. The $\{111\}$ and $\{100\}$ facets are both closed-packed facets, where the $\{100\}$ is more open than $\{111\}$. $\{110\}$, $\{211\}$ and $\{311\}$ are all three kinds of stepped surfaces, and the $\{532\}$ facet has both step and kink sites. As discussed earlier for the terrace atom in $\{111\}$ and $\{100\}$ surfaces, the coordination number is 9 and 8 respectively; for the step atom in $\{110\}$, $\{211\}$, $\{311\}$ and $\{532\}$ surfaces, the coordination number is 7 and for the kink atom in $\{532\}$ surface, the coordination number is 6.

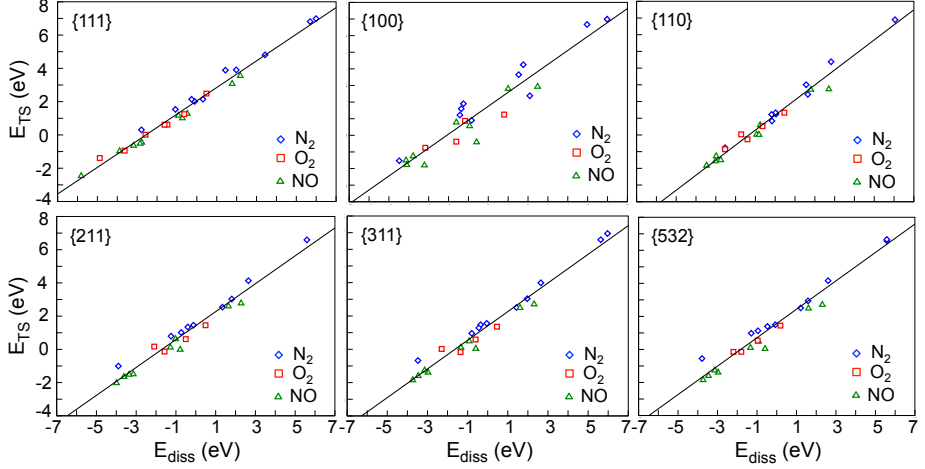


Figure 4.2: The transition energy versus the dissociative chemisorption energy for a range of transition metal facets. The lines represent the linear best fits.

4.3.1 Brønsted-Evans-Polanyi and Scaling Relationship

In Figure 4.2, I have plotted the universal BEP lines for the N_2 , O_2 and NO dissociation over different metal surfaces. As the transition state is in general final state like (they have similar geometry) they varies linearly. The transition state energy and dissociative chemisorption energy for,

$AB(g) + 2^* \rightarrow A^* + B^*$ are defined as,

$$E_{TS} = E_{TS/slabb} - E_{slabb} - E_{gas} \quad (4.2)$$

$$E_{diss} = E_{A/slabb} + E_{B/slabb} - 2E_{slabb} - E_{gas} \quad (4.3)$$

where $E_{x/slabb}$, E_{slabb} and E_{gas} are the energies of the adsorbate+surface system, the clean surface, and the gas phase species, respectively.

As reported earlier,^{6,70-72} here also the N_2 , O_2 and NO dissociation follow the universal BEP relation over the different surfaces. However when we look more closely, we observe an underlying fine structure in the individual BEP lines for N_2 , O_2 and NO dissociation over each surface. In general the BEP line for the N_2 dissociation for most of the surfaces lays 0.6 eV higher than the O_2 and NO BEP lines. The bond energy of N_2 is stronger than O_2 and NO and this cause the upper shift of the N_2 BEP line by approximately 0.6 eV. The slope of the N_2 and NO BEP lines are close to 0.8, which validate the assumption that the transition state is final state like. However the slope of BEP line for O_2 dissociation varies from ~ 0.5 to ~ 0.8 , which we believe is due to

Table 4.2: The fitted parameters for transition state scaling with respect to the gas-phase energies of NO, O₂ and N₂.

Reaction	Slope(α)	Consant (β) (eV)	RMSE (eV)
{111}			
NO(g) + 2* \rightarrow N* + O*	0.74 \pm 0.02	1.74 \pm 0.06	0.15
O ₂ (g) + 2* \rightarrow 2O*	0.71 \pm 0.05	1.84 \pm 0.13	0.22
N ₂ (g) + 2* \rightarrow 2N*	0.78 \pm 0.03	2.32 \pm 0.09	0.25
All	0.80 \pm 0.02	2.05 \pm 0.06	0.30
{100}			
NO(g) + 2* \rightarrow N* + O*	0.73 \pm 0.10	1.26 \pm 0.28	0.69
O ₂ (g) + 2* \rightarrow 2O*	0.53 \pm 0.18	0.93 \pm 0.35	0.51
N ₂ (g) + 2* \rightarrow 2N*	0.80 \pm 0.07	2.25 \pm 0.23	0.71
All	0.84 \pm 0.06	1.75 \pm 0.17	0.79
{110}			
NO(g) + 2* \rightarrow N* + O*	0.80 \pm 0.04	0.90 \pm 0.10	0.27
O ₂ (g) + 2* \rightarrow 2O*	0.71 \pm 0.10	0.98 \pm 0.15	0.22
N ₂ (g) + 2* \rightarrow 2N*	0.93 \pm 0.04	1.33 \pm 0.11	0.30
All	0.90 \pm 0.03	1.19 \pm 0.07	0.34
{211}			
NO(g) + 2* \rightarrow N* + O*	0.79 \pm 0.04	1.09 \pm 0.10	0.25
O ₂ (g) + 2* \rightarrow 2O*	0.55 \pm 0.16	1.03 \pm 0.22	0.32
N ₂ (g) + 2* \rightarrow 2N*	0.81 \pm 0.04	1.76 \pm 0.09	0.27
All	0.84 \pm 0.04	1.43 \pm 0.09	0.40
{311}			
NO(g) + 2* \rightarrow N* + O*	0.77 \pm 0.04	1.01 \pm 0.10	0.24
O ₂ (g) + 2* \rightarrow 2O*	0.53 \pm 0.18	0.95 \pm 0.25	0.37
N ₂ (g) + 2* \rightarrow 2N*	0.83 \pm 0.03	1.72 \pm 0.10	0.28
All	0.86 \pm 0.03	1.40 \pm 0.08	0.42
{532}			
NO(g) + 2* \rightarrow N* + O*	0.81 \pm 0.04	1.24 \pm 0.10	0.23
O ₂ (g) + 2* \rightarrow 2O*	0.71 \pm 0.08	1.26 \pm 0.12	0.15
N ₂ (g) + 2* \rightarrow 2N*	0.80 \pm 0.04	1.93 \pm 0.11	0.32
All	0.86 \pm 0.03	1.57 \pm 0.09	0.39

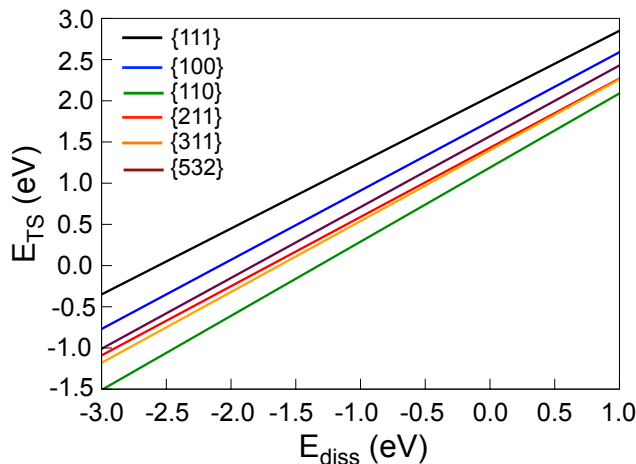


Figure 4.3: The fitted universal BEP-lines for the different surface structures.

the fewer points available for the O_2 BEP relation over the reactive metal surfaces. On many reactive metal surfaces O_2 is spontaneously dissociated without any barrier. The universal BEP line can be regarded as the average of the three individual BEP lines. However one can also see in Table 4.2, that the standard deviation (RMSE) of the universal BEP line is only little higher than the individual BEP lines and hence can be used as a first guess when we do not have enough data to make individual BEP lines. In the end of this chapter I will discuss the reaction rate sensitivity, where the effect of reducing the number of microkinetic model descriptors on the catalytic activity is shown.

In Figure 4.3, I have plotted the universal BEP lines for different surfaces, and it can be seen that the surface structure plays an important role in determining the BEP relations and hence also the catalytic activity. The stepped surfaces have lower laying BEP compared to the closed packed $\{111\}$ surface, which is in accordance with previous result from Nørskov et al.^{6,70} The lower laying BEP is due to both electronic and geometric effect.^{49,56,59,70,73} For the same reaction energy the transition state for any of the more open facets ($\{100\}$, $\{110\}$, $\{211\}$, $\{311\}$ and $\{532\}$) is at least 0.5 eV lower than the closed packed $\{111\}$ facet. Hence we should expect an increase in the reactivity while going from the $\{111\}$ surface to the stepped and kinked surface.

The shift in the BEP-lines going from the $\{111\}$ facet to the other facet is both correlated to the changes in the reaction energy and the transition state energy. In Figure 4.4, I have shown the effect of surface structure on both the reaction energy and transition state energy separately. In Figure 4.4 (top), I have plotted the reaction energy of the different facets versus the reaction energy of the $\{111\}$ facet. The $\{110\}$ facet has comparable reaction energy to the $\{111\}$ facet. The $\{100\}$ facet has the largest reaction energy and on average the reaction energy for the N_2 , O_2 and NO

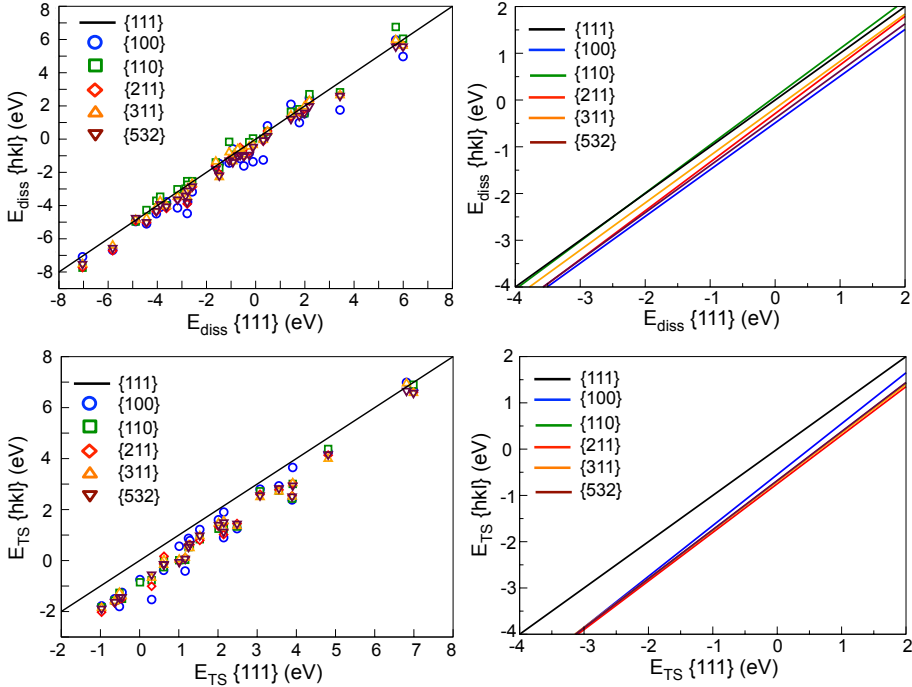


Figure 4.4: The reaction energy for dissociative chemisorption on the more reactive transition metal facets versus the reaction energy for dissociative chemisorption on the closed-packed transition metal surfaces.

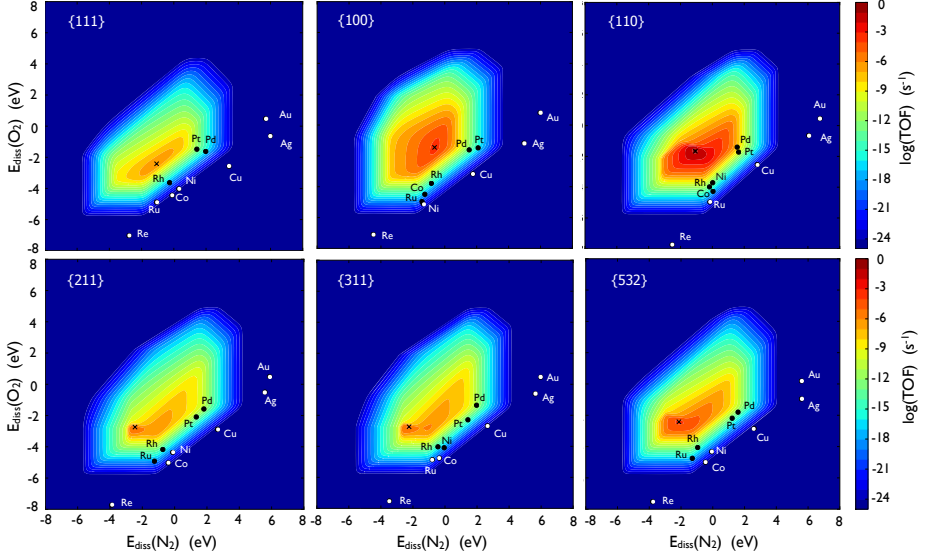
dissociation is 0.49 eV larger than the $\{111\}$ facet. Similarly In Figure 4.4 (bottom), I have plotted the transition state energies of the other surfaces versus the transition state energies over the $\{111\}$ surface. The transition state energy of the open facets $\{100\}$, $\{110\}$, $\{211\}$, $\{311\}$ and $\{532\}$ are shifted lower in energy by a constant 0.9 eV (see Table 4.3) for all the facets compared to the $\{111\}$ facets, due to the geometrical effect explained in section 3.5. The transition state for the open surfaces are shifted down by a constant value compared to the $\{111\}$ surface and the different in constant (β) of the the universal BEP lines for different open surfaces (shown in Figure 4.3) is due to the difference in the reaction energy among the open facets.

4.4 Catalytic Activity

The scaling based microkinetic modeling is used to obtain the catalytic rates of the different surfaces. The adsorption energy scaling relation is used to express the NO

Table 4.3: The fitted parameters for the reaction energy and transition state scaling with respect to the gas-phase energies of NO, O₂ and N₂.

Surface	Slope(α)	Consant (β) (eV)	RMSE (eV)
$E_{diss}^{\{hkl\}} = \alpha^{\{hkl\}} E_{diss}^{\{111\}} + \beta^{\{hkl\}}$			
{110}	1.03±0.02	0.07±0.07	0.38
{211}	1.04±0.02	-0.29±0.06	0.29
{311}	1.01±0.02	-0.18±0.06	0.30
{532}	1.01±0.02	-0.39±0.05	0.24
{100}	1.00±0.04	-0.49±0.12	0.62
$E_{TS}^{\{hkl\}} = \alpha^{\{hkl\}} E_{TS}^{\{111\}} + \beta^{\{hkl\}}$			
{110}	1.06±0.03	-0.93±0.08	0.27
{211}	1.05±0.03	-0.95±0.07	0.25
{311}	1.05±0.03	-0.90±0.08	0.27
{532}	1.06±0.02	-0.92±0.07	0.24
{100}	1.10±0.05	-0.95±0.13	0.47

**Figure 4.5:** The NO decomposition rate versus $E_{diss}(N_2)$ and $E_{diss}(O_2)$. The temperature is set to 700K and a total pressure of 1 bar is used. The partial pressures are set to $p_{NO} = 0.001$ bar, $p_{N_2} = 0.7$ bar and $p_{O_2} = 0.1$ bar.

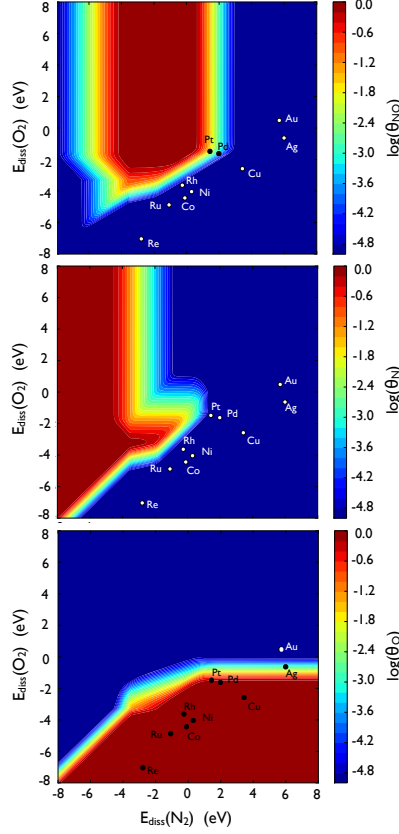


Figure 4.6: The coverage of the surface intermediates, NO, N and O, versus $E_{diss}(N_2)$ and $E_{diss}(O_2)$ for the $\{111\}$ facet.

binding energy as a function of N adsorption energy. The BEP relations for N_2 , O_2 and NO are used to obtain the activation barriers of the elementary steps. It is assumed that the NO adsorption has only an entropic barrier (no activation barrier). So one can express all the 7 independent parameters determining the kinetics (E_{NO} , E_N , E_O , E_{TS1} , E_{TS2} , E_{TS3} , E_{TS4}) as a function of only two independent parameters, the dissociative chemisorption of nitrogen and oxygen (E_N and E_O). In Figure 4.5, I have plotted the catalytic rate of NO decomposition under lean burn condition for the different surfaces in terms of N and O binding energy. In the rate volcano plots, I also have plotted the location of the transition metals and the position of the top points for all the different surfaces (depicted as black cross 'x'). It can be seen that the catalytic activity of the $\{111\}$ facet is significantly lower ($\sim 10^{-6} s^{-1}$) than any other open surfaces. We can write the reactivity trend for the different surfaces as $\{111\} < \{211\} \sim \{311\} < \{532\} \sim \{100\} < \{110\}$. The $\{110\}$ surface is the most active with

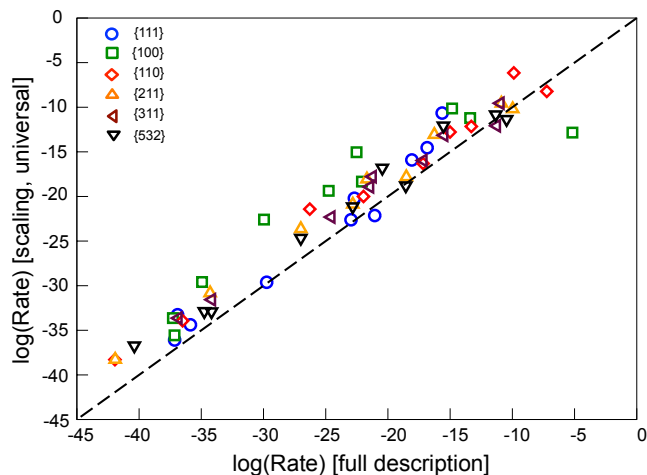


Figure 4.7: The rate for direct NO decomposition obtained from using the universal BEP relations versus the rate obtained from using the density functional theory energies.

NO decomposition catalytic rate $\sim 1s^{-1}$. The catalytic activity of the $\{110\}$ facet is 6 orders of magnitude higher than the $\{111\}$ facet. The $\{532\}$ and $\{100\}$ facet are the next most active catalyst with catalytic activity $\sim 10^{-2}s^{-1}$. The $\{211\}$ and $\{311\}$ step surfaces only show slightly higher activity ($\sim 10^{-5}s^{-1}$) than $\{111\}$ facet. Also the catalytic activity of the transition metal closest to the top of volcano increases as we do from the $\{111\}$ facet to any more reactive facet. For most of the surfaces Pd shows the highest activity among the transition metals studied here. The catalytic activity of Pd $\{110\}$ for the direct NO decomposition is more than a million times higher than the Pd $\{111\}$ surface.

In Figure 4.6, one can see that the $\{111\}$ facet of most of the reactive metals are completely covered by oxygen. All the reactive transition metals are poisoned by oxygen and hence show very low NO decomposition activity. Over a specific transition metal, the binding energy of N is much lower than oxygen. And as the N and O adsorption energy of the transition metals follow a close correlation, it is impossible to change the binding energy of N without changing the O binding energy. From this we can also assume that, as the simple transition metal alloys also follow the same N and O binding energy correlation, they will be also inactive for the direct NO decomposition.

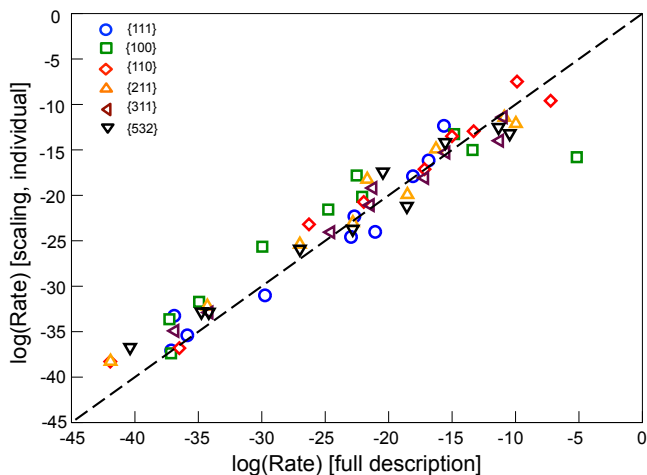


Figure 4.8: The rate for NO decomposition obtained from using the reactant dependent BEP relations for the individual elementary steps versus the rate obtained from using the density functional theory energies.

4.5 Reaction Rate Sensitivity

In the previous section while describing the catalytic rate in the catalytic volcano plots, we reduce the number of independent descriptors from 7 to only 2. In this section I have studied the effect of reduction in number of descriptors on the catalytic rates. In Figure 4.7, I have plotted the logarithm of the rate obtained with the full microkinetic model (with all 7 descriptors obtained from DFT) versus the scaling based microkinetic model (with only 2 descriptors, the other parameters are obtained using universal BEP and adsorption energy scaling relationships). In general, the predicted catalytic rates using the scaling based microkinetic model are higher than the predicted rates using the full microkinetic model. For some metal surfaces, the predicted rates using the scaling based microkinetic modeling are more than 5 orders of magnitude higher. However if we want to use it for screening of catalysts, this simple universal BEP scaling based approach is accurate enough to give the correct trends.

In Figure 4.8, I have plotted the logarithm of the rate obtained from with the full microkinetic model versus the scaling based microkinetic model, using the individual BEP relations. With the individual BEP scalings one can predict the rate much better. From Figure 4.8 one can see that the catalytic rates for all the facets except {100} facet are described very well and the catalytic trends are in good agreement with the trends obtained using the full microkinetic model.

4.6 Summery

Both the individual and universal BEP relations for the NO, O₂ and N₂ dissociation over closed packed, stepped and kinked surfaces have been presented in this chapter. I have shown that the BEP relations are structure dependent and the stepped and kink metal surfaces have low laying transition state scaling lines than the flat {111} terrace. The transition state energy of any of the other surfaces studied here are lowered by a constant ~ 0.9 eV, than the {111} surface. The consequence of lower BEP lines for the more open facets can be seen in the catalytic activity of the direct NO decomposition. The catalytic rate of direct NO decomposition for the open facets are 1-5 order of magnitudes higher than the closed packed {111} facet. The catalytic rate of Pt and Pd metals in the {110} surface structure is $\sim 10^6$ times higher than the Pd and Pt in the {111} surface structure. However for all of the surface structures studied here the top of the volcano do not change significantly, and for all of the surfaces Pd and Pt are the two best direct NO decomposition catalysts. However it will be interesting to do the Wulff construction⁸⁸ of the nanoparticles under the reaction condition and obtain the total catalytic rate of nanoparticles.

CHAPTER 5

Adsorbate-Adsorbate Interaction Model

Most of the industrial catalysis are operated under high pressure condition where the surface coverage over the catalysts are often very high. Hence the study of adsorbate-adsorbate interaction among the adsorbed species is important for the understanding the effect of this on catalytic activity and selectivity. So it could be potentially important to include the adsorbate-adsorbate interactions in our microkinetic model if we want to tailor a new catalyst by using DFT calculations. Adsorbate-adsorbate interaction also plays significant role in determining the structure of the nanoparticle catalyst under reaction condition. In this chapter I will present the parameterization of an adsorbate-adsorbate interaction model. In the subsequent sections of this chapter I will show the effect of adsorbate-adsorbate interaction for three important catalytic process, ‘direct NO decomposition’, ‘CO methanation’ and ‘steam reforming of methane’. Adsorbate-adsorbate interaction model is successfully combined with the microkinetic models to include the coverage dependent adsorption energy and obtain better catalytic activity trends for the catalytic processes stated above.

5.1 Parameterization of a Model for Adsorbate-Adsorbate Interactions

Adsorbate-adsorbate interactions between reaction intermediates adsorbed to the surface of a catalyst can significantly change the adsorption energy of a given reaction intermediate.^{89,90} A model to describe such interactions is therefore important in order to describe the catalytic reactivity, the surface structure of the catalyst under reaction conditions and the temperature of adsorption/desorption.⁹¹ For a large range of coverages, it has been shown that the adsorption energy of oxygen on the closed-packed facets of the transition metals, scales linearly with coverage for coverages above ≈ 0.2 ML.^{90,92} In Figure 5.1 (top), this is shown for oxygen at coverages between $\frac{1}{4}$ - 1 ML for a range of transition metals. Here the average adsorption energy of oxygen is plotted versus the coverage of oxygen on the surface. Kitchin et al. also described that the interaction between the adsorbed oxygen atoms was different on Au compared to Pt.⁹¹ We also observe that the change in adsorption energy with coverage is metal dependent, since the slope of the fitted lines changes from one metal to the next. In Figure 5.1(bottom) the linear dependence of the adsorption energy with surface coverage is shown for a range of atoms and molecules adsorbed on Rh{111}. Here it can be seen that the change in adsorption energy with coverage is not only metal dependent, but also adsorbate dependent. Since the adsorption energy changes significantly with coverage, it is crucial to include such effects in a theoretical description of catalytic reactions and trends in catalytic activity. Recently Grabow et al.⁹⁰ proposed an interaction model, and combined it with a simple mean field kinetic model.⁸² For the catalytic CO oxidation reaction on the transition metals, it was shown that including the description of the adsorbate-adsorbate interactions, the traditionally reactive metals became significantly more active, and almost as active as the most active catalyst, Pd.

A linear interaction model was first introduced by V.P. Zhdanov to study the effect of the adsorbate-induced surface reconstruction on the apparent Arrhenius parameters for desorption processes.⁹³ Rupprechter et al.⁹⁴ studied the adsorbate-adsorbate interactions for the CO+H system on Pd{111}. They explained the fact that it is neither possible to dissociate H₂ on a CO covered surface, nor adsorb CO on a H covered surface, due to a strong repulsive interaction between H and CO. Mason et al.⁹⁵ explained the effect of adsorbate-adsorbate interactions on adsorption energy on different transition metals and identified factors influencing the interaction. A. Hellman and K. Honkala⁹⁶ described lateral interactions between adsorbents by a simple mean field model. By applying this model for the NH₃ synthesis on Ru{0001} step surface, they showed that compared to the highly sophisticated Monte Carlo simulations the simple mean field interaction model describes the adsorbate-adsorbate interactions reasonably well.

Kitchin et al. in their articles^{91,92,97} have given a detailed description of the origin of the adsorbate-adsorbate interaction based on the d-band model⁴⁸⁻⁵¹. They also did a systematic study to show factors important for variation for the adsorbate-adsorbate interaction parameter for the different metals and adsorbates. However the interaction

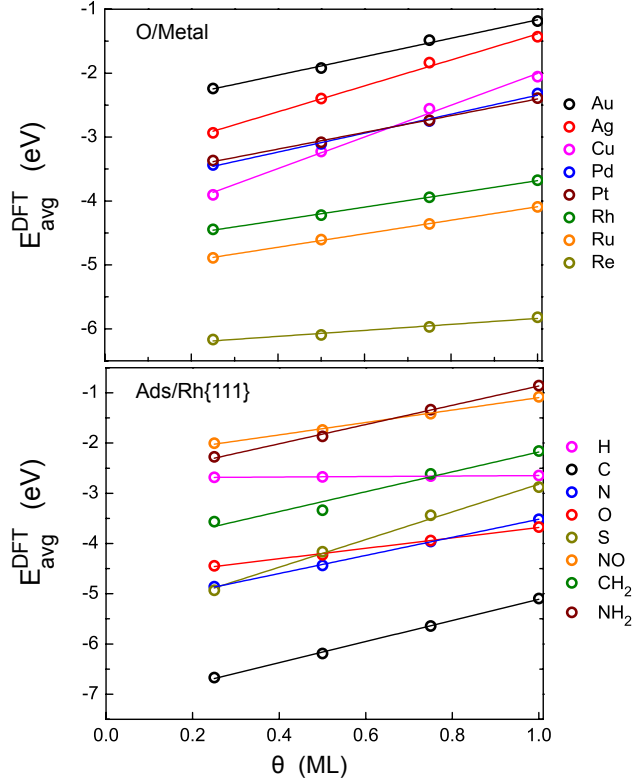


Figure 5.1: Linear variation of average adsorption energy with coverage for (top) O adsorption on the closed-packed facet of the following transition metals: Au, Ag, Cu, Pd, Pt, Rh, Ru and Re, (bottom) H, C, N, O, S, NO, CH₂ and NH₂ adsorption on the Rh{111} surface.

model proposed by Kitchen et al. contains many parameters related to both metals and adsorbate, and hence very difficult to parameterize for a full catalytic reaction. The adsorbate-adsorbate interaction model proposed by A. Hellman and K. Honkala in ref.⁹⁶ and Grabow et al. in ref.⁹⁰, introduced the piecewise interaction model, where the adsorption energy remains constant up-to a threshold coverage and then increases linearly with coverage. Both the model use the ‘interaction parameter’ to describe change in adsorption energy with coverage. They also successfully coupled the interaction model with the micro kinetic model to study the effect of adsorbate-adsorbate interactions on the catalytic activity. However the number of interaction parameters in both these model varies as $N_{surface} \times N_{sp}(N_{sp} + 1)/2$, where N_{sp} is the number of adsorbed species and $N_{surface}$ is the number of surfaces. This is why these models can only be used for simple reaction over a very few catalyst. A. Hellman and K. Honkala used the interaction model to study the effect of adsorbate-adsorbate interactions on

NH₃ synthesis over Ru metal, only consist of five adsorbates. Grabow et al. used the interaction parameters obtained for Pt metal for all the other transition metals to obtain the catalytic CO oxidation rates over transition metals {111} surfaces. As I already have shown in that the Figure 5.1 that the interaction parameters are metal dependent, when using constant Pt interaction for all transition metals we either overestimates or underestimates the adsorbate-adsorbate interaction. And due to this use of constant Pt interaction for all transition metals in the left leg of become highly active for CO oxidation. Also the piecewise interaction model proposed by Grabow et al. is only applicable for two adsorbate system, like the CO oxidation, which only have two adsorbates CO and O. Due to the use of individual threshold coverage for each adsorbate-metal system the model will not be able to describe the coverage dependent adsorption energy for multi (> 2) adsorbate systems. And most importantly none of these interaction model describe the correlation of the interaction parameter with the microkinetic model descriptors. The description of the interaction parameters in terms of the independent descriptors is important for the necessary improvement of the existing non-interacting mean field microkinetic model.

To overcome the limitations of the previous model, here in this chapter I propose a new parameterized adsorbate-adsorbate interaction model in section 5.1.1, with the goal of including coverage dependent adsorption energy into our microkinetic models. In our interaction model, where the adsorption energy varies linearly with the coverage of the surface species and is closely related to the model proposed by A. Hellman and K. Honkala in ref.⁹⁶ and Grabow et al. in ref.⁹⁰. From density functional theory calculations, I obtain the interaction parameters for both the self-interaction parameters between the same surface species and the cross-interaction parameters for interactions between two different surface species. In order to make the linear interaction model more useful and applicable to catalysis, I show how the number of parameters can be reduced. First by showing how the cross-interaction parameters can be obtained from self-interaction parameters. Second by proposing two submodels : i) An interaction model, where the interaction parameters obtained for one metal can be applied for description of interaction on all the considered transition metals, same as proposed by Grabow et al.⁹⁰, ii) a scaling based model, where we use scaling between adsorbate-adsorbate interaction parameters and adsorption energies to describe the interaction on different metals. I also construct a piecewise interaction model, where the adsorption energy is kept constant until the threshold coverage and then varies linearly with the coverage of the surface species. The threshold coverage is ‘universal’ and does not vary with metals or adsorbates and hence can be used for multi-adsorbate reaction schemes. I will discuss the accuracy, usefulness and limitations of each of the different adsorbate-adsorbate interaction models separately. In the next three section of this chapter I will show how to combine the adsorbate-adsorbate interaction model to the micro kinetic model and then use it to three important catalytic reactions to show the effect of adsorbate-adsorbate interaction on catalytic activity and trends.

5.1.1 Method

We propose an interaction model, where the total adsorption energy per surface site varies quadratically with coverage:

$$E_T(\underline{\theta}) = \underline{E}^0 \underline{\theta} + \frac{1}{2} \underline{\theta}^T \underline{\epsilon} \underline{\theta}, \quad (5.1)$$

where E^0 is the differential adsorption energy at zero coverage, and $\underline{\epsilon}$ is the i times i dimensional interaction matrix, with the interaction parameters for interactions between the i different species. In the matrix the interaction parameters, $\epsilon_{ij} = \epsilon_{ji}$. The average adsorption energy, $E_{avg}(\underline{\theta})$, is defined as the total adsorption energy per surface site divided by the sum of the coverages:

$$E_{avg}(\underline{\theta}) = \frac{E_T(\underline{\theta})}{\sum \underline{\theta}} = \frac{\underline{E}^0 \underline{\theta} + \frac{1}{2} \underline{\theta}^T \underline{\epsilon} \underline{\theta}}{\sum \underline{\theta}} \quad (5.2)$$

For a single adsorbate system it has the form:

$$E_{avg}(\theta_i) = \frac{E_T(\theta_i)}{\theta_i} = E_i^0 + \frac{1}{2} \epsilon_{ii} \theta_i \quad (5.3)$$

The self-interaction parameters, ϵ_{ii} , can be obtained by calculating the average adsorption energy at two different coverages with density functional theory:

$$\epsilon_{ii} = \frac{2(E_{avg}(\theta_1) - E_{avg}(\theta_2))}{(\theta_1 - \theta_2)} \quad (5.4)$$

The cross-interaction terms, ϵ_{ij} , are obtained from a system, where the adsorbates, i and j , are co-adsorbed and have the coverages θ_i and θ_j respectively with average co-adsorption energy $E_{avg}(\theta_i, \theta_j)$ as,

$$\epsilon_{ij} = \frac{(\theta_i + \theta_j)E_{avg}(\theta_i, \theta_j) - E_i^0 \theta_i - E_j^0 \theta_j - \frac{1}{2}(\epsilon_{ii} \theta_i^2 + \epsilon_{jj} \theta_j^2)}{\theta_i \theta_j} \quad (5.5)$$

In catalysis we are often interested in the adsorption energy of the species taking part in a reaction has for a given coverage, this is the differential adsorption energy. The differential adsorption energy, $E_{diff}(\underline{\theta})$, can be obtained from $E_T(\underline{\theta})$ as,

$$E_{diff}^i(\underline{\theta}) = \frac{dE_T(\underline{\theta})}{d\theta_i} \quad (5.6)$$

So one can express the differential adsorption energy, when only one specific adsorbate is adsorbed with coverage θ_i as,

$$E_{diff}^i(\theta_i) = \frac{dE_T(\theta_i)}{d\theta_i} = E_i^0 + \epsilon_{ii} \theta_i \quad (5.7)$$

When multiple species are adsorbed we can express the differential adsorption energy as,

$$E_{diff}^i(\theta) = \frac{dE_T(\theta)}{d\theta_i} = E_i^0 + \sum_j \epsilon_{ij}\theta_j \quad (5.8)$$

5.1.2 DFT Setups

The plane wave DFT code, DACAPO, was used to calculate adsorption and gas phase energies.⁴⁰ Kohn-Sham one-electron valence states were expanded in a plane-wave basis. A plane wave cutoff of 340.15 eV and a density wave cutoff of 680eV were used for the calculation. The core electrons were described by Vanderbilt ultrasoft pseudopotentials.⁸⁵ RBPE was used to describe the exchange-correlation energy.⁹⁸ Fermi population of the Kohn-Sham states was calculated at $k_B T = 0.1$ eV. All energies are extrapolated to $k_B T = 0$ eV. The convergence limit was set as a maximum change in the force constant of 0.03 eV.

The most stable closed-packed surface of the metals in their favorable crystal structure were modeled by a 2×2 surface cell, with a slab thickness of 4 layers, where the two topmost layers were allowed to relax. A $8 \times 8 \times 1$ Monkhorst-Pack k-point⁸⁶ sampling in the irreducible Brillouin zone was used. Adsorption energies for the individual species have been calculated at $\frac{1}{4}$ ML, $\frac{1}{2}$ ML, $\frac{3}{4}$ ML and 1 ML coverage for the most stable adsorption site at low coverage. For the determination of the cross-interaction terms, calculations were performed with coverage $\frac{1}{2}$ ML of each of the involved adsorbates. Finally, for the low coverage adsorption energy calculations on the transition metals, we used 3×3 and 4×4 unit cells, with $6 \times 6 \times 1$ and $4 \times 4 \times 1$ k-point sampling respectively.

5.1.3 Result and Discussion

Catalytic trend studies are often performed without describing the coverage effect on the adsorption energy of the reaction intermediates. Often the adsorption energy calculated at $\frac{1}{4}$ ML coverage is assumed to be representative for the adsorption energy at any coverage. In Figure 5.2 the average adsorption energy on transition metals for a number of different atoms and molecules at surfaces coverage $\frac{1}{4}$, $\frac{1}{2}$, $\frac{3}{4}$, and 1ML is plotted versus the adsorption energy at $\frac{1}{4}$ ML coverage. Clearly the adsorption energy changes significantly with coverage, and this can affect the catalytic rate of a given reaction, and most probably also the activity trends when going from one metal to the next.^{9,90,96,99}

The linear interaction model has been parametrized for a number of atoms and molecules adsorbed on transition metal surfaces. The self-interaction parameter for interactions between adsorbates of the same species have been obtained using equation (5.4) and

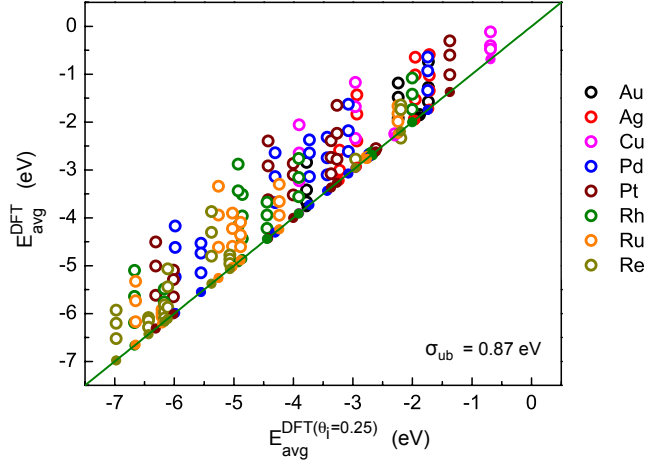


Figure 5.2: Parity plot of the average adsorption energy from DFT at $\frac{1}{4}$ ML, $\frac{1}{2}$ ML, $\frac{3}{4}$ ML and 1 ML surface coverage versus the adsorption energy from DFT at $\frac{1}{4}$ ML coverage. The filled circles are for $\frac{1}{4}$ ML coverage. The studied adsorbents are: H, C, N, O, S, CH, NH and NO.

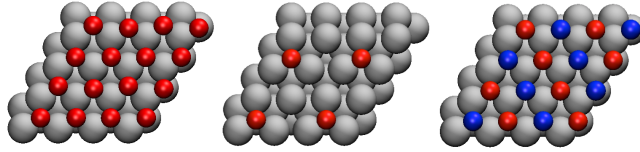


Figure 5.3: Adsorption geometries of O at $\frac{1}{4}$ ML and 1 ML coverage and co-adsorbed N and O at $(\frac{1}{2} + \frac{1}{2})$ ML on Rh{111} metal surface. Oxygen and nitrogen atoms are denoted with red and blue color respectively

the DFT calculated adsorption energies at $\frac{1}{4}$ ML and 1ML. The cross-interaction parameter for the interaction between different adsorbates have been obtained using (5.5) and the $\frac{1}{2}$ ML + $\frac{1}{2}$ ML coverage calculation. The adsorption geometries used in the parametrization of the interaction model are illustrated for O (and N) adsorption on Rh(111) in Figure 5.3. The interaction parameters obtained for the atoms and molecules on the most stable closed packed facet of transition metals are given in Table 5.1 and in appendix A.2.

We first discuss the results obtained from the description of the coverage dependent adsorption energy using the full linear interaction model.

The full linear interaction model

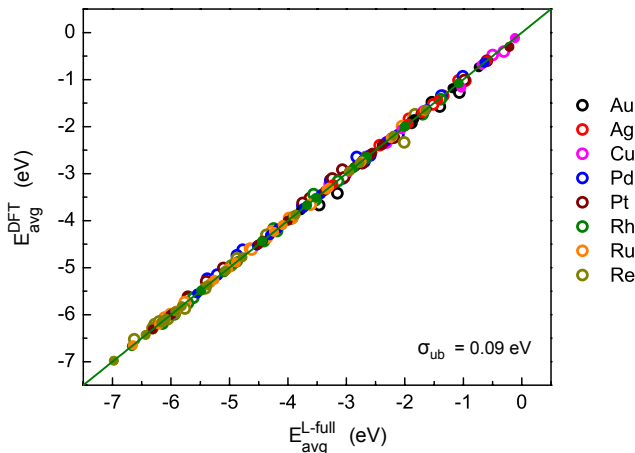


Figure 5.4: Parity plot of the average adsorption energy from DFT at $\frac{1}{4}$ ML, $\frac{1}{2}$ ML, $\frac{3}{4}$ ML and 1 ML surface coverage versus the adsorption energy obtained using the full interaction model at those corresponding surface coverages. The filled circles are for $\frac{1}{4}$ ML and 1 ML coverage. The studied adsorbates are: H, C, N, O, S, CH, NH and NO.

In Figure 5.4 we apply the full interaction model to predict the average adsorption energy at coverages $\frac{1}{4}$, $\frac{1}{2}$, $\frac{3}{4}$ and 1 ML. The adsorption energies are obtained using eq. 5.3, where an interaction parameter has been calculated for each adsorbate on each metal. The linear interaction model effectively predicts the DFT calculated adsorption energy for all of the studied adsorbates, at surface coverages between $\frac{1}{4}$ and 1 ML. Since the interaction parameters are obtained from the slope of the fitted line through the DFT energies at $\frac{1}{4}$ ML and 1 ML, the average adsorption energies from the full linear interaction model will be exactly the DFT energies at these coverages. The unbiased standard deviation (the RMS error, where the modeled energies at $\frac{1}{4}$ ML and 1 ML have not been included) on the average adsorption energy is 0.09 eV. The full linear interaction model thus gives a very accurate description of the coverage dependent adsorption energy for a large region of coverages and a far more accurate description than neglecting lateral interactions. The full linear interaction model is very useful, when we are interested in simple catalytic model systems, that has few reaction intermediates, over a few specific surfaces. However obtaining the interaction parameters for larger systems becomes heavy, as the number of parameters increases rapidly with number of adsorbates and metal surfaces. One need to reduce the number of independent parameters to make the model more applicable to catalysis in general.

Obtaining the cross-interaction terms from the self-interaction terms

In Figure 5.5 the DFT calculated adsorption energy for co-adsorption of two different

Table 5.1: Self-interaction parameters for atoms and molecules on the most stable closed packed facet of transition metals

Metal	ϵ_H	ϵ_C	ϵ_N	ϵ_O	ϵ_S	ϵ_{CH}	ϵ_{NH}	ϵ_{NO}
Au	0.09	*	2.66	2.81	*	2.50	*	*
Ag	0.09	*	3.01	4.01	*	1.69	3.48	*
Cu	0.15	*	*	4.92	*	*	4.77	1.53
Pd	0.14	4.84	3.62	2.98	4.45	2.72	3.86	2.95
Pt	0.16	4.82	3.04	2.60	5.41	2.46	4.31	2.85
Rh	0.10	3.78	3.29	2.05	5.23	1.38	2.63	2.02
Ru	0.13	2.86	2.48	1.78	5.01	0.81	2.24	1.30
Re	0.49	2.81	2.79	0.93	4.02	0.92	0.77	1.47
Mo***	0.09	*	3.28	1.61	4.36	1.82	1.60	1.47
W***	0.17	*	2.80	0.80	4.33	3.34	1.12	1.39
Sc***	0.02	*	*	-0.04	2.95	*	0.29	**
Ti***	-0.14	*	1.29	0.80	3.88	2.37	1.51	**

* the adsorption at 1 ML coverage is not stable.

** NO dissociates on adsorption at $\frac{1}{4}$ ML coverage.

*** For Mo, W, Sc and Ti we only studied the adsorption at $\frac{1}{4}$ ML and 1 ML coverage.

species at $\frac{1}{2}$ ML coverage each is plotted versus the average of the adsorption energy of the two species at $\frac{1}{4}$ ML coverage. The interactions between different adsorbates are also significant.

We investigated two ways of parametrizing the cross-interaction parameter for interaction between adsorbate i and adsorbate j, from their respective self-interaction parameters, ϵ_{ii} , and ϵ_{jj} :

$$\epsilon_{ij}^{AM} = \frac{1}{2}(\epsilon_{ii} + \epsilon_{jj}) \quad (5.9)$$

$$\epsilon_{ij}^{GM} = \sqrt{\epsilon_{ii} \times \epsilon_{jj}} \quad (5.10)$$

Eq. 5.9 is the arithmetic mean (AM), and eq. 5.10 is the geometric mean (GM), of the self-interaction parameters. In Figure 5.6 and 5.7, we show for rhodium, how well the coverage dependent adsorption energy is described for co-adsorbed systems, where the cross-interaction parameters have been obtained from the arithmetic mean and the geometric mean, respectively.

By using the geometric mean (GM) to obtain the cross-interaction parameters, the RMS error on the prediction of the adsorption energy for co-adsorbed species is 0.22

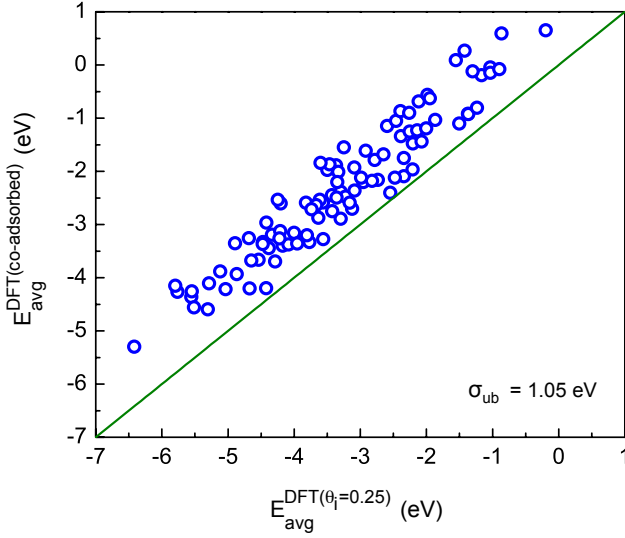


Figure 5.5: Parity plot of average adsorption energy from DFT for co-adsorbed H, C, N, O, S, CH, CH₂, CO, NH, NH₂, NO, N₂, N₂O, OH and SH on Rh{111} versus adsorption energy calculated using the average of the DFT calculated adsorption energy at $\frac{1}{4}$ ML coverage of those two corresponding species.

eV, whereas the use of the arithmetic mean, gives a slightly higher RMS error of 0.26 eV. Both of these methods can be used to obtain the cross-interaction parameters. With a relatively small error, we can now reduce the number of independent parameters from $N_{sp}(N_{sp} + 1)/2 \times N_{surface}$ to only $N_{sp} \times N_{surface}$ by using the parametrization for cross-interaction parameters.

The linear interaction model based on the interaction parameters from Rhodium

In Figure 5.8 we have plotted the interaction parameters obtained for a number of different adsorbates on the different metals versus the interaction parameters obtained for rhodium. Clearly there is a large variation in the interaction parameters among the transition metals, however using the interaction parameters for Rh gives an average description of the adsorbate-adsorbate interactions. Therefore we propose a simple sub-model, where we use the interaction parameters obtained for the adsorption of the different species on rhodium, to describe the interactions on all the considered transition metals.

In Figure 5.9 the adsorption energy calculated by DFT is plotted versus the coverage dependent adsorption energy obtained from this sub-model for a given coverage. We can see that even by using this simple model one can predict the coverage dependent

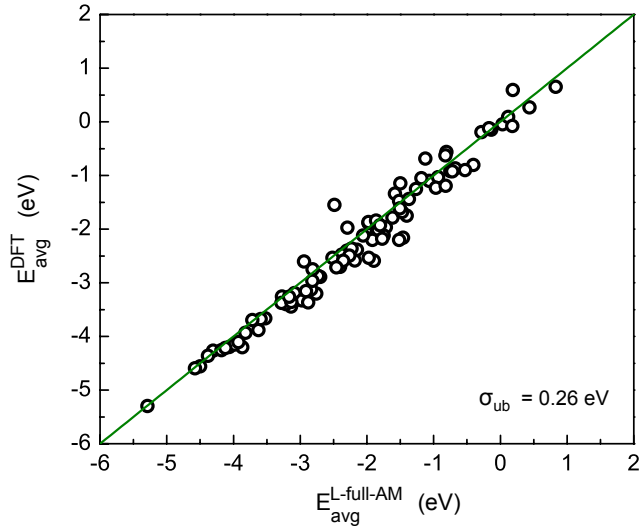


Figure 5.6: Parity plot of average adsorption energy from DFT of co-adsorbed H, C, N, O, S, CH, CH₂, CO, NH, NH₂, NO, N₂, N₂O, OH and SH on Rh{111} versus the adsorption energy calculated using the interaction model, with the cross-interaction parameters are obtained from the arithmetic mean of the self-interaction parameters.

adsorption energy with reasonable accuracy for all the metals for a large range of coverages. In comparison to neglecting the effect of interaction on the adsorption energies, this simple model certainly gives a more accurate description of the adsorption energies as we reduce the unbiased standard deviation from 0.87 eV to 0.27 eV using this model. We therefore propose this model as a very simple and reasonably accurate sub-model to describe the coverage dependent adsorption energy.

A scaling based model

Though the rhodium interaction model effectively describes the change in adsorption energy with coverage for the transition metals, I also find that the adsorbate-adsorbate interaction on the less reactive metals, (Pd and Pt) is in general stronger and on more reactive metals (Ru and Re) in general weaker than those on Rh, as seen in Figure 5.8. The interaction parameters for the noble metals are scattered on both sides of the Rh-line and do not seem to follow any general trend.

The d-band model proposed by Hammer-Nørskov^{48–51} correlates the systematic change in the adsorption energy along any metal series to the position of the d-band center compared to the Fermi level of the metal surfaces. As the coverage of the adsorbates increases, due to increased overlap between the electron orbitals of the adsorbates and the surface metal atoms, the d-band width of the surface metal atom increases and

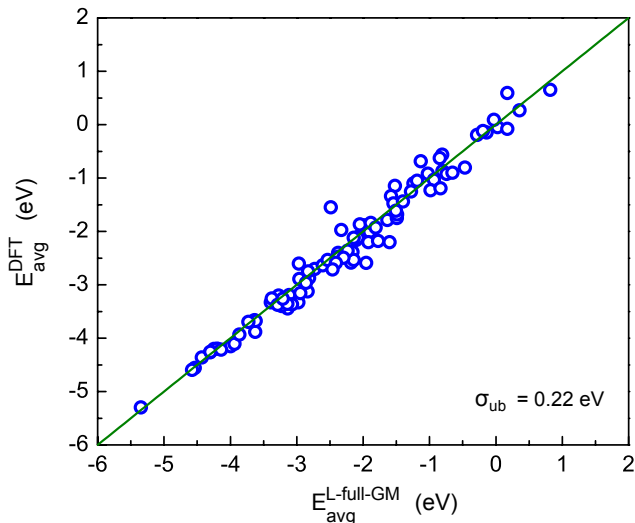


Figure 5.7: Parity plot of average adsorption energy from DFT of co-adsorbed H, C, N, O, S, CH, CH₂, CO, NH, NH₂, NO, N₂, N₂O, OH and SH on Rh{111} versus the adsorption energy calculated using the interaction model, with the cross-interaction parameters are obtained from the geometric mean of the self-interaction parameters.

consequently the d-band center shifts down to lower energies with respect to the Fermi level. This downshift of the d-band center combined with broadening of the d-band can be explained by the rectangular d-band model⁴⁹. Generally the lowering of the d-band center relates to decrease in the adsorption energy due to the weakening of the metal-adsorbate bonding. As the metal d-band center is downshifted or the d-band become broadened the anti-bonding orbitals become more occupied, and this causes the weakening the metal-adsorbate bonding. Generally it has been observed that the adsorption energy changes linearly with d-band center of the metal surfaces. With increasing coverage of the adsorbates the metal d-band width increases along with a downshift of the d-band center of the surface metal atoms^{91,92,97,100}, resulting in a decrease in adsorption energy with increasing coverage. The change in the adsorption energy with coverage thus also follows the Hammer-Nørskov d-band model.

In the rectangular d-band model the change in the d-band center on adsorption of adsorbate is also related to the d-band center of the metal surface⁵⁸. The change in the d-band center for the reactive metals is relatively smaller than the less reactive transition metals.⁴⁸ So for a more reactive transition metal the change in adsorption energy while going from coverage $\frac{1}{4}$ ML to coverage 1.0 ML will be smaller than a less reactive transition metal.⁹² As interaction parameter (ϵ_{ii}) is the two times the slope of the adsorption energy versus coverage linear correlation, when one move from a less reactive metal to a more reactive metal the interaction parameter (ϵ_{ii}) also

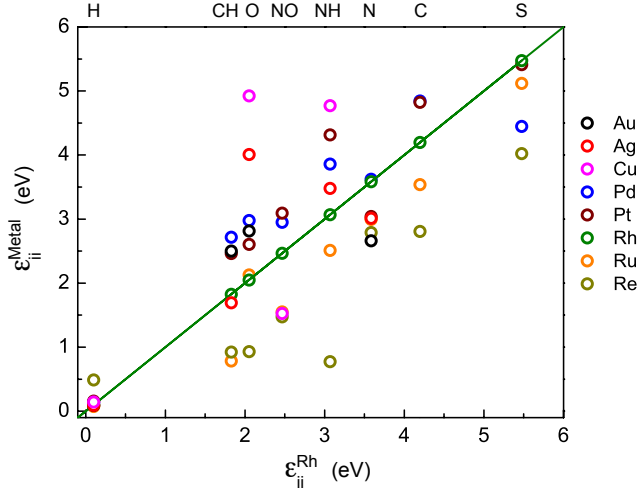


Figure 5.8: Plot for adsorbate-adsorbate interaction parameter for H, C, N, O, S, CH, NH and NO on the closed packed facet of Au, Ag, Cu, Pd, Pt, Ru and Re with respect to the adsorbate-adsorbate interaction parameter for Rh{111}.

becomes smaller. This is consistent with the systematic variation in the interaction parameter along the transition metal series, where we found $\epsilon_{ii}\{\text{Pd}\} > \epsilon_{ii}\{\text{Pt}\} > \epsilon_{ii}\{\text{Rh}\} > \epsilon_{ii}\{\text{Ru}\} > \epsilon_{ii}\{\text{Re}\}$ in general for most the adsorbates, given in Table 5.1. The noble metals (Cu, Ag and Au) generally do not follow this general trend as the d-bands do not contribute to the adsorption energy for these metals. The coupling matrix is the main contributor to the adsorption energy for Cu, Ag and Au. Due to these underlying correlations, the interaction parameter also varies linearly with the position of the d-band center of the metal surfaces for a specific adsorbate, shown in Figure 5.11 (see Table A.5 in appendix for details).

In Figure 5.10 it is seen that the adsorbate-adsorbate interaction parameter scales linearly with the adsorption energy. The interaction among the adsorbates thus decreases going from less to more reactive transition metals. In order to establish this systematic trend calculations of the interaction parameters for the adsorbates on Mo, W, Sc and Ti have been included. The scaling is surprisingly good for most adsorbates, however for CH on W and Ti the scaling does not hold and we suggest using the scaling for CH only for less reactive metals than Mo (plotted in dotted lines in Figure 5.10). We have not found any credible reason for this anomaly of yet. Also the interaction parameters for the noble metals do not follow the scaling. Hence a cut-off adsorption energy after which the interaction parameter remains constant is suggested. In order to obtain this cut-off the scaled interaction parameters for Rh, Pt, Pd and Cu were fitted to the interaction parameters for the noble metals. We found that the scaled Pd interaction parameters to describe the interactions on the noble metals the best. To make this cutoff more general, a metal-specific adsorption energy is suggested here. In

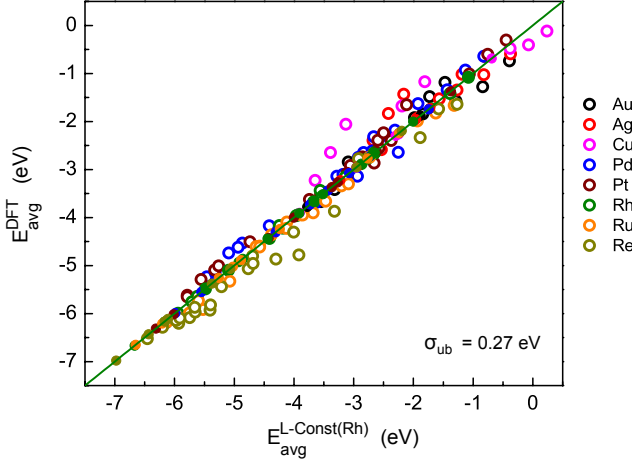


Figure 5.9: Parity plot of the average adsorption energy from DFT at $\frac{1}{4}$ ML, $\frac{1}{2}$ ML, $\frac{3}{4}$ ML and 1 ML surface coverage versus the adsorption energy obtained using the interaction model based on the interaction parameters of Rh from table 5.1, at those corresponding surface coverages. The filled circles are for $\frac{1}{4}$ ML coverage on all the metals and 1 ML coverage on Rh only. The studied adsorbents are: H, C, N, O, S, CH, NH and NO.

Figure 5.12 the adsorption energy calculated with DFT is plotted versus the coverage dependent adsorption energy obtained from this scaling based linear interaction model. The unbiased standard deviation is 0.18 eV for the studied systems. As expected this model describes the adsorption energy more precisely than the Rh interaction model.

From scaling of the interaction parameters to the adsorption energy, we are now able to include the systematic change in the adsorbate-adsorbate interaction parameter for a complete adsorption energy range of interested metals to get a full descriptive adsorbate-adsorbate interaction model applicable to micro-kinetic modeling.

5.1.4 Piecewise Interaction Model

Up until now we have used a linear interaction model to describe the coverage dependent adsorption energy in the $\frac{1}{4}$ - 1 ML coverage range. In Figure 5.13 and also in work by Grabow et al.⁹⁰ and Kitchin et al.⁹¹, it has been shown that below some threshold coverage θ^0 , the change in the adsorption energy with coverage is negligible. To correct our linear interaction model in the low coverage regime, I have proposed a piecewise interaction model, where the differential adsorption energy remains constant below the threshold coverage θ^0 and changes linearly with coverage after θ^0 . For coverages above the threshold coverage θ^0 , the linear and the piecewise models are the

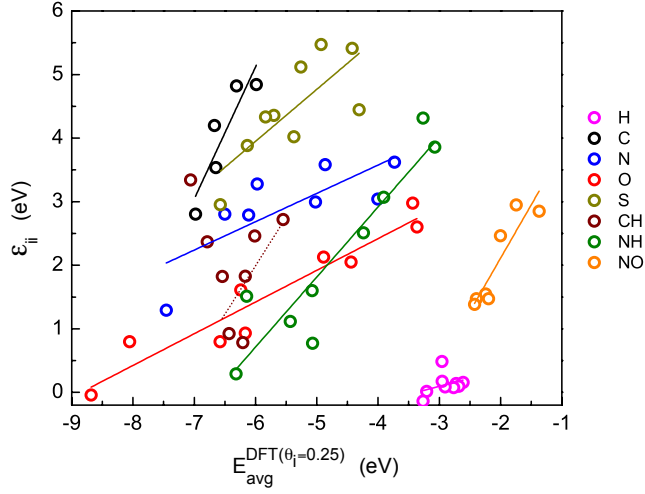


Figure 5.10: Plot for adsorbate-adsorbate interaction parameter for H, C, N, O, S, CH, NH and NO on the closed packed facet of Pd, Pt, Rh, Ru, Re, Mo, W, Sc and Ti with respect to the adsorption energy of the corresponding adsorbates at $\frac{1}{4}$ ML coverage on the above transition metal surfaces.

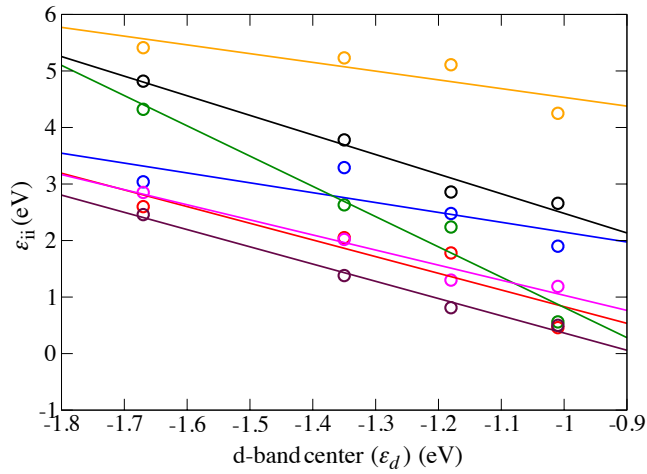


Figure 5.11: Plot for adsorbate-adsorbate interaction parameter for different adsorbates on FCC {111} surface of transition metal Pt, Rh, Ru and Re with respect to the d-band center of the transition metal clean surfaces.

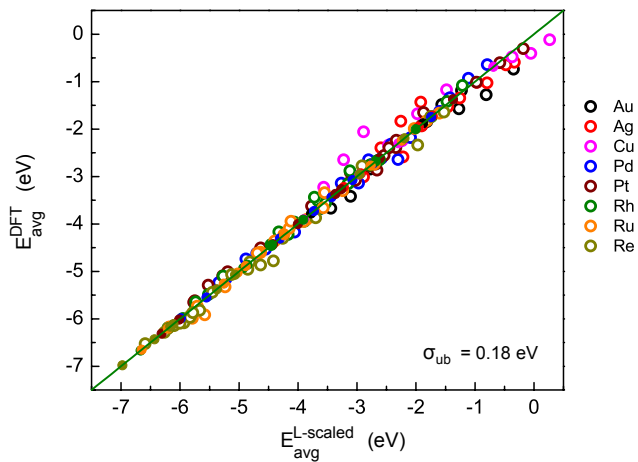


Figure 5.12: Parity plot of the average adsorption energy from DFT at $\frac{1}{4}$ ML, $\frac{1}{2}$ ML, $\frac{3}{4}$ ML and 1 ML surface coverage versus the adsorption energy obtained using the interaction model based on the interaction parameters and adsorption energy scaled interaction parameters, at those corresponding surface coverages. The filled circles are for $\frac{1}{4}$ ML coverage. The studied adsorbents are: H, C, N, O, S, CH, NH and NO.

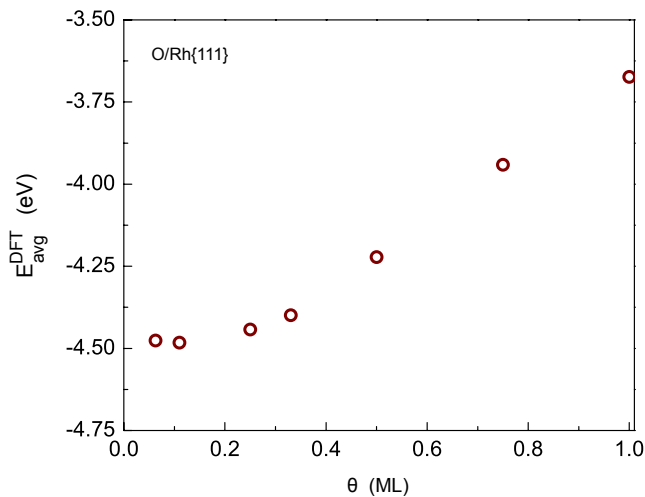


Figure 5.13: Variation in the average adsorption energy for O adsorption with surface coverage for the full coverage range on Rh{111} facet.

same for single adsorbate system. This piecewise interaction model is similar to the one proposed by Grabow et al.⁹⁰. However our proposed piecewise interaction model uses a universal threshold coverage and hence can be used for systems with multiple adsorbates.

The equation for the differential adsorption energy $E_{diff}(\theta)$ can be written as,

$$\begin{aligned} E_{diff}^i(\underline{\theta}) &= \underline{E}^0, \text{ when } |\underline{\theta}| \leq \theta^0 \\ &= \underline{E}^0 + f(\underline{\epsilon} \underline{\theta}), \text{ when } |\underline{\theta}| > \theta^0 \end{aligned} \quad (5.11)$$

where E^0 is the adsorption energy at coverage θ^0 , $|\underline{\theta}| = \sum_i \theta_i$ where θ_i are the elements in $\underline{\theta}$, $f = \frac{(|\underline{\theta}| - \theta^0)}{|\underline{\theta}|}$ and $\underline{\epsilon}$ is the interaction matrix. In the matrix the interaction parameters, $\epsilon_{ij} = \epsilon_{ji}$. The cross-interaction parameters (ϵ_{ij}) will be obtained as the geometric mean of the corresponding self interaction parameters.

One can now express the differential adsorption energy for a single adsorbate with coverage θ_i as,

$$\begin{aligned} E_{diff}^i(\theta_i) &= E_i^0, \text{ when } \theta_i \leq \theta^0 \\ &= E_i^0 + \epsilon_{ii}(\theta_i - \theta^0), \text{ when } \theta_i > \theta^0 \end{aligned} \quad (5.12)$$

For multiple adsorbates the differential adsorption energy can be expressed as,

$$\begin{aligned} E_{diff}^i(\underline{\theta}) &= E_i^0, \text{ when } \theta_i \leq \theta^0 \\ &= E_i^0 + \sum_j f \epsilon_{ij} \theta_j, \text{ when } |\underline{\theta}| > \theta^0 \end{aligned} \quad (5.13)$$

In previous study by Grabow et al.⁹⁰ we have seen that the threshold coverage is very much dependent on the metal surfaces and also on the adsorbates. In order to determine a general threshold coverage I have calculated the average adsorption energy for a range of adsorbates on the transition metals at different low coverages.

For a single adsorbate system the average adsorption energy has the form:

$$\begin{aligned} E_{avg}(\theta_i) &= E_i^0, \text{ when } \theta_i \leq \theta^0 \\ &= E_i^0 + \frac{1}{2} \epsilon_{ii}(\theta_i - \theta^0), \text{ when } \theta_i > \theta^0 \end{aligned} \quad (5.14)$$

In order to obtain the threshold coverage, I have calculated adsorption energies at coverages $\frac{1}{16}$ ML, $\frac{1}{9}$ ML, $\frac{1}{4}$ ML, $\frac{1}{3}$ ML and $\frac{1}{2}$ ML. For the condition, when the threshold coverage θ^0 is lower than 0.25 ML, the self-interaction parameters, ϵ_{ii} remains the same as the one obtained from the linear interaction model, using equation (5.4). However, when the threshold coverage θ^0 is higher than 0.25 ML, the self-interaction parameters, ϵ_{ii} , are obtained from equation:

$$\epsilon_{ii} = \frac{2 \left(E_{avg}(\theta = 1) - E_{avg}(\theta = 0.25) \right)}{(1 - \theta^0)} \quad (5.15)$$

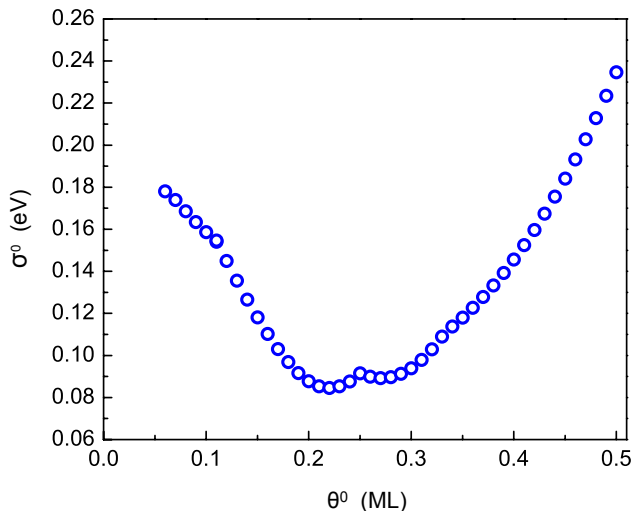


Figure 5.14: The RMS Error of the fitted piecewise interaction model versus the threshold coverage. The studied adsorbates: C, N, O, S, CH, NH and NO; metals: Au, Ag, Cu, Pd, Pt, Rh, Ru and Re and coverages are: $\frac{1}{16}$ ML, $\frac{1}{9}$ ML, $\frac{1}{4}$ ML, $\frac{1}{3}$ ML and $\frac{1}{2}$ ML.

As the $\theta^0 > 0.25$ ML, the adsorption energy at θ^0 should be equal to the adsorption energy calculated at 0.25 ML, i.e $E_{avg}(\theta^0) = E_{avg}(\theta = 0.25)$.

In Figure 5.14 the RMS errors in the average adsorption energies predicted from the fitted piecewise interaction model with respect to the DFT calculated values has been plotted versus the threshold coverages. The adsorption energy of C, N, O, S, CH, NH and NO over Au, Ag, Cu, Pd, Pt, Rh, Ru and Re for coverages $\frac{1}{16}$ ML, $\frac{1}{9}$ ML, $\frac{1}{4}$ ML, $\frac{1}{3}$ ML and $\frac{1}{2}$ ML are used for the fitting. Though according to a mean field model the threshold coverage was expected to be $\frac{1}{3}$ ML, we found that the threshold coverage with lowest RMS error for the systems studied here is 0.22 ML.

In Figure 5.15 and 5.16 we compare the estimated adsorption energies using the linear interaction model and the piecewise interaction model, respectively. The linear interaction model predicts a lower adsorption energy than the actual DFT adsorption energy in the low coverage regime for most of the species. The piecewise interaction model is clearly better and predict the adsorption energy with good accuracy in the low coverage regime. The unbiased standard deviations for the linear and piecewise model are 0.23 eV and 0.08 eV respectively.

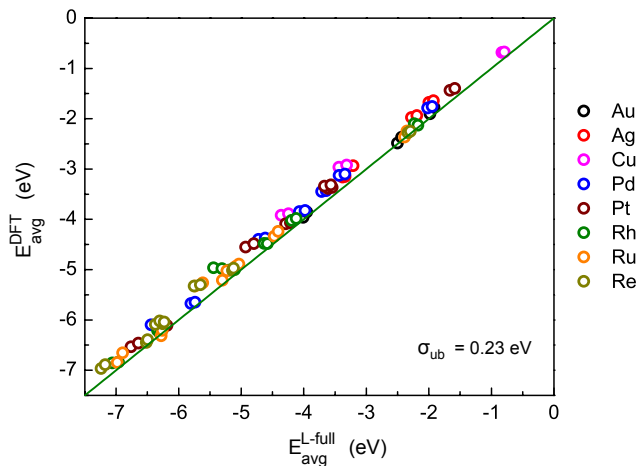


Figure 5.15: Parity plot of the average adsorption energy from DFT at $\frac{1}{16}$ ML and $\frac{1}{9}$ ML surface coverage versus the adsorption energy obtained using the full linear-interaction model and interaction parameter from Table 5.1, at those corresponding surface coverages. The studied adsorbents are: C, N, O, S, CH, NH and NO.

5.2 Effect of Adsorbate-Adsorbate Interactions in Catalytic NO Decomposition

Catalytic direct NO decomposition over the $\{111\}$ surface is taken as the first example to study the effect of adsorbate-adsorbate interactions on catalytic activity by including the interaction models in the microkinetic modeling. As we already have shown in the previous chapter 4 that the direct NO decomposition process mainly happens over the stepped and kinked surface, catalytic direct NO decomposition over the $\{111\}$ surface is only taken to illustrate the effect of different adsorbate-adsorbate interaction models on catalytic activity and propose the most consistent adsorbate-adsorbate interaction model for catalytic trends study. In the next two sections of this chapter I will show the effect of the adsorbate-adsorbate interaction on catalytic activity of two important catalytic process, CO methanation and steam reforming, using the interaction model chosen from this section. The reaction mechanism, scaling relations and formulation of the microkinetic model for the direct NO decomposition is described in the previous chapter 4.

We use the self-consistent mean field approach to solve the interaction model combined microkinetic model to determine the predicted rates and coverages. The mean field model assumes that every site is randomly occupied with a probability given by the average coverage. The mean field model is a good approximation in this reaction condition because of two reasons,

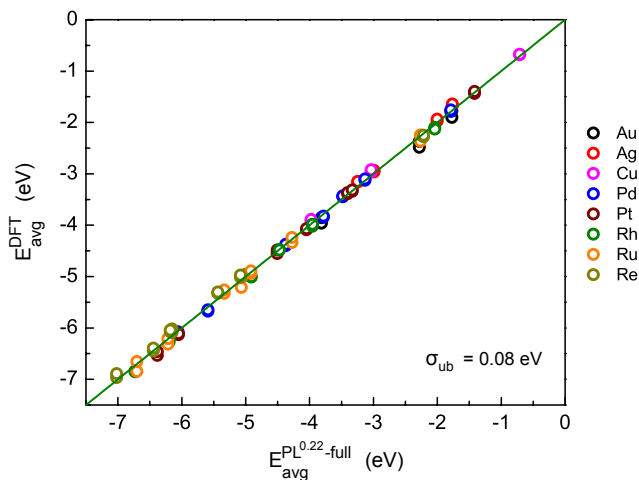


Figure 5.16: Parity plot of the average adsorption energy from DFT at $\frac{1}{16}$ ML and $\frac{1}{9}$ ML surface coverage versus the adsorption energy obtained using the piecewise full interaction model with 0.22 as the threshold coverage and interaction parameter from Table 5.1, at those corresponding surface coverages. The studied adsorbents are: C, N, O, S, CH, NH and NO.

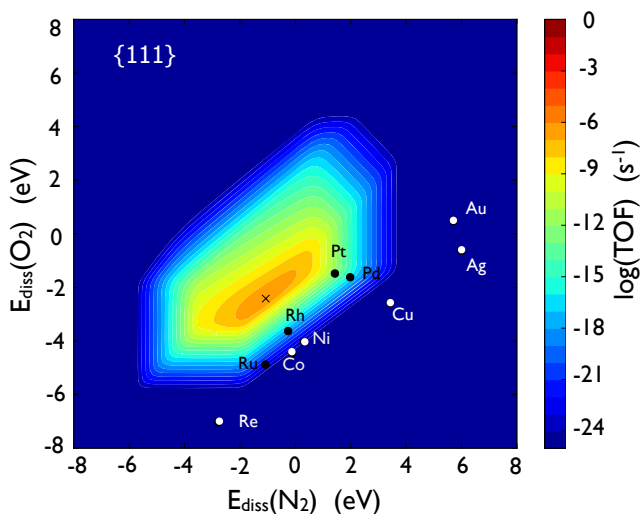


Figure 5.17: Volcano curve for direct NO decomposition on transition metals with no adsorbate-adsorbate interactions

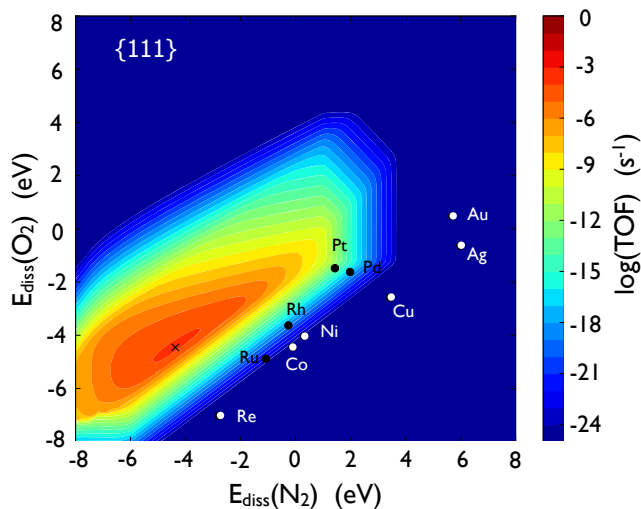


Figure 5.18: Volcano curve for direct NO decomposition on transition metals using the Rhodium model to describe adsorbate-adsorbate interactions

(a) The diffusion of the adsorbates is fast under these reaction condition. Typical diffusion barriers for the surface-adsorbate systems considered here are ~ 0.5 eV.

(b) As all the reaction parameters considered here are positive the differential adsorption energy is monotonically increasing with coverage, we can exclude the possibility of island formation.

However in the reactions where island formation occurs and the mean-field model would not give reasonable results for those instances.

In Figure 5.17 the rate for the direct decomposition of NO is calculated using the non-interacting mean field model.⁷³

Here I have applied two different sub-models to investigate the effect of adsorbate-adsorbate interaction on catalytic activity, namely the simple description, rhodium interaction model and the more useful and accurate, scaling based piecewise interaction model. It has been shown previously that the transition state scaling relations calculated at low coverage also holds for higher coverages.^{63,64,101} The scaling relations from article⁷³ therefore are also applied here.

We start out with the linear interaction model based on the constant rhodium interaction parameters and they remains constant for the whole adsorption energy range. The cross-interaction parameters are obtained from the geometric mean of the self-interaction parameters. In Figure 5.18 the catalytic activity is calculated using this rhodium interaction sub-model to include the coverage dependent adsorption energy in the microkinetic model. Due to the inclusion of the adsorbate-adsorbate interaction, the reactive metals are now less poisoned and regains some of their lost activity. The

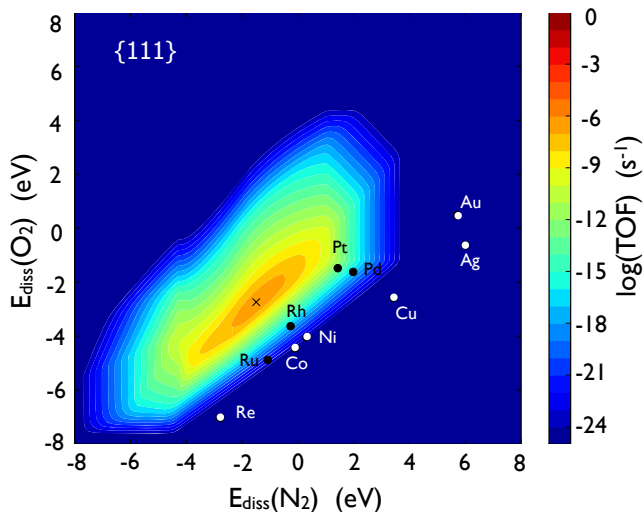


Figure 5.19: Volcano curve for direct NO decomposition on transition metals using the scaling based piecewise interaction model to describe adsorbate-adsorbate interactions

reactive metals are visibly more active here compared to the previous non-interacting mean field description shown in Figure 5.17. The inclusion of the interaction lifts up the lower left side of the volcano and makes it more flat. The right side of the volcano is not affected much and remains nearly the same. The maximum rate for the direct NO decomposition changes appreciably and is $\sim 10^3$ times higher than the maximum rate in Figure 5.17. Pt is still the best catalyst, and the catalytic rate obtained for Pt using the rhodium interaction model is similar to the catalytic rate of Pt obtained with non-interacting mean field description. The increment in catalytic rate is more prominent for the reactive metals.

After the simplest rhodium interaction sub-model we use the more accurate piecewise interaction model based on the scaled interaction model. The interaction parameters for adsorption energy up-to Pd adsorption energy are obtained using the ϵ vs E_{ads} linear scaling and for adsorption energies above Pd we use the same interaction parameter obtained for Pd. The cross-interaction parameters are obtained as the geometric mean of the self-interaction parameters. The threshold coverage is 0.22 ML.

Due to the use of constant rhodium interaction parameters for all the metals in the first sub-model in Figure 5.18, the effect of adsorption-adsorption interaction is visible all the way down to the very reactive metals and it has a very wide adsorption energy regime within which the catalytic decomposition is feasible. But as the interaction parameters in practice are smaller for the more reactive metals, we overestimate the effect of adsorbate-adsorbate interaction when we use the rhodium interaction model.

The scaling based interaction model takes into account these changes in the interaction parameters with the adsorption energy and provide more accurate catalytic rates for the direct decomposition of NO in Figure 5.19.

From Figure 5.17 and 5.19 we can clearly see that though the inclusion of a right adsorbate-adsorbate interaction with the scaling based piecewise interaction model, increases the catalytic rates for the reactive metals, the effect is not as prominent as using the rhodium interaction model and the shape of the volcano curve remains nearly unchanged. In Figure 5.19 the inclusion of the adsorbate-adsorbate interaction also widens the catalytic active area, but the maximum rate for the direct decomposition of NO at the top of the volcano and also the catalytic rate for the best metal Pt remains unchanged from the non-interacting mean field model in Figure 5.17. The inclusion of the adsorbate-adsorbate interaction do not change the catalytic trends among the transition metals.

5.3 Effect of Adsorbate-Adsorbate Interactions on CO Methanation

At temperatures where the surface mobility is high and coverages are low, the kinetic model can be solved using a non-interacting mean field approach. For situations with high surface coverages of intermediates, however, adsorbate-adsorbate interactions cannot necessarily be neglected as we have seen in the previous section of this chapter and the kinetic problem becomes substantially more complex. It is often found that for the catalytic surfaces with the optimal rate when the coverage of a key intermediate changes from low to high.⁶ However this may not be true for more complex reactions where multiple surface intermediates interact with each other. One example of this type of reaction is the conversion of synthesis gas (a mixture of CO and H₂) to hydrocarbons in the so-called Fischer-Tropsch process. In order to have a significant rate for carbon-carbon coupling, the coverages of carbon on the surface would need to be sufficiently high, hence adsorbate-adsorbate interactions may play a significant role in these type of reactions.^{89,102–105}

In order to investigate the effect of adsorbate-adsorbate interaction on the reaction rates, in this section we have used the production of CH₄ from CO and H₂ as a test reaction. A large number of catalytic studies have been done on methanation process over more than 100 years. Nickel, ruthenium, cobalt and iron have been found to be catalytically active for the methanation process. The four main reasons why methanation is important for catalytic study are:

- (1) to produce synthetic natural gas (SNG) with high methane and low CO content^{106,107}
- (2) to produce methane for the solid oxide fuel cells (SOFC) with high methane and no CO content^{108,109}
- (3) to avoid formation of methane as side product while producing alcohols (methanol synthesis) or higher hydrocarbons (Fischer-Tropsch reaction)^{110–112}

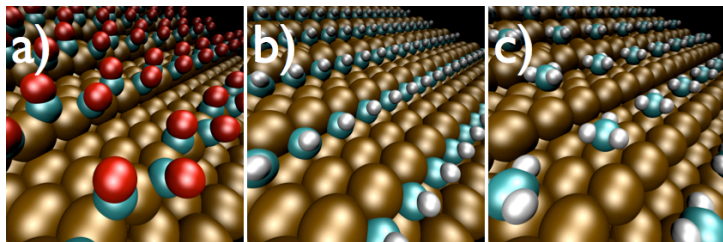


Figure 5.20: Adsorption for reaction intermediates on a) step (illustrated by CO*), b) four-fold (illustrated by CH*), and c) terrace sites (illustrated by CH₃*) on the (211) surface of Rh.

(4) to eliminate the last amount of CO from hydrogen (by converting it to CH₄) to prevent poisoning of the catalyst^{113,114}

Also methanation is used as a simple case study to understand the mechanism and determining factors of the complicated Fischer-Tropsch catalysis. We shall assume throughout this analysis that the reaction takes place at the steps of the catalyst surface, since this is the only site where the C-O bond splitting proceeds efficiently for the best catalysts for this process.⁹⁹ Reaction intermediates for CO methanation can adsorb on different sites of the stepped surface as shown in Figure 5.20. These are on-top of the step Figure 5.20(a), four-fold hollow beneath the step Figure 5.20(b), and on terrace sites Figure 5.20(c).⁹⁹ This complex reaction network makes CO methanation a challenging reaction to model and an attractive test case for the analysis of the effects of adsorbate-adsorbate interactions on its kinetics. We will investigate the adsorption energies of the reaction intermediates on the different facets (on-top, four-fold, and terrace) as a function of coverage, and model interactions between intermediates that are adsorbed on the different facets of the catalyst. We will assume a simple model of adsorbate-adsorbate interactions and show how catalytic trends are changed when we take those into account.

5.3.1 Microkinetic Model

The microkinetic model consists of the following elementary steps as reported elsewhere,^{3,6,9,99,115–120}

1. $\text{CO (g)} + * \leftrightarrow \text{CO}^*$
2. $\text{H}_2 \text{ (g)} + 2 * \leftrightarrow 2 \text{H}^*$
3. $\text{CO}^* + \text{H}^* \leftrightarrow \text{C}^* + \text{OH}^*$
4. $\text{C}^* + \text{H}^* \leftrightarrow \text{CH}^* + *$

5. $\text{CH}^* + \text{H}^* \leftrightarrow \text{CH}_2^* + ^*$
6. $\text{CH}_3^* + \text{H}^* \leftrightarrow \text{CH}_4(\text{g}) + 2^*$
7. $\text{OH}^* + \text{H}^* \leftrightarrow \text{H}_2\text{O}(\text{g}) + 2^*$
8. $\text{OH}^* + \text{OH}^* \leftrightarrow \text{H}_2\text{O}(\text{g}) + \text{O}^* + ^*$
9. $\text{O}^* + \text{H}^* \leftrightarrow \text{OH}^* + ^*$
10. $\text{CO}^* \leftrightarrow \text{C}^* + \text{O}^*$
11. $\text{CO}^* + \text{H}^* \leftrightarrow \text{COH}^*$
12. $\text{COH}^* \leftrightarrow \text{C}^* + \text{OH}^*$
13. $\text{CO}^* + \text{H}^* \leftrightarrow \text{CHO}^*$
14. $\text{CH}^* \leftrightarrow \text{CH}^* + \text{O}^*$

A number of different CO dissociation pathways are considered here as reported in previous literatures:^{99,115–119}

1. direct CO^* dissociation to C^* and O^*
2. via CHO^* formation
3. via COH^* formation
4. hydrogen assisted one step CO dissociation $\text{CO}^* + \text{H}^* \leftrightarrow \text{C}^* + \text{OH}^*$

However as the hydrogen assisted one step CO dissociation totally dominates over the other reaction pathways, (shown in Figure 5.23) which also agrees with previous work done on hydrogen assisted CO dissociation on Ni.⁹⁹ Hence in this work I have mainly focused on the hydrogen assisted one step CO dissociation for CO methanation on transition metals.

So the elementary reactions for the hydrogen assisted one step CO dissociation pathway for CO methanation are:

1. $\text{CO}(\text{g}) + ^* \leftrightarrow \text{CO}^*$
2. $\text{H}_2(\text{g}) + 2^* \leftrightarrow 2\text{H}^*$
3. $\text{CO}^* + \text{H}^* \leftrightarrow \text{C}^* + \text{OH}^*$
4. $\text{C}^* + \text{H}^* \leftrightarrow \text{CH}^* + ^*$
5. $\text{CH}^* + \text{H}^* \leftrightarrow \text{CH}_2^* + ^*$

6. $\text{CH}_3^* + \text{H}^* \leftrightarrow \text{CH}_4(\text{g}) + 2^*$
7. $\text{OH}^* + \text{H}^* \leftrightarrow \text{H}_2\text{O}(\text{g}) + 2^*$
8. $\text{OH}^* + \text{OH}^* \leftrightarrow \text{H}_2\text{O}(\text{g}) + \text{O}^* + ^*$
9. $\text{O}^* + \text{H}^* \leftrightarrow \text{OH}^* + ^*$

This reaction mechanism is used for the microkinetic model and further analysis and discussions on the effect of adsorbate-adsorbate interaction on catalytic rates.

Transition state energies for reactions on the {111} terrace (H-H, CH₂-H, CH₃-H) and {211} step (C-H, CH-H, H-OH, and O-H) on Ag, Cu, Pd, Pt, and Rh were taken from the literature.^{71,121,122} COH and CHO adsorption and transition state energies are calculated and are given in the appendix section A.3. Transition state energies for the C-O-H and O-H-OH reactions were calculated using the fixed bond length (FBL) method also can be found in the appendix section A.3. Vibration frequencies of the intermediated and transition states are calculated on the Cu{211} surface, and were assumed to be constant for all surfaces. The Zero point energies and entropies are calculated with the obtained vibrational frequencies using the harmonic oscillator approximation. The reaction condition used for this study is T = 523 K, P = 1 bar, 1% CO, 9% H₂, 1% CH₄, and 1% H₂O.^{123,124}

5.3.2 Adsorbate-Adsorbate Interaction Model

In order to investigate the effect of adsorbate-adsorbate interactions on the adsorption energies of reaction intermediates, adsorption energies were calculated at coverages of $\frac{1}{4}$ ML, $\frac{1}{3}$ ML, $\frac{1}{2}$ ML, $\frac{2}{3}$ ML, $\frac{3}{4}$ ML, and 1 ML in the adsorption sites where the intermediates were most stable at $\frac{1}{4}$ ML coverage. As described elsewhere, the adsorbate-adsorbate interaction effects were fitted using a piecewise continuous interaction model, similar to the one presented in the previous part of this chapter, and elsewhere.^{90,125}

The methanation reaction was assumed to involve four reaction sites: CO*, OH*, and O* adsorbed on the top row of the step (on-top site, *s), either on the bridge, or the three fold hollow site. C* and CH* adsorbed on the below the step on the four-fold hollow site (*f). CH₂* and CH₃* adsorbed on the terrace sites, either ontop, bridge or 3-fold hollow site (*t) and H* adsorbed on a separate site, the hydrogen reservoir site (*h). The hydrogen reservoir site has same energetics as terrace site. It has been shown both experimentally and theoretically that the interaction of H with itself and other adsorbates is negligible.^{38,64,126–130}

The differential adsorption energy, $E_i(\theta_i)$ can be written in the same way as in equation (5.13) as,

$$E_i(\theta_i) = E_i^0, \quad \text{when } |\theta| \leq \theta_0 \quad (5.16)$$

$$E_i(\theta_i) = E_i^0 + \sum_j f \epsilon_{ij} \theta_j, \quad \text{when } |\theta| > \theta_0 \quad (5.17)$$

where E_i^0 is the adsorption energy at coverage θ_0 and $f = \frac{(|\theta| - \theta_0)}{|\theta|}$, where $|\theta|$ is the sum of coverages of adsorbates on the on-top, four-fold, and terrace sites. ϵ_{ij} are the interaction parameters.

In order to get rid of the problem of derivative discontinuity at the threshold coverage θ_0 in (5.17), the piecewise interaction model introduced in the previous chapter is modified slightly to make the piecewise interaction model continuous and differentiable over the whole coverage range.

$$E_i(\theta_i) = E_i^0, \quad \text{when } |\theta| \leq \theta_0 - \frac{\epsilon_{ij}}{4} \quad (5.18)$$

$$E_i(\theta_i) = E_i^0 + (|\theta| - \theta_0 + \frac{\epsilon_{ij}}{4})^2 \frac{\theta_i}{|\theta|}, \quad \text{when } \theta_0 - \frac{\epsilon_{ij}}{4} < |\theta| \leq \theta_0 + \frac{\epsilon_{ij}}{4} \quad (5.19)$$

$$E_i(\theta_i) = E_i^0 + \sum_j f \epsilon_{ij} \theta_j, \quad \text{when } |\theta| > \theta_0 + \frac{\epsilon_{ij}}{4} \quad (5.20)$$

For this study we have used the sites both at the steps and terrace for adsorption. In order to reduce the complexity of the adsorbate-adsorbate interaction model, I assume that there is no interaction between the adsorbates adsorbed on the steps and terrace. The $|\theta|$ is the sum of coverages of adsorbates on the ontop and four-fold sites for the interaction over the step surface and for the terrace surface it is the sum of coverages of adsorbates on terrace sites (ontop, bridge and three-fold hollow).

The adsorption energies of all reaction intermediates are scaled with the binding energies of carbon (ΔE_C) and oxygen (ΔE_O)^{131–133}. Further details about the scaling used herein can be found in the Appendix. Transition state energies for each elementary reaction step are scaled with the dissociative chemisorption energies of the reaction products (see Appendix for further details).^{3,6,70–72,134,135}

5.3.3 DFT Setups

Self-consistent, periodic density functional theory (DFT) calculations were performed using the Dacapo code⁴⁰, which describes the valence electrons using a plane-wave implementation and represents the ionic cores using Vanderbilt ultrasoft pseudopotentials. A density cutoff of 500 eV and a kinetic energy cutoff of 340 eV were used. DFT calculations were performed using the RPBE functional, which uses a generalized gradient approximation³⁸. The self-consistent electron density was determined by iterative diagonalization of the Kohn-Sham Hamiltonian, with the occupation of the Kohn-Sham states being smeared according to a Fermi-Dirac distribution with a

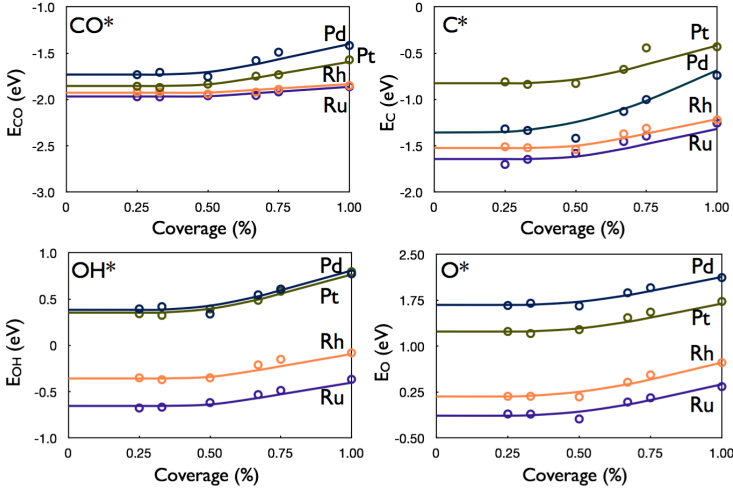


Figure 5.21: Adsorption energies of CO , C , OH , and O for the stepped $\{211\}$ surfaces of Pd, Pt, Rh, and Ru as a function of coverage. All adsorption energies are given relative to CO , H_2O and H_2 in the gas phase. Adsorption sites for CO^* , OH^* and O^* are on-top of the step, while C^* is adsorbed in the four-fold hollow site at the base of the step. The best-fit line is obtained from the adsorbate-adsorbate interaction model (see Methods section, Equation 6).

smearing factor of $k_B T = 0.1$ eV. All energies were extrapolated to $k_B T = 0$ eV. Sampling of the Brillouin zone was done using a $4 \times 4 \times 1$ Monkhorst-Pack k-point set.⁸⁶ Stepped $\{211\}$ surfaces of Ag, Cu, Pd, Pt, Rh, and Ru were modeled as nine-layer slabs (corresponding to three layers in the $\{111\}$ direction) with (1×3) unit cells. A vacuum of 15 Å separated successive slabs. All adsorbates and the top two layers were allowed to relax, while the bottom two layers were kept fixed in their bulk truncated positions.

Adsorption energies of the intermediates were calculated at coverages of $\frac{1}{4}$ ML, $\frac{1}{3}$ ML, $\frac{1}{2}$ ML, $\frac{2}{3}$ ML, $\frac{3}{4}$ ML, and 1 ML in their most stable adsorption sites at $\frac{1}{4}$ ML coverage. A 1 ML coverage for the $\{211\}$ surface is defined as one adsorbate per atom along the step. Different $\{211\}$ model slabs, (1×2) for ($\frac{1}{2}$ ML and 1 ML), (1×3) for ($\frac{1}{3}$ ML and $\frac{2}{3}$ ML), and (1×4) for ($\frac{1}{4}$ ML and $\frac{3}{4}$ ML) are used for the above adsorption energy calculations.

5.3.4 DFT Results

In Figure 5.21 I have shown the variation of average adsorption energy with coverage ranging from 0.25 ML to 1.0 ML for CO , C , OH and O on $\{211\}$ surfaces of Pt, Pd, Rh

Table 5.2: Adsorbate-adsorbate self-interaction parameters ϵ_{ii} for the {211} surfaces of Pd, Pt, Rh, and Ru. All energies are in eV. Data for the Rh(111) surface is taken from reference¹²⁵.

Adsorbate	Pd{211}	Pt{211}	Ru{211}	Rh{211}	Rh{111}
CH*	0.94	0.75	0.42	0.57	0.92
C*	1.34	0.81	0.65	0.63	2.10
CO*	0.66	0.52	0.21	0.17	1.27
OH*	0.85	0.82	0.50	0.53	0.60
O*	0.91	0.91	1.02	1.13	1.03
H*	0.02	0.05	0.18	-0.04	0.05

and Ru. The fitted line is the predicted average adsorption energy using the adsorbate-adsorbate interaction model and one can say that the interaction model is always qualitative and in most cases it is semi-quantitative. It can be seen that the change in the adsorption energy below coverage 0.5 ML is negligible, is in agreement with the previous theoretical studies^{38,64,126–130}. So I have taken 0.5 ML as the threshold coverage for the {211} surface. I previously have shown that in {111} the threshold coverage is significantly below at ~ 0.25 ML. This can be explained by nearest neighbor theory for adsorbate-adsorbate interaction. In {111} below 0.25 ML coverage there is no direct nearest neighbor and hence the adsorption energy remains nearly constant below 0.25 ML, whereas for {211} one can go up-to 0.5 ML coverage without any direct nearest neighbor interaction and hence for {211} the adsorption energy do not change significantly below 0.5ML. Once one go to higher coverage than 0.5 ML the adsorption energy decreases for {211} surface and the magnitude of these interactions for the transition metals is in the range of 0.1 to 0.7 eV at 1 ML coverage for the intermediates studied. Also the magnitude of adsorbate-adsorbate interactions for H on the transition metals in Table 5.2 are negligible and hence are taken as zero for further analysis. I have studied the adsorbate-adsorbate interactions on Rh {111} in details. The magnitude of interaction on {211} surface is typically lower than the {111} surface due to the facts that there is no nearest neighbor interaction below 0.5ML and at 1 ML coverage there is only 2 nearest neighbors, whereas for {111} we have 6 nearest neighbor at 1ML coverage (see Table 5.2). In Table 5.2 one can see that the magnitude of adsorbate- adsorbate interaction on the less reactive metals (Pd and Pt) is in general larger than the interaction on more reactive metals (Rh and Ru). I have include the variation in the adsorbate-adsorbate interaction for the different transition metals by using the scaled interaction model, where the the adsorbate-adsorbate interactions are scaled with the binding energy of carbon and oxygen, as shown in Table 5.3. As it has been described previous section of this chapter 5.1 all the cross interaction parameters between the adsorbed reaction intermediates is included in our model as the square root of the two corresponding self-interaction parameters. For the cross interaction of intermediates adsorbed I have considered interaction for adsorbates adsorbed on the same type of site also on different sites like the on-top and four-fold sites. I also have shown the interaction matrix in Table 5.4, using the interaction parameters from Table 5.3.

In Figure 5.22 I have shown the comparison of adsorption energy of all the possible

Table 5.3: Interaction parameters ϵ_{ii} were scaled with the sum of the carbon and oxygen binding energies (with respect to graphene and gas phase O₂, respectively).

Metal	C* + O*	CH ₃ *	CH ₂ *	CH*	C*	CO*	OH*	O*
Pd	-0.89	1.019	1.201	0.937	1.343	0.659	0.847	0.912
Pt	-0.53	1.263	1.018	0.747	0.813	0.521	0.823	0.912
Rh	-2.35	1.148	1.877	0.568	0.631	0.171	0.533	1.126
Ru	-2.70	0.886	1.532	0.416	0.649	0.209	0.503	1.024
Slope		0.092	-0.308	0.183	0.203	0.203	0.169	-0.082
Intercept		1.227	0.909	0.963	1.188	0.718	0.949	0.862

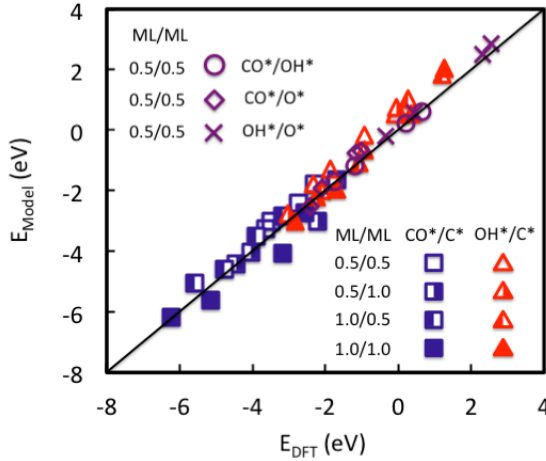


Figure 5.22: Comparison of adsorption energies of C*, CO*, OH*, O* on the stepped (211) surfaces of Pd, Pt, Rh, and Ru with coverages of 0.5 and 1.0 ML. Energies predicted by the adsorbate-adsorbate interaction model (y-axis) are compared to those derived from the full DFT calculations (x-axis). All adsorption energies are given relative to CO, H₂O and H₂ in the gas phase. CO*, OH* and O* are adsorbed on the on-top site, while C* is adsorbed in the four-fold site. Circles, routes and stars represent adsorption on the ontop sites. Squares and triangles represent cross interactions between adsorbates on the on-top and four-fold sites.

cross-interactions of CO*, OH*, O*, and C* on the {211} surfaces, as predicted by DFT calculation versus the ones obtained using the adsorbate-adsorbate interaction. The corresponding coverage for calculating the cross is the sum of coverages on the on-top and four-fold sites when calculating the interaction effects in Equation 6.

Table 5.4: Matrix of calculated interaction parameters for the stepped {211} surface of Ru. Self-interaction parameters (e.g., $\epsilon_{\text{CO}-\text{CO}}$) were calculated from the scaling parameters listed in Table 5.3. Unless otherwise indicated, cross-interaction parameters were calculated from the geometric average of the two interacting adsorbates.

ϵ_{i-j} i	j	CH_3^{*t}	CH_2^{*t}	CH^{*f}	C^{*f}	CO^{*s}	OH^{*s}	O^{*s}	H^{*h}
		0.905	1.987	0.323	0.478	0.007	0.358	1.149	0 ^a
CH_3^{*t}	0.905	0.905	1.341	0 ^b	0 ^b	0 ^b	0 ^b	0 ^b	0 ^a
CH_2^{*t}	1.987	1.341	1.987	0 ^b	0 ^b	0 ^b	0 ^b	0 ^b	0 ^a
CH^{*f}	0.323	0 ^b	0 ^b	0.323	0.392	0.049	0.34	0.609	0 ^a
C^{*f}	0.478	0 ^b	0 ^b	0.392	0.478	0.06	0.413	0.741	0 ^a
CO^{*s}	0.007	0 ^b	0 ^b	0.049	0.06	0.007	0.052	0.093	0 ^a
OH^{*s}	0.358	0 ^b	0 ^b	0.34	0.413	0.052	0.358	0.641	0 ^a
O^{*s}	1.149	0 ^b	0 ^b	0.609	0.741	0.093	0.641	1.149	0 ^a
H^{*h}	0 ^a	0 ^a	0 ^a	0 ^a	0 ^a	0 ^a	0 ^a	0 ^a	0 ^a

^a Interactions between adsorbed hydrogen and other reaction intermediates is negligible, as discussed in the paper.

^b Adsorbate-adsorbate interactions between reaction intermediates on the terrace (e.g., CH_3 and CH_2) and the four-fold/on-top sites are assumed to be zero.

^c A modified interaction matrix is used for the microkinetic modes to incorporate the high coverage C-O-H BEP line.

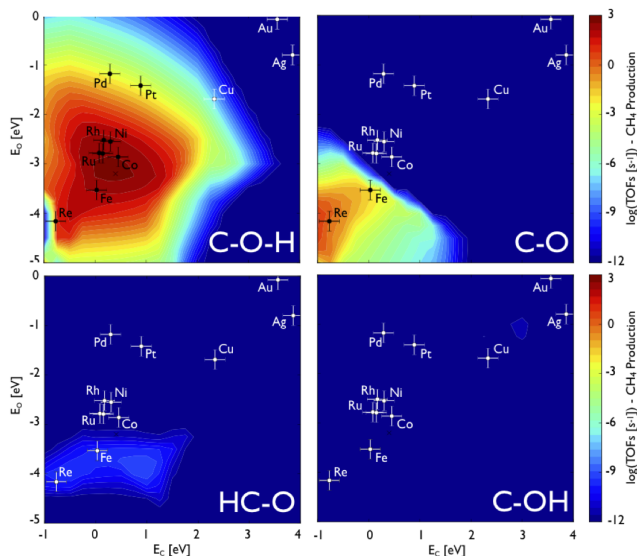


Figure 5.23: Predicted CH_4 production rates for various pathways. Activity volcanos are also given for 523 K and 1 bar with a gas composition of 1% CO , 97% H_2 , 1% CH_4 , and 1% H_2O .

5.3.5 Microkinetic Modeling Results

In Figure 5.23 we can see that the dominant pathway for CO methanation is the hydrogen assisted one step CO dissociation and other CO dissociation pathways considered here contribute very little to the overall CH_4 production rate. The rate of other CO dissociation pathways are negligible due to high activation barriers.

In this second part of the chapter, I have studied the effect of adsorbate-adsorbate interaction on surface coverage of the reaction intermediates, as well as the reaction rate. I have used the binding energy of carbon (ΔE_C) and oxygen (ΔE_O) as our two independent descriptors. The adsorption energy of the other reaction intermediates and the transition states are obtained using the scaling relations. In previous CO methanation studies it has always been assumed that a particular step is rate-determining (either C-O dissociation, OH_x , or CH_x hydrogenation).^{6,9,99} In this study I use the microkinetic model, where all the elementary reaction steps are treated as potentially rate determining one. In Figure 5.24 I have shown the coverage of CH^* , C^* , O^* , CO^* and total coverage of all the adsorbates as a function of ΔE_C and ΔE_O , obtained from microkinetic model solution for both without interaction (Figure 5.24 (a) – (c) (on-top and four-fold) and with interaction model 5.24 (d) – (f)) (on-top and four-fold). C^* and CH^* binds preferably on the 4-fold site whereas O^* and CO^* binds on-top on the step. We can also see for the coverage obtained using the microkinetic model without

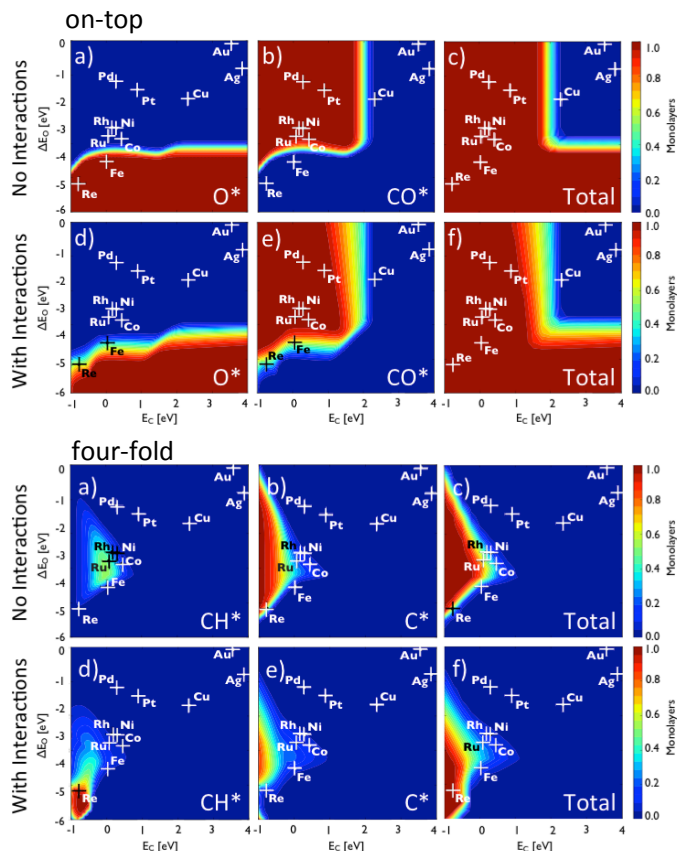


Figure 5.24: (on-top) Coverages of O*, CO*, and the total coverage on the on-top site as a function of the carbon (ΔE_C) and oxygen (ΔE_O) binding energies as obtained by the solutions to the microkinetic model without (a-c) and with (d-f) adsorbate-adsorbate interactions. (four-fold) Coverages of CH*, C*, and the total coverage on the four-fold site as a function of the carbon (ΔE_C) and oxygen (ΔE_O) binding energies as obtained by the solutions to the microkinetic model without (a-c) and with (d-f) adsorbate-adsorbate interactions. The carbon and oxygen binding energies for the {211} surfaces of selected transition metals are depicted. Reaction conditions are 523 K and 1 bar with a gas composition of 1% CO, 97% H₂, 1% CH₄, and 1% H₂O.

interaction, the metals with high carbon and oxygen binding energy (Re and Fe) are covered with O* on the on-top site whereas metals with moderate oxygen binding energy (Ru, Rh, Ni, Co, Pd and Pt) are covered with CO*, as shown in Figure 5.24 (on-top).

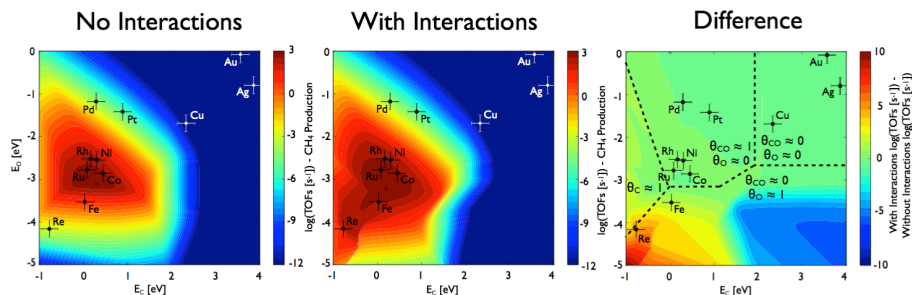


Figure 5.25: Theoretical activity volcanoes for the production of methane from CO and H₂ without (a) and with (b) the inclusion of adsorbate-adsorbate interactions, as well as (c) the difference in rates between the two scenarios. Turnover frequencies for the {211} surfaces are plotted as a function of the carbon (ΔE_C) and oxygen (ΔE_O) binding energies as obtained by the solutions to the microkinetic model. The carbon and oxygen binding energies for the (211) surfaces of selected transition metals are depicted. Reaction conditions are 523 K and 1 bar with a gas composition of 1% CO, 97% H₂, 1% CH₄, and 1% H₂O.

There is no drastic change in coverage picture when I included the adsorbate-adsorbate interactions. Though the onset binding energy where the surface started to become covered with adsorbates remains relatively unchanged, the change in the coverage is more gradual and smooth when I used the adsorbate-adsorbate interactions. Figure 5.24 (four-fold) also signal to the dividing line between the transition metals (Ni, Co, Rh, Ru and Ni) that are selective towards methane formation (low CH_x coverage) and those (Fe and Re) that produce higher hydrocarbons (higher CH_x coverage).

As it has been previously shown, here also I have scaled the transition state energies for the elementary reactions steps with the energies of the reaction products calculated at low coverages^{3,6,70–72,134,135}; here I have assumed that the scaling relationship calculated at low coverage holds true even at high coverages as well. However it is not always true and the BEP line for the high coverage C- OH splitting step has been found to be significantly lower compared to the low coverage line.^{9,99} To obtain a correct rate volcano it is essential to have the correct BEP hence in this study for the C-OH splitting I have used the high coverage BEP relation (a comparison plot of the low and high coverage BEP and corresponding activity volcano plots is shown in appendix Figure A.1). Apart from the C-OH bond splitting, however all the other elementary reaction steps are either simple hydrogenation or dehydrogenation reactions and it have seen before that the adsorbate-adsorbate interaction between hydrogen and other adsorbate is negligible the low coverage and the high coverage BEP relations for these elementary steps should be nearly the same.

The possible explanation can be found from the correlation between the transition

state energy and adsorption energies.

$$E^a = E^{TS} - E_I, \quad (5.21)$$

Where E^a , E^{TS} and E_I are the activation energy, transition state energy and initial state energy respectively.

Where as,

$$E^{TS} = \alpha^{TS} E_F + \beta^{TS}, \quad (5.22)$$

Where E_F is the final state energy. α^{TS} and β^{TS} are the slope and intercept of that linear correlation respectively.

From (5.21) and (5.22) one can obtain,

$$E^a = \alpha^{TS} E_F + \beta^{TS} - E_I = \alpha^{TS} (E_F - E_I) + \{\beta^{TS} - E_I(1 - \alpha^{TS})\} \quad (5.23)$$

$$E^a = \alpha^{TS} \Delta E_r + \{\beta^{TS} - E_I(1 - \alpha^{TS})\}, \quad \text{where } \Delta E_r = (E_F - E_I) \quad (5.24)$$

With the assumption that the transition state scaling obtained at low temperatures still holds for the high coverage, one can write,

$$E^a[\theta] = E^{TS}[\theta] - E_I[\theta], \quad (5.25)$$

Where $E^a[\theta]$, $E^{TS}[\theta]$ and $E_I[\theta]$ are the activation energy, transition state energy and initial state energy at coverage θ respectively.

Where as,

$$E^{TS}[\theta] = \alpha^{TS} E_F[\theta] + \beta^{TS}, \quad (5.26)$$

Where $E_F[\theta]$ is the final state energy. α^{TS} and β^{TS} are the slope and intercept of that linear correlation respectively, and are same as the low-coverage values.

From (5.25) and (5.26) one can obtain,

$$E^a[\theta] = \alpha^{TS} E_F[\theta] + \beta^{TS} - E_I[\theta] = \alpha^{TS} (E_F[\theta] - E_I[\theta]) + \{\beta^{TS} - E_I[\theta](1 - \alpha^{TS})\} \quad (5.27)$$

$$E^a[\theta] = \alpha^{TS} \Delta E_r[\theta] + \{\beta^{TS} - E_I[\theta](1 - \alpha^{TS})\}, \quad \text{where } \Delta E_r[\theta] = (E_F[\theta] - E_I[\theta]) \quad (5.28)$$

As $(1 - \alpha^{TS}) > 0$ and $E_I[\theta] > E_I$, for any coverage $\theta > \theta_0$, where θ_0 is threshold coverage, from equations (5.24) and (5.28), one can write,

$$\{\beta^{TS} - E_I[\theta](1 - \alpha^{TS})\} < \{\beta^{TS} - E_I(1 - \alpha^{TS})\} \quad (5.29)$$

And hence the BEP lines at the high coverage are low laying than the low coverage BEP, even though they follow the same transition state scaling. However for the hydrogenation/dehydrogenation steps of CO methanation reaction, as one of the co-adsorbate is H and also the coverage of CH_x species is negligible in most of the region,

the assumption of same low coverage and the high coverage BEP relations is still a good first approximation.

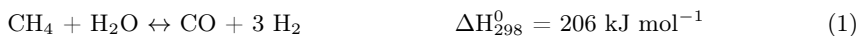
The effects of adsorbate-adsorbate interactions on the catalytic rate of CO methanation over the {211} transition metal surface is shown in Figures 5.25(a) and (b) for the two microkinetic models, without and with interactions respectively; and in Figure 5.25(c) I also have shown the difference plot for these theoretically predicted catalytic rates. For both the microkinetic models, with and without adsorbate-adsorbate interaction Ru and Co are predicted to be the most active catalyst for CO methanation, while Rh, Ni, and Fe shows moderate activity, in agreement with earlier theoretical^{6,9,99} and experimental^{123,136} studies. Due to the inclusion of the adsorbate-adsorbate interactions, the catalytic active region extends more to the reactive metal surfaces by falling off less steeply with the higher carbon and oxygen binding energies. The position of the top of the volcano though remains nearly unchanged.

Also the catalytic activity in the weak-binding region ($\Delta E_C > 2$ eV, $\Delta E_O > -3$ eV) also remains the same. As the coverages of all the intermediates are close to zero at this region and the total coverage is well below the threshold of 0.5 ML, there is no effect of including the adsorbate-adsorbate interactions. When the surface coverage goes above the threshold coverage ($|\theta| > 0.5$), the binding energies of the reactants and products decreases, and as the transition states also scale with the binding energies of the products, hence affecting the transition state energies as well. And as the decrease in the reactant and product binding energies are in general higher than the decrease in corresponding transition state energies the activation barrier are in general smaller at the high coverage. But in some cases, like the C-O bond splitting here, an increase in reaction barriers is observed, contrary to expectation. This can again be explained in terms of the effects the interactions have on the activation barrier for CO splitting. While high coverages of CO* decrease the adsorption energy of CO*, the adsorption energies of the C-O splitting products (C* and OH*) are destabilized even more resulting in a higher C-O splitting barrier. Consequently, a catalyst with a low carbon binding energy ($\Delta E_C > 2$ eV) and a high oxygen binding energy ($\Delta E_O < -3$ eV) is predicted to have an overall rate that is 2-3 orders of magnitude lower when interaction effects are included. Similar effects are predicted for materials with relatively modest oxygen and carbon binding energies, as can be seen in the predicted reaction rates of Pt and Pd that decrease upon inclusion of adsorbate-adsorbate interactions.

For catalysts with high adsorption energies of both carbon and oxygen, however, the opposite effect is predicted. For example, the predicted rates of Re and Fe, which bind oxygen strongly, are increased by the inclusion of interactions by 2-3 orders of magnitude. A similar effect is seen for very high carbon binding energies ($\Delta E_C < -0.5$ eV). Adsorbate-adsorbate interactions in these regions decrease the binding energies of reaction products (C* and O*), preventing the surface from becoming poisoned by reaction products. This increases the concentration of vacant (i.e., active) sites and consequently increases the expected reaction rates. Similar trends have been observed for CO oxidation and NO decomposition.^{90,125}

5.4 Catalyst Screening for Steam Reforming of Methane using Adsorbate-Adsorbate Interaction Model

In this section I show the use of interaction model for the catalyst screening for steam reforming of methane, using DFT calculations and microkinetic modeling. Here I will demonstrate a very efficient way of screening transition metals and metal alloys based on the predicted rates and stability for a given catalytic reaction using the DFT calculations. Steam reforming of methane is a very important reaction in chemical industry for hydrogen and syngas production.¹³⁷ In order to use DFT for the search of a catalyst with high reactivity and stability, one must have a good understanding of the reaction mechanism of that catalytic reaction.



As the steam reforming is a highly endothermic reaction, we need to run the reaction at a very high temperature (750 – 1000 °C) to have considerable conversion. Also industrially the reaction needs to be operated at a high water to methane ratio ($\text{H}_2\text{O}/\text{CH}_4 > 3$) in order to prevent the deactivation of the catalyst due to the possibility of coking. And because of these two reasons the cost of hydrogen production using steam reforming of methane is very high. Three potential reaction pathways for CO formation in steam reforming of methane have been proposed previously.

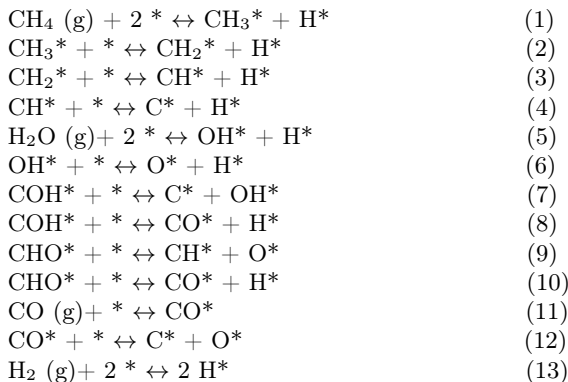
1. direct C* and O* combination¹³⁸
2. via CHO* formation^{139–143}
3. via COH* formation^{144–146}

I have investigated all these three reaction pathways in our descriptor based microkinetic model using binding energy of carbon and oxygen as the two independent parameters.¹⁴⁴ Using this simple description based approach, I will establish the method of screening a large number of transition metal alloys, and find out the most promising catalysts for industrial production of hydrogen and syngas using steam reforming of methane.

5.4.1 Microkinetic Model

The developed microkinetic model using the adsorption and transition state energies from the CatApp, a web based database for adsorption and transition state energies.^{121,122} The correlation between the adsorption energy and transition states with

the binding energy of carbon and oxygen are used to obtain the adsorption energy scaling parameters for the intermediates and transition state scaling parameters for the activation barriers. Here I constructed a reaction mechanism for the steam reforming of methane with the following elementary reaction steps:



The construction of the thermodynamics and kinetics of the microkinetic model has been described in the previous chapter in details. Here also I assume the reaction takes place at the stepped surface. So I only consider four different sites on the stepped surface, the on-top of the step (*s), four-fold site below the step (*f), terrace sites (*t) and hydrogen reservoir sites (*h) as explained in the previous section 5.3. I also have included the adsorbate-adsorbate interaction model to describe the coverage dependent adsorption energy. The adsorbate-adsorbate interaction model has been discussed in details in previous section of this chapter. Some of the interaction parameters used in the microkinetic model is given in the Table 5.5 and others are taken from previous section Table 5.3. The steam reforming of methane is studied at both the laboratory

Table 5.5: Self-interaction parameter for various adsorbates. The adsorption energy of C* and O* are relative to gas phase methane, water and hydrogen. Other values of interaction parameters are taken from section 5.3.

Metal	$E_{\text{C}^* + \text{O}^*}$	CH_3^*	CH_2^*	CHO^*	COH^*
Pd	3.09	1.02	1.2	0.66	1.57
Pt	3.45	1.26	1.02	0.32	1.43
Rh	1.63	1.15	1.88	0.9	1.08
Ru	1.28	0.89	1.53	1.27	0.51
Slope		0.09	-0.31	-0.35	0.39
Interscept		0.86	2.13	1.61	0.21

and industrial conditions, given in Table 5.6.^{144,147}

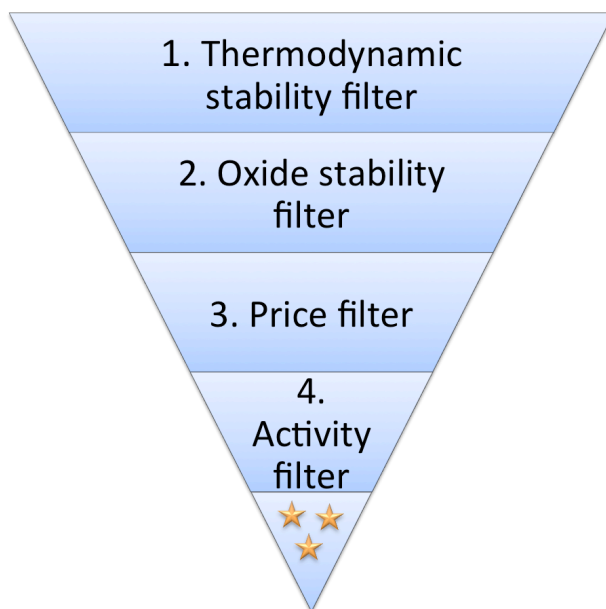


Figure 5.26: Schematic for searching transition metal alloy catalysts based on their predicted rates, costs, and stabilities for steam reforming.

Table 5.6: The conditions in steam reforming reactor as described in Ref. ^{144,148}.

Condition	Lab scale	Inlet-low	Outlet-high
T (K)	773	638	1066
P (bar)	2	14.3	12.2
Conversion (%)	29 ^a	0.3 ^b	50 ^c
H ₂ O (mol. %)	40	83.1	65.8
H ₂ (mol. %)	15	1.9	25.0
CH ₄ (mol. %)	40	14.5	2.4
N ₂ (mol. %)	0	0.4	0.3
CO (mol. %)	5	0.1	6.5

^a, ^b, ^c Conversions are respect to their equilibrium conversions.

5.4.2 Alloy Screening Method

In Figure 5.26 I have outlined the screening method used here based on DFT calculated stability data, price of the alloy and catalytic activity obtained from solving the microkinetic model. The alloy screening is performed in four steps:

1. Thermodynamic stability filter: The metal alloy should be stable with respect to its pure metal constituents.
2. Oxidation stability filter: The bulk metal alloy towards formation of oxide in the given reaction condition.
3. Price filter: The cost of the metal should not be high, i.e. it must not contain any precious metal as its constituents.
4. Activity filter: The catalyst must show reasonable activity in the given reaction condition

After performing these screening processes I will point out the most promising catalyst for the given catalytic reaction.

Thermodynamic stability filter

The ability of two metals to form a metal alloy is determined its alloy formation energy. The alloy formation energy of a given alloy can be defined as:

$$E_f = E_{\text{alloy}} - N_A E_{A(\text{bulk})} - N_B E_{B(\text{bulk})} \quad (5.30)$$

where E_f is the alloy formation energy, E_{alloy} is the calculated energy of the alloy, N_i and $E_{i(\text{bulk})}$ is the molar ratios and calculated energy of the bulk individual metal constituents respectively. For this study I only have considered the metal alloys having alloy formation energy less than + 0.2 eV/unit cell, as potentially stable.

Oxidation stability filter

Industrially a high $\text{CH}_4/\text{H}_2\text{O}$ ratio is used to prevent coking, but due to high H_2O pressure the catalyst still may be deactivated due to formation of metal oxide. Hence we use this oxidation stability filter to pick out the catalyst stable towards oxidation under the given reaction conditions. The stability of the metal alloy towards oxidation can be given by the Gibbs free energy of oxidation, and can be calculated using,

$$\Delta G_{\text{oxide}}^{\text{alloy}} = -E_f + x \Delta G_{A-\text{oxide}} + y \Delta G_{B-\text{oxide}} \quad (5.31)$$

where $\Delta G_{\text{oxide}}^{\text{alloy}}$ is the alloy Gibbs free energy of oxidation, E_f is the alloy formation energy, $\Delta G_{A-\text{oxide}}$ and $\Delta G_{B-\text{oxide}}$ are the energies of oxidation of metal A and B, respectively.

The oxidation energy of a metal M, forming a stable metal oxide M_mO_n can be calculated using,

$$\Delta G_{M-oxide} = \Delta H_{reaction}^0 - T\Delta S_{reaction}^0 - \frac{n}{m}RT\ln\frac{p_{H_2O}}{p_{H_2}} \quad (5.32)$$

where $\Delta G_{M-oxide}$ is the oxidation energy of a metal M towards the formation of M_mO_n , $\Delta H_{reaction}^0$ and $\Delta S_{reaction}^0$, the enthalpy and entropy of the reaction respectively, are calculated using reference values from literature¹⁴⁹.

Cost and activity filter

For a metal alloy to be promising on an industrial scale, the cost must not be too high and hence we should always try not to use the expensive noble metals, whenever possible. In order to use the cost filter for the metal alloys for steam reforming I excluded the metal alloys whose cost exceeds \$5000 per kg. In this way we will be able to exclude the metal alloy having precious metal (e.g. Pt, Pd, Ir, Ru, Rh, Os and Au). The reference costs for the pure metals were obtained from the website, www.chemicool.com, on February 1, 2013¹⁵⁰ is given in Table A.18. The alloy to be a potential candidate as an industrially viable catalyst it also must have an appreciable turnover number (TOF). For this steam reforming of methane study, I have screened the alloys using activity filter with TOF larger than 10^{-4} s^{-1} and 10^{-2} s^{-1} for the inter and outlet reactor condition respectively.

Table 5.7: Prices for the pure metals, values taken from Chemicool website¹⁵⁰.

Metal	Price (\$/kg)	Metal	Price (\$/kg)	Metal	Price (\$/kg)
Sc	14000	W	110	Pt	130000
Y	4300	Mn	65	Cu	97
La	8000	Re	16000	Ag	1200
Ti	6610	Fe	72	Au	55400
Zr	1570	Ru	14000	Zn	53
Hf	1200	Os	77000	Cd	460
V	2200	Co	210	Hg	480
Nb	180	Rh	130000	Ga	2200
Ta	4500	Ir	42000	In	9680
Cr	3800	Ni	77	Tl	480
Mo	440	Pd	58330	Al	157
Sn	240	As	3200	Bi	39
Pb	24.5	Sb	45	Ge	3600
Si	54				

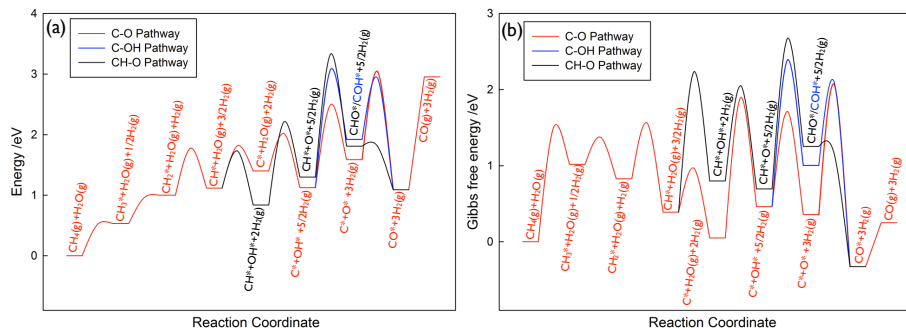


Figure 5.27: (a) Potential energy diagram for CH_4 steam reforming to $\text{CO}(\text{g})$ and $\text{H}_2(\text{g})$ on a $\text{Rh}(211)$ surface; (b) Free energy diagram for CH_4 steam reforming to $\text{CO}(\text{g})$ and $\text{H}_2(\text{g})$ on a $\text{Rh}(211)$ surface. Reaction conditions are: $T = 773 \text{ K}$, $P = 1 \text{ bar}$, with a gas composition of 40% CH_4 , 40% H_2O , 5% CO and 15% H_2 (corresponding to 29% approach to equilibrium). Three pathways are depicted in red, black, and blue for the formation of $\text{CO}(\text{g})$ via $\text{C}^* + \text{O}^*$, $\text{C}^* + \text{OH}^*$, and $\text{CH}^* + \text{O}^*$, respectively. The main pathway is depicted in red. Values for the adsorption energies of reaction intermediates were taken from CatApp^{121,122}.

5.4.3 Microkinetic Modeling Results

The PES diagram and the Gibbs free energy diagram for the CH_4 steam reforming reaction over $\text{Rh}\{211\}$ are shown in Figure 5.27 (a) and (b) respectively. I have shown the energetics for the three reaction pathways for CO^* formation via direct C^* and O^* coupling, COH^* formation and CHO^* formation as mentioned before. For all the three reaction pathways the formation of the C-O bond has the highest reaction barrier. However from Figure 5.27 (b) it is difficult to say which one will be the dominant pathway for the steam reforming reaction and also the dominant pathway may vary for different metals. It has been previously proposed that the COH^* and CHO^* pathways can be significant at lower temperature¹⁵¹.

The steam reforming catalytic rate obtained from the microkinetic model (at the laboratory condition) has been plotted versus the two descriptors E_C and E_O in Figure 5.28. The metals with highest catalytic rates are Ni, Ir, Rh and Ru. Re and Fe shows moderate activity but they are known to form coke and hence the catalyst get deactivated very soon. Pd and Pt show much lower activity at this reaction condition. The activity volcano can also be understood from the coverage plot of the adsorbates shown in Figure 5.29. As it has been written earlier the O^* and CO^* binds on the on-top of the step, whereas C^* binds on the 4-fold site. For a catalyst to show high activity one of the key-intermediate coverage should change abruptly. Hence, in Figure 5.29 Ni, Co, Ir, Rh and Ru having coverage of O^* , CO^* and C^* changing abruptly in the region, show the highest activity.

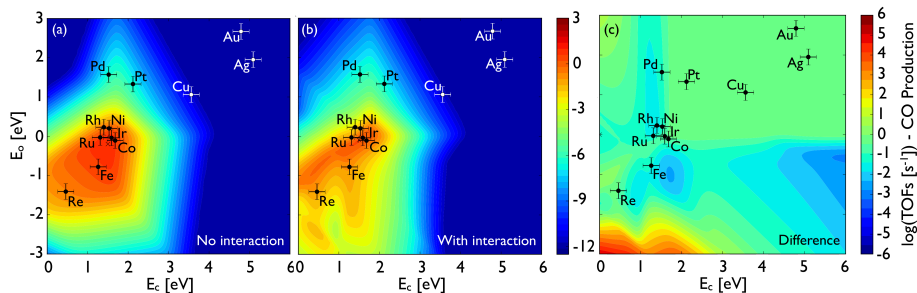


Figure 5.28: Calculated turnover frequencies (TOFs) for CH_4 steam reforming to CO and H_2 (a) without adsorbate-adsorbate interactions; (b) with adsorbate-adsorbate interactions and (c) differences of the reaction rates between models with and without adsorbate-adsorbate interaction. The carbon and oxygen binding energies for the stepped (211) surfaces of selected transition metals are depicted. The error bars indicate an estimated error of 0.2 eV for E_C and E_O . Reaction conditions are: $T = 773$ K, $P = 1$ bar, with a gas composition of 40% CH_4 , 40% H_2O , 5% CO and 15% H_2 (corresponding to 29% approach to equilibrium).

On including the adsorbate-adsorbate interaction in the microkinetic model the changes in the coverages are not that sharp and the coverage of the O^* , CO^* and C^* changes more gradually from 0 ML to 1 ML. The adsorbate-adsorbate interaction also affects the catalytic rates as shown in Figure 5.28 (a) and (b) for without and with adsorbate-adsorbate interaction respectively. In Figure 5.28 (c) I have plotted the difference in rate between the two microkinetic models with and without adsorbate-adsorbate interaction. No drastic change is observed when the adsorbate-adsorbate interactions are applied. The shape of the volcano and also the top remains essentially unchanged. The rate at the bottom right and the region near the top of the volcano is predicted to be lower when including of the adsorbate-adsorbate inclusions. When doing more closer study on the effect of the adsorbate-adsorbate interactions on the activation barriers of the rate limiting step, I found that the rate limiting step in the bottom right and the region near the top of the volcano is the formation of CO^* from the C^* and O^* direct coupling, and due to high O^* coverage the activation barrier increase upon including the adsorbate-adsorbate interaction and hence causes the lowering of the reaction rate. The rate in the lower left region increases upon introducing the adsorbate-adsorbate interaction in the microkinetic model. Inclusion of adsorbate-adsorbate interactions increases the number of free sites and the catalyst surface is less poisoned by O^* now and hence we observe an increase in the rate in this region.

In Figure 5.30, I have shown the catalytic rates of steam reforming of the three different pathways discussed before, working separately. The catalytic rate of the direct CO^* formation by C^* and O^* coupling is higher than the COH^* and CHO^* pathway by many orders of magnitude at the most active region of the rate volcano. Though the activation barrier for the CH-O pathway sometimes can be lower than the direct CO^* formation pathway, due to much higher C^* coverage than the CH^* coverage, the

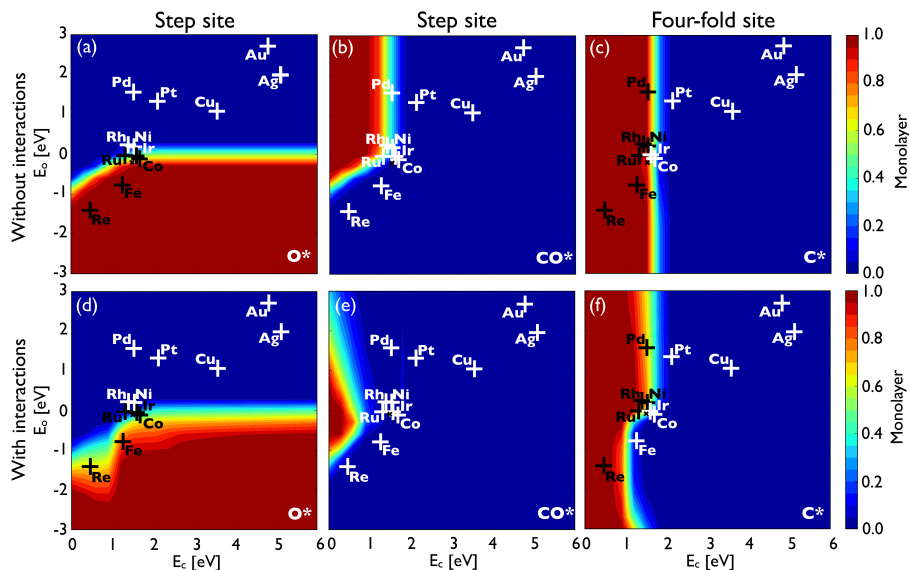


Figure 5.29: Coverages of O^* , CO^* , and C^* as a function of the carbon (E_C) and oxygen (E_O) binding energies as obtained by the solutions of the microkinetic model without (a-c) and with (d-f) adsorbate-adsorbate interactions. Reaction conditions are: $T = 773$ K, $P = 1$ bar, with a gas composition of 40% CH_4 , 40% H_2O , 5% CO and 15% H_2 (corresponding to 29% approach to equilibrium).

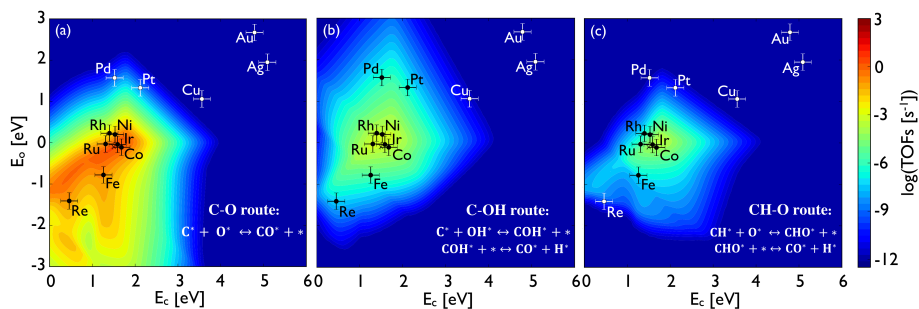


Figure 5.30: Three routes for CO^* formation: (a) direct C-O coupling, (b) COH^* decomposition and (c) CHO^* decomposition. Reaction conditions are: $T = 773$ K, $P = 1$ bar, with a gas composition of 40% CH_4 , 40% H_2O , 5% CO and 15% H_2 (corresponding to 29% approach to equilibrium).

reaction rate for the direct CO^* formation route still remains higher than the CHO^* pathway. However the coverage effect is not that prominent for less reactive metals

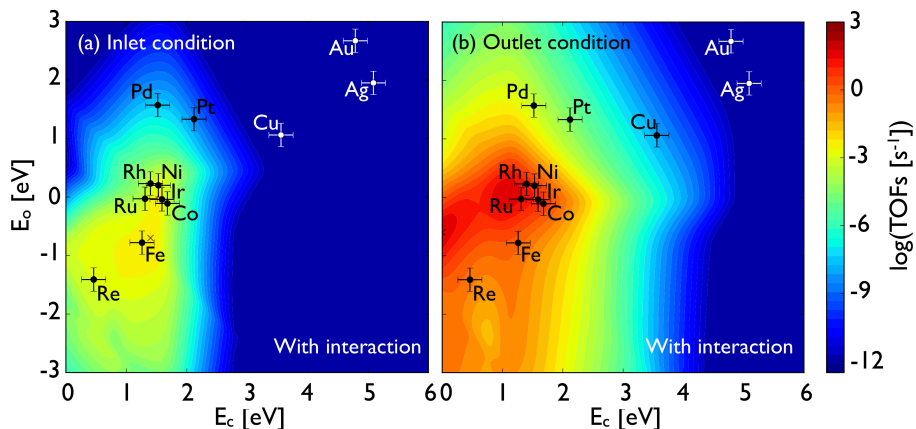


Figure 5.31: Calculated turnover frequencies (TOFs) for CO production (calculated in the microkinetic model with interaction between adsorbates considered) under industrial (a) inlet conditions: $T = 638$ K, $P = 14.3$ bar, with a gas composition of 14.5% CH_4 , 83.1% H_2O , 0.1% CO , 0.4% N_2 , and 1.9% H_2 (corresponding to 0.3% approach to equilibrium); and (b) outlet conditions: $T = 1066$ K, $P = 12.2$ bar, with a gas composition of 2.4% CH_4 , 65.8% H_2O , 6.5% CO , 0.3% N_2 , and 25% H_2 (corresponding to 50% approach to equilibrium); for CH_4 steam reforming as a function of C and O binding energies.

like Pd and Pt and hence for the H-assisted COH^* and CHO^* pathway they show comparable activity to the best metals (Rh, Ru, Ni, Ir, Co). For Pd and Pt the C-OH route is the dominant reaction pathway in accordance to previous experimental work by Chen¹⁴² and Inderwildi¹⁴³.

The reaction rate also depends on the reaction conditions and changes with the gas composition and reaction temperature. In Figure 5.31 (a) and (b), I have shown the catalytic volcano diagram obtained at the inlet and outlet condition (listed in Table 2). The catalytic rate at the outlet condition is much higher than the inlet condition mainly due to higher temperature at the outlet. The shape of the volcano does not change appreciably for these two different conditions and the one I showed in Figure 5.28(b) for the laboratory condition. The top-point moves towards strong binding energy region for the inlet condition, which is expected due to the lower temperature at the inlet.

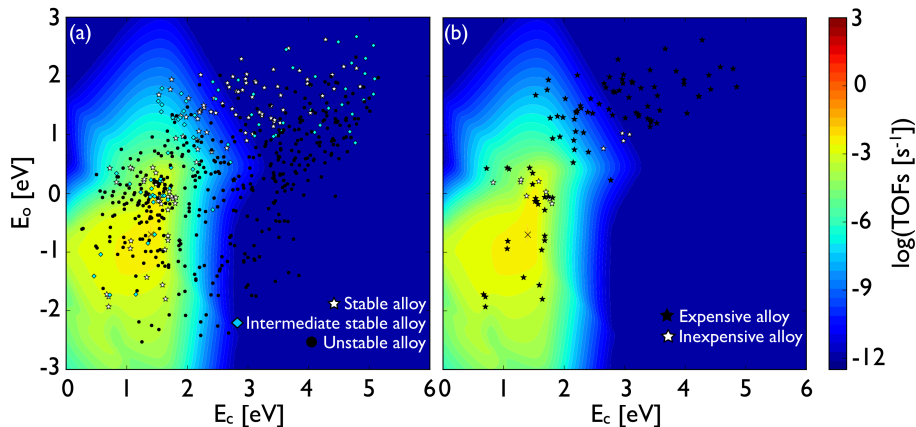


Figure 5.32: Theoretical activity volcanoes for the production of CO under industrial inlet conditions: $T = 638$ K, $P = 14.3$ bar, with a gas composition of 14.5% CH_4 , 83.1% H_2O , 0.1% CO , 0.4% N_2 , and 1.9% H_2 (corresponding to 0.3% approach to equilibrium). (a) Alloys are divided into three categories based on their predicted stabilities with respect to oxidation: 1) alloys with high stability (white stars), 2) alloys with intermediate stability (cyan diamonds), and 3) alloys with low stability (black circles). Alloy labels are omitted for clarity. (b) Alloys are divided into two categories based on the material costs of their component metals [chemicool.com]: 1) expensive alloys (black star, cost $\geq \$5000 \text{ kg}^{-1}$, and 2) inexpensive alloys (white stars $< \$5000 \text{ kg}^{-1}$).

5.4.4 Alloy Screening Results

After obtaining the rate volcano plot at different reaction condition, the alloy screening method is applied on the transition metal alloys to find out the industrially most promising methane steam reforming catalysts. As discussed earlier the alloys with formation energy less than 0.2 eV per unit cell is only considered to be potentially stable. Due to the high $\text{H}_2\text{O}/\text{CH}_4$ ratio in the inlet gas mixture, the alloy catalyst are susceptible to get oxidized hence I only have used the oxidation filter as discussed earlier. As shown in Figure 5.32 (a), I have divided the metal alloys in three categories in terms of their stability towards oxidation:

1. metal alloys that are very stable ($\Delta G_{\text{oxide}}^{\text{alloy}} > 0.05 \text{ eV}$),
2. metal alloys that have intermediate stability ($-0.05 \text{ eV} < \Delta G_{\text{oxide}}^{\text{alloy}} < 0.05 \text{ eV}$), and
3. the metal alloys that are unstable and predicted to get oxidized under the reaction conditions ($\Delta G_{\text{oxide}}^{\text{alloy}} < -0.05 \text{ eV}$).

After getting the potentially stable alloys under reaction conditions I use the price filter to remove the rare and expensive metal containing alloys. The metals alloys with estimated cost less than \$5000 are considered inexpensive and are denoted as white stars, while the expensive ones are denoted as black stars shown in Figure 5.32(b). Then I apply the activity filter as discussed earlier to screen the alloys for the inter and outlet reactor conditions and obtain the industrially promising candidates for methane steam reforming, shown in Figure 5.33, I have denoted the most promising alloy candidates, as yellow stars in Figure 5.33, which are mostly alloys of Ni, Co and Fe in the A_3B composition. The number of the promising alloy candidates for the inlet condition is less than the outlet condition because the metal alloys are more susceptible to oxidation in the more oxidizing inlet environment. For the metal A_3B alloys in the {211} surface structure we have possibility of both ‘AA’ and ‘AB’ type termination (shown in Figure 5.34). Both terminations have been investigated for the alloy screening method in this study. Ni_3Fe and Co_3Ni are the only two candidates, which are suggested to be promising for both ‘AA’ and ‘AB’ type termination. Both Ni-Fe¹⁵² and Ni-Co¹⁵³ alloy catalyst has been previously reported to be active for CH_4 steam reforming where as Ni-Ge and Ni-Ga alloy catalysts have not been investigated yet.

Coking can still be a serious problem for the catalyst. So I have plotted a C^*/CO^* equilibrium line in Figure 5.33 to outline the region of possible coke formation. Any metal or metal alloy below to the C^*/CO^* equilibrium line or even close to the C^*/CO^* equilibrium line will have a high driving force for producing atomic carbon, which is considered as a precursor for formation of graphitic carbon or coke. The C^*/CO^* equilibrium line is determined by at which C^* and O^* binding energy the Gibbs free energy change for the CO decomposition reaction $CO^* + * \leftrightarrow C^* + O^*$ becomes zero.

5.5 Summary

In this chapter I have presented a well parameterized linear adsorbate-adsorbate interaction model. Then in the subsequent section of this chapter I have applied the proposed adsorbate-adsorbate interaction model for three important catalytic reaction direct NO decomposition, CO methanation and steam reforming of methane to investigate the effects of adsorbate-adsorbate interactions on catalytic activity.

To make the interaction model useful for catalytic trend studies one need to reduce the number of independent parameters. I have presented two ways obtaining the cross-interaction parameters, as the arithmetic or geometric mean of the self interaction parameters. Among the two ways I found that the geometric mean method is slightly better than the arithmetic mean method. The rhodium based sub-model is proposed where I used the interaction parameters obtained for rhodium for all the transition metals. This proposed rhodium interaction model can be used as a first guess to study the adsorbate-adsorbate interaction effect for a certain catalytic process before

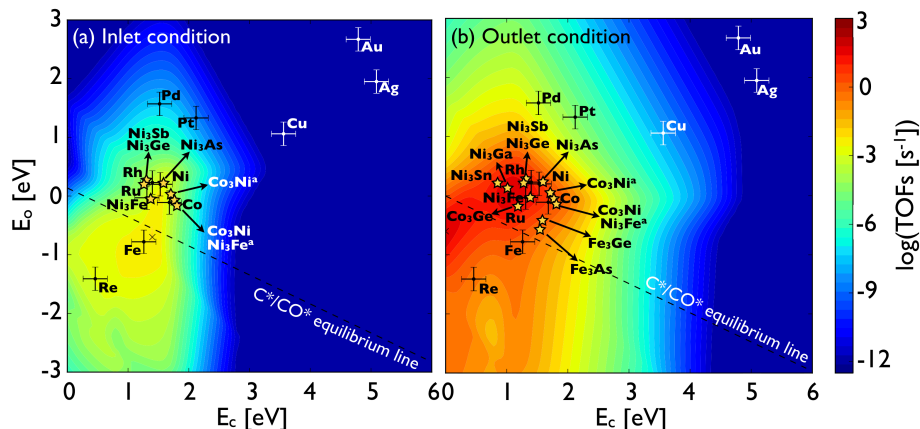


Figure 5.33: Calculated turnover frequencies (TOFs) for CO production under industrial (a) inlet: $T = 638$ K, $P = 14.3$ bar, with a gas composition of 14.5% CH_4 , 83.1% H_2O , 0.1% CO , 0.4% N_2 , and 1.9% H_2 (corresponding to 0.3% approach to equilibrium); and (b) outlet conditions: $T = 1066$ K, $P = 12.2$ bar, with a gas composition of 2.4% CH_4 , 65.8% H_2O , 6.5% CO , 0.3% N_2 and 25% H_2 (corresponding to 50% approach to equilibrium); for CH_4 steam reforming. A superscript "a" denotes AA type surface terminal of A_3B alloy. Carbon equilibrium line is determined by the Gibbs free energy change of reaction $\text{CO}^* + * \leftrightarrow \text{C}^* + \text{O}^*$.

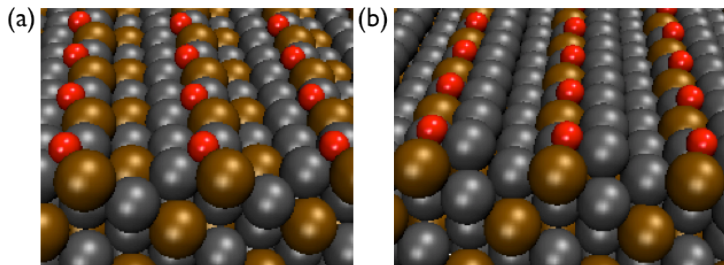


Figure 5.34: Sketch for the surface structure of two terminals for A_3B alloy. Grey balls and golden balls denote elementary A and B, respectively. Red balls represent adsorbate O atoms. (a) Terminal AB; (b) Terminal AA.

moving to a complicated interaction model. A scaling based method is proposed to include the variation in the interaction parameters among the transition metals. One can capture the systematic change in the interaction parameter among the different transition metals by using the correlation between the adsorbate-adsorbate interaction parameters and the adsorption energies of that certain species over the transition metals. The scaling based adsorbate-adsorbate interaction model can be used in a

consistent manner with the microkinetic model to obtain better catalytic trends for any reaction. To correct our linear interaction model at the low coverage region a piecewise interaction model is proposed, where the adsorption energy remains constant until the coverage reaches a threshold coverage and then changes linearly. For the {111} surface the fitted threshold coverage is found to be 0.22 ML. With all these different proposed models, considering their limitations, precision and applicability, two very useful lateral interaction sub-models are proposed for catalytic trend study, the simpler rhodium based interaction model and the more accurate and useful piecewise linear scaling based interaction model.

In our study of the effect of including the adsorbate-adsorbate interaction in the catalytic activity of the direct NO decomposition reaction I found that the rhodium interaction model overestimates the adsorbate-adsorbate interactions for the reactive metals making the lower-left region of the rate-volcano highly reactive all the way down to the most reactive transition metals. However when I used the more accurate scaling based piecewise adsorbate-adsorbate interaction model, a better catalytic activity and trend for the direct NO decomposition is obtained. The inclusion of adsorbate-adsorbate interaction through the piecewise scaling based interaction model do not change the shape of the volcano drastically from the non-interacting mean field model and also the position and catalytic rate of the top of the volcano remains approximately unchanged. However there is a increase in the catalytic rates for the reactive metals when using the scaling based model. Adsorbate-adsorbate interactions widens up the adsorption energy range where the catalytic activity is appreciable and hence gives us more choices in our search for the best catalyst.

In the CO methanation section 5.3, I applied the interaction model to obtain the catalytic rate of CO methanation over the transition metals {211} surfaces. In this section, I used the modified interaction model to get rid of the derivative discontinuity problem at the threshold coverage and make it continuous and differentiable over the whole coverage range. For the {211} surface the threshold coverage is 0.5 ML. Subsequently I used the modified scaling bases piecewise interaction model to obtain the catalytic rates for the CO methanation. For this study also that the inclusion of adsorbate-adsorbate interaction do change the the overall shape of the volcano and the position top of the volcano, but have distinct effect on the rates for the reactive metals. On inclusion of the adsorbate-adsorbate interaction the catalytic active region for CO methanation extends more to the reactive metal surfaces by falling off less steeply with the higher carbon and oxygen binding energies. For more complicated schemes like the Fischer-Tropsch synthesis, the inclusion of adsorbate-adsorbate interactions is likely to play an important role in predicting the of product selectivities, as we have seen the coverage of CH_x species are greatly influenced by adsorbate-adsorbate interactions.

I also used the adsorbate-adsorbate interaction model in the alloy screening study of steam reforming of methane over transition metal alloys. In this section, I gave detailed description of an alloy screening method based on stability, cost and reactivity. This alloy screening method can be used in the search of industrially promising alloy catalyst for any catalytic reaction. For the steam reforming of methane we also observed that the overall shape of the volcano, as well as the position of the maximum rates, remains

essentially unaffected on inclusion of the adsorbate-adsorbate interaction. Therefore, I suggest the presented alloy screening method combined with microkinetic model with in-built adsorbate-adsorbate interaction model could become useful for the design of better catalysts in the future.

CHAPTER 6

Ammonia Oxidation over Transition Metal Surfaces

In recent years the selective oxidation of NH_3 has received a lot of attention in the scientific community. The study of NH_3 oxidation has potential applications in fields like:

1. cleaning of NH_3 from air
2. developing better ammonia slip catalyst (ASC)
3. using NH_3 as clean fuel
4. developing a catalyst for selective oxidation of NH_3 in presence of H_2
5. developing a catalyst for solid oxide fuel cells (SOFC)
6. activation of NH_3 is a very important part in the selective catalytic reduction of NO_x by NH_3 . Understanding the reaction mechanism of NH_3 oxidation will give the required insight.

Emission of NH_3 causes acidification of the environment in indirect ways. NH_3 in the air reacts with the nitric and sulfuric acid (formed by NO_x and SO_x) to form aerosols of ammonium sulphate and ammonium nitrate. These aerosols get deposited on the fields and increase the acidity or stay in the air as particulate matter. The acidification

caused by NH_3 have already caused severe damage to the ecosystem in many countries like the Netherlands.

The main source of NH_3 in air comes from the intensive farming areas due to the livestock manure. The other main source of NH_3 pollution is ammonia “slip” from the diesel engine using the selective catalytic reduction catalyst to reduce NO_x emission. The unreacted ammonia is mostly removed using the ammonia slip catalyst in the secondary step using the ammonia slip catalyst. Many other industrial units like soda production, nitric acid production and coal or biomass gasification units also contribute to NH_3 pollution. Due to environmental hazards, emission of NH_3 is strictly controlled both in European countries and USA. NH_3 can potentially be the fuel for the future due to its characteristics for ideal fuel.

1. It is cost effective compared to the conventional fuels like gasoline and natural gas.
2. NH_3 as fuel is environmental friendly and it do not produce any CO or CO_2 , hence the carbon footprint is zero. The only significant pollutant of NO_x , which emission can be reduced using the SCR technique by reacting it with small amount of NH_3 .
3. NH_3 can be used in the most conventional engines (diesel engines, fuel cells, gas turbines, etc.) as the only fuel or as a co-fuel with the conventional fuels(diesel and natural gas).
4. transportation and storage of NH_3 is relatively safe and we have existing infrastructure.
5. NH_3 is sustainable source of energy as it can be produced from wind, solar and any other renewable fuels.

However both for the NH_3 removal from the air and also for using NH_3 as a ‘green’ fuel we must develop a highly selective and inexpensive NH_3 oxidation catalyst. An industrially attractive ammonia oxidation catalyst must have the following qualities:

1. high oxidation activity
2. low formation of N_2O and NO_x (high N_2 selectivity)
3. high stability in the reaction condition and
4. low cost (low Platinum group metals loading)

Our aim is to develop an ammonia oxidation catalyst with the qualities attributed above using the, “*in-silico*” approach using DFT calculation.

The main reaction for the NH_3 oxidation is,

Table 6.1: NH_3 oxidation activity of the transition metals. Reaction condition: $p_{\text{NH}_3} = 0.1$ atm and $p_{\text{O}_2} = 0.9$ atm. Data taken from¹⁵⁴.

Catalyst	rate ($\text{mol cm}^{-1}\text{s}^{-1}$) (at 300°C)
Pt	1.70×10^{17}
Pd	2.69×10^{16}
Cu	3.31×10^{15}
Ag	2.52×10^{15}
Ni	1.23×10^{15}
Au	8.32×10^{14}
Fe	6.76×10^{14}
W	5.90×10^{14}
Ti	2.24×10^{14}



The other two important side reaction to consider are for the N_2O and NO production:



N. I. Il'chenko in his review article on catalytic ammonia oxidation compared the catalytic activity of transition and transition metal oxides toward the low temperature NH_3 oxidation.¹⁵⁴ He found that the catalytic activity for the metals towards the NH_3 oxidation at 300°C decreases as $\text{Pt} > \text{Pd} > \text{Cu} > \text{Ag} > \text{Ni} > \text{Au} > \text{Fe} > \text{W} > \text{Ti}$ and the selectivity (N_2 selectivity) for the metals decreases as $\text{Pt}, \text{Pd} > \text{Ni} > \text{Fe} > \text{W} > \text{Ti}$. (see Table 6.1)

Holder Topsøe, a Danish catalysis company, has recently developed a highly active and selective NH_3 slip catalyst. The patented catalyst consists of silica supported Cu, Co and Ni oxides doped with small amount of noble metals (100-2000ppm). The activity of the catalyst is claimed to be improved drastically upon sulfating.¹⁵⁵ Yuejin Li in their article¹⁵⁶ studied the selective NH_3 oxidation over ZSM-5 and alumina supported Pd, Rh and Pt catalyst at $200\text{-}350^\circ\text{C}$. They find that the ion-exchanged ZSM-5 catalyst are more active than the alumina supported catalyst with identical metal loading. They also find that the N_2 selectivity is relatively high on Rh and Pd and low on Pt catalysts.

In this chapter I will present the results obtained from the study on NH_3 oxidation on transition metal $\{111\}$ and $\{211\}$ facets. A systematic study on the BEP-scaling relation of the direct NH_3 dissociation and oxygen assisted NH_3 dissociation pathways will also be presented. This is the most probably first study the oxygen assisted BEP-scaling relations for NH_3 dehydrogenation process. I have combined the DFT

calculated data with the microkinetic model to obtain the reaction rates for the different reaction pathways and to propose a consistent reaction mechanism for the NH_3 oxidation reaction. A good knowledge of reaction mechanism is always important for catalyst development. I'll also show the catalytic trends for the NH_3 oxidation reaction and propose the best transition metals catalyst for this reaction.

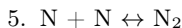
In the second part of this chapter I will show the results from the study on the selective oxidation of NH_3 in presence of H_2 . NH_3 is decomposed to produce N_2 and H_2 , and then the produced H_2 is used in the fuel cells. However, due to incomplete NH_3 decomposition, a very small amount of NH_3 is always present in the gas mixture. For many fuel cells this NH_3 works as catalyst poison and damages the fuel cells. Hence it is always preferable to remove the last amount of NH_3 from the gas mixture before using it in the fuel cells. For the selective oxidation of NH_3 in presence of H_2 , the ammonia oxidation catalyst must have high $\text{N}_2/\text{H}_2\text{O}$ selectivity, on top of the qualities stated above. This is probably the first catalytic reactivity and selectivity trend study for selective oxidation of NH_3 in presence of H_2 , using DFT calculations.

6.1 Microkinetic model

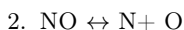
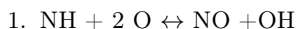
The microkinetic model is developed using the adsorption and transition state energies from the CatApp, a web based database for adsorption and transition state energies.^{121,122} I also use the correlation between the adsorption energy and transition states with the binding energy of nitrogen and oxygen to obtain the adsorption energy scaling parameters for the intermediates and BEP scaling parameters for the activation barriers.

The reaction mechanism of ammonia oxidation over transition metal catalyst is still not well established. A lot of work has been done on Pt to find the correct ammonia oxidation mechanism. Many reaction pathway was proposed with key intermediates like HNO , NH_2NO , NH , N_2H_2 etc. Only recently Meier and Ho¹⁵⁷ did through mechanistic study on the NH_3 oxidation on the $\text{Pt}\{111\}$ surface with TPD, TPRS, EELS and LEED. Using EELS they found some key intermediates OH , NH and NH_2 . They were unable to confirm the presence or absence of NO due to ambiguous frequency data. They propose that the reaction proceeds via the O assisted H stripping of NH_3 and then combination of two N atom to form $\text{N}_2(\text{g})$. The NO is formed by combination of adsorbed N and O.

1. $\text{NH}_3 + \text{O} \leftrightarrow \text{NH}_2 + \text{OH}$
2. $\text{NH}_2 + \text{O} \leftrightarrow \text{NH} + \text{OH}$
3. $\text{NH} + \text{O} \leftrightarrow \text{N} + \text{OH}$
4. $\text{N} + \text{O} \leftrightarrow \text{NO}$



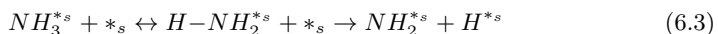
Bradley and King¹⁵⁸ in their studies also propose similar O assisted dehydrogenation mechanism. However they propose that the NO is formed from NH in a single step and the N₂ is formed from the dissociation of NO.

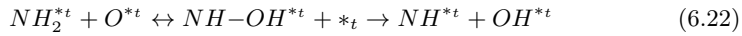
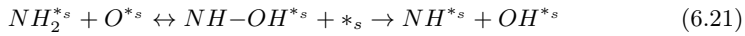
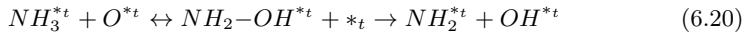
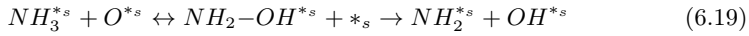
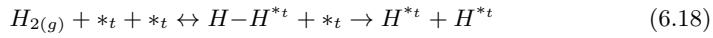
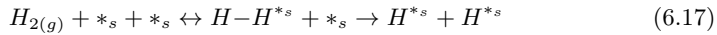
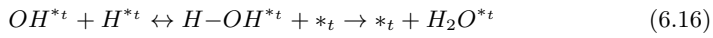
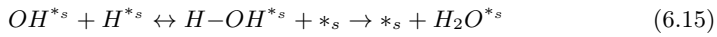
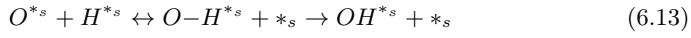
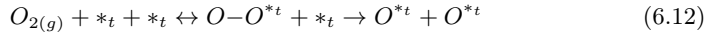
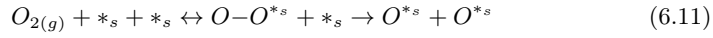
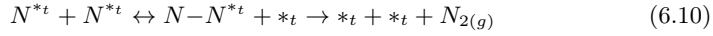
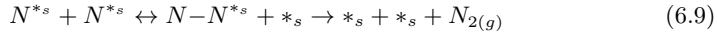
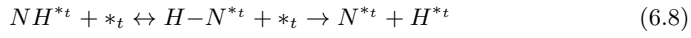
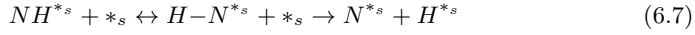
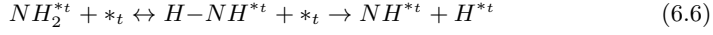
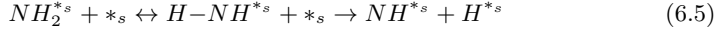
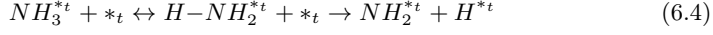


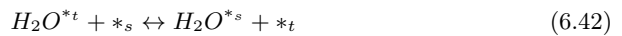
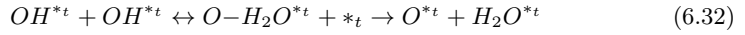
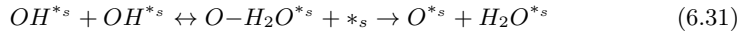
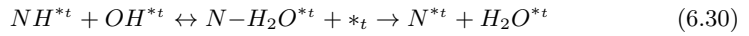
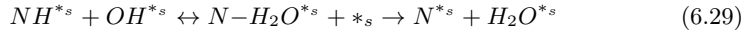
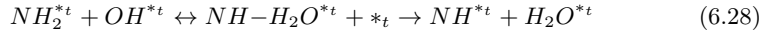
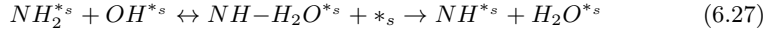
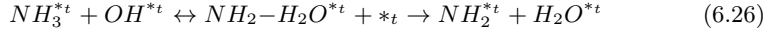
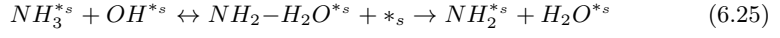
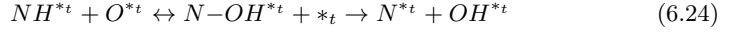
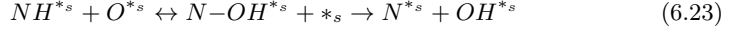
Van der Broek and van Santen¹⁵⁹ in their recent work also showed NH and OH as the main surface species during the NH₃ oxidation over Pt sponge catalyst under atmospheric pressure. M.W. Robert and his group used XPS, EELS and STM technique to analysis the NH₃ oxidation reaction on the copper surface.^{160–162} They found that at low temperature (<300 K) the NH₃ is oxidized to NH₂ and NH species via the O assisted dehydrogenation steps, same as proposed by Meier and Ho¹⁵⁷. At higher temperature the imide (NH) is further oxidized to atomic N.

For this catalytic NH₃ oxidation study I have used a ‘dual facet’ model as our catalysis surface. The ‘dual facet’ model surface is a combination of {111} terrace and {211} stepped surface. The adsorbates can adsorb on both the {111} and {211} and they are allowed to diffuse from one surface to another. The barrier of diffusion is assumed to be ~0.5eV for all the adsorbates. The total coverage of both the {111} and {211} surface can go to maximum 1 ML. The adsorbate sites on the {211} and {111} surface are denoted as ‘*s’ and ‘*t’ respectively. For the {211} surface the adsorption of the adsorbates are performed at the bridge, on-top, three-fold hollow site and four-fold hollow sites, and only the lowest energy adsorption site for each adsorbate is used in this study. For the {111} surface the adsorbates can adsorb as bridge, on-top, three-fold hollow sites. For the {111} surface also the lowest energy adsorption site is used for each adsorbates. I also consider the H-reservoir site which has the same binding energy of the {111} terrace surface, as discussed in the earlier chapter 5. More details about the microkinetic model used here can be found in webpage¹⁶³.

The reaction mechanism proposed by Meier and Ho¹⁵⁷ is widely accepted as the NH₃ oxidation reaction mechanism. I have constructed the reaction mechanism for the NH₃ oxidation based on the mechanism proposed by Meier and Ho with the following elementary reaction steps:







Three different NH_3 oxidation mechanisms are studied here,

1. direct NH_3 dehydrogenation pathway,
2. O^*/OH^* assisted NH_3 dehydrogenation pathway with H-reservoir sites and
3. O^*/OH^* assisted NH_3 dehydrogenation pathway without H-reservoir sites

In the microkinetic model reaction mechanism above, I have given the reaction steps for the O^*/OH^* assisted NH_3 dehydrogenation pathway without H-reservoir sites microkinetic model.

One can decompose the NH_3 oxidation mechanism in the following parts:

(a) NH_3 adsorption	elementary step (6.1), (6.2)
(b) direct NH_3 dehydrogenation	elementary step (6.3) – (6.8)
(c) N_2 desorption	elementary step (6.9), (6.10)
(d) dissociative O_2 chemisorption	elementary step (6.11), (6.12)
(e) H_2O formation	elementary step (6.13) – (6.16), (6.33), (6.34)
(f) dissociative H_2 chemisorption	elementary step (6.17), (6.18)
(g) O assisted NH_3 dehydrogenation	elementary step (6.19) – (6.24)
(h) OH assisted NH_3 dehydrogenation	elementary step (6.25) – (6.30)
(i) OH assisted H_2O formation	elementary step (6.31), (6.32)
(j) diffusion reactions	elementary step (6.35) – (6.42)

Direct NH_3 dehydrogenation pathway only consist of (a), (b), (c), (d), (e), (f) and (j) reaction steps. It does not contain the O^*/OH^* assisted NH_3 dehydrogenation steps (g) and (h) reaction steps. In the O^*/OH^* assisted NH_3 dehydrogenation pathway with H-reservoir site microkinetic model, the H^{*s} and H^{*t} (the step and terrace H's) are replaced by H^{*h} (H-reservoir H's). In the direct NH_3 dehydrogenation pathway we also use the H-reservoir model. Both the direct NH_3 dehydrogenation and O^*/OH^* assisted NH_3 dehydrogenation pathway with H-reservoir sites are given in the appendix A.5.

I have used the binding energy of nitrogen (ΔE_N) and oxygen (ΔE_O) as our two independent descriptors. The adsorption energy of the other reaction intermediates and the transition states are obtained using the scaling relations. (The values of the scaling parameters are given in the appendix A.5) The construction of the thermodynamics and kinetics of the microkinetic model has been described in the previous chapter in details. The formation energies of the gas phase molecules $\text{NH}_3(\text{g})$, $\text{O}_2(\text{g})$, $\text{N}_2(\text{g})$, $\text{H}_2\text{O}(\text{g})$ and $\text{H}_2(\text{g})$ were obtained from NIST website.⁸⁷ I have run the microkinetic model at the laboratory experiment condition for NH_3 oxidation in the absence of H_2 and also in the presence of H_2 . The gas composition for the NH_3 oxidation in absence of H_2 is: $P = 1$ bar, with a gas composition of 1980 ppm NH_3 , 1985 ppm O_2 , 10 ppm N_2 , 30 ppm H_2O , 0.1 ppm H_2 (corresponding to 1% conversion from initial gas composition of: 2000 ppm NH_3 , 2000 ppm O_2). The gas composition for the NH_3 oxidation in presence of H_2 is: $P = 1$ bar, with a gas composition of 1000 ppm NH_3 , 500 ppm O_2 , 25 % N_2 , 15 ppm H_2O , 74.5 % H_2 .

6.2 DFT Setups

The DFT-calculated adsorption energies of surface intermediates and transition states for on the stepped $\{211\}$ surfaces and flat $\{111\}$ surfaces of Au, Ag, Co, Cu, Ni, Pd, Pt, Rh, Ru and Re were accessed via CatApp^{121,122,164}. Transition state energies for the O* and OH* assisted NH₃ dehydrogenation steps are calculated using Nudged Elastic Band (NEB) method. O* assisted NH₃ dehydrogenation processes on the $\{111\}$ surface is carried out on Pd, Pt, Rh and Ru transition metals. Whereas O* assisted NH₃ dehydrogenation processes on the $\{211\}$ surface is carried out on Ag, Cu, Pd, Pt, Rh, Ru and Re transition metals. For the OH* assisted NH₃ dehydrogenation processes on both the $\{111\}$ and $\{211\}$ surfaces, the NEB calculation were performed on Pd, Pt, Rh and Ru transition metals. For the stepped $\{211\}$ surfaces and flat $\{111\}$ surfaces I have used (1×3) and (3×3) unit cells respectively. I used a nine-layered slabs for the $\{211\}$ surfaces (which correspond to three layers in the $\{111\}$ direction), where all adsorbates and the top three layers were allowed to relax, while the remaining layers were kept fixed in their bulk-truncated positions. For the $\{111\}$ surfaces four-layered slabs were used where all adsorbates and the top two layers were allowed to relax, while the remaining bottom two layers were kept fixed in their bulk-truncated positions. Self-consistent, periodic density functional theory (DFT) calculations for the surface intermediates and transition states were performed using the Dacapo plane wave code⁴⁰, which represents the ionic cores using Vanderbilt ultrasoft pseudopotentials.⁴³ Calculations were performed using the RPBE exchange-correlation functional³⁸, which uses a generalized gradient approximation, with a kinetic energy cutoff of 340.15 eV and a density cutoff of 680 eV. Self-consistent electron densities were determined by iterative diagonalization of the Kohn-Sham Hamiltonian, where the occupation of the Kohn-Sham states were smeared according to a Fermi-Dirac distribution with a smearing factor of $k_B T = 0.1$ eV.¹⁶⁵ Energies were extrapolated to $k_B T = 0$ eV. Brillouin zones were sampled using Monkhorst-Pack k-point meshes of 4×4×1 is used for the $\{111\}$ and $\{211\}$ surfaces. Successive slabs were separated with a vacuum of 15 Å.⁸⁶

Zero-point energies, entropies and internal energies of adsorbed intermediates were included due to the relatively high reaction temperatures. These values were calculated using the harmonic oscillator approximation from their vibrational frequencies on the Cu $\{211\}$ and Cu $\{111\}$ surface and were assumed to be constant on all the metals.

6.3 DFT Results

A diagram explaining the different energy expressions used for the transition state scaling relations of the hydrogenation/dehydrogenation process of NH₃ is shown in Figure 6.1. In Figure 6.1(A), I have shown the scheme for the transition state scaling is based on the correlation between E_{TS} and E_{diss} . E_{TS} is the transition state energy and E_{diss} is the final state energy of the dissociated products. All energies are with respect to the gas phase molecule of NH₃, H₂O and H₂. Whereas in Figure 6.1(B) the reference point for the transition state has been changed to the O*/OH* pre-adsorbed

Table 6.2: The fitted parameters for the reaction energy and transition state scaling with respect to the gas-phase energies of NO, O₂ and N₂.

Surface	Slope(α)	Consant (β) (eV)	RMSE (eV)
$\text{NH}_3^* + * \rightarrow \text{NH}_2^* + \text{H}^*$			
Closed Packed	0.69	0.94	0.21
Step	0.69	1.45	0.13
All	0.60	1.20	0.22
$\text{NH}_2^* + * \rightarrow \text{NH}^* + \text{H}^*$			
Closed Packed	0.81	1.25	0.14
Step	0.78	1.43	0.16
All	0.78	1.34	0.17
$\text{NH}^* + * \rightarrow \text{N}^* + \text{H}^*$			
Closed Packed	0.88	1.11	0.15
Step	0.91	1.41	0.20
All	0.88	1.30	0.22
Direct pathway			
All	0.81	1.35	0.23
$\text{NH}_3^* + \text{O}^* \rightarrow \text{NH}_2^* + \text{OH}^*$			
Closed Packed	0.77	0.53	0.09
Step	0.95	0.94	0.23
All	0.81	0.76	0.27
$\text{NH}_2^* + \text{O}^* \rightarrow \text{NH}^* + \text{OH}^*$			
Closed Packed	0.96	1.04	0.04
Step	0.95	1.40	0.16
All	0.93	1.30	0.23
$\text{NH}^* + \text{O}^* \rightarrow \text{N}^* + \text{OH}^*$			
Closed Packed	1.10	0.80	0.08
Step	1.02	1.16	0.25
All	1.02	1.07	0.23
O assisted pathway			
All	0.99	1.03	0.31
$\text{NH}_3^* + \text{OH}^* \rightarrow \text{NH}_2^* + \text{H}_2\text{O}^*$			
Closed Packed	x	x	x
Step	1.02	0.47	0.11
All	1.02	0.47	0.11
$\text{NH}_2^* + \text{OH}^* \rightarrow \text{NH}^* + \text{H}_2\text{O}^*$			
Closed Packed	1.05	0.80	0.09
Step	0.86	0.63	0.04
All	0.95	0.72	0.14
$\text{NH}^* + \text{OH}^* \rightarrow \text{N}^* + \text{H}_2\text{O}^*$			
Closed Packed	1.08	0.82	0.07
Step	1.08	0.79	0.11
All	1.07	0.80	0.08
OH assisted pathway			
All	1.13	0.66	0.14
O and OH assisted pathway			
All	1.04	0.88	0.27

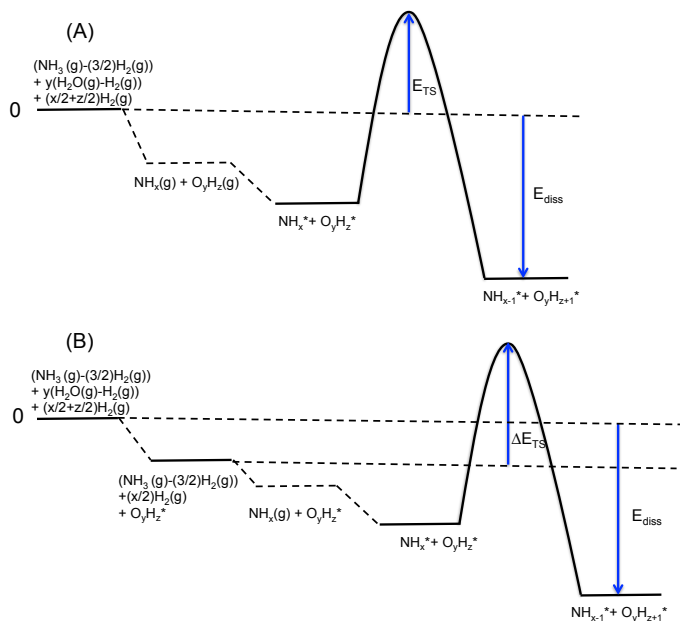


Figure 6.1: The definition of energies used in the chapter for the hydrogenation/dehydrogenation process. All energies are with respect to the gas phase molecule of NH_3 , H_2O and H_2 . In Figure 6.1(A) (Top) the transition state scaling is based on the correlation between E_{TS} and E_{diss} denoted by the two blue arrows. E_{TS} is the transition state energy and E_{diss} is the final state energy of the dissociated products. In Figure 6.1(B) (Bottom) the reference point for the transition state has been changed to the O^*/OH^* preadsorbed surface. This transition state scaling is the correlation between the ΔE_{TS} (transition state energy, reference O^*/OH^* preadsorbed surface and gas phase molecule of NH_3 , H_2O and H_2) and E_{diss} (final state energy of the dissociated products, reference clean surface and gas phase molecule of NH_3 , H_2O and H_2).

surface. This transition state scaling is the correlation between the ΔE_{TS} (transition state energy, reference O^*/OH^* pre-adsorbed surface and gas phase molecule of NH_3 , H_2O and H_2) and E_{diss} (final state energy of the dissociated products, reference clean surface and gas phase molecule of NH_3 , H_2O and H_2).

A brief discussion on the Brønsted-Evans-Polanyi (BEP) and universal BEP have been given in chapter 3. In Figure 6.2, I have shown the universal transition state scaling relation both for the O^*/OH^* assisted NH_3 dehydrogenation and direct NH_3 dehy-

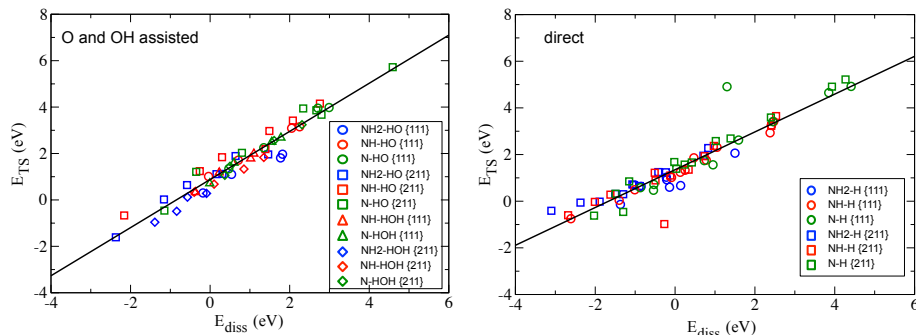


Figure 6.2: The transition state energy vs the final state energy of the O and OH assisted NH_3 dehydrogenation steps (left) and direct NH_3 dehydrogenation steps are plotted. The reference is $\text{NH}_3(\text{g})$, $\text{H}_2\text{O}(\text{g})$ and $\text{H}_2(\text{g})$. Blue, red and green colors are attributed to the first, second and third dehydrogenation steps respectively. The $\text{NH}_3^* + \text{OH}^* \rightarrow \text{NH}_2^* + \text{H}_2\text{O}^*$ reaction on $\{111\}$ facet does not have a proper transition state as the final state dissociates back to the initial state without any barrier. The data for the direct NH_3 dehydrogenation are taken from ref.⁷¹

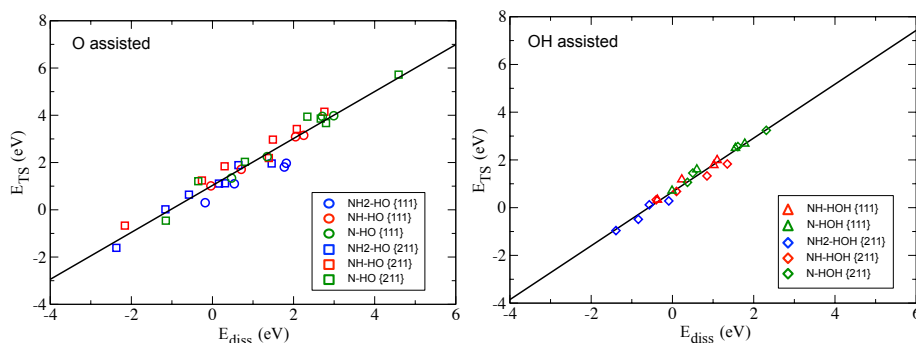


Figure 6.3: The transition state energy vs the final state energy of the O (left) and OH (right) assisted NH_3 dehydrogenation steps are plotted separately. The reference is $\text{NH}_3(\text{g})$, $\text{H}_2\text{O}(\text{g})$ and $\text{H}_2(\text{g})$. Blue, red and green colors are attributed to the first, second and third dehydrogenation steps respectively. The $\text{NH}_3^* + \text{OH}^* \rightarrow \text{NH}_2^* + \text{H}_2\text{O}^*$ reaction on $\{111\}$ facet does not have a proper transition state as the final state dissociates back to the initial state without any barrier.

drogenation steps. I have plotted the transition state energy data for both $\{111\}$ and $\{211\}$ surfaces. The data for the direct NH_3 dehydrogenation are taken from ref.⁷¹. The $\text{NH}_3^* + \text{OH}^* \rightarrow \text{NH}_2^* + \text{H}_2\text{O}^*$ reaction on $\{111\}$ facet does not have a proper transition state as the final state dissociates back to the initial state without any barrier. The two outliers in the direct NH_3 dehydrogenation universally plot in Figure 6.2

(right) are NH-H^{TS} on $\text{Ni}\{211\}$ and N-H^{TS} on $\text{Pt}\{111\}$ surface. These two points have not been included in the transition state scaling. Figure 6.3 shows the universal transition state scaling relation for the O^* and OH^* assisted NH_3 dehydrogenation pathways separately.

The fitted data for all the NH_3 dehydrogenation reactions are given in Table 6.2. The fitted data for the transition state scaling for the individual, grouped and overall reaction pathways for the NH_3 dehydrogenation are given. The individual fit is based on a particular reaction on a certain surface. Then the scaling and fitting parameters for a particular reaction on both $\{111\}$ and $\{211\}$ surface grouped together, are presented. I have also given the overall fit for the direct pathways, O assisted pathways and OH assisted pathways and O & OH assisted pathways for the NH_3 dehydrogenation. The mean absolute error (MAE) of the fitted individual reaction, grouped reaction and overall reaction pathways also have been presented in the Table 6.2. The MAE for the overall reaction pathways are less than 0.3 eV (0.31 eV for O assisted pathways). The MAE for the individual reactions and for grouped ones ($\{111\} + \{211\}$) are always less than 0.3 eV. Any transition energy scaling with MAE less than 0.3 eV is considered small enough to be extensively used for obtaining the first estimate of the activation barrier for any catalytic reaction in this “*in-silico*” approach using DFT.⁷¹ The universality of the transition state scaling is due to the geometrical similarity of the transition states and final states for the hydrogenation/dehydrogenation reactions.^{70–72,166} The MAE for the individual reactions on a certain surface are smaller as their geometry on the different metals for the transition states and final states are also very similar.

In Figure 6.4, I have presented the scaling between the transition state energy (relative to the O and OH pre-adsorbed surface and gas phase molecules NH_3 , H_2O and H_2 , ΔE_{TS}) and the final state energy (E_{diss}), as described in the PES diagram in Figure 6.1(B). The transition state energy scaling used in Figure 6.4 gives us the information if the presence of O actually activates the NH_3 dehydrogenation as reported earlier^{157,158}, or not. We can see from Figure 6.4 that the O^* assisted transition state scaling lines cross the direct NH_3 decomposition scaling lines for most of the dehydrogenation reactions at around 0.0 eV final state energy for both $\{111\}$ and $\{211\}$ surface (~ -2.0 eV for $\text{NH}_2\text{-HO}^{TS}$ on the $\{211\}$ surface). The OH^* assisted transition state scaling lines cross the direct NH_3 decomposition lines at much lower final state energy on the $\{111\}$ surface (~ -2.5 eV for NH-HOH^{TS} and ~ -1.5 eV for N-HOH^{TS}). However, on the $\{211\}$ facet both the O^* and OH^* assisted NH_3 dehydrogenation transition state scaling lines crosses at approximately the same final state energy. That means on the $\{111\}$ surface the OH^* can activate the NH_3 dehydrogenation even at a much lower final state energy than the O^* . Whereas on the $\{211\}$ surface their effect is same. But after the point where the O^*/OH^* assisted NH_3 dehydrogenation transition scaling lines crosses the direct NH_3 dissociation transition scaling lines, there is no O^*/OH^* activation as there the barrier for the O^*/OH^* assisted NH_3 dehydrogenation steps are higher than the direct NH_3 dehydrogenation steps. So for very reactive metals with high N and O binding energies we will not see any activation by adsorbed O or OH. So the O^*/OH^* pathway is important for the less or moderately reactive transition metals.

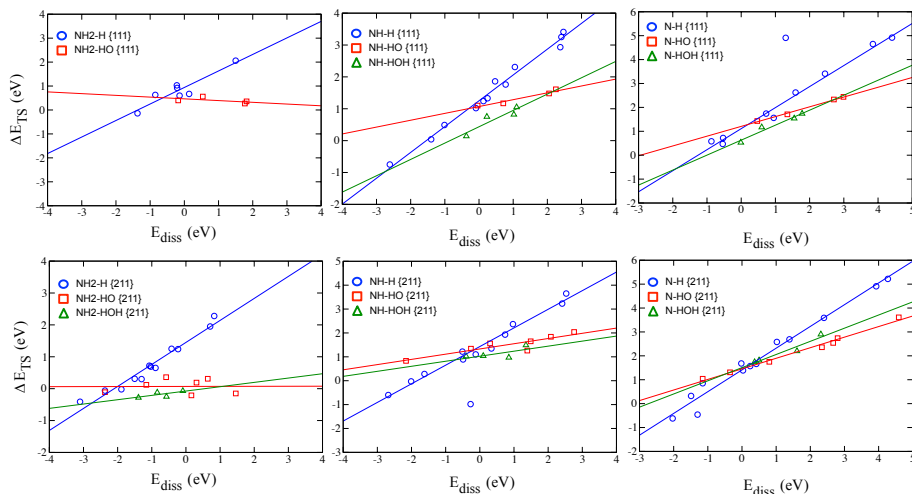


Figure 6.4: The transition state energy (relative to the O and OH preadsorbed surface and gas phase molecules NH_3 , H_2O and H_2 , ΔE_{TS}) vs the final state energy (E_{diss}), shown in Figure 6.1(B) is plotted. of the O and OH assisted NH_3 dehydrogenation steps (left) and direct NH_3 dehydrogenation steps are plotted. The reference is NH_3 (g), H_2O (g) and H_2 (g). Blue, red and green colors are attributed to the direct NH_3 dehydrogenation, O assisted NH_3 dehydrogenation and OH assisted NH_3 dehydrogenation steps respectively. The NH_3 dehydrogenation process on {111} surface are in the (top) and {211} surface are at the (bottom) of Figure 6.4. The $\text{NH}_3^* + \text{OH}^* \rightarrow \text{NH}_2^* + \text{H}_2\text{O}^*$ reaction on {111} facet does not have a proper transition state as the final state dissociates back to the initial state without any barrier. The data for the direct NH_3 dehydrogenation are taken from ref.⁷¹

6.4 Catalytic Activity

After obtaining the O^*/OH^* assisted NH_3 dehydrogenation transition state scaling parameters, I use these parameters combined with the adsorption and transition state energies obtained from CatApp and previous DFT studies to construct the microkinetic model for the NH_3 oxidation over the transition metal surfaces, as discussed before in the section 6.1. The catalytic activity and selectivity results for the NH_3 oxidation at different conditions using different microkinetic models are presented here.

6.4.1 NH_3 Oxidation in Absence of H_2

First, I will discuss the results obtained from the study done for NH_3 oxidation in the absence of H_2 . In Figure 6.5 I have plotted the catalytic rate for the NH_3 oxidation

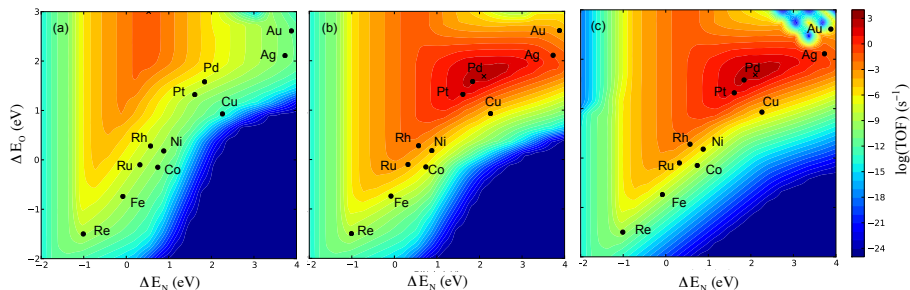


Figure 6.5: Catalytic rate of NH_3 oxidation (N_2 formation rate) on a $(\{111\} + \{211\})$ dual facet model surface is plotted versus the two descriptors $E_{\text{diss}}(\text{N}_2)$ and $E_{\text{diss}}(\text{O}_2)$. (a) NH_3 oxidation using the direct NH_3 dehydrogenation pathway, (b) NH_3 oxidation using the O^*/OH^* assisted NH_3 dehydrogenation pathway and with the H-reservoir model, (c) NH_3 oxidation using the O^*/OH^* assisted NH_3 dehydrogenation pathway and without the H-reservoir model. The reaction condition is: $T = 400^\circ\text{C}$, $P = 1$ bar, with a gas composition of 1980 ppm NH_3 , 1985 ppm O_2 , 10 ppm N_2 , 30 ppm H_2O , 0.1 ppm H_2 (corresponding to 1% conversion from initial gas composition of: 2000 ppm NH_3 , 2000 ppm O_2)

(N_2 formation rate) on a $(\{111\} + \{211\})$ dual facet model surface versus the two descriptors ΔE_N and ΔE_O at reaction condition: $T = 400^\circ\text{C}$, $P = 1$ bar, with a gas composition of 1980 ppm NH_3 , 1985 ppm O_2 , 10 ppm N_2 , 30 ppm H_2O , 0.1 ppm H_2 (corresponding to 1% conversion from initial gas composition of: 2000 ppm NH_3 , 2000 ppm O_2). I have studied three different microkinetic models mentioned in the section 6.1 to study the NH_3 oxidation reaction and determine the possible reaction mechanism. In Figure 6.5(a), (b) and (c), I have plotted the catalytic rate using the three different NH_3 oxidation models: direct NH_3 dehydrogenation pathway, O^*/OH^* assisted NH_3 dehydrogenation pathway with H-reservoir sites and O^*/OH^* assisted NH_3 dehydrogenation pathway without H-reservoir sites.

The maximum catalytic rate for the NH_3 oxidation through the direct NH_3 dehydrogenation pathway is three orders of magnitude smaller than the O^*/OH^* assisted pathway. This is both due to the fact that the activation barriers are lower for the O/OH assisted NH_3 dehydrogenation steps and most importantly, in the O^*/OH^* mechanism the NH_3 dehydrogenation can take place from the adsorbed NH_3^* even without the presence of the free site in a surface totally covered by adsorbed oxygen (which is the case for most of the transition metals in these conditions). Also the top of the volcano for the direct NH_3 oxidation mechanism is at the wrong nitrogen and oxygen binding energy (ΔE_N and ΔE_O), as in NH_3 oxidation experiments over the transition metals it is well known that Pt and Pd are the two best catalyst in this reaction. The O^*/OH^* assisted NH_3 oxidation mechanism got the top of the volcano at the correct position (close to Pd). From these findings one can propose that the O^*/OH^* assisted NH_3 dehydrogenation pathway is the main reaction pathway for the NH_3 oxidation catalytic reaction over the transition metal catalyst, which is consistent

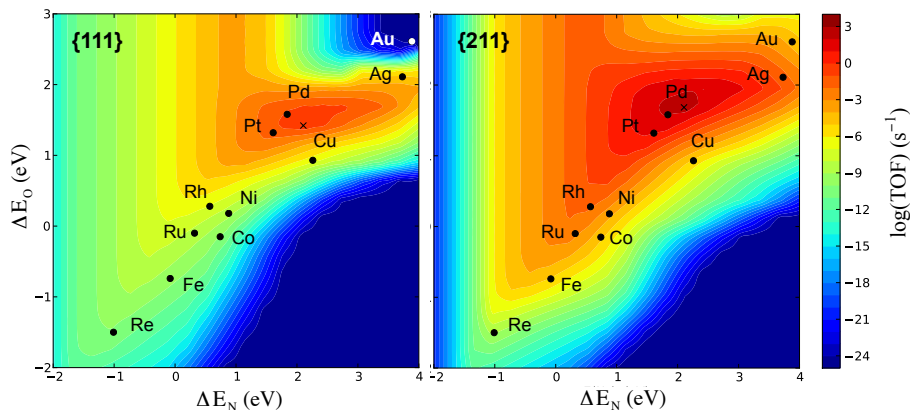


Figure 6.6: Catalytic rate of NH_3 oxidation (N_2 formation rate) is plotted versus the two descriptors $E_{\text{diss}}(\text{N}_2)$ and $E_{\text{diss}}(\text{O}_2)$ using the O^*/OH^* assisted NH_3 dehydrogenation pathway and with the H-reservoir model for the {111} (left) and {211} (right) facets. Reaction condition: $T = 400^\circ\text{C}$, $P = 1$ bar, with a gas composition of 1980 ppm NH_3 , 1985 ppm O_2 , 10 ppm N_2 , 30 ppm H_2O , 0.1 ppm H_2 (corresponding to 1% conversion from initial gas composition of: 2000 ppm NH_3 , 2000 ppm O_2)

with the previously proposed mechanism by Meier and Ho¹⁵⁷.

From Figure 6.5(b) and (c), we can see that the inclusion of the H-reservoir sites in the microkinetic model Figure 6.5(b) has no drastic effect on either the shape of the rate volcano, or the catalytic activity trends of the transition metals. Due the very low pressure of H_2 gas in the reaction gas composition, the presence of H-reservoir site or the absence of it does not drastically change the coverage of H^* and other intermediates and hence similar activity is observed. The catalytic trend obtained using the O^*/OH^* assisted NH_3 dehydrogenation pathway with H-reservoir site microkinetic model is:

$$\text{Pd} > \text{Pt} > \text{Ag} > \text{Rh} > \text{Ru} \sim \text{Au} > \text{Ni} > \text{Cu} > \text{Co} > \text{Fe} > \text{Re}$$

Whereas the catalytic trend obtained using the O^*/OH^* assisted NH_3 dehydrogenation pathway without H-reservoir site microkinetic model is:

$$\text{Pd} > \text{Pt} > \text{Ag} > \text{Rh} > \text{Ru} \sim \text{Cu} > \text{Ni} > \text{Co} > \text{Fe} > \text{Re} \text{ (have convergence problem in the region of Au)}$$

These catalytic trends are similar to the findings by Il'chenko¹⁵⁴.

In Figure 6.6, I have shown the rate for the NH_3 oxidation on the {111} and {211} surface separately, using the O^*/OH^* assisted NH_3 dehydrogenation pathway with H-reservoir microkinetic model. It can also be seen from Figure 6.6 that the {211} is

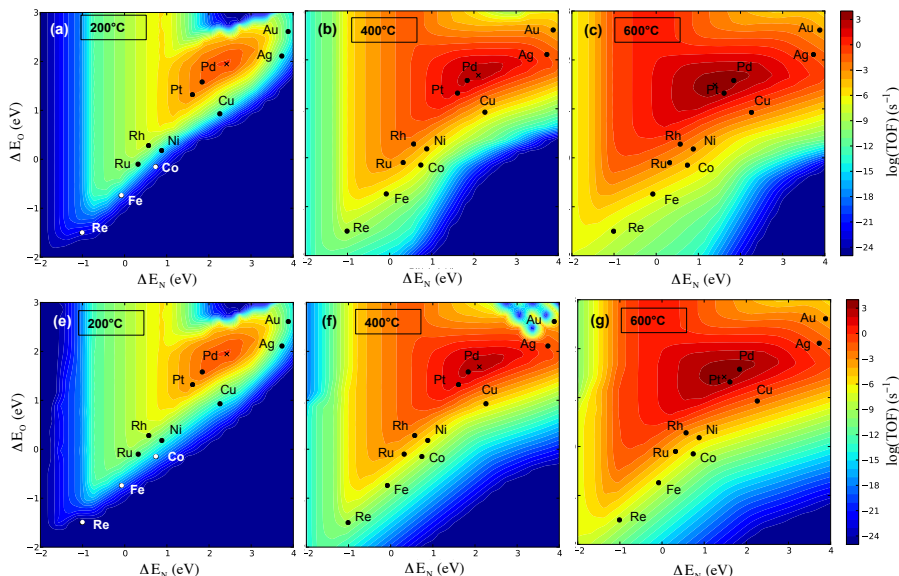


Figure 6.7: Catalytic rate of NH_3 oxidation (N_2 formation rate) on a ($\{111\} + \{211\}$) dual facet model surface is plotted versus the two descriptors $E_{\text{diss}}(\text{N}_2)$ and $E_{\text{diss}}(\text{O}_2)$ at different temperatures, (Top) using the O^*/OH^* assisted NH_3 dehydrogenation pathway and with the H-reservoir model, (a) 200 °C, (b) 400 °C, (c) 600 °C and (Bottom) using the O^*/OH^* assisted NH_3 dehydrogenation pathway and without the H-reservoir model, (e) 200 °C, (f) 400 °C, (g) 600 °C. Reaction condition: $P = 1$ bar, with a gas composition of 1980 ppm NH_3 , 1985 ppm O_2 , 10 ppm N_2 , 30 ppm H_2O , 0.1 ppm H_2 (corresponding to 1% conversion from initial gas composition of: 2000 ppm NH_3 , 2000 ppm O_2)

the main reactive surface for the NH_3 oxidation processes. The maximum activity for the stepped $\{211\}$ surface is $\sim 10^2$ times higher than the flat $\{111\}$ surface. The top of the volcano for both the $\{111\}$ and $\{211\}$ surface are approximately at the same nitrogen and oxygen binding energy (ΔE_N and ΔE_O).

The catalytic rate of the NH_3 oxidation using the O^*/OH^* assisted NH_3 dehydrogenation pathway with and without H-reservoir microkinetic models at different reaction temperatures are shown in Figure 6.7. For both the with (Top) and without (Bottom) H-reservoir model the catalytic reaction rate increases significantly with temperature. However the top of the volcano and the catalytic trends of the transition metals remain nearly unchanged in the whole temperature range of 200–600 °C. The catalytic activity plots for the O^*/OH^* assisted NH_3 dehydrogenation pathway with H-reservoir model at 200 °C, 400 °C and 600 °C are given in Figure 6.7(a), (b) and (c) respectively. The catalytic reactivity using this model at different temperature are:

at 200 °C: Pd > Pt > Rh > Ru > Ag ~ Au > Cu ~ Ni > Co ~ Fe > Re

at 400 °C: Pd > Pt > Ag > Ru ~ Au > Ni > Cu > Co > Fe > Re

at 600 °C: Pd > Pt > Rh ~ Ag > Cu > Ru ~ Au ~ Ni > Co > Fe > Re

The catalytic activity plots for the O*/OH* assisted NH₃ dehydrogenation pathway without H-reservoir model at 200 °C, 400 °C and 600 °C are given in Figure 6.7(d), (e) and (f) respectively. The catalytic reactivity using this model at different temperature are:

at 200 °C: Pd > Pt > Rh > Ru > Ni > Ag ~ Au > Cu > Co > Fe > Re

at 400 °C: Pd > Pt > Ag > Rh > Ru ~ Cu > Ni > Co > Fe > Re (have convergence problem in the region of Au)

at 600 °C: Pd > Pt > Ag > Cu > Rh > Au > Ru > Ni > Co ~ Fe > Re

So for all these these temperature range Pd and Pt have the the highest NH₃ oxidation rate, followed by Ag. Rh, Cu, Ru and Ni shows moderate activity. Co, Fe and Re shows very little activity.

6.4.2 NH₃ Oxidation in Presence of H₂

In this part of the ammonia oxidation chapter I will discuss the possible mechanism, catalytic activity and selectivity of the NH₃ oxidation in the presence of H₂ exclusively. Though a lot of work has been done on the ammonia oxidation in general, the selective NH₃ oxidation in presence of H₂ has not been addressed much. This is probably the first attempt to study the selective NH₃ oxidation in presence of H₂ over the transition metals using DFT.

In Figure 6.8, I have plotted the catalytic rate of the N₂ formation and H₂O formation during the NH₃ oxidation reaction on a ({111} + {211}) dual facet model surface plotted versus the two descriptors ΔE_N and ΔE_O at reaction condition: T = 750 °C, P = 1 bar, with a gas composition of 1000 ppm NH₃, 500 ppm O₂, 25 % N₂, 15 ppm H₂O, 74.5 % H₂, using the three different microkinetic models discussed before. In Figure 6.8(a) and (b), I have plotted the catalytic rate of the N₂ formation and H₂O formation during the NH₃ oxidation reaction using the direct NH₃ dehydrogenation pathway. In Figure 6.8(c) and (d), the catalytic rate of the N₂ formation and H₂O formation during the NH₃ oxidation reaction using the O*/OH* assisted NH₃ dehydrogenation pathway with H-reservoir sites have been plotted. Whereas in Figure 6.8(e) and (f), I have plotted the catalytic rate of the N₂ formation and H₂O formation during the NH₃ oxidation reaction using the O*/OH* assisted NH₃ dehydrogenation pathway without H-reservoir sites. The N₂ selectivity plotted versus the two descriptors ΔE_N and ΔE_O corresponding to each of the pathways are also shown in the right

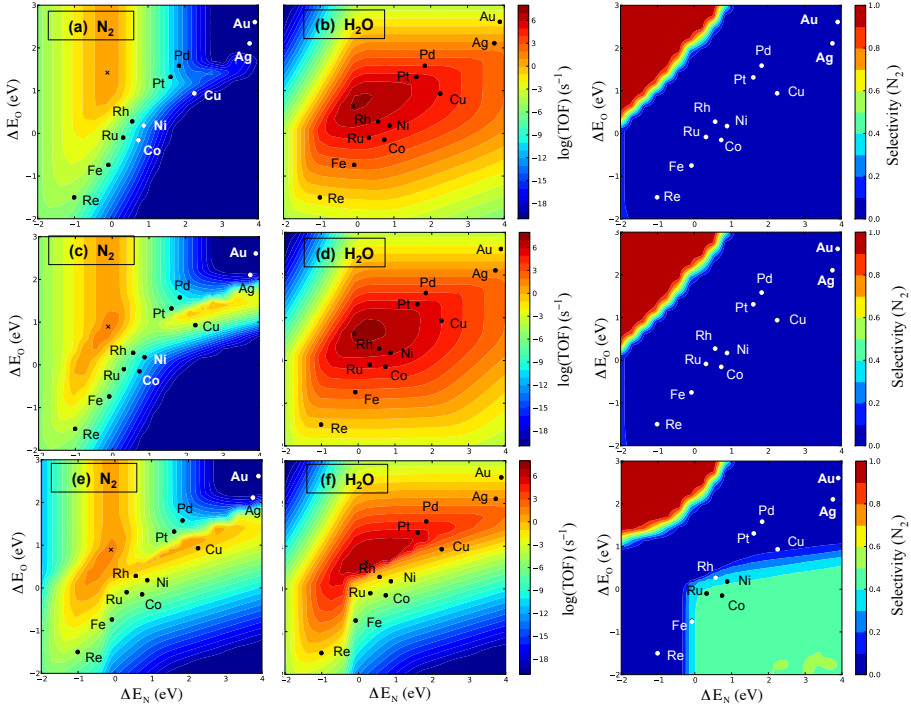


Figure 6.8: Catalytic rate of N_2 formation rate and H_2O formation rate during the NH_3 oxidation on a $(\{111\} + \{211\})$ dual facet model surface is plotted versus the two descriptors $E_{diss}(N_2)$ and $E_{diss}(O_2)$ using different reaction pathways: (Top) using direct NH_3 dehydrogenation pathway, (Middle) NH_3 oxidation using the O^*/OH^* assisted NH_3 dehydrogenation pathway and with the H-reservoir model, (Bottom) NH_3 oxidation using the O^*/OH^* assisted NH_3 dehydrogenation pathway and without the H-reservoir model. The N_2 selectivity corresponding to each of the pathways are plotted in the right hand column. The reaction condition is: $T = 750^\circ C$, $P = 1$ bar, with a gas composition of 1000 ppm NH_3 , 500 ppm O_2 , 25 % N_2 , 15 ppm H_2O , 74.5 % H_2

hand column corresponding the each of the three pathway rows. The N_2 selectivity is defined as:

$$\text{Selectivity}(N_2) = \frac{3 * R(N_2)}{R(H_2O) + 3 * R(N_2)}, \quad (6.43)$$

where $R(N_2)$ = rate of formation of $N_2(g)$ and $R(H_2O)$ = rate of formation of $H_2O(g)$.

On the reactivity plots for the N_2 formation and H_2O formation rates using the O^*/OH^* assisted NH_3 dehydrogenation pathway both with and without H-reservoir model, the top of the volcano for both N_2 formation and H_2O formation are situated at

approximately at the same place. The top of the volcano for H_2O formation using the direct NH_3 dehydrogenation pathway also situated at the same place as the O^*/OH^* assisted NH_3 dehydrogenation pathway, but the top of the N_2 formation volcano has been shifted to lower O binding energy, keeping the N binding energy approximately same as the O^*/OH^* assisted NH_3 dehydrogenation pathway.

The volcano for the H_2O formation for both the direct NH_3 dehydrogenation (it also uses the H-reservoir site model) and O^*/OH^* assisted NH_3 dehydrogenation pathway with the H-reservoir site model in Figure 6.8(b) and (d) has the same shape. Whereas the volcano for the N_2 formation using these two microkinetic model given in Figure 6.8(a) and (c) are different. The rate of N_2 formation using the O^*/OH^* assisted NH_3 dehydrogenation pathway is higher than the direct NH_3 dehydrogenation, with all the extra N_2 formation for the O^*/OH^* assisted ammonia oxidation coming from the O^*/OH^* assisted NH_3 dehydrogenation steps. However for these two pathways the rate for H_2O formation is higher for almost all N and O binding energies, all transition metals studied here produce much more H_2O than N_2 . Hence none of the metals are selective for N_2 formation according to these two reaction mechanisms. According to these two reaction mechanisms all the transition metals selectively oxidize the H_2 to H_2O .

However, when I use the O^*/OH^* assisted NH_3 dehydrogenation pathway without the H-reservoir model everything changes. In Figure 6.8(e) and (f), I have plotted the catalytic rate of the N_2 formation and H_2O formation respectively using this microkinetic model. The volcano for the N_2 formation in Figure 6.8(e) using this microkinetic model is same as the one obtained in Figure 6.8(c) using the O^*/OH^* assisted NH_3 dehydrogenation pathway with the H-reservoir site model. This means the N_2 formation rate do not depend on the presence of H-reservoir sites under these reaction condition. However we can see a big difference in the H_2O formation between these two model. The presence of H-reservoir facilitates the H_2O formation reaction without influencing the N_2 formation rates. One of the possible reasons for this higher H_2O formation reaction rates in the H-reservoir model is that the presence of H-reservoir model makes it certain that there is always free site for H and hence the coverage for H under these reaction condition is always close to 1 ML for almost all metals (except Ag and Au). And as under these condition coverage for O^* is also ~ 1 ML for most of the transition metals (except Ag and Au), the rate for H_2O formation is very high. H^* coverage in the H-reservoir model is not limited by O^* coverage, and hence both the coverages are close to 1 ML. However when we remove the H-reservoir sites in the “ O^*/OH^* assisted NH_3 dehydrogenation pathway without the H-reservoir site model”, we see the H_2O formation rate drops drastically for all the metals which are covered by O^* . Now the H^* has to compete with O^* for the coverage in the stepped and terrace site and hence the coverage of H^* obtained from this microkinetic model is very low on the transition metals as most of the sites are already blocked by O adsorption. Though the H_2O formation rate still dominates the N_2 formation rate even in the “ O^*/OH^* assisted NH_3 dehydrogenation pathway without the H-reservoir site model”, I found that in some region in the two volcanos Figure 6.8(e) and (f), where the N_2 and H_2O formation rates are comparable, as in those N and O binding energies, the main portion of the H_2O formation comes from the NH_3 oxidation not the

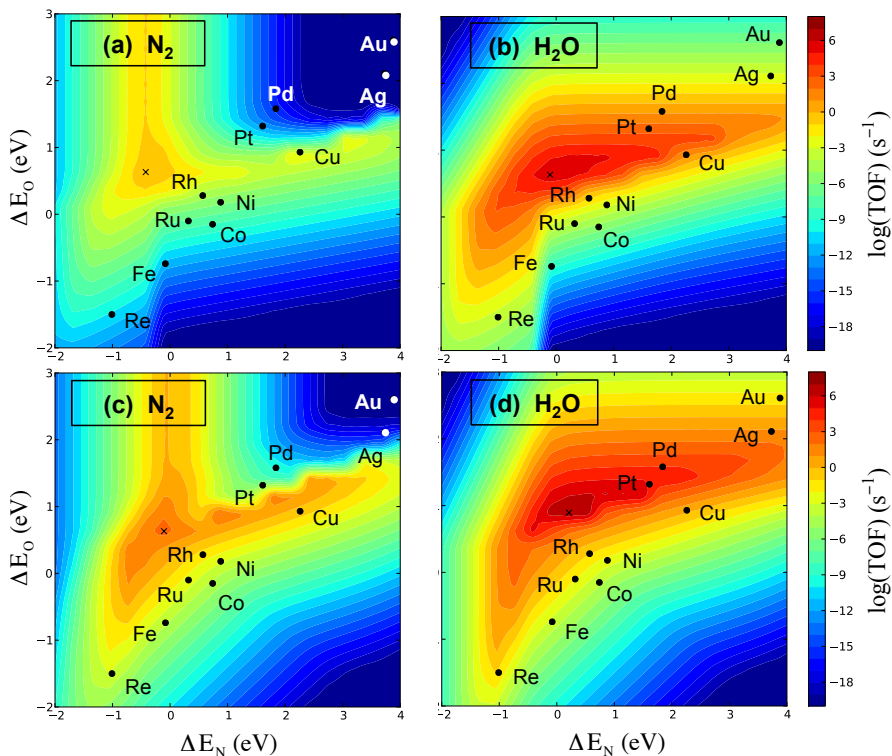


Figure 6.9: Catalytic rate of N₂ formation rate and H₂O formation rate during the NH₃ oxidation plotted versus the two descriptors E_{diss} (N₂) and E_{diss} (O₂) using the O*/OH* assisted NH₃ dehydrogenation pathway and without the H-reservoir model for the {111} facet (a) and (b) (Top) and {211} facets (c) and (d) (Bottom). The reaction condition is: T = 750 °C, P = 1 bar, with a gas composition of 1000 ppm NH₃, 500 ppm O₂, 25 % N₂, 15 ppm H₂O, 74.5 % H₂

H₂ oxidation. This can also be seen on the N₂ selectivity plots corresponding to this microkinetic modeling in Figure 6.10. In Figure 6.9, I have plotted the catalytic rate for the N₂ formation and H₂O formation during the NH₃ oxidation in presence of H₂ on the {111} and {211} surface separately. The {211} surface is more reactive for both the N₂ formation and H₂O formation reaction than the {111} surface. The top of the volcano for N₂ formation on both the {111} and {211} surface are approximately at the same nitrogen and oxygen binding energy (ΔE_N and ΔE_O), whereas the top of the H₂O formation volcano on the {211} surface is shifted towards lower O binding energy than the {111} surface, while keeping the N binding energy same. From the Figure 6.9 one can also say that the {211} surface is more selective towards NH₃ oxidation in presence of H₂ than the {111} surface.

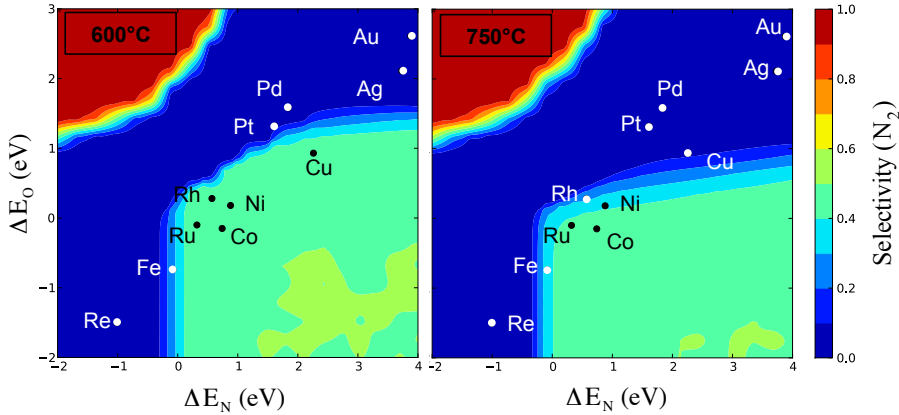


Figure 6.10: The N_2 selectivity of the NH_3 oxidation reaction on a $(\{111\} + \{211\})$ dual facet model surface plotted versus the two descriptors $E_{\text{diss}}(\text{N}_2)$ and $E_{\text{diss}}(\text{O}_2)$ using the O^*/OH^* assisted NH_3 dehydrogenation pathway and without the H-reservoir model for two different temperatures, 600°C (left) and 750°C (right). The reaction condition is: $P = 1$ bar, with a gas composition of 1000 ppm NH_3 , 500 ppm O_2 , 25 % N_2 , 15 ppm H_2O , 74.5 % H_2

In Figure 6.10, the N_2 selectivity using O^*/OH^* assisted NH_3 dehydrogenation pathway without H-reservoir microkinetic model have been plotted versus the two descriptors ΔE_{N} and ΔE_{O} at two different temperatures 600°C and 750°C . From the two plots in Figure 6.10 we can say that the N_2 selectivity for all the transition metals except Fe, decreases with temperature. At 600°C Co, Ni, Cu, Rh and Ru all show good selectivity towards N_2 formation. Whereas at 750°C only Co and Ru show good N_2 selectivity. The N_2 selectivity of the NH_3 oxidation over Fe increases with temperature, which is an anomaly from the other transition metals. The highest N_2 selectivity for the NH_3 oxidation in presence of H_2 is ~ 0.5 - 0.6 eV. Most of the transition metals Au, Ag, Pt, Pd, Cu and Re are still highly selective for H_2O formation.

6.5 Summary

I have presented the individual and universal transition state scaling relations for the O^*/OH^* assisted NH_3 dehydrogenation steps on both $\{111\}$ and $\{211\}$ facets of the transition metals. Three different microkinetic models for NH_3 oxidation on the ‘dual facet’ model have been studied. It is found that the O^*/OH^* assisted NH_3 dehydrogenation is the main NH_3 oxidation reaction pathway in the reaction conditions studied here. The H-reservoir model does not affect the catalytic activity drastically for the NH_3 oxidation in absence of H_2 . Pd and Pt are the best catalyst for the NH_3

oxidation in absence of H_2 in the temperature range 200 – 600 °C and gas composition of 1980 ppm NH_3 , 1985 ppm O_2 , 10 ppm N_2 , 30 ppm H_2O , 0.1 ppm H_2 (corresponding to 1% conversion from initial gas composition of: 2000 ppm NH_3 , 2000 ppm O_2). I also found that the {211} surface is the main reactive surface for the NH_3 oxidation process in this condition. However for the NH_3 oxidation in presence of H_2 (reaction condition: $T = 750$ °C, $P = 1$ bar, with a gas composition of 1000 ppm NH_3 , 500 ppm O_2 , 25 % N_2 , 15 ppm H_2O , 74.5 % H_2), the H-reservoir model has huge effect on the H_2O formation rate and this makes all the transition metals unselective towards NH_3 oxidation. However, the “ O^*/OH^* assisted NH_3 dehydrogenation without H-reservoir” model gives us the ‘correct’ reactivity volcano for both the N_2 formation and H_2O formation and predicts Co, Ru to show good N_2 selectivity in the NH_3 oxidation in presence of H_2 .

This work on NH_3 oxidation is still an ongoing project with close theoretical and experimental collaboration. For future work, I have plan to include the adsorbate-adsorbate interaction in the microkinetic modeling to obtain better accuracy for the catalytic rates under the real reaction condition. I also have plan to calculate the transition state scaling relations at high O^* coverage and use those scaling parameters instead of the low-coverage transition state scaling parameters used in this study. The results for the NO_x formation (NO , N_2O and NO_2) during the NH_3 oxidation will also be addressed in our future work.

CHAPTER 7

H₂ assisted Selective Catalytic Reduction of NO_x using NH₃

Catalytic removal of NO_x under the lean-burn condition from the exhaust gasses of motor vehicles and thermal plants is one of the most challenging targets in this decade. In chapter 4 it has been shown that none of the transition metal catalyst are active enough for the direct NO decomposition. One of the most promising NO_x removal technology under the lean-burn condition is the selective catalytic reduction of NO_x (NO_x-SCR) using reducing agents. Different reducing agents such as diesel soot, hydrocarbons, DME, H₂ and NH₃ have been tried. Among this different SCR techniques the H₂ assisted NO_x-SCR by NH₃ over Ag/Al₂O₃ catalyst has been shown to be very promising with nearly 90% conversion even at a very lower temperature 200 °C. In this chapter I will present a mechanistic study of the H₂ assisted NO_x-SCR by NH₃ over Ag/Al₂O₃. It will help us to establish the well documented ‘Fast-SCR’ mechanism for this reaction. The importance of each constituent in gas feed in the NO_x-SCR activity are tested and discussed. DFT calculations are performed to evaluate the proposed mechanism.

Sulfur poisoning of the Ag/Al₂O₃ catalyst during the NO_x-SCR catalysis cycle is well known and is regarded as one of the main obstacle for the catalyst being used commercially worldwide. In the second section of this chapter, the results obtained on sulfur poisoning and regeneration of Ag/Al₂O₃ catalyst studies will be presented.

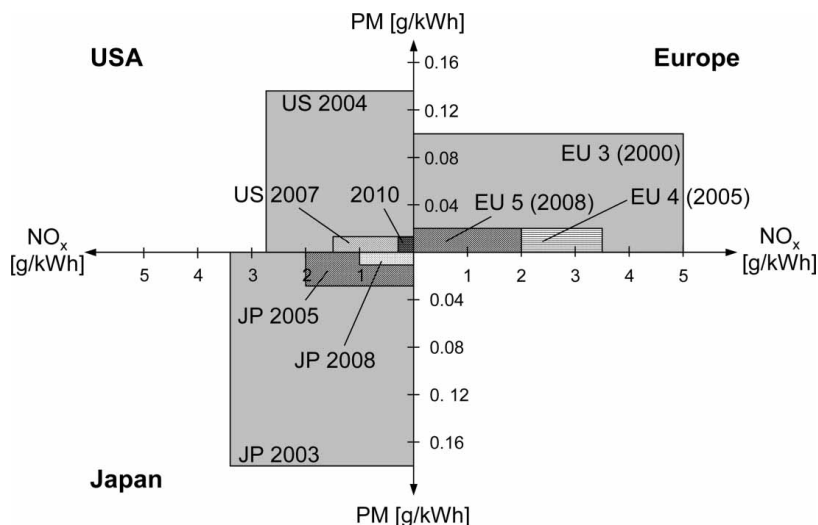


Figure 7.1: The emissions regulations for heavy-duty diesel vehicles. Adapted from ref. 79

A possible sulfur poisoning and regeneration mechanism will be also proposed in this section.

7.1 Mechanistic Study of the H₂-assisted NO_x-SCR by NH₃

Due to high fuel efficiency, the diesel and lean-burn gasoline engines have seen unprecedented growth in the previous decade. These engines burn the fuel in surplus air, hence the emission of the pollutants like CO, hydrocarbons and CO₂ is significantly reduced.^{78–80} However for these engines the conventional three-way catalysts⁷⁹ are not effective for NO_x reduction.⁷⁹ NO_x are highly potent environmental pollutants. Due to environmental and health hazards, strong emission regulations of NO_x are already in effect and are becoming more and more stringent over the years, as shown in Figure 7.1.^{78–80} Removal of NO_x in the lean-burn condition is still one of the major challenges in environmental catalysis. Selective catalytic reduction of NO_x using NH₃ as reductant has been proposed as one of the most promising NO_x removal technology under the lean-burn condition. Commonly used catalyst for NO_x-SCR by NH₃ are vanadia-based catalysts and Cu or Fe containing zeolites. However none of these catalysts show good thermal stability and high NO_x conversion in the whole temperature range of 150 - 550 °C.^{78,79,167} Alumina supported metal catalysts like

Ag, In and Sn, have been shown to be active for NO_x-SCR by hydrocarbons under the lean-burn condition.⁷⁸ However the poor low-temperature activity of all these catalysts is a major drawback. Co-feeding H₂ during the NO_x-SCR reaction increases the low-temperature activity significantly.^{79,168–170} H₂ assisted NO_x-SCR by NH₃ over Ag/Al₂O₃ shows high NO_x conversion activity at low temperatures (nearly 90% conversion at 200 °C.)^{171–173}

In this section, I will present the results from our studies on the Ag metal catalyst over different supports (γ -Al₂O₃, TiO₂ and ZrO₂), and Al₂O₃ supported Sn and In metal catalysts for the H₂ assisted NO_x-SCR by NH₃. Catalytic tests are also performed with pure γ -Al₂O₃ for NO_x-SCR under the same reaction condition. A mechanistic study for the H₂ assisted NO_x-SCR by NH₃ over Ag/Al₂O₃ and pure Al₂O₃ is executed to get the valuable insight into the 'Fast-SCR' type mechanism operating during the reaction. The significance of both the metal catalyst and support have been discussed. The influence of the individual gas component the reaction gas feed is tested and discussed.

These valuable informations about the H₂ assisted NO_x-SCR by NH₃ mechanism over Ag/Al₂O₃ will help us in the development of a stable, active, non-expensive and non-toxic NO_x-SCR catalyst in future.

7.1.1 Experimental Setups

Catalyst Preparation

1% Ag/Al₂O₃, 3% Sn/Al₂O₃ and 3% In/Al₂O₃ were prepared by the wetness impregnation of γ -Al₂O₃ by AgNO₃, SnCl₄.5H₂O and InCl₃.4H₂O solutions in de-ionised water. 1% Ag/TiO₂ and 1% Ag/ZrO₂ are also prepared using the same wetness impregnation of TiO₂ and ZrO₂ by AgNO₃ aqueous solution. The impregnated catalysts are dried at room temperature overnight and then calcined at 550 °C for 4 hour in static air. Next the calcined catalysts are crushed and shived to obtain the desired particle size distribution of 0.18-0.35 mm (mesh size: 80- 45).

Catalytic study

Catalysis test reactions were performed in a fixed bed quartz reactor (inner diameter - 4 mm). The temperature is decreased from 400 °C to 150 °C at a rate of 2 °C/min. 45 mg of catalyst was diluted with 100 mg of SiC(mesh size 60). The GHSV (Reactant Gas Flow Rate/Reactor Volume) used in this study was ~11000 h⁻¹. The gas composition normally used is: 500 ppm NO, 520 ppm NH₃, 8.3% O₂ and 7% H₂O and rest Ar gas. Some tests are also carried out 500 ppm NO, 520 ppm NH₃, 1200 ppm H₂, 8.3% O₂ and 7% O₂ and rest Ar, to study the effect of H₂ in the NO_x-SCR by NH₃ reaction. To study the previously proposed 'fast-SCR' mechanism we also carried out test reactions using NO and NO₂ mixture (26 - 47% NO₂) in the gas feed. The reaction products are analyzed using a Thermo Fisher Nicolet 6700 FT-IR analyzer. The conversions

corresponding to this study were calculated using the following equations,

$$X_{NO_x} = 1 - \frac{C_{NO_x}^{outlet}}{C_{NO_x}^{inlet}} \quad (7.1)$$

where X_{NO_x} is the conversion of NO_x, $C_{NO_x}^{inlet}$ and $C_{NO_x}^{outlet}$ are the NO_x concentration at the inlet and outlet of the reactor. C_{NO_x} is the total composition of NO and NO₂, $C_{NO_x} = C_{NO} + C_{NO_2}$

Similarly the NH₃ conversion is given by,

$$X_{NH_3} = 1 - \frac{C_{NH_3}^{outlet}}{C_{NH_3}^{inlet}} \quad (7.2)$$

where $C_{NH_3}^{inlet}$ and $C_{NH_3}^{outlet}$ are the NH₃ concentration at the inlet and outlet of the reactor.

Fraction of NH₃ converted to NO_x is given by,

$$X_{NH_3 \rightarrow NO_x} = \frac{C_{NO_x}^{outlet}}{C_{NH_3}^{inlet}} \quad (7.3)$$

And the fraction of NO converted to NO₂ is given by,

$$X_{NO \rightarrow NO_2} = \frac{C_{NO_2}^{outlet}}{C_{NO}^{inlet}} \quad (7.4)$$

The ratio of converted NO to converted NO₂ during the SCR experiments with NO+NO₂ mixtures are given by,

$$\frac{C_{NO}^{conv.}}{C_{NO_2}^{conv.}} = \frac{C_{NO}^{inlet} - C_{NO}^{outlet}}{C_{NO_2}^{inlet} - C_{NO_2}^{outlet}} \quad (7.5)$$

7.1.2 DFT Setups

The plane wave DFT code, DACAPO, was used to calculate adsorption and gas phase energies.⁴⁰ Kohn-Sham one-electron valence states were expanded in a plane-wave basis. A plane wave cutoff of 340.15 eV and a density wave cutoff of 680 eV were used for the calculation. The core electrons described by the Vanderbilt ultrasoft pseudopotential.⁸⁵ RPBE was used to describe the exchange-correlation energy.⁹⁸ Fermi population of the Kohn-Sham states was calculated at $k_B T = 0.1$ eV. All energies are extrapolated to $k_B T = 0$ eV. The convergence limit was set to a maximum change in the force constant of 0.03 eV.

The adsorption energies of the H₂ assisted NO_x-SCR by NH₃ reaction intermediates were studied over the transition metals {111} and {211} surfaces, and over a γ -Al₂O₃

model stepped surface. I used a 3×3 surface cell for the {111} and 3×1 surface cell for the {211} surfaces. A 4×4×1 Monkhorst-Pack k-point sampling in the irreducible Brillouin zone is used for both {111} and {211} surfaces. For the gas phase species 1×1×1 Monkhorst-Pack k-point sampling is used. For the {111} surface I used a four-layer slab where the two top-most layers were allowed to relax, whereas for the {211} surfaces I used a slab model with nine layers and the topmost three layers are allowed to relax. In all the clean surface, adsorbates and gas phase calculations, neighboring slabs or gas phase species were separated by more than 10 Å of vacuum. The transition states for the NO_x formation over the transition metals {111} and {211} surfaces are calculated using NEB method. For the calculation of transition states I have used the same DFT setup and same surface slabs as for the adsorption energy calculations.

A 4×4×1 Monkhorst-Pack k-point sampling in the irreducible Brillouin zone was used for γ-Al₂O₃. The γ-Al₂O₃ surface was modeled by a step on a nonspinel γ-Al₂O₃ structure which was derived from bulk γ-Al₂O₃ model adapted from ref.¹⁷⁴. The cell parameters for the γ-Al₂O₃ model step surface are a = 8.0680 Å, b = 10.0092 Å and α = β = γ = 90°. For the γ-Al₂O₃ surface the bottom two layers were fixed whereas the top-most three layers were allowed to relax. In all the model γ-Al₂O₃ surfaces, the neighboring slabs are separated by more than 10 Å of vacuum.

7.1.3 Microkinetic Model

Oxidation of NO to NO₂ has been proposed as one of the important reaction step for the low-temperature NO_x-SCR activity of the transition metal and metal oxide and metal zeolites catalysts.^{173,175–180} The “Fast-SCR” is the main pathway at the low temperature (150–300 °C), as the “Standard SCR” pathway only starts at higher temperatures.^{175,179} NO₂ believed to take part in the “Fast-SCR” by combining up with NH₃ to form NH₄NO₂, which can dissociate to N₂ and H₂O even at very low temperatures.^{173,175,179} It has been previously proposed that in the H₂ assisted NO_x-SCR by NH₃ Ag component is responsible for the oxidation of NO to NO₂ and NO₃.^{181,182} Removing or changing Ag from the catalyst makes the catalyst completely inactive for the low-temperature H₂ assisted NO_x-SCR by NH₃ as shown in Table 7.1. It has been previously shown that the Ag metals in the Ag/Al₂O₃ catalyst are mainly present in small Ag_n metal clusters.^{182–185} NO_x adsorption energy and structures have been shown to be dependent on both Ag cluster size and number of Al₂O₃ layers. Binding energy of NO₂ increases with the increasing number of Al₂O₃ layers, whereas the NO_x adsorption energy fluctuates with the size of the Ag_n cluster. In general even number Ag_n clusters are more stable and hence bind NO₂ more weakly than the odd number Ag_n clusters.^{184,186,187}

Though the Ag metal in the Ag/Al₂O₃ catalyst are highly dispersed Ag_n clusters, study of NO oxidation over flat {111} and stepped {211} surfaces can still give us valuable insights about the reasons behind the unique activity of Ag/Al₂O₃ catalyst for the low-temperature H₂ assisted NO_x-SCR by NH₃ reaction. It has been shown by Anders et. al. that the formation of NO₂ and NO₃ is favorable on both Ag{111}

and Ag{211} metal surfaces.¹⁸¹ They also showed that contrary to the experimental results, the NO₂ does not decompose spontaneously on Ag{111} surface. They also suggested that over the Ag metal surfaces NO₂ instead of O₂, works as the O carrier during the NO_x-SCR reactions.¹⁸¹

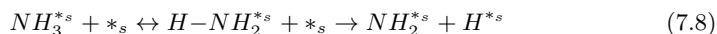
Though the NO_x can be formed through number of different reactions^{173,181}, for the microkinetic modeling study I only consider the following three reaction steps for the NO_x formation:

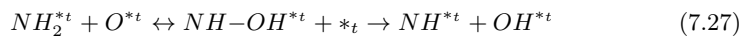
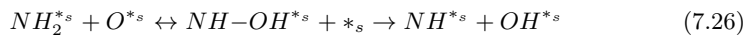
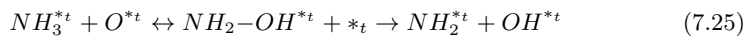
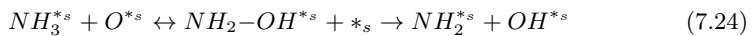
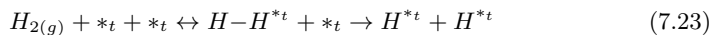
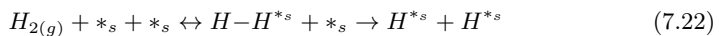
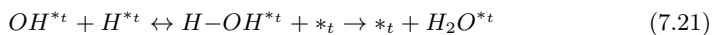
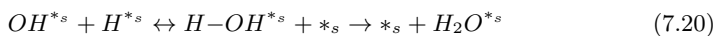
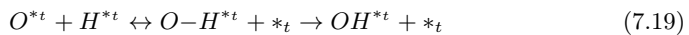
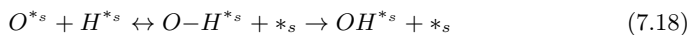
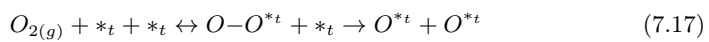
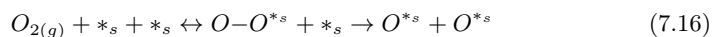
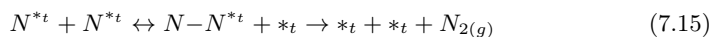
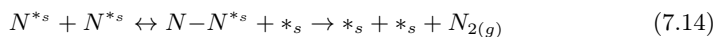
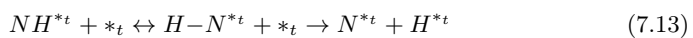
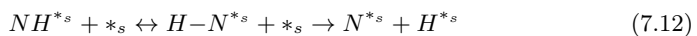
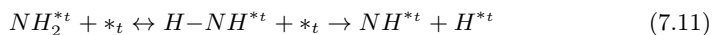
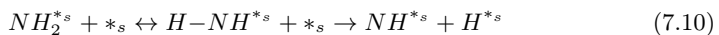
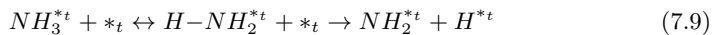
1. $\text{NO} + \text{O} \leftrightarrow \text{NO-O} \rightarrow \text{NO}_2$
2. $\text{NO} + \text{N} \leftrightarrow \text{NO-N} \rightarrow \text{N}_2\text{O}$
3. $\text{NO}_2 + \text{O} \leftrightarrow \text{NO}_2\text{-O} \rightarrow \text{NO}_3$

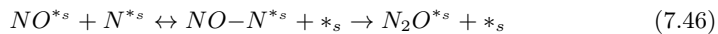
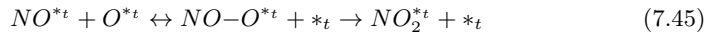
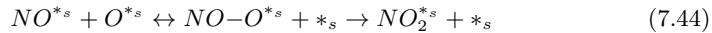
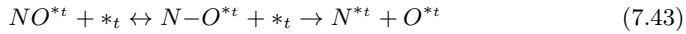
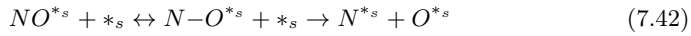
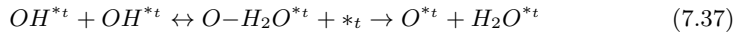
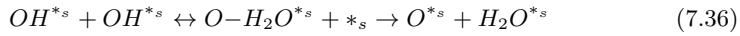
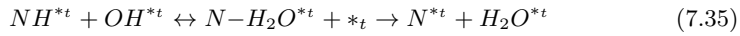
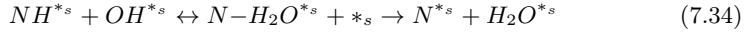
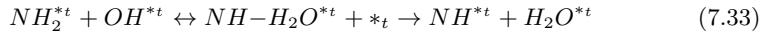
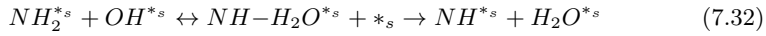
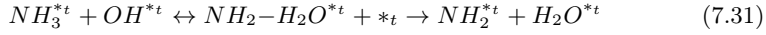
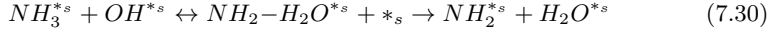
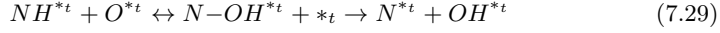
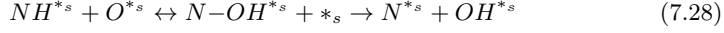
The DFT-calculated adsorption energies of surface intermediates and transition states on the stepped {211} surfaces and flat {111} surfaces of Au, Ag, Co, Cu, Ni, Pd, Pt, Rh, Ru and Re were accessed via CatApp^{121,122,164}. Here I have calculated the adsorption energy of NO₂, N₂O and NO₃ over Au, Ag, Cu, Pd, Pt, Rh, Ru and Re transition metals for the {111} and {211} surfaces. The transition state energy calculation for the NO_x formation reactions are performed with NEB method over transition metals Ag, Cu, Pd, Pt, Rh and Ru {111} and {211} surfaces. The adsorption and transition state energies were scaled with N and O binding energies to obtain the adsorption energy and transition state scaling relations.

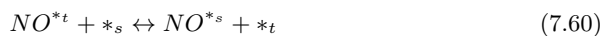
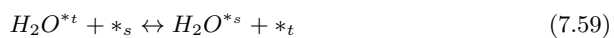
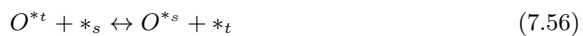
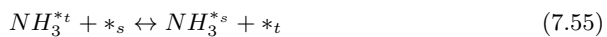
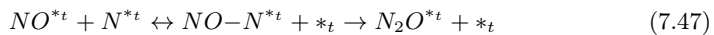
With the obtained adsorption energy and transition state scaling parameters, I constructed the microkinetic model for the NO → NO₂ and N₂O formation based on N and O binding energy. The microkinetic model for NO oxidation is mainly based on the NH₃ oxidation microkinetic model, I proposed in the previous NH₃ oxidation chapter 6. The NH₃ oxidation is an intrinsic part of H₂ assisted NO_x-SCR by NH₃. I only have modified the NH₃ oxidation mechanism to input the NO_x pathway, to construct the microkinetic model for the NO oxidation given below. For this study also I have used a ‘dual facet’ model as our catalyst surface as described in chapter 6. More details about the microkinetic model used here can be found in webpage¹⁶³. The scaling relations used in the microkinetic modeling can be found in appendix section A.6.2.

Elementary Reactions









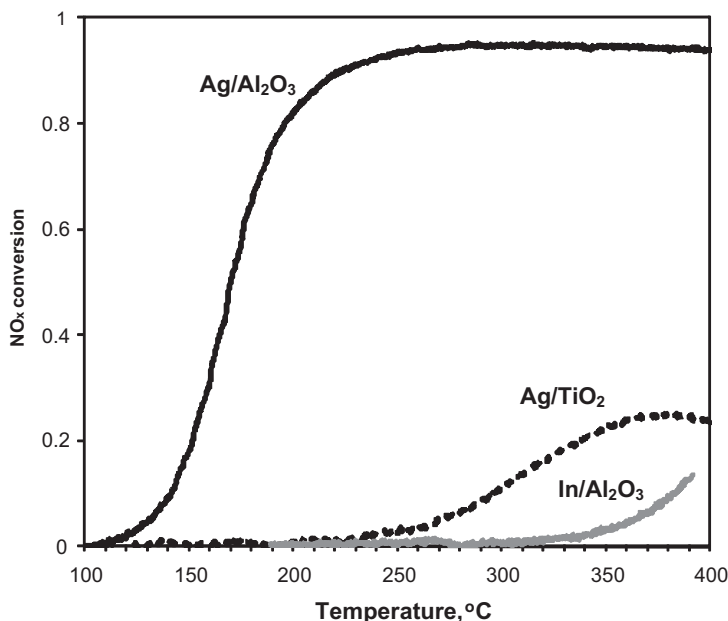


Figure 7.2: NO_x conversion profiles obtained over Ag/Al₂O₃ (black solid line), over Ag/TiO₂ (black dashed line) and over In/Al₂O₃ (gray solid line). Reaction conditions: 500 ppm NO, 520 ppm NH₃, 1200 ppm H₂, 8.3% O₂, 7% H₂O in Ar, GHSV = 110000 h⁻¹.

7.1.4 Experimental Results

Unique activity of Ag/Al₂O₃ in H₂-assisted NO_x-SCR by NH₃

The NO_x conversion during the H₂ assisted NO_x-SCR by NH₃ over Ag/Al₂O₃, Ag/TiO₂ and In/Al₂O₃ for a wide range of temperature have been plotted in Figure 7.2. In figure 7.2 we can see that only Ag/Al₂O₃ is active for H₂ assisted NO_x-SCR by NH₃, with nearly 90% conversion at 200 °C. The other two catalyst Ag/TiO₂ and In/Al₂O₃ are almost inactive for this reaction, with Ag/TiO₂ showing only 25% conversion at 350 °C and In/Al₂O₃ almost zero conversion. NO_x conversion activity for more combinations of catalyst/support are given in Table 7.1. From Table 7.1 it can be observed that the removal or change of any of the two component (Ag and Al₂O₃), make the catalyst almost inactive. Therefore it is most likely that both Ag and Al₂O₃ take part in the reaction or the active sites are positioned at the interface of Ag & Al₂O₃.

TEM measurement of Ag/Al₂O₃ and Ag/TiO₂

Table 7.1: Studied catalysts and NO_x conversions obtained at 380 °C without and with H₂ in the feed gas. Reaction conditions: 500ppm NO, 520ppm NH₃, 8.3% O₂, 7% H₂O in Ar, GHSV = 110,000 h⁻¹.

Catalyst	Metal loading, wt%	NO _x conversion(%) (0ppm H ₂)	NO _x conversion (%) (1200 ppm H ₂)
Al ₂ O ₃	-	0	0
Ag/Al ₂ O ₃	1	0	94
Ag/TiO ₂	1	1.5	25
Ag/ZrO ₂	1	0	0
Sn/Al ₂ O ₃	3	0	0
In/Al ₂ O ₃	3	0	10.5

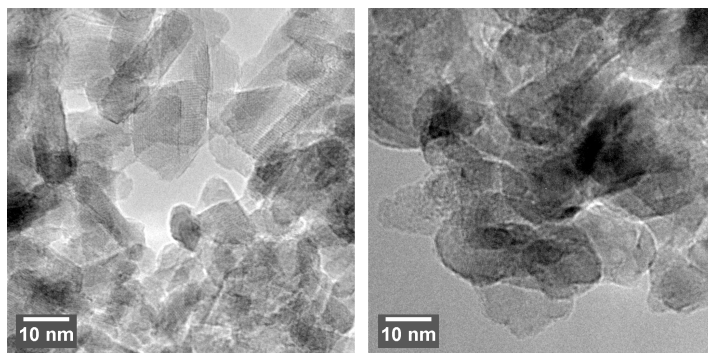


Figure 7.3: . TEM images of Ag/Al₂O₃ (left) and Ag/TiO₂ (right) calcined at 550 °C in air.

The TEM measurements were performed to study the particle size distribution in the two catalysts, Ag/Al₂O₃ and Ag/TiO₂ (shown in Figure 7.3). The EDX data obtained from the experiment show presence of ~1% Ag in both the catalyst samples. However we can not locate any metal particle with diameter more than 2-3 nm in both the catalysts. This means that for both the catalysts, the Ag metal particles are highly dispersed. From this TEM study we conclude that the unique activity of Ag/Al₂O₃ is not due to difference in metal dispersion. The small Ag particles have been previously attributed to clusters of Ag with 4-8 metal atoms.¹⁸²

Study of mechanism of H₂ assisted NO_x-SCR by NH₃ over Ag/Al₂O₃

To find out the influence of the individual components of the reaction gas feed, we did catalytic tests over Ag/Al₂O₃ with one or more component missing from the gas mixture. From Table 7.1 we can see that removal of H₂ from the feed leads to a

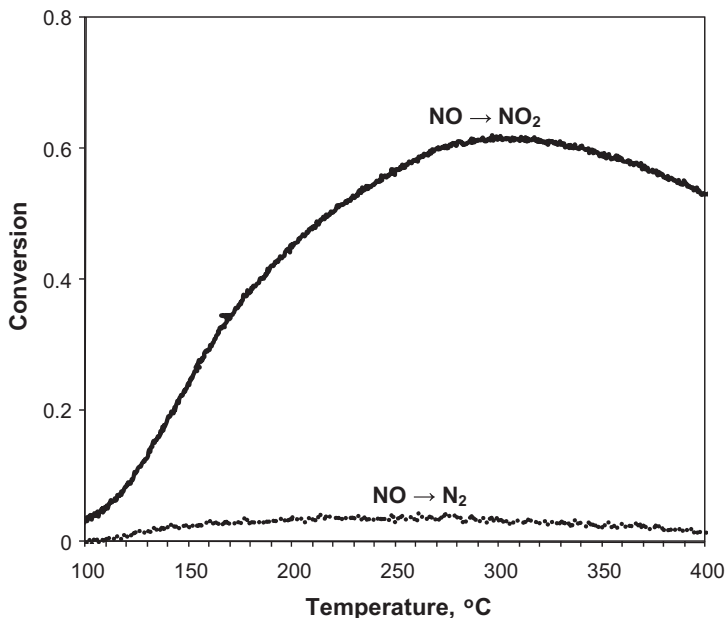


Figure 7.4: NO conversion to NO₂ (solid line) and NO_x conversion to N₂ (dotted line) over Ag/Al₂O₃ without ammonia in the feed. Reaction conditions: 500 ppm NO, 1200 ppm H₂, 8.3% O₂, 7% H₂O in Ar, GHSV = 110000 h⁻¹.

completely inactive NO_x-SCR catalyst. When O₂ is omitted from the gas feed, the catalyst turned inactive for both NO reduction and NH₃ oxidation. However when the NH₃ gas is switched off from the feed, pronounced oxidation of NO to NO₂ is observed, shown in Figure 7.4. However we only observed very low NO→N₂ conversion in this test reaction. This also shows that H₂ normally plays the role of co-reductant, whereas NH₃ is the main reducing agent in the H₂ assisted NO_x-SCR by NH₃ reaction. When both the NH₃ and H₂ are removed from the gas feed, no NO oxidation is observed. This suggests that H₂ promotes the oxidation of NO to NO₂ on Ag/Al₂O₃ catalyst, whereas for Ag/TiO₂ and Ag/Zr₂ the NO to NO₂ oxidation is not observed. This again proves that not only metal catalyst Ag, but the support Al₂O₃ is also important for the H₂ assisted NO_x-SCR by NH₃ reaction. When NO is omitted from the gas feed, a pronounced oxidation of NH₃ to N₂ and NO_x is seen only after 250 °C (shown in Figure 7.5). Comparing Figure 7.4 and Figure 7.5 we can conclude that the oxidative NO activation starts significantly below the starting temperature of NH₃ activation. These findings disapproves the hypothesis that the oxidative dehydrogenation of NH₃ is the main elementary steps for the H₂ assisted NO_x-SCR by NH₃ over Ag/Al₂O₃.¹⁸⁸ These experimental data suggest that most possibly the NO first gets oxidized to other NO_x intermediates (H₂ works as the promoter for this step), which then reacts with the main reductant NH₃ to form N₂.¹⁸²

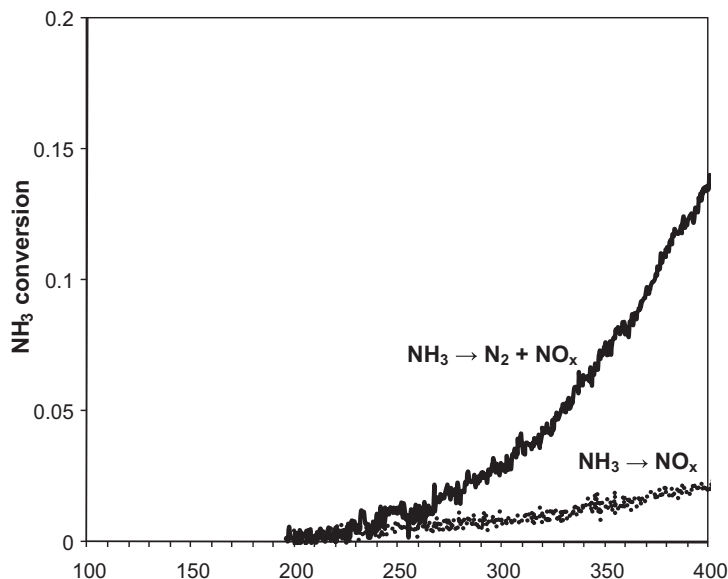


Figure 7.5: NH₃ conversion (solid line) and NH₃ conversion to NO_x (dotted line) over Ag/Al₂O₃ with no NO in the feed. Reaction conditions: 520 ppm NH₃, 1200 ppm H₂, 8.3% O₂, 7% H₂O in Ar, GHSV = 110000 h⁻¹.

As it already have been shown that the NO oxidation to other NO_x is an important step for H₂ assisted NO_x-SCR by NH₃ over Ag/Al₂O₃^{189,190}, we run more catalyst test reaction with NO+NO₂ mixture in the gas feed. We also switched off the H₂ gas from the feed to remove the possibility of further NO to NO₂ conversion during the test reactions. The test runs are performed with three different gas composition with 26%, 34% and 47% NO₂ in the NO_x mixture over Ag/Al₂O₃ catalyst. Also catalytic test is performed with Ag/ZrO₂ with 26% NO₂ in the NO_x mixture. The data obtained from the experiments have been plotted in Figure 7.6. For all there experiments performed over Ag/Al₂O₃ with different percent NO₂ in the NO_x mixture, similar NO_x conversion profile is obtained, with maximum 30% NO_x conversion for all of them. It also can be observed that here the effect of changing the support is not that drastic, as Ag/ZrO₂ shows 15% NO_x conversion compared to the 30% conversion observed for Ag/Al₂O₃. In Figure 7.7 the ratio of NO converted to the NO₂ converted has been plotted. This is done to check is the H₂ assisted NO_x SCR with NH₃ actually follow the 'Fast-SCR' mechanism^{191,192} or not. When feed with 26% NO₂ we see the NO:NO₂ conversion ratio is ~1, which suggest it follows the 'Fast-SCR' pathway. But it can also be seen that when feed with NO+ NO₂ mixture the maximum conversion is only 30%, where as for the H₂ assisted NO_x SCR with NH₃ the NO_x conversion is nearly 100%. This means only a part of the reaction follows the 'Fast-SCR' mechanism. The lower conversion of the NO+NO₂-SCR has been attributed to the blocking of the catalyst by surface nitrates.^{189,193} H₂ can effectively remove the nitrates and help in the regeneration of

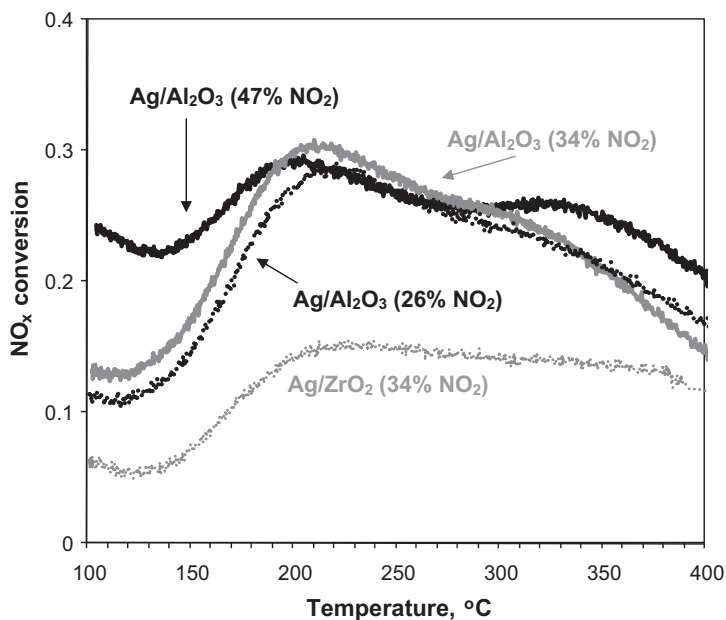


Figure 7.6: NO_x conversion over Ag/Al₂O₃ without H₂ in the feed, when NO and NO₂ mixture is fed as NO_x. Conditions: 500 ppm NO_x, 520 ppm NH₃, 8.3% O₂, 7% H₂O in Ar, GHSV = 110 000 h⁻¹. Black line - 47% NO₂, gray line - 34% NO₂, dotted line - 26% NO₂ (NO is the rest of 500 ppm NO_x).

the surface and thus removes the 30% conversion limit.¹⁹³ Higher the NO₂ content in the feed, lower the NO:NO₂ conversion ratio. This suggests that NO₂ is more easily converted to N₂ than NO.

To study the influence of Al₂O₃ in the NO_x-SCR activity, pure γ-Al₂O₃ is tested under the reaction condition with NO+NO₂ co-feeding. γ-Al₂O₃ is inactive for the NO_x-SCR when NO is the only component in the NO_x (both with and without H₂). However when NO₂ is present with NO (26% NO₂ in the NO_x mixture) both Ag/Al₂O₃ and pure Al₂O₃ shows similar NO_x conversion profile (30% maximum conversion), shown in Figure 7.8. This suggests that presence of Ag in the catalyst is only important for the H₂ assisted reaction. And as it already has been shown in Figure 7.4, that in presence of H₂, NO gets oxidized to NO₂, alumina can contribute significantly to the overall NO_x-SCR reaction over Ag/Al₂O₃.^{194,195} The ratio of converted NO:NO₂ over Ag/Al₂O₃ and pure-Al₂O₃ also follow the same profile, shown in Figure 7.9. This gives us another reason to suggest that the NO_x-SCR reaction mechanism over Ag/Al₂O₃ and pure-Al₂O₃ are completely or partially same. The presence of H₂ and Ag is important for oxidative activation of NO and removal of adsorbed nitrate species poisoning the catalyst surface.

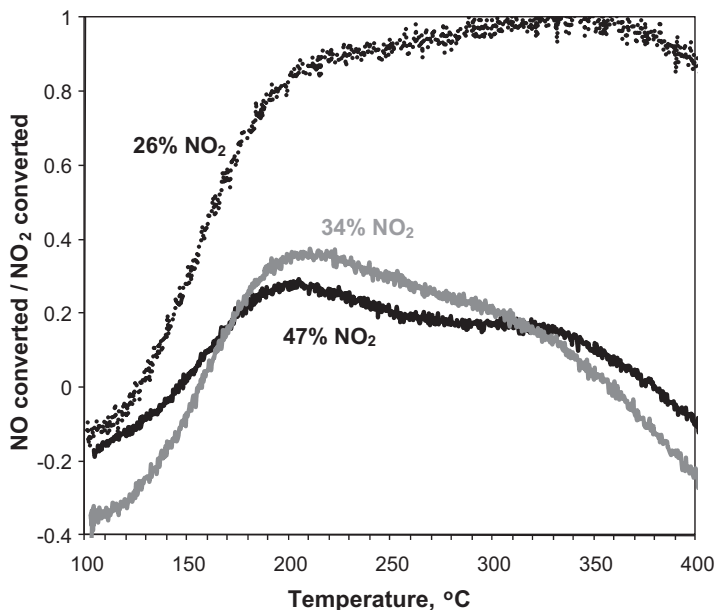
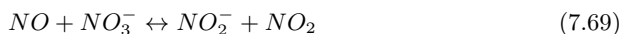
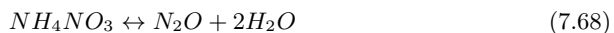
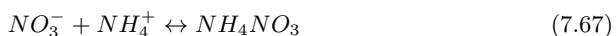
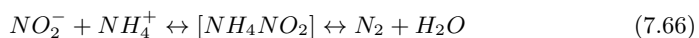
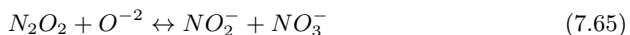
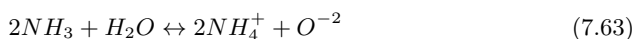


Figure 7.7: Ratio of consumed NO to consumed NO₂ for simultaneous NO + NO₂ reduction by NH₃. Reaction conditions: 500 ppm NO_x, 520 ppm NH₃, 8.3% O₂, 7% H₂O in Ar, GHSV = 110000 h⁻¹. Black line - 47% NO₂, gray line - 34% NO₂, dotted line - 26% NO₂ (NO is the rest of 500 ppm NO_x).

Based on the findings and knowledge of ‘Fast-SCR’ mechanism beforehand, the following reaction mechanism is proposed:



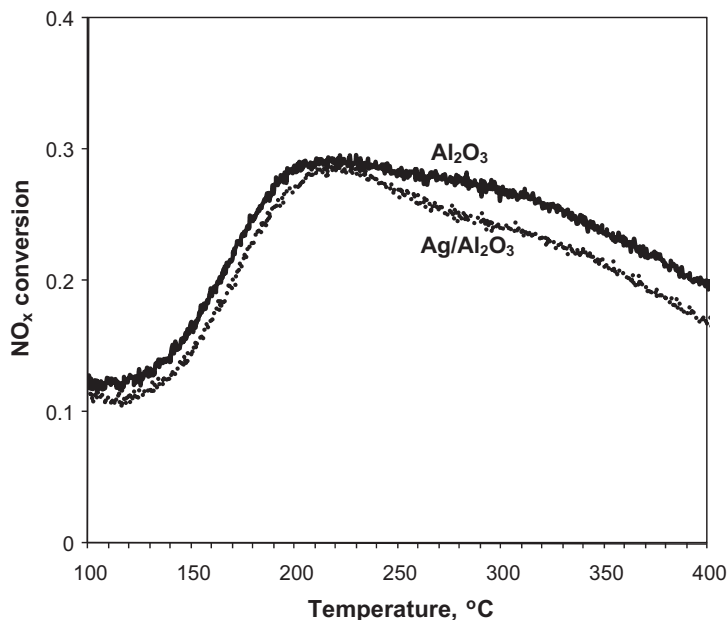
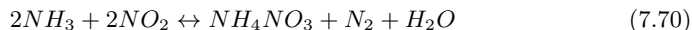


Figure 7.8: NO_x conversion over Al₂O₃ (solid line) and Ag/Al₂O₃ (dotted line, for a comparison) without H₂ in the feed, when NO and NO₂ mixture is fed as NO_x. Reaction conditions: 500 ppm NO_x (37% NO₂), 520 ppm NH₃, 8.3% O₂, 7% H₂O in Ar, GHSV = 110000 h⁻¹.

At temperature higher than 150 °C, reactions (7.63)– (7.67) operate, yielding N₂ and surface nitrates. Only a tiny portion of the surface nitrates gets decomposed at these temperature (< 5 ppm N₂O). For temperatures T < 150 °C, NO is produced from NO₂ following reverse of reaction (7.69). At higher temperatures T > 150 °C, NO reacts with nitrates to form NO₂ and nitrite (reaction (7.69)) and then nitrite react with NH₄⁺ to form NH₄NO₂, which readily gets decomposed to N₂. With decreasing temperature 400 °C to 200 °C, an increase in the NO_x conversion is observed due to the formation of NH₄NO₃ (shown in Figure 7.6). A lower NO_{converted}/ NO_{2 converted} ratio below 180 °C in Figure 7.9 is due to the NH₄NO₃ formation reaction:



The reaction (7.70) is actually the combination of reaction (7.63) + (7.64) + (7.65) + (7.66) + (7.67). The reaction (7.68) and (7.69) are too slow at this temperature. Therefore formation of NH₄NO₃ blocks the surface sites and limits the NO_x conversion below 200 °C.

In Figure 7.10 NO_x-SCR catalytic tests were performed with pure-Al₂O₃ to check the

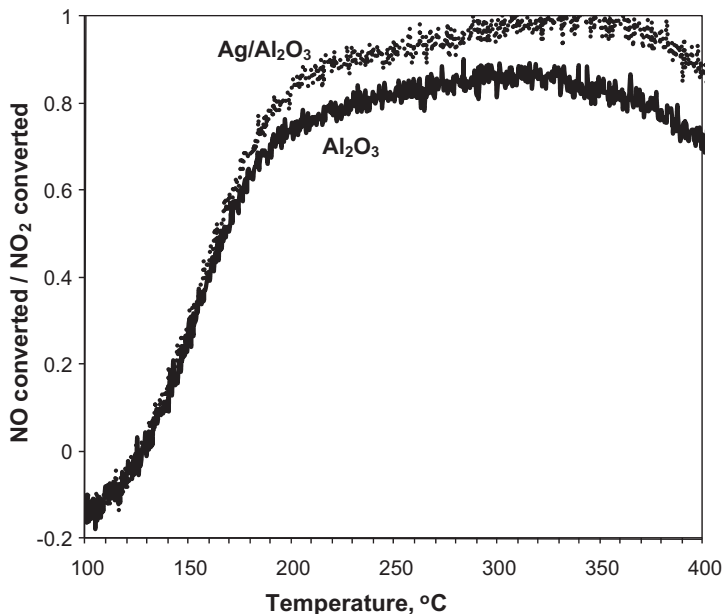


Figure 7.9: Ratio of consumed NO to consumed NO₂ for NO + NO₂ simultaneous reduction by NH₃ over Al₂O₃ (solid line) and Ag/Al₂O₃ (dotted line, for a comparison). Reaction conditions: 500 ppm NO_x (26% NO₂), 520 ppm NH₃, 8.3% O₂, 7% H₂O in Ar, GHSV = 110000 h⁻¹.

reaction scheme over it. During the tests, temperature ramp was stopped at 500 °C, 210 °C and 100 °C. After each stop the outlet gas is stabilized and then NH₃ gas is switched off from the feed. The removal of NH₃ from the inlet gas at 500 °C and 100 °C have no effect on the NO and NO₂ concentration (no reaction of NO with surface nitrates). However at 210 °C, a prominent increase in NO₂ concentration and subsequent decrease in NO concentration is observed. This suggests that NO reacts with surface NO₃⁻, to form NO₂, following reaction (7.69). The ratio of NO₂ evolved to the NO consumed is ~1.7. This ratio can be obtained from the proposed mechanism by combining reaction (7.66), reverse of (7.65) and (7.64) and reaction (7.69). Thus we have proved that the NO_x-SCR over Ag/Al₂O₃ and pure-Al₂O₃ share most of the reaction steps of the ‘Fast-SCR’ reaction mechanism.

7.1.5 DFT and Microkinetic Modeling Results

With the ultimate goal of modeling the full H₂ assisted NO_x-SCR by NH₃ reaction mechanism over the transition metals, I did a complete study on the adsorption of possible intermediates over Ag{211} surface. I performed adsorption energy calculations

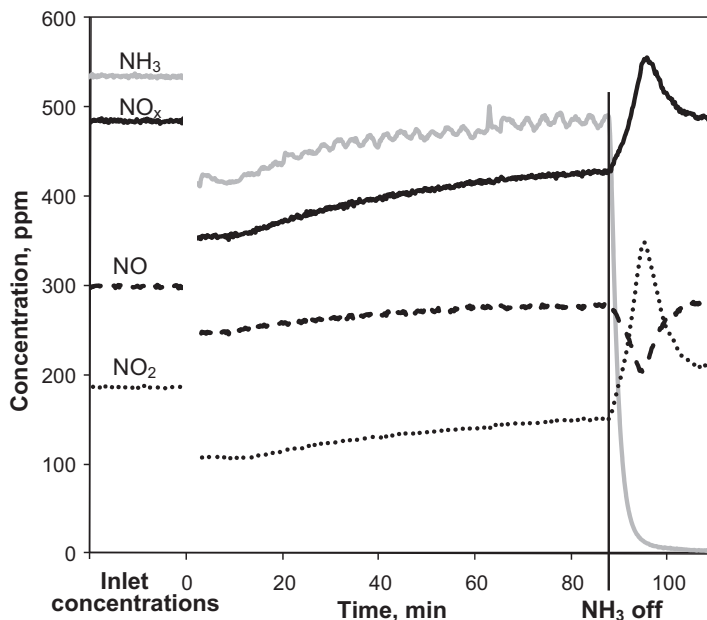


Figure 7.10: Change of NO, NO₂ and NO_x concentrations after removing NH₃ from the feed. Catalyst: Al₂O₃. Reaction conditions: 500 ppm NO_x (37% NO₂), 520 ppm NH₃, 8.3% O₂, 7% H₂O in Ar, GHSV = 110000 h⁻¹, temperature 210 °C.

for sixty-six possible intermediates for this reaction, given in appendix section A.6.1. I also have calculated the formation energies of the gas phase species and their corresponding magnetic moments. Among the sixty-six possible intermediates, fifty intermediates are stable on adsorption over Ag{211} surface. Though all of these fifty stable intermediates should be studied carefully, due to time constrain we choose some important intermediates proposed in previous reports, and do a detail DFT study on them. In many proposed reaction mechanism for NO_x-SCR by NH₃, NH₂NO has been mentioned as a very key intermediate.^{196–199}

The decomposition of NH₄NO₂ → N₂ + 2H₂O, is suggested to occur in two steps,

1. NH₄NO₂ → NH₂NO + H₂O (g)
2. NH₂NO → N₂ (g) + H₂O (g)

In the first step NH₄NO₂ dissociates to NH₂NO and H₂O(g). Then in the next step NH₂NO dissociates giving rise to the N₂ (g) and H₂O(g). Here I have studied a few 'H_xNNO_y' intermediates, which also contain similar N-N bond as in NH₂NO. The

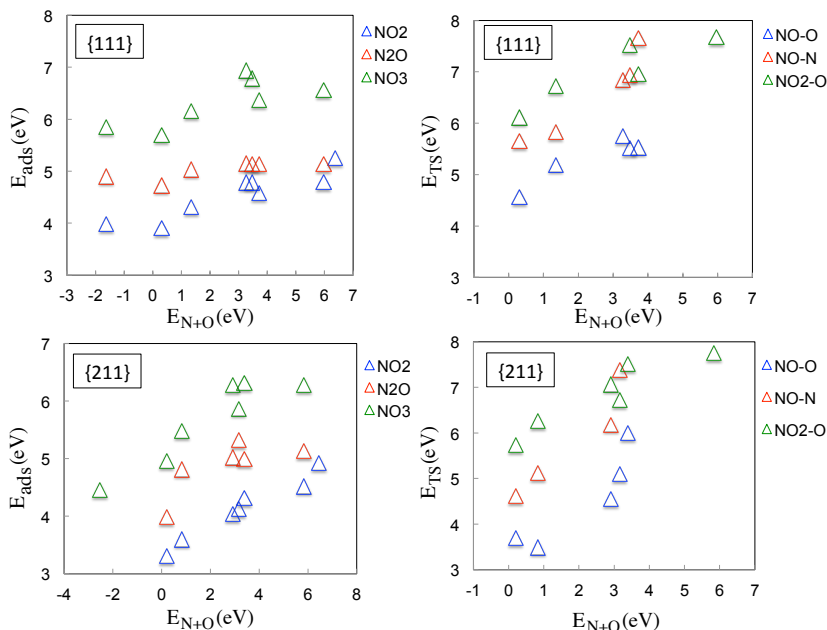


Figure 7.11: Adsorption and transition state energies of the NO_x species plotted versus the (N+O) binding energy for Au, Cu, Ag, Pd, Pt, Rh, Ru and Re {111} and {211} surfaces. The adsorption energies are calculated relative to NH₃, H₂O and H₂ gas phase energies.

adsorption energy calculation of HNNO, H₂NNO, H₂NNO₂, HNNO₂ were performed over over Ag, Pt, Rh and Re transition metals {111} and {211} facets given in Table 7.2. The adsorption energies of some other key intermediates O₂, N₂, N₂O₂, NOH, HNO, HNO₃, HNO₂, NHOH, NH₂O, NH₂OH are also given in Table 7.2. I also have obtained the adsorption energy scaling for the above intermediates, given in Table 7.2. These adsorption energy scaling will be used in future to construct a “Fast-SCR” like mechanism proposed by Mark Anstrom et. al.¹⁹⁶ and Ru-Ming Yuan et. al.¹⁹⁷ for the NO_x-SCR by NH₃ for the transition metals to calculate the catalytic rates.

Adsorption energies of NO₂, N₂O and NO₃ are performed over transition metals Au, Ag, Cu, Pd, Pt, Rh, Ru and Re transition metals {111} and {211} surfaces, given in Table 7.3. Transition state energies for the formation of these three NO_x species are also calculated over Ag, Cu, Pd, Pt, Rh and Ru transition metals {111} and {211} surfaces, given in Table 7.4. In Figure 7.11 the adsorption and transition state energies of the NO_x species have been plotted versus the N and O binding energies. The adsorption energy and transition state scaling parameters are given in Table 7.3 and 7.4. With the obtained adsorption energy and transition state scalings (given in appendix section A.6.2) and the reaction mechanism mentioned in section 7.1.3, I

Table 7.2: Adsorption energies of the H₂ assisted NO_x-SCR by NH₃ reaction intermediates over Ag, Pt, Rh and Re {111} and {211} transition metal surfaces. The energies are calculated relative to their own gas phase energies.

Adsorption energies{111}				
Adsorbates	Ag	Pt	Rh	Re
O ₂	0.43	-0.08	-1.04	
H ₂ O ₂	-0.05		-0.03	
NOH	-0.57	-2.13	-2.87	-3.5
HNO	-0.53	-1.35	-2.29	-2.9
N ₂	-0.01	0.08	-0.36	-0.43
HNOH	-0.06	-1.11	-1.46	
HNO ₂ (trans)	0.01	-0.29	-0.42	
ONHO	0.02	0.04	-0.18	-0.72
HNO ₃	0.14	0.16	0.15	0.15
N ₂ O ₂	-0.35	-0.06	-0.89	-1.8
H ₂ NO	-0.09	-0.42	-0.6	-1.19
H ₂ NOH	-0.05		-0.49	-0.56
H ₂ NNO	-0.27	-0.66	-0.85	-1.25
H ₂ NNO ₂	-0.26	-0.34	-0.17	
HNNO	-1.18	-2.34	-3	
HNNO ₂	-1.88	-1.56	-2.34	-2.68
Adsorption energies {211}				
Adsorbates	Ag	Pt	Rh	Re
O ₂	0.2	-0.95	-1.76	
H ₂ O ₂				
NOH	-0.58	-1.75	-2.62	-3.09
HNO	-0.85	-2.09	-2.2	-3.82
N ₂	0	-0.35	-0.66	-0.79
HNOH	-0.24	-1.22	-1.57	
HNO ₂ (trans)	-0.03			
ONHO	-0.1	-0.2	-0.91	-2.41
HNO ₃	0.13	0.15	0.13	
N ₂ O ₂	-0.53	-0.76	-1.71	-3.43
H ₂ NO	-0.31	-0.64	-1.18	-1.96
H ₂ NOH	-0.1		-0.67	
H ₂ NNO	-0.39	-1.11	-1.19	-1.48
H ₂ NNO ₂	-0.38	-0.19	-0.82	
HNNO	-1.45			
HNNO ₂	-2.2	-2.24	-3.02	-4.11

Table 7.3: Adsorption energies of the NO_x species over Au, Ag, Cu, Pd, Pt, Rh, Ru and Re {111} and {211} transition metal surfaces. The energies are calculated relative to NH₃, H₂O and H₂ gas phase energies. The slope and intercept of the scaling between the NO_x species adsorption energy and (N+O) binding energies over the metal surfaces are also given.

Adsorption energies{111}				
Metals	(N*+O*)	NO ₂ *	N ₂ O*	NO ₃ *
Ag	5.97	4.79	5.13	6.56
Pt	3.27	4.78	5.15	6.94
Rh	1.35	4.31	5.03	6.16
Ru	0.31	3.9	4.72	5.7
Pd	3.47	4.78	5.13	6.78
Cu	3.72	4.58	5.13	6.37
Au	6.38	5.26		
Re	-1.62	3.99	4.9	5.85
slope		0.15	0.05	0.14
intercept		4.11	4.91	6.01
Adsorption energies {211}				
Metals	(N*+O*)	NO ₂ *	N ₂ O*	NO ₃ *
Ag	5.83	4.52	5.13	6.28
Pt	2.91	4.04	5.02	6.27
Rh	0.83	3.6	4.81	5.48
Ru	0.2	3.31	3.98	4.96
Pd	3.39	4.31	4.99	6.31
Cu	3.16	4.13	5.32	5.87
Au	6.46	4.93		
Re	-2.53	2.75		4.46
slope		0.23	0.17	0.25
intercept		3.36	4.41	5.17

Table 7.4: Transition state energies for the formation of the NO_x species over Ag, Cu, Pd, Pt, Rh and Ru {111} and {211} transition metal surfaces. The energies are calculated relative to NH_3 , H_2O and H_2 gas phase energies. The slope and intercept of the transition state scaling between the transition state energy of NO_x species and $(\text{N}+\text{O})$ binding energies over the metal surfaces are also given.

Transition state energies{111}				
Metals	(N^*+O^*)	NO_2^*	N_2O^*	NO_3^*
Ag	5.97			7.67
Pt	3.27	5.75	6.85	
Rh	1.35	5.19	5.83	6.73
Ru	0.31	4.57	5.65	6.11
Pd	3.47	5.51	6.94	7.52
Cu	3.72	5.53	7.66	6.95
slope		0.28	0.52	0.26
intercept		4.63	5.32	6.23
Transition state energies {211}				
Metals	(N^*+O^*)	NO_2^*	N_2O^*	NO_3^*
Ag	5.83			7.75
Pt	2.91	4.55	6.18	7.06
Rh	0.83	3.49	5.13	6.26
Ru	0.2	3.69	4.61	5.73
Pd	3.39	6		7.51
Cu	3.16	5.1	7.39	6.73
slope		0.63	0.78	0.35
intercept		3.25	4.44	5.88

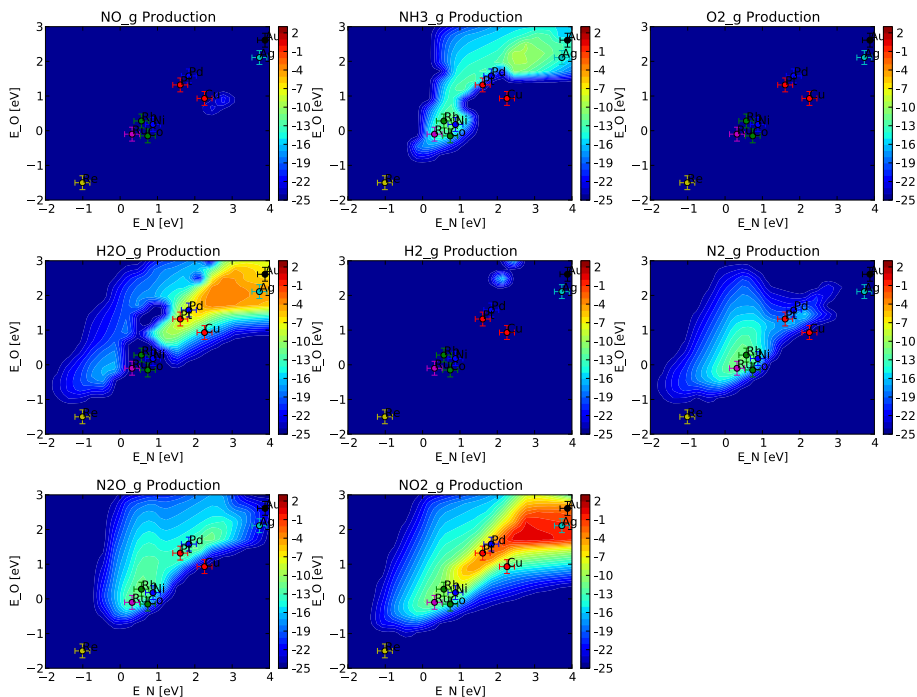


Figure 7.12: Catalytic rates of formation of NO, NH₃, O₂, H₂O, H₂, N₂, N₂O and NO₂ over the dual ({111} + {211}) model surface during the H₂ assisted NO_x-SCR by NH₃. The reaction condition is: T = 200 °C, P = 1 bar, with a gas composition of 500 ppm NO, 520 ppm NH₃, 8.3% O₂, 7% H₂O, 1200 ppm H₂

constructed the microkinetic model for the NO oxidation during the H₂ assisted NO_x-SCR by NH₃ over a dual ({111} + {211}) model surface. The NO activation studies are performed at normal H₂ assisted NO_x-SCR by NH₃ reaction condition: T = 200 and 400 °C, P = 1 bar, with a gas composition of 500 ppm NO, 520 ppm NH₃, 8.3% O₂, 7% H₂O, 1200 ppm H₂.

Catalytic rates of formation of different gas components NO, NH₃, O₂, H₂O, H₂, N₂, N₂O and NO₂ during the H₂ assisted NO_x-SCR by NH₃ reaction at 200 and 400 °C over a dual ({111} + {211}) model surface have been plotted in Figure 7.12 and 7.13, respectively. In Figure 7.12 and 7.13 we can see that at lower temperature (200 °C) Ag is the best metal for NO₂ formation, whereas at higher temperature (400 °C) Pd and Pt shows best NO₂ formation reactivity. NO₂ formation rate over Ag metal surface at 200 °C is 10⁻¹ s⁻¹. Though Pd and Pt are the best NO₂ formation catalyst at 400 °C (TOF = 10² s⁻¹), Ag also shows appreciable NO₂ formation activity (TOF = 10⁻¹ s⁻¹). From these two observations from Figure 7.12 and 7.13, one can conclude that Ag metal will be a very good NO → NO₂ oxidation catalyst in the whole low-

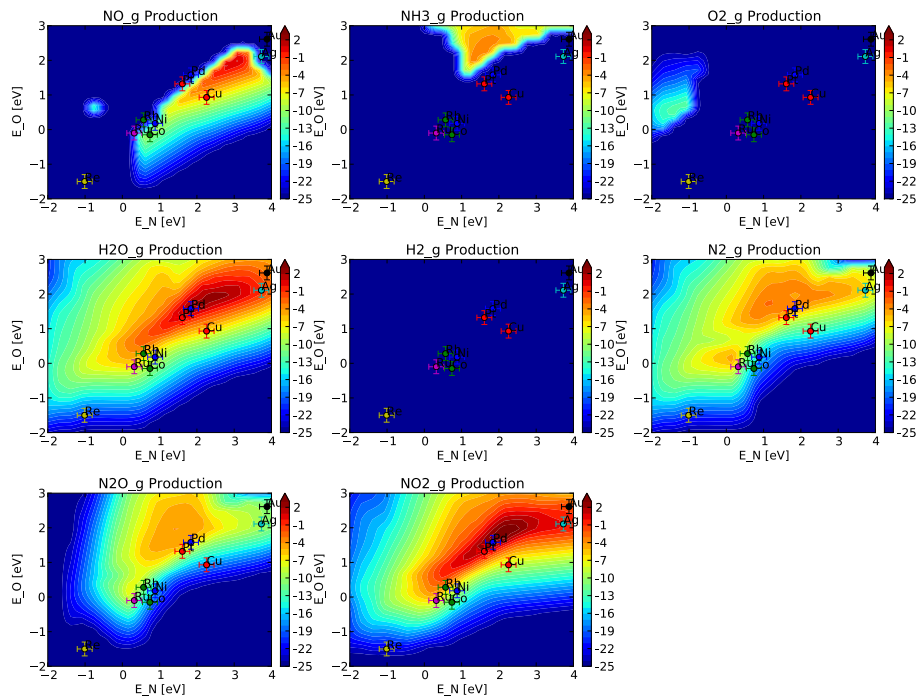


Figure 7.13: Catalytic rates of formation of NO, NH₃, O₂, H₂O, H₂, N₂, N₂O and NO₂ over the dual ({111} + {211}) model surface during the H₂ assisted NO_x-SCR by NH₃. The reaction condition is: T = 400 °C, P = 1 bar, with a gas composition of 500 ppm NO, 520 ppm NH₃, 8.3% O₂, 7% H₂O, 1200 ppm H₂

temperature region, in agreement with the proposed mechanism. At 200 °C, Ag is almost inactive for N₂ and N₂O formations. Rh and Ru show the best N₂ and N₂O formations activity, however the rates are very low (TOF = 10⁻¹⁰ s⁻¹). With increase in temperature, at 400 °C, Ag shows better N₂ formation activity (TOF = 10⁻⁵ s⁻¹, however the N₂O formation rate is still very low. At 200 °C, Pd is the best N₂ and N₂O formation catalyst, with TOF ~ 10⁻⁴ s⁻¹. Also from Figure 7.12 and 7.13, one can see that the rate of H₂O formation over Ag is much higher than the rate of N₂ formation, both at 200 and 400 °C. This also suggest the preferential direct H₂ oxidation over the Ag metal surfaces, same as proposed in the reaction mechanism.

In Figure 7.14 we have plotted the potential energy diagram for the formation of NO₂ and NO₃ from oxidation of NO over Ag, Cu, Pd, Pt, Rh and Ru {111} and {211} transition metal surfaces. The potential energy diagram shows that for the {111} surface the NO₂* formation is favorable over Ag and Cu metals, where as NO₃* formation is favorable over Ag metal only. For the {211} surface Ag is the only metal where formation of NO₂* and NO₃* via NO oxidation is favorable, in agreement with

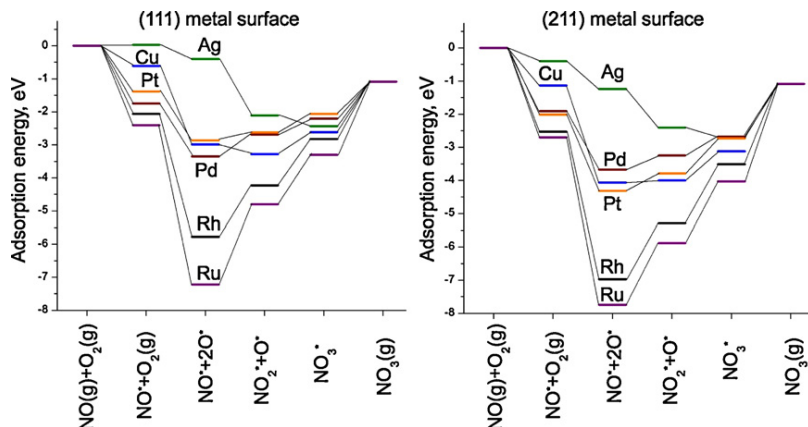


Figure 7.14: Potential energy surface diagram for the formation of NO_x via the oxidation of NO over (111) and (211) surfaces of the selected transition metals.

Anders et. al.¹⁸¹. This support the suggestion that Ag is necessary for the NO oxidation to NO₂ and NO₃, known to be important for low temperature "Fast-SCR" pathway.

However NO₃* binds strongly to the γ -Al₂O₃ surface and hence can potentially block the surface, as suggested also by¹⁸³. We also have suggested before in section 7.1.4 that NO₃* blocks the Ag/Al₂O₃ surface and H₂ works as a promoter by removing the NO₃ and the catalyst. Here I have calculated the adsorption energies of NO₃ and HNO₃ over the model γ -Al₂O₃ step surface, given in Figure 7.15. The adsorption energy of HNO₃ over the γ -Al₂O₃ is much lower than than of NO₃. And hence HNO₃ will be more easily desorbed from the surface. This supports our suggestion that H₂ facilitates the removal of NO₃ and thus works as a promoter in the H₂ assisted NO_x-SCR by NH₃ reaction.

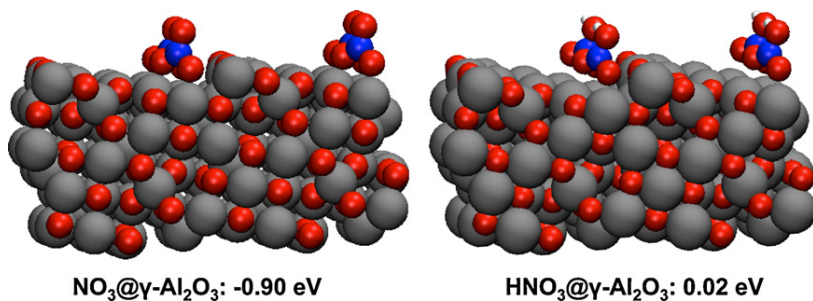


Figure 7.15: NO₃ and HNO₃ adsorption geometries and adsorption energies on the model step closed packed gamma alumina surface. All the adsorption energies are given with the reference to the gas phase zero energy points of the respective species.

7.2 Study of the Sulphur Poisoning of Ag/Al₂O₃ during the H₂-assisted NO_x-SCR by NH₃

Ag/Al₂O₃ has been shown as one of the most promising NO_x-SCR catalyst in the lean burn condition. It shows nearly 90% NO_x conversion even at temperature as low as 200 °C.^{171–173} However, one of the main obstacle for practical use of Ag/Al₂O₃ in the catalytic converter (car catalyst) is its poor sulfur tolerance.²⁰⁰

Park and Boyer²⁰¹ conducted sulfur poisoning test with 2 and 8% Ag/Al₂O₃ catalyst. They found 8% Ag/Al₂O₃ shows higher catalytic activity than 2% Ag/Al₂O₃ after sulfur treatment. They concluded that high Ag loading may be preferential for obtaining a sulfur tolerant Ag/Al₂O₃ NO_x-SCR catalyst. The authors also suggested the formation of very active silver sulfate phase during the sulfur treatment as the reason for the high catalytic activity of the 8% Ag/Al₂O₃. Breen et al.²⁰² in their study on sulfur poisoning during the NO_x-SCR by octane and toluene observed: at low temperature (T < 235 °C) little deactivation; for temperature between 235–500 °C severe deactivation and at higher temperature (T > 500 °C) activation due to the suppression of unselective oxidation of hydrocarbons. The authors proposed that the main poisoning species for sulfur deactivation of Ag/Al₂O₃ is SO₃. At low temperature (T < 235 °C), under the NO_x-SCR reaction condition, the oxidation of SO₂ to SO₃ is very slow over Ag/Al₂O₃ catalyst. Hence the poisoning effect at this temperature range is minimal. However with increasing temperature (235–500 °C), the SO₂ oxidation to SO₃ becomes prominent and the catalysts get severely deactivated. The authors also showed promotional effect of H₂ during the regeneration of the deactivated Ag/Al₂O₃ catalysts.

Results from other groups^{203,204} also agrees to the sulfur poisoning mechanism proposed by Breen et al. They also suggested oxidation of SO₂ to SO₃ by NO₂ is the

major step for sulfur poisoning of Ag/Al₂O₃, during the NO_x-SCR catalysis.

7.2.1 Experimental Setups

Catalyst Preparation

1-3% Ag/Al₂O₃ were prepared by the wetness impregnation of γ-Al₂O₃ by AgNO₃ solutions in deionised water. The impregnated catalyst is dried at room temperature overnight and then calcined at 550 °C for 4 hour in static air. Next the calcined catalyst are crushed and shived to obtain the desired particle size distribution of 0.18-0.35 mm (mesh size: 80 - 45).

Catalytic study

Catalyst measurement were done in a fixed bed quartz reactor (inner diameter - 4 mm). The temperature of the catalysis study is decreased from 400 °C to 150 °C at a rate of 2 °C/min. 45 mg of catalyst was diluted to 100 mg of SiC(mesh size 60). The GHSV (Reactant Gas Flow Rate/Reactor Volume) used in this study was ~11000 h⁻¹. The gas composition normally used is, 500 ppm NO, 520 ppm NH₃, 8.3% O₂ and 7% H₂O and rest Ar gas. Some test are also carried out 500 ppm NO, 520 ppm NH₃, 1200 ppm H₂, 8.3% O₂ and 7% H₂O and rest Ar. For the sulfur poisoning study, catalytic test are performed with 10 ppm SO₂ admixed to the gas feed.

The reaction products are analyzed using a Thermo Fisher Nicolet 6700 FT-IR analyzer. The conversions corresponding to this study were calculated using the following equations,

$$X_{NO_x} = 1 - \frac{C_{NO_x}^{outlet}}{C_{NO_x}^{inlet}} \quad (7.71)$$

where X_{NO_x} is the conversion of NO_x, $C_{NO_x}^{inlet}$ and $C_{NO_x}^{outlet}$ are the NO_x concentration at the inlet and outlet of the reactor. C_{NO_x} is the total composition of NO and NO₂, $C_{NO_x} = C_{NO} + C_{NO_2} + C_{N_2O}$

Similarly the NH₃ conversion is given by,

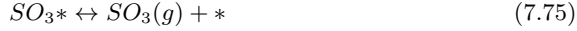
$$X_{NH_3} = 1 - \frac{C_{NH_3}^{outlet}}{C_{NH_3}^{inlet}} \quad (7.72)$$

where $C_{NH_3}^{inlet}$ and $C_{NH_3}^{outlet}$ are the NH₃ concentration at the inlet and outlet of the reactor.

7.2.2 DFT Setups

Same DFT calculation setups are used for the SO_x adsorption energy calculation over the metal surfaces and γ -Al₂O₃ surface, as the one used in previous section 7.1.

Adsorption energies of SO_x and HSO_x species were calculated relative to formation energies of SO₂(g), O₂(g) and H₂(g). In the case of the Ag {111} and Ag {211} surfaces desorb directly as SO₂(g) + O₂(g). For calculation of desorption temperatures for SO₂ and SO₃ we used the following procedure. Starting from the chemical equation:



The ratio of occupied and free sites can be given by:

$$\begin{aligned} \frac{\theta_{SO_x}}{\theta_*} &= K_{ads} p_{SO_x} = \exp\left(-\frac{\Delta G_{ads}}{k_B T}\right) p_{SO_x} \\ &= \exp\left(\frac{-(\Delta G_{ads}^\phi - k_B T \ln p_{SO_x})}{k_B T}\right) \end{aligned} \quad (7.78)$$

Where θ_{SO_x} and θ_* are coverages of the adsorbed SO_x species and free sites, respectively. p_{SO_x} is the partial pressure of the SO_x gases. We take the assumption that at the desorption temperature the number of SO_x occupied and free sites are equal ($\theta_{SO_x} = \theta_*$). With this assumption one can rewrite the equation (7.78) as,

$$\Delta G_{ads}^\phi - k_B T \ln p_{SO_x} = 0 \quad (7.79)$$

or

$$\Delta E_{ads} - \Delta ZPE_{ads} - T \Delta S_{ads} - k_B T \ln p_{SO_x} = 0 \quad (7.80)$$

The desorption temperature,

$$T = \frac{\Delta E_{ads} - \Delta ZPE_{ads}}{k_B T \ln p_{SO_x} - T \Delta S_{ads}} \quad (7.81)$$

The entropies and zero point energies (ZPE) of the adsorbed SO_x species are calculated from the vibrational frequencies using the harmonic oscillator approximation. SO_x entropy and ZPE found for γ -Al₂O₃ surface, are also used for the single Ag atom sites on the γ -Al₂O₃ surfaces. The gas phase entropies for SO₂ and SO₃ are obtained from NIST²⁰⁵ (neglecting entropy change with temperature). Partial pressure of SO_x and O₂ used for this study are 4×10^{-7} bar (0.4 ppm) and 0.07 bar, respectively.²⁰²

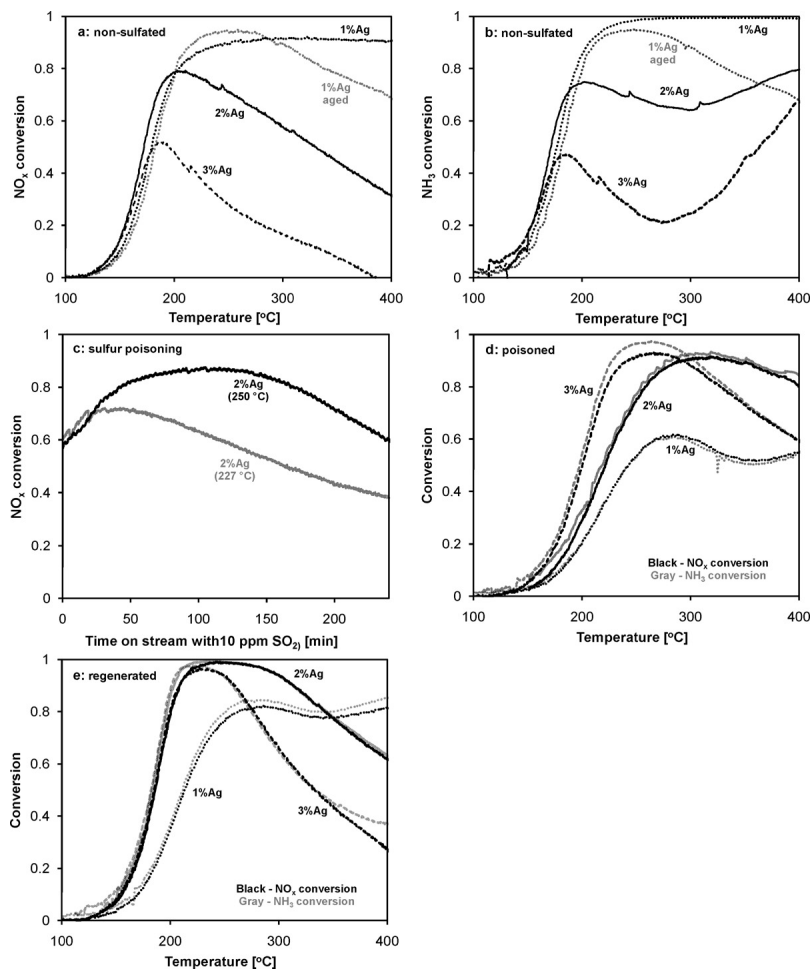


Figure 7.16: NO_x (a) and NH₃ (b) conversion profiles obtained over fresh 1–3%Ag/Al₂O₃ (black) and hydrothermally aged 1%Ag/Al₂O₃ (gray dotted) catalysts. (c) Evolution of NO_x conversion at 227 and 250 °C over 2%Ag/Al₂O₃ with 10 ppm SO₂ in the feed. (d) NO_x and NH₃ conversion profiles obtained over sulfur poisoned 1–3%Ag/Al₂O₃ catalysts. (e) NO_x and NH₃ conversion profiles obtained over 1–3%Ag/Al₂O₃ catalysts after 40 min. regeneration at 670 °C. Reaction conditions: 500 ppm NO, 520 ppm NH₃, 1200 ppm H₂, 8.3% O₂, 7% H₂O in Ar, GHSV = 110000 h⁻¹.

7.2.3 Experimental Results

Catalytic activity: the catalyst choice

The NO_x and NH₃ conversion profiles for 1-3% Ag/Al₂O₃ catalysts are shown in Figure 7.16(a) and (b). The NO_x conversion over 1% Ag/Al₂O₃ reaches ~50% at T= 130 °C (SCR onset), ~80% at T= 200 °C and ~90% at T > 300 °C. For the 2 and 3% Ag/Al₂O₃ SCR onset is shifted to lower temperature by 7 °C, and it means 2 and 3% Ag/Al₂O₃ have a lower light-off temperature (SCR onset) than 1% Ag/Al₂O₃ catalyst. However the maximum conversion for the 2 and 3% Ag/Al₂O₃ catalysts are only ~80% and ~50% respectively. Also for 2 and 3% Ag/Al₂O₃ catalysts show lower NO_x conversion at higher temperatures. Three possible reasons for the lower activity at high temperature can be: (a) at the high temperature NH₃ start to gets oxidized unselectively (can be seen in Figure 7.16) and NH₃ conversion is higher than NO_x conversion; (2) the direct oxidation of H₂ at high temperature. Without H₂, Ag/Al₂O₃ catalyst is almost inactive for the NO_x-SCR by NH₃. Though NH₃ play a role for the lower NO_x-SCR activity of 2 and 3% Ag/Al₂O₃, the main reason for lower NO_x conversion at at higher temperature is the direct oxidation of H₂; (3) another possible explanation can be lack of strong acid sites in 2 and 3% Ag/Al₂O₃ catalysts. The strong acid sites are important for NH₃ adsorption.²⁰⁶

To test the thermal stability, the catalysts are hydrothermally treated at 750 °C for 16 h. The NO_x and NH₃ conversion activity or the hydrothermally treated 1% Ag/Al₂O₃ catalyst is shown in Figure 7.16(a) and (b) in gray lines. Though the low temperature activity is only shifted by 3 °C, the gradual decrease in activity at high temperature (> 300 °C) is very prominent. The hydrothermally treated 1% Ag/Al₂O₃ following the NO_x conversion profile of 2 and 3% Ag/Al₂O₃ at higher temperature may suggest the sintering of Ag particles leading to larger size particles. The larger Ag particles prefer H₂ oxidation and hence give lower NO_x-SCR activity. Catalyst deactivation of 1- 3% Ag/Al₂O₃ were performed at 200 - 227 °C and following deactivation - regeneration of the 2% Ag/Al₂O₃ were performed at 240-250 °C. The deactivation test are performed with 10 ppm SO₂ in the SCR feed for 4 h. The NO_x-SCR performance of 1- 3% Ag/Al₂O₃ after the sulfur treatment are presented in Figure 7.16(d). 1% Ag/Al₂O₃ shows the highest deactivation. 2 and 3% Ag/Al₂O₃ catalysts show better NO_x conversion activity. Higher Ag loading gives better sulfur tolerance. 3% Ag/Al₂O₃ shows highest NO_x-SCR activity at lower temperature (T < 300 °C). The NO_x and NH₃ conversion profiles of all the three sulfated catalyst coincide. This suggest that sulfur treatment Ag/Al₂O₃ catalysts quench the NH₃ oxidation observed before in Figure 7.16(b) for 2 and 3% Ag/Al₂O₃. The light off temperature for the sulfated 2 and 3% Ag/Al₂O₃ catalysts are shifted to higher temperature. The temperature for maximum NO_x conversion also shifted to higher temperature. The maximum NO_x conversions get shifted to higher values, ~100% and ~90% for 3% Ag/Al₂O₃ and 2% Ag/Al₂O₃, respectively. We propose that SO_x blocks the sites active for NH₃ and H₂ oxidation and thus increase the activity for 2-3% Ag/Al₂O₃. In creases acidity of Ag/Al₂O₃ due to sulfating also helps the NH₃ adsorption and it also can play a role in the higher NO_x-SCR activity

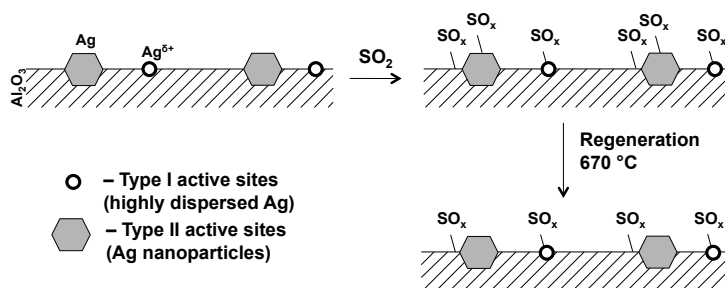


Figure 7.17: The scheme of Ag/Al₂O₃ sulfation and regeneration.

Regeneration for sulfated Ag/Al₂O₃ for NO_x-SCR by NH₃ without H₂ is ineffective. Regeneration is done at 670 °C under the H₂ assisted NO_x-SCR by NH₃ reaction condition. The activity of the regenerated samples are shown in Figure 7.16(e). All three catalysts regain their low temperature activity partially. Also the maximum conversion temperatures for the 2-3% Ag/Al₂O₃ are shifted to much lower temperatures (~200 °C) compared to the sulfated catalyst. The maximum conversion of the regenerated catalyst are higher than both the sulfated and parent untreated catalysts. However, the high temperature activity of the regenerated 3% Ag/Al₂O₃ catalyst is lower compared to the corresponding sulfated catalyst. The deactivated-regenerated 2% Ag/Al₂O₃ catalyst shows the best NO_x conversion activity for the whole low-temperature range (150-350 °C). Therefore 2% Ag/Al₂O₃ is our choice of catalyst for H₂ assisted NO_x-SCR by NH₃ and hereafter 2% Ag/Al₂O₃ will be referred as Ag/Al₂O₃.

Mechanism of sulfation and regeneration of Ag/Al₂O₃

During the sulfur poisoning experiments, small amount of SO_x is not desorbed after the regeneration cycle. The Ag/Al₂O₃ catalyst in the same time also losses some of its low temperature activity, which can not be regained even after treating the catalyst in a very rich environment. The SCR onset for the sulfated-regenerated catalysts are always shifted to higher temperatures. With these observed experimental facts, here we propose the presence of two kind of active sites in Ag/Al₂O₃ catalyst, 'Type I' sites – active for low temperature NO_x-SCR and 'Type II' sites – active for NO_x-SCR only at higher temperatures (see Figure 7.17).

These 'Type I' sites get blocked by SO_x and can not be regenerated using the standard regeneration technique. Hence the sulfated-regenerated Ag/Al₂O₃ catalyst lose the low temperature active partially. Considering the very low sulfur tolerance of the low-loaded Ag/Al₂O₃, we attribute 'Type I' active sites to the highly dispersed Ag (e.g. Ag^{δ+} atoms or Ag⁺ ions), shown in Figure 7.17.^{207,208} Adsorption of SO_x on these single Ag-atom sites or at the interface between these single Ag-atom sites and alumina support will block these highly active 'Type I' sites. Removal of SO_x from

‘Type I’ sites are not possible upto temperature 670 °C.²⁰⁹ These ‘Type I’ sites can not be regenerated with the commonly used regeneration techniques.

However as we were able to regenerate most of the high temperature NO_x-SCR activity of the Ag/Al₂O₃ catalyst, it also suggests the presence of another kind of active site, which can be regenerated by the regeneration technique used here. These active sites are attributed as ‘Type II’ sites (see in Figure 7.17). As these ‘Type II’ sites are more sulfur tolerant like the high loaded Ag/Al₂O₃ catalyst. These sites were attributed to the larger Ag nano-particles. It has been previously shown that SO₂ can be desorbed from Ag surface at around 600 °C.²⁰⁹ As these ‘Type II’ sites can be re-

Table 7.5: Adsorption energies* and desorption temperatures of SO_x for the most energetically favorable adsorption geometries in case of different adsorption sites.

<i>TypeII(metalic Ag)</i>			
Surface	Adsorbates	E _{ads} (eV)	T _{des} (K)
Ag{111}			
	SO ₂	Not adsorbed	-
	SO ₃	-1.61	390
	SO ₄	-2.65	454
Ag{211}			
	SO ₂	-0.26	81
	SO ₃	-1.82	458
	SO ₄	-2.97	597
<i>TypeI(dispersed Ag)</i>			
Surface	Adsorbates	E _{ads} (eV)	T _{des} (K)
γ-Al ₂ O ₃			
	SO ₂	-1.43	558
	SO ₃	-2.66	630
	SO ₄	-1.15	222
Ag built in γ-Al ₂ O ₃			
	SO ₂	-2.06	791
	SO ₃	-3.34	781
	SO ₄	-1.77	331
Ag on the step of γ-Al ₂ O ₃			
	SO ₂	-1.29	506
	SO ₃	-2.64	625
	SO ₄	-3.14	572

* Adsorption energies of the SO_x species are given with respect to SO₂ (g), O₂ (g) and H₂ (g).

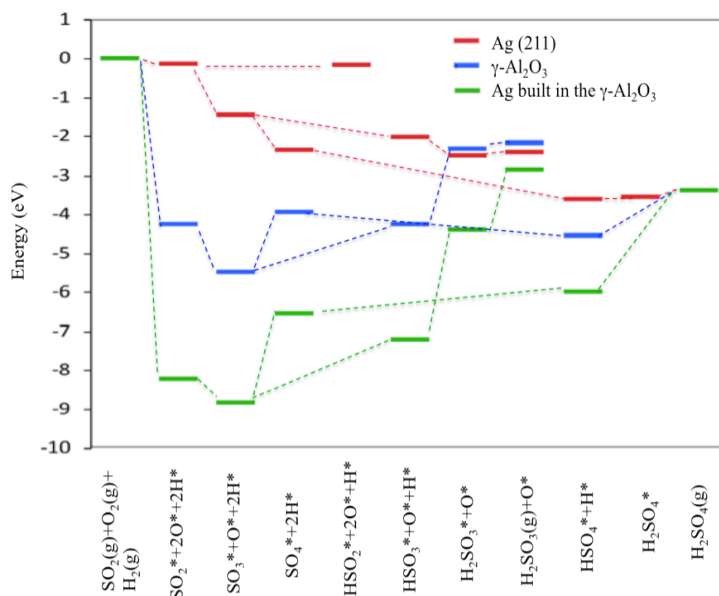


Figure 7.18: Potential energy diagram of SO_x and HSO_x formation over Ag/Al₂O₃ model surfaces.

generated, the NO_x-SCR activity can also be regained partially. In Figure 7.20(a) and (b) we have compared the NO_x-SCR catalytic activity profiles of fresh Ag/Al₂O₃ and sulfated-regenerated Ag/Al₂O₃ catalyst at (normal regeneration at 670 °C (normal regeneration) and 950 °C). It can also be seen that the sulfur treated and regenerated (at 670 °C) loses the low temperature activity as suggested previously due to the blocking of the 'Type I' sites. However one can regain most of the high temperature activity in the regenerated catalyst. Actually the NO_x conversion of the sulfated-regenerated catalyst is higher compared to the fresh catalyst due to quenching of the direct H₂ oxidation as explained before. When the sulfated Ag/Al₂O₃ catalyst is regenerated at 950 °C under the SCR condition, it regains the low temperature activity, shown in Figure 7.20(a). Also this high temperature (950 °C) regenerated catalyst produces much more NO₂ compared to the normally regenerated (at 670 °C) catalyst (see Figure 7.20(b)). The lower maximum of the NO_x conversion of this regenerated catalyst (regenerated at 950 °C) is possibly due to the sintering of the small Ag particles forming larger Ag nanoparticles.

SO_x also gets adsorbed irreversibly over the alumina support. But as the 'Fast-SCR' reaction can take place even on the sulfated alumina and oxidative activation of NO takes place over free Ag surface, SO_x adsorption over Al₂O₃ does not affect the NO_x-SCR activity.^{173,210}

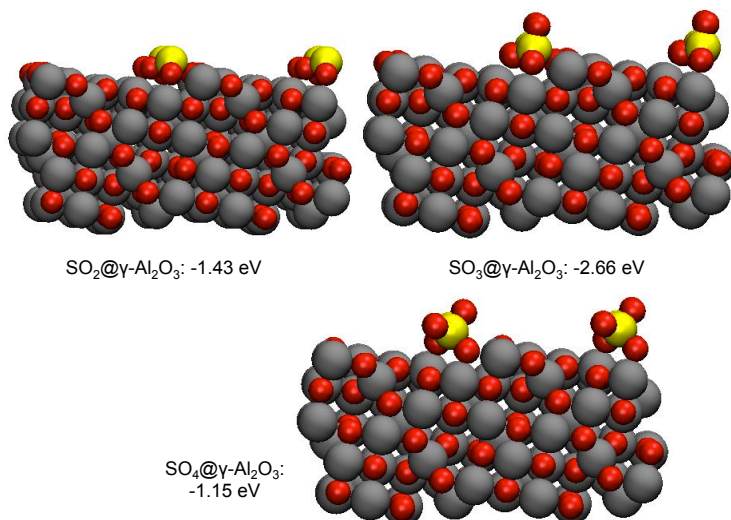


Figure 7.19: The most energetically favorable adsorption geometries for adsorption of SO₂, SO₃, and SO₄ on $\gamma\text{-Al}_2\text{O}_3$ model surface (with corresponding adsorption energies).

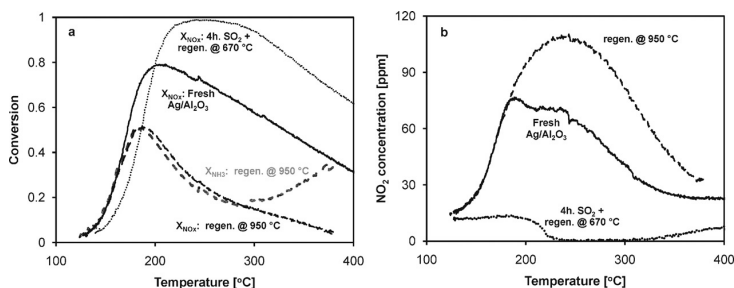


Figure 7.20: (a) NO_x conversion profiles obtained over fresh 2%Ag/Al₂O₃ (solid line), 2%Ag/Al₂O₃ after 4 h. with 10 ppm SO₂ at 240 °C, followed by 40 min. regeneration at 670 °C (dotted line) and after additional regeneration at 950 °C (dashed line). (b) Temperature dependence of NO₂ concentration at the reactor outlet obtained over fresh 2%Ag/Al₂O₃ (solid line), 2%Ag/Al₂O₃ after 4 h. with 10 ppm SO₂ at 240 °C, followed by 40 min. regeneration at 670 °C (dotted line) and after additional regeneration at 950 °C (dashed line). Reaction conditions: 500 ppm NO, 520 ppm NH₃, 1200 ppm H₂, 8.3% O₂, 7% H₂O in Ar, GHSV = 110000 h⁻¹.

7.2.4 Evaluation of the Proposed Sulfation and Regeneration Mechanism by DFT

The adsorption energies of the SO_x species (SO₂, SO₃ and SO₄) over the model surfaces (Ag{111}, Ag{211}, γ -Al₂O₃, Ag built in γ -Al₂O₃ and Ag on the step of γ -Al₂O₃) are given in Table 7.5. The corresponding geometries of SO_x adsorption on γ -Al₂O₃ are shown in Figure 7.19. SO_x species can adsorb on Ag and γ -Al₂O₃ in many different configurations. Only adsorption energies corresponding to the most stable configuration are given in Table 7.5. (see appendix A.5 for details on adsorption geometries of the SO_x adsorption on Ag built in γ -Al₂O₃ model surface)

All the SO_x species adsorb more strongly on the stepped Ag{211} surface compared to the flat Ag{111} surface. The SO_x species adsorb preferentially at the step site due to low coordination number and more steric freedom available at these step sites.^{48,54,58,211} The small Ag nanoparticles 1-3 nm contain many of these low coordinated step sites.⁵⁴⁻⁵⁷ Three main trends are observed in Table 7.5. First the alumina surface binds the SO_x species significantly stronger than the Ag metal surfaces. Secondly the adsorption of the SO_x species on the Ag atom built in γ -Al₂O₃ is significantly stronger than the Ag atom at the step of γ -Al₂O₃. Third global trend is that the oxidation of SO₂ to SO₃ is energetically favorable over all the model surfaces (see in Figure 7.18). These SO₃ blocks the active sites and deactivates the Ag/Al₂O₃ catalyst. SO₂ can not be adsorbed on the Ag metal surfaces. Hence under the NO_x-SCR reaction condition SO₂ can only poison (adsorbs on) the γ -Al₂O₃ surface or the single Ag atom site on γ -Al₂O₃ surface ('Type I' sites).

The desorption temperature for the SO_x species obtained from DFT calculations (given in Table 7.5) are significantly lower than the experimentally observed values.^{204,209} However the trends in the desorption temperatures of SO_x from the 'Type II' sites (Ag metal surface sites) and 'Type I' sites (highly dispersed single Ag atoms on γ -Al₂O₃ surface) are in agreement with the proposed sulfur poisoning and regeneration mechanism.

Table 7.6: Energies of HSO_x species in the gas phase and adsorbed on the most energetically favorable adsorption sites.

Energy* (eV)	HSO ₂	HSO ₃	H ₂ SO ₃	HSO ₄	H ₂ SO ₄
Gas phase	0.21	-0.75	-2.15	-1.48	-3.39
Adsorbed on γ -Al ₂ O ₃	Dissociates**	-2.84	-2.18	-3.16	Dissociates**
Adsorbed on Ag built in the γ -Al ₂ O ₃	Dissociates**	-4.10	-3.38	-3.61	Dissociates**
Adsorbed on Ag {211}	0.02	-2.56	-2.22	-3.94	-3.57

* Energy of the HSO_x species is given with respect to SO₂ (g), O₂ (g) and H₂ (g).

** Dissociates to H_{ad} + SO_x.

The promotional effect of H₂ in the regeneration step is also studied using DFT calculations. Hydrogen significantly enhances the catalyst regeneration by facilitating the SO_x removal through the formation of HSO_x species. The formation of the HSO_x species are avorable only on the Ag{211} facet, shown in Figure 7.18. The adsorption energies of HSO_x species with respect to the gas phase H₂SO₃ and H₂SO₄ are very small (given in Table 7.6) and can be easily desorbed. However the formation of the HSO_x species are not favorable on the γ -Al₂O₃ and Ag built in γ -Al₂O₃ sites. Thus the presence of H₂ in the feed have the promotional effect for the removal of SO_x species only from the Ag{211} surface but not γ -Al₂O₃ and Ag built in γ -Al₂O₃ surfaces.

7.3 Summary

In this chapter, I have presented a detail analysis of the H_2 assisted NO_x -SCR by NH_3 over $\text{Ag}/\text{Al}_2\text{O}_3$ catalyst using both experimental and theoretical techniques. The unique low temperature activity of $\text{Ag}/\text{Al}_2\text{O}_3$ for the H_2 assisted NO_x -SCR by NH_3 is presented here. Both the metal catalyst (Ag) and support (Al_2O_3) are important for the high activity of $\text{Ag}/\text{Al}_2\text{O}_3$ catalyst and change of any of these two component leads to a nearly inactive NO_x -SCR catalyst. TEM data presented here shows highly dispersed Ag metal particles over the Al_2O_3 support. A mechanistic study for the H_2 assisted NO_x -SCR by NH_3 over $\text{Ag}/\text{Al}_2\text{O}_3$ and pure Al_2O_3 is carried out to obtain valuable insight of the reaction mechanism. The influence of each individual gas component in the reaction gas feed is tested and discussed. Through the mechanistic study, it is found that the H_2 assisted NO_x -SCR by NH_3 over $\text{Ag}/\text{Al}_2\text{O}_3$ involves the 'Fast-SCR' reaction pathway. Both the $\text{Ag}/\text{Al}_2\text{O}_3$ and pure Al_2O_3 can participate in the reaction. Ag is important for the oxidative activation of NO_x , suggested to be important for low-temperature NO_x -SCR activity. DFT calculations are performed to evaluate the proposed H_2 assisted NO_x -SCR by NH_3 . A complete reaction mechanism may involve as much as fifty stable intermediates. Among them only a few have been studied in details. The scaling relations found for those important adsorbates will be used in future to model the NO_x -SCR reaction. The adsorption and transition states energies of NO_2 , N_2O and NO_3 are calculated over the transition metal surfaces. These adsorption and transition state energies are coupled with a microkinetic model to obtain the NO oxidation activity for the transition metals. It is found that in the low temperature region, Ag is the best NO_2 formation catalyst, in agreement to our proposed reaction mechanism. It is found that Ag metal is also good for direct H_2 oxidation, as suggested before for the cause of low activity of the catalyst with higher Ag loadings. From the DFT calculation it is found that the formation of both NO_2 and NO_3 are favorable over both $\text{Ag}\{111\}$ and $\{211\}$ surfaces. NO_3^* binds strongly to both Ag and Al_2O_3 surfaces and can poison the surface. H_2 helps to remove the NO_3^* from Ag and Al_2O_3 surface through the formation of HNO_3 , which can be easily desorbed.

A detailed study and analysis is also carried out for the sulfur poisoning and regeneration of $\text{Ag}/\text{Al}_2\text{O}_3$ during the NO_x -SCR cycle. The deactivated-regenerated 2% $\text{Ag}/\text{Al}_2\text{O}_3$ catalyst showed the best NO_x conversion activity over the whole temperature range 150-350 °C. A simple mechanism for sulfur poisoning and corresponding regeneration of catalyst is also suggested. The presence of two type of active sites 'Type I' (highly dispersed Ag) and 'Type II' (metallic Ag) sites is proposed. The 'Type I' sites are important for low temperature NO_x -SCR activity. These sites gets blocked irreversibly by SO_x species and can not be regenerated under normal regeneration procedure and hence the sulfated catalyst lose some of its low temperature activity. Interestingly the sulfated catalyst shows higher maximum NO_x conversion activity, believed to be due to significant decrease in the unselective H_2 and NH_3 oxidation. DFT calculation of the SO_x adsorption is carried out over model Ag , pure Al_2O_3 and $\text{Ag}/\text{Al}_2\text{O}_3$ surfaces. DFT calculation gives the right trends for the desorption temperature of SO_x species from the Type I' and 'Type II' sites as proposed in

the mechanism. DFT calculation also backed the claim that SO₃ is the main poisoning species among the SO_x. The presence of H₂ helps the regeneration of the Ag/Al₂O₃ catalyst. This is also evaluated using the DFT calculations. DFT calculation shows that the adsorbed SO_x species in presence of H₂ are converted to HSO_x species and can be easily desorbed from the catalyst as H₂SO₃(g) or H₂SO₄(g).

These important insight of the H₂ assisted NO_x SCR by NH₃ and sulfur poisoning mechanism will immensely help us developing active and stable NO_x-SCR catalyst in future.

Summary and Outlook

In this present work I have tried to develop new methods to overcome two major shortcomings of the approach of using DFT for catalytic modeling. Using DFT to obtain the shape and total catalytic rate of a nanoparticle under the reaction condition has always been a challenge.

First, I have presented the work on the structure sensitivity of the low-index transition metal facets for the direct NO decomposition. I showed that the shift in the BEP scaling lines from the closed packed $\{111\}$ facet to the other more open facets is due to both electronic and geometric effects. The BEP relations and the adsorption energy scaling relations are used with the micro kinetic model to obtain the catalytic activity of the different transition metal surfaces. The catalytic activity increases going from $\{111\} \rightarrow \{211\} \sim \{311\} \rightarrow \{532\} \sim \{100\} \rightarrow \{110\}$. For most of the low-index facets Pd metal shows the highest activity. The direct NO decomposition catalytic rate over the Pd $\{110\}$ surface is $\sim 1\text{s}^{-1}$. In future I will extend this work to obtain the structure of the nanoparticle under the reaction condition and also to calculate the catalytic rate.

In the ‘in-silico’ search of catalyst with high reactivity, selectivity and stability two things are very important:

- (a) use of correct mechanism for the reaction, and
- (b) using the microkinetic model to describe the kinetics and thermodynamics of the reaction steps correctly.

In order to improve upon the previous non-interacting mean field approach for adsorption energy, in this thesis I have proposed a newly parametrized adsorbate-adsorbate interaction model to include the coverage dependent adsorption energy directly into

our micro kinetic model. The adsorbate-adsorbate interaction model is then applied to one model catalyst and two important industrial catalytic processes to show the significance of including the adsorbate-adsorbate interaction in micro kinetic modeling. Successful inclusion of the adsorbate-adsorbate interaction in our microkinetic model will help us to obtain catalytic rates and trends with higher accuracy, which is very important for catalyst screening. I also have presented a very efficient catalyst screening method based on predicted rate, stability and cost. The method is used for steam reforming of methane to screen industrially promising metal alloy catalyst for the reaction. Among the metal alloys Ni, Co and Fe binary alloys (in A_3B composition) are found to be the best alloy catalyst for steam reforming of methane.

In the last two chapters two environmental catalysis process of immense importance are studied in detail. NH_3 and NO_x are very potent pollutants and causes environmental and health hazards. Cleaning of NH_3 and NO_x from their source is very important and challenging. Here I have combined the DFT calculated adsorption and transition state energies with the microkinetic model to describe the catalytic activity and selectivity trends of the transition metal catalyst for these two important reaction.

Selective oxidation of NH_3 is a very efficient process for removing NH_3 even at ppm level. In this thesis I have studied the NH_3 oxidation both in presence and absence of H_2 . DFT calculated adsorption and transition state energies are coupled with the micro kinetic model to obtain the catalytic activity and selectivity of the transition metals for the reaction. The O-assisted NH_3 dehydrogenation pathway is found to be the main reaction pathway for the NH_3 oxidation over transition metals. Pd shows the best NH_3 oxidation activity among the transition metals, closely followed by Pt and Ag (at 400 °C). However for the NH_3 oxidation in presence of H_2 , we are mainly interested about the N_2 selectivity. Among the transition metals Ni, Co and Ru showed moderate selectivity for the NH_3 oxidation process in presence of H_2 (at 750 °C).

A mechanistic study of the H_2 assisted selective catalytic reduction of NH_3 over Ag/ Al_2O_3 is performed using both experimental and theoretical techniques. Ag/ Al_2O_3 shows unique activity for the hydrogen assisted NO_x -SCR by NH_3 with light-off temperature at $\sim 150^\circ C$ and nearly 90% conversion at 200 °C. We found that the H_2 assisted NO_x -SCR by NH_3 also follows the 'Fast-SCR' mechanism and both Ag and Al_2O_3 can take part in the reaction. Ag is important for the oxidative activation of NO, important for low temperature NO_x -SCR activity. Sulfur poisoning and regeneration of Ag/ Al_2O_3 is also studied here. Sulfated-regenerated 2% Ag/ Al_2O_3 shows the best activity and hence is suggested as the catalyst of choice. A simple sulfur poisoning and regeneration mechanism is also proposed, where the presence of two different active sites on Ag/ Al_2O_3 is suggested. DFT calculations are used to evaluate the proposed H_2 assisted NO_x -SCR by NH_3 and sulfur poisoning and regeneration mechanisms. The promotional effect of H_2 on both the catalytic activity and regeneration are also proved using the DFT calculations. The selective NH_3 oxidation and H_2 assisted NO_x -SCR by NH_3 are still very much two ongoing projects with strong experimental and theoretical collaborations.

In summery, I have shown that the DFT calculated adsorption and transition state

energies can be successfully coupled with a microkinetic model to obtain the trends for catalytic rates and selectivity. The catalytic methods and mechanisms developed in the thesis will give us better understanding and higher capability in developing highly reactive, selective and stable future industrial and environmental catalysts.

APPENDIX A

Appendix

A.1 Adsorption Sites of O, N and NO over Low-index Facets.

Table A.1: Oxygen(O) adsorption sites over low-index facets.

	{111}	{110}	{211}	{311}	{532}	{100}
Ag	h(fcc)	h	h (b)	h	h (b)	h
Au	h(fcc)	h	step	step	h (b)	h
Co	h (fcc)	step	h (a)	h	h (a)	h
Cu	h (fcc)	h	h (a)	h	h (a)	h
Ni	h (fcc)	h	h (a)	h	h (b)	h
Pd	h (fcc)	h	h (a)	H	h (b)	h
Pt	h (fcc)	step	step	step	step	bridge
Re	h (hcp)	step	h (a)	step	step	bridge
Rh	h (fcc)	step	step	step	step	h
Ru	h (hcp)	step	step	step	step	h

Table A.2: Nitrogen(N) adsorption sites over low-index facets.

	{111}	{110}	{211}	{311}	{532}	{100}
Ag	h (fcc)	5-fold	5-fold	5-fold	5-fold	h
Au	h (fcc)	step	h(a)	h	h(b)	h
Co	h (fcc)	4-fold	5-fold	5-fold	5-fold	h
Cu	h (fcc)	5-fold	5-fold	5-fold	5-fold	h
Ni	h (fcc)	4-fold	h (a)	5-fold	4-fold	h
Pd	h (fcc)	4-fold	h (a)	h	4-fold	h
Pt	h (fcc)	step	h(a)	h	h(b)	h
Re	h (hcp)	step	h (a)	h	h(a)	h
Rh	h (hcp)	step	h(a)	h	h(a)	h
Ru	h (hcp)	4-fold	h(a)	h	h(a)	h

Table A.3: Nitrogen Oxide (O) adsorption sites over low-index facets

	{111}	{110}	{211}	{311}	{532}	{100}
Ag	h (fcc)	step	step	step	step	h
Au	top	step	step	step	step	bridge
Co	h (hcp)	step	h (a)	step	step	bridge
Cu	h (fcc)	step	step	step	step	h
Ni	h (fcc)	step	step	step	step	h
Pd	h (fcc)	step	h (a)	step	h(a)	h
Pt	h (fcc)	step	step	step	step	bridge
Re	top	step	step	4-fold	h(a)	bridge
Rh	h (hcp)	step	step	step	step	bridge
Ru	h (hcp)	step	step	step	step	bridge

A.2 Interaction Matrix for Rh{111}

ϵ_{ij}	H	C	N	O	S	CH	NH	NO	OH	SH	CO	N ₂	N ₂ O	CH ₂	NH ₂
H	0.10														
C	0.83	3.78													
N	0.85	4.05	3.29												
O	0.62	3.22	2.50	2.05											
S	1.03	4.18	3.91	3.83	5.23										
CH	0.44	2.99	2.48	1.87	3.36	1.38									
NH	0.84	2.93	2.11	1.84	3.70	2.09	2.63								
NO	0.37	2.91	2.41	1.87	4.41	1.77	1.64	2.02							
OH	0.24	2.16	1.85	1.89	2.47	1.62	1.21	2.02	1.21						
SH	0.60	*	2.36	2.13	*	2.31	2.14	3.82	*	6.69					
CO	0.33	4.72	2.13	1.77	3.30	1.30	1.19	2.11	1.60	3.13	2.53				
N ₂	1.03	4.51	4.34	3.12	*	5.79	4.42	2.72	0.93	4.36	2.37	2.24			
N ₂ O	0.99	4.07	3.94	2.69	*	*	4.12	2.54	0.62	4.31	1.86	2.03	3.22		
CH ₂	0.72	2.96	2.52	1.95	4.54	2.35	2.40	2.45	2.23	*	2.31	3.80	*	3.76	
NH ₂	0.47	2.58	2.08	2.01	4.74	2.44	2.94	2.09	1.13	*	1.67	3.23	*	3.34	3.79

Table A.4: Interaction matrix table with the interaction parameters (ϵ_{ij}) of H, C, N, O, S, CH, NH, NO, OH, SH, CO, N₂, N₂O, CH₂ and NH₂ on Rh{111}.

* the adsorption at $\frac{1}{2} + \frac{1}{2}$ ML coverage is not stable.

Table A.5: Interaction parameters of FCC {111} surfaces and d-band center of the metal surfaces. The scaling parameters of the correlation between the interaction parameters and d-band center of the metal surfaces are also given.

Metals	ϵ_d	ϵ_{C-C}	ϵ_{N-N}	ϵ_{O-O}	ϵ_{NO-NO}	ϵ_{S-S}	ϵ_{NH-NH}	ϵ_{CH-CH}
Ru{111}	-1.18	2.86	2.48	1.78	1.3	5.01	2.24	0.81
Re{111}	-1.01	2.66	1.9	0.46	1.19	4.25	0.56	0.5
Pt{111}	-1.67	4.82	3.04	2.6	2.85	5.41	4.32	2.46
Rh{111}	-1.35	3.78	3.29	2.05	2.02	5.23	2.63	1.38
slope		-3.47	-1.75	-2.95	-2.67	-1.55	-5.35	-3.05
intercept		-0.99	0.4	-2.12	-1.64	2.99	-4.53	-2.68
R ²		0.97	0.63	0.84	0.96	0.72	0.96	0.99

Table A.6: DFT-calculated energies of the CO methanation transition states on metal surfaces (relative to CO, H₂O, and H₂ in the gas phase) scaled versus the dissociated products of those reactions. Transition states for the C-O-H reaction were calculated at high (1.0 monolayer) and low (0.25 monolayer) coverages of CO. Energies are from this work

Metal(211)	C-O-H ^{*_s} _{High}	C-O-H ^{*_s} _{Low}	O-H-OH ^{*_s}
Ag	2.687	3.644	1.861
Cu	0.770	1.837	0.924
Pd	-0.552	0.586	1.829
Pt	0.079	0.669	1.557
Rh	-0.908	0.097	0.454
Au			2.903
Ni			0.325
Ir			0.37
Ru			-0.102
Slope	0.806	0.802	0.887
Intercept	0.328	1.280	1.094

Table A.7: DFT calculated energies of CH₃* adsorption (per adsorbate) on Metal(111) surfaces at various coverages. Self-interaction parameter is calculated from the slope of the adsorption energies versus the coverage from 0.25 - 1.00 ML.

Coverage (ML)	Pd	Pt	Rh	Ru
0.25	-1.310	-1.591	-1.404	-1.691
0.50	-1.056	-1.275	-1.117	-1.470
Slope	1.019	1.263	1.148	0.886

A.3 CO Methanation

Table A.8: DFT calculated energies of CH_2^* adsorption (per adsorbate) on Metal(111) surfaces at various coverages. Self-interaction parameter is calculated from the slope of the adsorption energies versus the coverage from 0.25 - 0.50 ML.

Coverage (ML)	Pd	Pt	Rh	Ru
0.25	-3.159	-3.443	-3.562	-3.801
0.50	-2.859	-3.189		
1.00			-2.154	-2.652
Slope	1.201	1.018	1.877	1.532

Table A.9: DFT calculated energies of CH^* adsorption (per adsorbate) on Metal(211) surfaces at various coverages. Self-interaction parameter is calculated from the slope of the adsorption energies versus the coverage from 0.50 - 1.00 ML.

Coverage (ML)	Pd	Pt	Rh	Ru
0.25	-1.279	-1.198	-1.791	-2.109
0.33	-1.288	-1.216	-1.805	-2.09
0.50	-1.356	-1.207	-1.82	-2.077
0.67	-1.141	-1.107	-1.688	-2.019
0.75	-1.048	-1.085	-1.628	-1.991
1.00	-0.88	-0.835	-1.532	-1.87
Slope	0.94	0.75	0.57	0.42

Table A.10: DFT calculated energies of C^* adsorption (per adsorbate) on Metal(211) surfaces at various coverages. Self-interaction parameter is calculated from the slope of the adsorption energies versus the coverage from 0.50 - 1.00 ML.

Coverage (ML)	Pd	Pt	Rh	Ru
0.25	-1.317	-0.809	-1.51	-1.7
0.33	-1.334	-0.836	-1.52	-1.645
0.50	-1.418	-0.826	-1.544	-1.581
0.67	-1.129	-0.674	-1.37	-1.453
0.75	-1	-0.442	-1.313	-1.395
1.00	-0.739	-0.43	-1.219	-1.254
Slope	1.34	0.81	0.63	0.65

Table A.11: DFT calculated energies of CO* adsorption (per adsorbate) on Metal(211) surfaces at various coverages. Self-interaction parameter is calculated from the slope of the adsorption energies versus the coverage from 0.50 - 1.00 ML.

Coverage (ML)	Pd	Pt	Rh	Ru
0.25	-1.732	-1.857	-1.921	-1.97
0.33	-1.706	-1.87	-1.916	-1.971
0.50	-1.753	-1.833	-1.937	-1.96
0.67	-1.579	-1.747	-1.916	-1.956
0.75	-1.489	-1.732	-1.887	-1.917
1.00	-1.417	-1.571	-1.854	-1.861
Slope	0.66	0.52	0.17	0.21

Table A.12: DFT calculated energies of OH* adsorption (per adsorbate) on Metal(211) surfaces at various coverages. Self-interaction parameter is calculated from the slope of the adsorption energies versus the coverage from 0.50 - 1.00 ML.

Coverage (ML)	Pd	Pt	Rh	Ru
0.25	0.395	0.343	-0.348	-0.675
0.33	0.42	0.325	-0.366	-0.667
0.50	0.34	0.394	-0.35	-0.617
0.67	0.547	0.488	-0.21	-0.531
0.75	0.609	0.585	-0.147	-0.486
1.00	0.773	0.797	-0.078	-0.366
Slope	0.85	0.82	0.53	0.5

Table A.13: DFT calculated energies of O* adsorption (per adsorbate) on Metal(211) surfaces at various coverages. Self-interaction parameter is calculated from the slope of the adsorption energies versus the coverage from 0.50 - 1.00 ML.

Coverage (ML)	Pd	Pt	Rh	Ru
0.25	1.664	1.24	0.181	-0.109
0.33	1.701	1.206	0.181	-0.111
0.50	1.655	1.27	0.166	-0.19
0.67	1.872	1.465	0.41	0.086
0.75	1.954	1.556	0.527	0.156
1.00	2.119	1.73	0.735	0.338
Slope	0.91	0.91	1.13	1.02

Table A.14: DFT calculated energies of H* adsorption (per adsorbate) on Metal(211) surfaces at various coverages. Self-interaction parameter is calculated from the slope of the adsorption energies versus the coverage from 0.50 - 1.00 ML.

Coverage (ML)	Pd	Pt	Rh	Ru
0.25	-0.425	-0.23	-0.263	-0.493
0.50	-0.38	-0.177	-0.251	-0.417
0.75	-0.399	-0.183	-0.279	-0.387
1.00	-0.403	-0.185	-0.286	-0.357
Slope	0.019	0.051	-0.039	0.176

Table A.15: Modified matrix of calculated interaction parameters for the stepped (211) surface of Ru. This matrix was used specifically to calculate interaction effects for the C-O-H reaction. Since the transition state calculations for that reaction were calculated with a high (1 monolayer coverage) of CO, the matrix was modified to prevent the double counting of the interactions of CO* with itself and other adsorbates. Self-interaction parameters (e.g., $\epsilon_{\text{CO-CO}}$) were calculated from the scaling parameters listed in Table 5.3. Unless otherwise indicated, cross-interaction parameters were calculated from the geometric average of the two interacting adsorbates.

ϵ_{i-j} i	j	CH ₃ ^{*t}	CH ₂ ^{*t}	CH ^{*f}	C ^{*f}	CO ^{*s}	OH ^{*s}	O ^{*s}	H ^{*h}
		0.905	1.987	0.323	0.478	0.007	0.358	1.149	0 ^a
CH ₃ ^{*t}	0.905	0.905	1.341	0 ^b	0 ^b	0 ^b	0 ^b	0 ^b	0 ^a
CH ₂ ^{*t}	1.987	1.341	1.987	0 ^b	0 ^b	0 ^b	0 ^b	0 ^b	0 ^a
CH ^{*f}	0.323	0 ^b	0 ^b	0.323	0.392	0 ^c	0.34	0.609	0 ^a
C ^{*f}	0.478	0 ^b	0 ^b	0.392	0.478	0 ^c	0.413	0.741	0 ^a
CO ^{*s}	0.007	0 ^b	0 ^b	0.049	0.06	0 ^d	0.044 ^d	0.085 ^d	0 ^a
OH ^{*s}	0.358	0 ^b	0 ^b	0.34	0.413	0.044 ^d	0.35 ^d	0.633 ^d	0 ^a
O ^{*s}	1.149	0 ^b	0 ^b	0.609	0.741	0.085 ^d	0.633 ^d	1.142 ^d	0 ^a
H ^{*h}	0 ^a	0 ^a	0 ^a	0 ^a	0 ^a	0 ^a	0 ^a	0 ^a	0 ^a

^a Interactions between adsorbed hydrogen and other reaction intermediates is negligible, as discussed in the paper.

^b Adsorbate-adsorbate interactions between reaction intermediates on the terrace (e.g., CH₃ and CH₂) and the four-fold/on-top sites are assumed to be zero.

^c Interactions between CO* on the on-top site and adsorbates on the fourfold site (e.g., C* and CH*) were included in the transition state calculations, so they are specifically excluded here to prevent double counting.

^d Interactions between CO* with itself (CO-CO interactions) and other on-top adsorbates (OH* and O*) were included in the transition state calculations, so they are subtracted from these interaction parameters to prevent double counting.

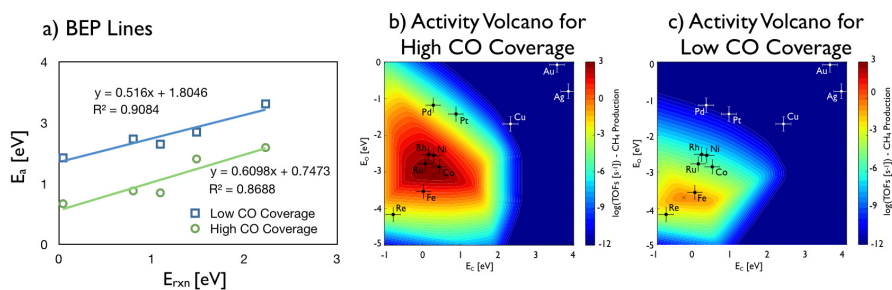


Figure A.1: a) Brønsted-Evans-Polanyi relations between the C-O-H activation barrier versus the Gibbs free energy of reaction for low (0.25 monolayer) and high (1.0 monolayer) coverages of CO on the stepped (211) surfaces of Cu, Pd, Pt, and Rh. All energies are relative to CO and H₂ in the gas phase. Activity volcanos for the b) high and c) low coverage regimes are also given for 523 K and 1 bar with a gas composition of 1% CO, 97% H₂, 1% CH₄, and 1% H₂O, corresponding to 10⁻⁹ % approach to equilibrium.

Table A.16: DFT-calculated energies for the adsorption of steam reforming intermediates on metal surfaces (relative to CH_4 , H_2O and H_2 in the gas phase) scaled versus the carbon binding energies of those metals (relative to methane). Energies for other intermediates are taken from Ref. [?].

Metal(211)	HCO^{*t}	COH^{*s}
Ag	3.2	4.58
Cu	2.74	3.56
Pd	1.83	1.89
Pt	1.77	1.90
Rh	1.81	1.93
Au	2.87	
Slope	0.378	0.775
Interception	1.204	0.645

Table A.17: DFT-calculated energies for the adsorption of methane steam reforming transition states on metal surfaces (relative to CH_4 , H_2O , and H_2 in the gas phase, eV) scaled versus the dissociated products of those reactions. Other transition states energies are taken from Ref. [?].

Metal(211)	C-OH^{*f}	CO-H^{*s}	HC-O^{*f}	H-CO^{*s}
Ag	5.55	5.35	6.98	3.68
Cu	5.24	4.3	5.06	3.09
Pd	3.5	2.59	4.67	1.95
Pt	4.46	2.5	4.77	1.83
Rh	3.09	2.93	3.34	1.8
Ru	3.04			
Slope	0.571	1.067	0.757	0.747
Interception	2.647	1.94	2.494	1.353

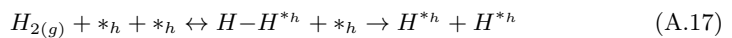
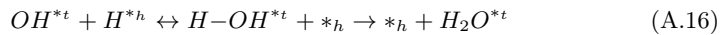
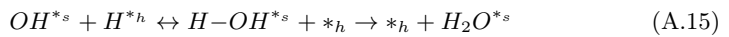
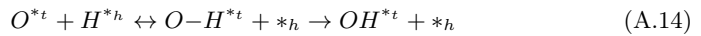
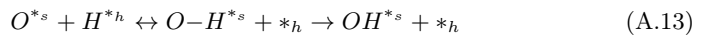
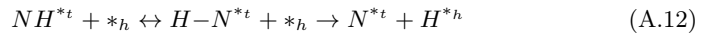
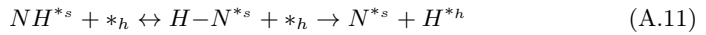
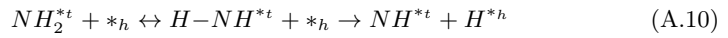
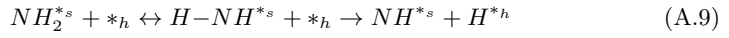
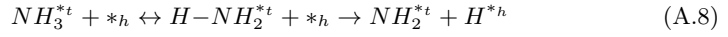
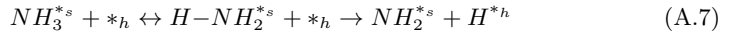
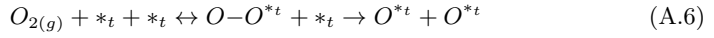
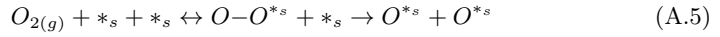
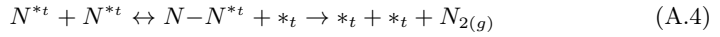
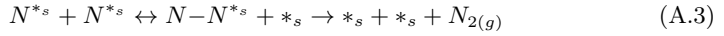
A.4 Steam Refoming of Methane

Table A.18: Prices for the pure metals, values taken from Chemicool website¹⁵⁰.

Metal	Price (\$/kg)	Metal	Price (\$/kg)	Metal	Price (\$/kg)
Sc	14000	W	110	Pt	130000
Y	4300	Mn	65	Cu	97
La	8000	Re	16000	Ag	1200
Ti	6610	Fe	72	Au	55400
Zr	1570	Ru	14000	Zn	53
Hf	1200	Os	77000	Cd	460
V	2200	Co	210	Hg	480
Nb	180	Rh	130000	Ga	2200
Ta	4500	Ir	42000	In	9680
Cr	3800	Ni	77	Tl	480
Mo	440	Pd	58330	Al	157
Sn	240	As	3200	Bi	39
Pb	24.5	Sb	45	Ge	3600
Si	54				

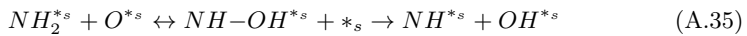
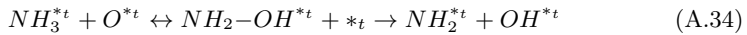
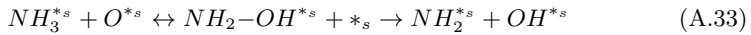
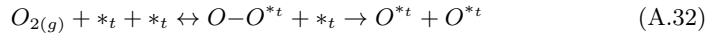
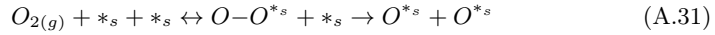
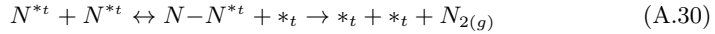
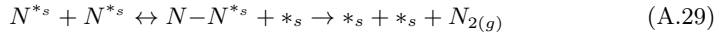
A.5 NH₃ Oxidation over Transition Metal Surfaces

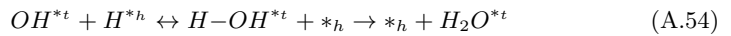
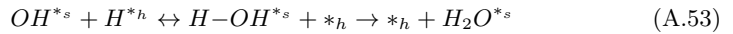
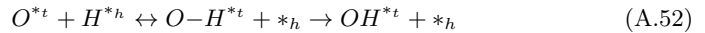
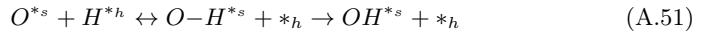
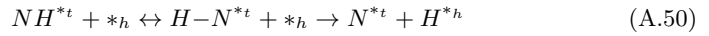
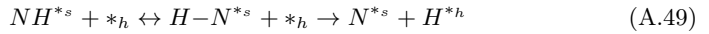
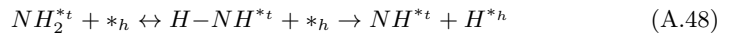
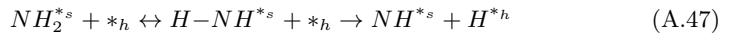
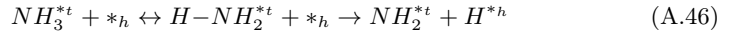
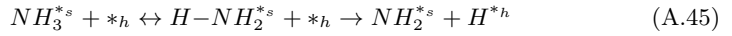
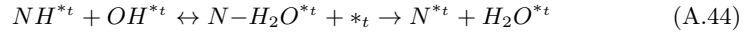
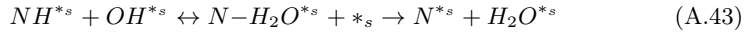
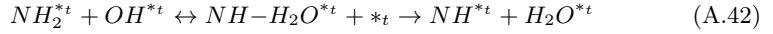
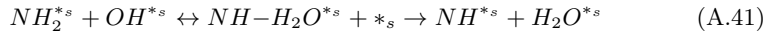
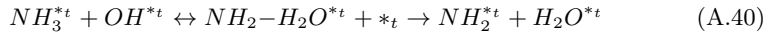
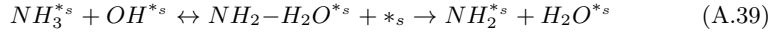
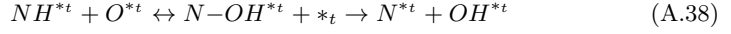
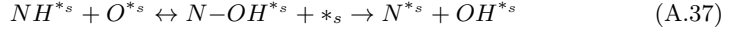
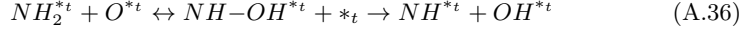
Direct NH₃ dehydrogenation





O assisted NH₃ dehydrogenation with H reservoir





$$OH^{*s} + OH^{*s} \leftrightarrow O-H_2O^{*s} + *s \rightarrow O^{*s} + H_2O^{*s} \quad (A.55)$$

$$OH^{*t} + OH^{*t} \leftrightarrow O-H_2O^{*t} + *t \rightarrow O^{*t} + H_2O^{*t} \quad (A.56)$$

$$H_{2(g)} + *h + *h \leftrightarrow H-H^{*h} + *h \rightarrow H^{*h} + H^{*h} \quad (A.57)$$

$$H_2O^{*s} \leftrightarrow H_2O_{(g)} + *s \quad (A.58)$$

$$H_2O^{*t} \leftrightarrow H_2O_{(g)} + *t \quad (A.59)$$

$$N^{*t} + *s \leftrightarrow N^{*s} + *t \quad (A.60)$$

$$NH^{*t} + *s \leftrightarrow NH^{*s} + *t \quad (A.61)$$

$$NH_2^{*t} + *s \leftrightarrow NH_2^{*s} + *t \quad (A.62)$$

$$NH_3^{*t} + *s \leftrightarrow NH_3^{*s} + *t \quad (A.63)$$

$$O^{*t} + *s \leftrightarrow O^{*s} + *t \quad (A.64)$$

$$OH^{*t} + *s \leftrightarrow OH^{*s} + *t \quad (A.65)$$

$$H_2O^{*t} + *s \leftrightarrow H_2O^{*s} + *t \quad (A.66)$$

Adsorption and transition state energy scaling

Adsorption Scaling Parameters

$$E_{NH_3^{*s}} = 0.155E_{N^{*s}} - 0.874 \quad (A.67)$$

$$E_{NH_3^{*t}} = 0.146E_{N^{*s}} - 0.668 \quad (A.68)$$

$$E_{NH_2^{*s}} = 0.408E_{N^{*s}} - 0.951 \quad (A.69)$$

$$E_{H^{*s}} = 0.19E_{N^{*s}} - 0.605 \quad (A.70)$$

$$E_{NH_2^{*t}} = 0.308E_{N^{*s}} - 0.054 \quad (A.71)$$

$$E_{H^*t} = 0.159E_{N^*s} - 0.482 \quad (\text{A.72})$$

$$E_{NH^*s} = 0.695E_{N^*s} - 0.313 \quad (\text{A.73})$$

$$E_{NH^*t} = 0.542E_{N^*s} + 0.092 \quad (\text{A.74})$$

$$E_{N^*t} = 0.934E_{N^*s} + 0.285 \quad (\text{A.75})$$

$$E_{O^*t} = 0.912E_{O^*s} + 0.211 \quad (\text{A.76})$$

$$E_{OH^*s} = 0.56E_{O^*s} - 0.552 \quad (\text{A.77})$$

$$E_{OH^*t} = 0.389E_{O^*s} + 0.194 \quad (\text{A.78})$$

$$E_{H_2O^*s} = 0.005E_{N^*s} + 0.129E_{O^*s} - 0.381 \quad (\text{A.79})$$

$$E_{H_2O^*t} = 0.028E_{N^*s} - 0.124 \quad (\text{A.80})$$

Transition-state Scaling Parameters

$$E_{H-NH_2^*s} = 0.456E_{N^*s} + 0.293 \quad (\text{A.81})$$

$$E_{H-NH_2^*t} = 0.339E_{N^*s} + 0.576 \quad (\text{A.82})$$

$$E_{H-NH^*s} = 0.693E_{N^*s} + 0.669 \quad (\text{A.83})$$

$$E_{H-NH^*t} = 0.622E_{N^*s} + 0.879 \quad (\text{A.84})$$

$$E_{H-N^*s} = 1.125E_{N^*s} + 0.812 \quad (\text{A.85})$$

$$E_{H-N^*t} = 0.844E_{N^*s} + 1.69 \quad (\text{A.86})$$

$$E_{N-N^*s} = 1.627E_{N^*s} + 2.112 \quad (\text{A.87})$$

$$E_{N-N^*t} = 1.458E_{N^*s} + 3.173 \quad (\text{A.88})$$

$$E_{O-O^*s} = 1.105E_{O^*s} + 3.151 \quad (\text{A.89})$$

$$E_{O-O^*t} = 1.347E_{O^*s} + 3.429 \quad (\text{A.90})$$

$$E_{O-H^*s} = 0.391E_{N^*s} + 0.505E_{O^*s} + 0.282 \quad (\text{A.91})$$

$$E_{O-H^*t} = 0.268E_{N^*s} + 0.469E_{O^*s} + 1.081 \quad (\text{A.92})$$

$$E_{H-OH^*s} = 0.236E_{N^*s} + 0.253E_{O^*s} + 0.076 \quad (\text{A.93})$$

$$E_{H-OH^*t} = 0.293E_{N^*s} + 0.68 \quad (\text{A.94})$$

$$E_{H-H^*s} = 0.353E_{N^*s} - 0.328 \quad (\text{A.95})$$

$$E_{H-H^*t} = 0.439E_{N^*s} - 0.492 \quad (\text{A.96})$$

$$E_{NH_2-OH^*s} = 0.951(E_{NH_2^*s} + E_{OH^*s}) + 0.94 \quad (\text{A.97})$$

$$E_{NH_2-OH^*t} = 0.773(E_{NH_2^*t} + E_{OH^*t}) + 0.531 \quad (\text{A.98})$$

$$E_{NH-OH^*s} = 0.949(E_{NH^*s} + E_{OH^*s}) + 1.404 \quad (\text{A.99})$$

$$E_{NH-OH^*t} = 0.964(E_{NH^*t} + E_{OH^*t}) + 1.042 \quad (\text{A.100})$$

$$E_{N-OH^*s} = 1.016(E_{N^*s} + E_{OH^*s}) + 1.156 \quad (\text{A.101})$$

$$E_{N-OH^*t} = 1.102(E_{N^*t} + E_{OH^*t}) + 0.803 \quad (\text{A.102})$$

$$E_{NH_2-H_2O^*s} = 1.016(E_{NH_2^*s} + E_{H_2O^*s}) + 0.47 \quad (\text{A.103})$$

$$E_{NH_2-H_2O^*t} = 1.0(E_{NH_2^*t} + E_{H_2O^*t}) + 0.0 \quad (\text{A.104})$$

$$E_{NH-H_2O^*s} = 0.861(E_{NH^*s} + E_{H_2O^*s}) + 0.633 \quad (\text{A.105})$$

$$E_{NH-H_2O^*t} = 1.054(E_{NH^*t} + E_{H_2O^*t}) + 0.796 \quad (\text{A.106})$$

$$E_{N-H_2O^*s} = 1.076(E_{N^*s} + E_{H_2O^*s}) + 0.788 \quad (\text{A.107})$$

$$E_{N-H_2O^*t} = 1.077(E_{N^*t} + E_{H_2O^*t}) + 0.815 \quad (\text{A.108})$$

$$E_{O-H_2O^*s} = 1.012E_{O^*s} + 0.092 \quad (\text{A.109})$$

$$E_{O-H_2O^*t} = 1.012(E_{O^*t}) + 0.092 \quad (\text{A.110})$$

A.6 H₂ assisted NO_x-SCR by NH₃

A.6.1 Ag{211} Adsorption Summary

Table A.19: Adsorption energies of the possible NO_x-SCR intermediates over Ag{211} surface, with the corresponding gas phase energies and magnetic moment(MOM) value

Adsorbate	Ag{211}	gas phase energy	MOM
H	-1.97	-13.73	1
H2	-0.01	-32.03	0
O	-2.89	-432.73	2
O ₂	0.2	-870.73	2
OH	-2.58	-450.91	1
OOH	-1.01	-886.64	1
H ₂ O	-0.06	-469.74	0
H ₂ O ₂	-0.05	-903.95	0
H ₃ O	dissociates		
N	-1.93	-266.72	3
NO	-0.16	-705.86	1
NO ₂	-1.08	-1142.24	1
NO ₃	-1.63	-1577.45	1
NOH	-0.58	-720.99	2
HNO	-0.85	-721.81	0
HNOH	-0.24	-738.31	1
H ₂ NO	-0.31	-738.75	1
H ₂ NOH	-0.1	-754.69	0
HNO ₂	-0.03	-1159.16	0
ONHO	-0.1	-1159.02	0
HNOOH	dissociates		
ON(H)OH	dissociates		
H ₂ NOOH	-0.26	-1190.33	0
HN(OH) ₂	-0.27	-1191.12	0
H ₂ N(OH) ₂	dissociates		
HNO ₃	0	-1595.23	0
N(OH) ₂	-0.67	-1174.08	1
ON(OH) ₂	dissociates		
N(OH) ₂	-0.38	-1626.98	0
NH	-2.03	-284.19	2
NH ₂	-1.79	-302.03	1
NH ₃	-0.22	-320.43	0
N ₂	0.01	-542.9	0
N ₂ O	0	-978	0
N ₂ O ₂	-0.91	-1411.91	0

Adsorbate	Ag{211}	gas phase energy	MOM
N ₂ O ₃	dissociates	-1848.66	0
N ₂ O ₃ (assymetic)	dissociates	-1848.42	0
N ₂ O ₄	dissociates	-2285.14	0
N ₂ H	-0.19	-556.95	1
HNNO	-1.45	-989.91	1
NNOH	dissociates		
NO(H)N	-0.69	-987.51	1
NONH	-1.45	-989.91	1
H ₂ NNO	-0.39	-1010.02	0
H ₂ NNOH	-0.39	-1025.38	1
HNNO ₂	-2.2	-1427.75	1
H ₂ NNO ₂	-0.38	-1446.09	0
HNN(O)OH	-0.32	-1445.69	0
ONN(H)OH	-0.5	-1445.16	0
ON(H)NOH	-0.35	-1445.31	0
NN(OH) ₂	dissociates		
(OH)NN(OH)	-0.33	-1445.63	0
O ₂ NN(OH) ₂	dissociates		
H ₂ NNH	-0.53	-589.51	1
(OH) ₂ N(O)OH	dissociates		
HNN(OH) ₂	dissociates		
OHNN(H)OH	dissociates		
N ₂ H ₄	-1.38	-605.62	0
N ₂ H ₂	-0.06	-573.5	0
H ₂ NN(H)(OH)	-0.28	-1042.3	0
H ₂ NN(OH)(OH)	-0.32	-1478.03	0
(OH) ₂ NN(H)OH	-0.27	-1913.44	0
(OH) ₂ NN(OH) ₂	dissociates		
(OH)NN(H)OH	dissociates		
(OH)(H)NN(H)OH	-0.17	-1478.03	0
NNH ₂	0.34	-573.28	0

A.6.2 Scaling Summary

Adsorption Scaling Parameters

$$E_{NH_3^{*s}} = 0.155E_{N^{*s}} - 0.874 \quad (\text{A.111})$$

$$E_{NH_3^{*t}} = 0.146E_{N^{*s}} - 0.668 \quad (\text{A.112})$$

$$E_{NH_2^{*s}} = 0.408E_{N^{*s}} - 0.951 \quad (\text{A.113})$$

$$E_{H^*s} = 0.19E_{N^*s} - 0.605 \quad (\text{A.114})$$

$$E_{NH_2^*t} = 0.308E_{N^*s} - 0.054 \quad (\text{A.115})$$

$$E_{H^*t} = 0.159E_{N^*s} - 0.482 \quad (\text{A.116})$$

$$E_{NH^*s} = 0.695E_{N^*s} - 0.313 \quad (\text{A.117})$$

$$E_{NH^*t} = 0.542E_{N^*s} + 0.092 \quad (\text{A.118})$$

$$E_{N^*t} = 0.934E_{N^*s} + 0.285 \quad (\text{A.119})$$

$$E_{O^*t} = 0.912E_{O^*s} + 0.211 \quad (\text{A.120})$$

$$E_{OH^*s} = 0.56E_{O^*s} - 0.552 \quad (\text{A.121})$$

$$E_{OH^*t} = 0.389E_{O^*s} + 0.194 \quad (\text{A.122})$$

$$E_{H_2O^*s} = 0.005E_{N^*s} + 0.129E_{O^*s} - 0.381 \quad (\text{A.123})$$

$$E_{H_2O^*t} = 0.028E_{N^*s} - 0.124 \quad (\text{A.124})$$

$$E_{NO^*s} = 0.656E_{N^*s} + 1.477 \quad (\text{A.125})$$

$$E_{NO^*t} = 0.561E_{N^*s} + 1.896 \quad (\text{A.126})$$

$$E_{NO_2^*s} = 0.528E_{O^*s} + 3.423 \quad (\text{A.127})$$

$$E_{NO_2^*t} = 0.405E_{O^*s} + 4.084 \quad (\text{A.128})$$

$$E_{N_2O^*s} = 0.131E_{N^*s} + 0.235E_{O^*s} + 3.762 \quad (\text{A.129})$$

$$E_{N_2O^*t} = 0.157E_{O^*s} + 4.244 \quad (\text{A.130})$$

Transition-state Scaling Parameters

$$E_{H-NH_2^*s} = 0.456E_{N^*s} + 0.293 \quad (\text{A.131})$$

$$E_{H-NH_2^*t} = 0.339E_{N^*s} + 0.576 \quad (\text{A.132})$$

$$E_{H-NH^*s} = 0.693E_{N^*s} + 0.669 \quad (\text{A.133})$$

$$E_{H-NH^*t} = 0.622E_{N^*s} + 0.879 \quad (\text{A.134})$$

$$E_{H-N^*s} = 1.125E_{N^*s} + 0.812 \quad (\text{A.135})$$

$$E_{H-N^*t} = 0.844E_{N^*s} + 1.69 \quad (\text{A.136})$$

$$E_{N-N^*s} = 1.627E_{N^*s} + 2.112 \quad (\text{A.137})$$

$$E_{N-N^*t} = 1.458E_{N^*s} + 3.173 \quad (\text{A.138})$$

$$E_{O-O^*s} = 1.105E_{O^*s} + 3.151 \quad (\text{A.139})$$

$$E_{O-O^*t} = 1.347E_{O^*s} + 3.429 \quad (\text{A.140})$$

$$E_{O-H^*s} = 0.391E_{N^*s} + 0.505E_{O^*s} + 0.282 \quad (\text{A.141})$$

$$E_{O-H^*t} = 0.268E_{N^*s} + 0.469E_{O^*s} + 1.081 \quad (\text{A.142})$$

$$E_{H-OH^*s} = 0.236E_{N^*s} + 0.253E_{O^*s} + 0.076 \quad (\text{A.143})$$

$$E_{H-OH^*t} = 0.293E_{N^*s} + 0.68 \quad (\text{A.144})$$

$$E_{H-H^*s} = 0.353E_{N^*s} - 0.328 \quad (\text{A.145})$$

$$E_{H-H^*t} = 0.439E_{N^*s} - 0.492 \quad (\text{A.146})$$

$$E_{NH_2-OH^*s} = 0.951(E_{NH_2^*s} + E_{OH^*s}) + 0.94 \quad (\text{A.147})$$

$$E_{NH_2-OH^*t} = 0.773(E_{NH_2^*t} + E_{OH^*t}) + 0.531 \quad (\text{A.148})$$

$$E_{NH-OH^*s} = 0.949(E_{NH^*s} + E_{OH^*s}) + 1.404 \quad (\text{A.149})$$

$$E_{NH-OH^*t} = 0.964(E_{NH^*t} + E_{OH^*t}) + 1.042 \quad (\text{A.150})$$

$$E_{N-OH^*s} = 1.016(E_{N^*s} + E_{OH^*s}) + 1.156 \quad (\text{A.151})$$

$$E_{N-OH^*t} = 1.102(E_{N^*t} + E_{OH^*t}) + 0.803 \quad (\text{A.152})$$

$$E_{NH_2-H_2O^*s} = 1.016(E_{NH_2^*s} + E_{H_2O^*s}) + 0.47 \quad (\text{A.153})$$

$$E_{NH_2-H_2O^*t} = 1.0(E_{NH_2^*t} + E_{H_2O^*t}) + 0.0 \quad (\text{A.154})$$

$$E_{NH-H_2O^*s} = 0.861(E_{NH^*s} + E_{H_2O^*s}) + 0.633 \quad (\text{A.155})$$

$$E_{NH-H_2O^*t} = 1.054(E_{NH^*t} + E_{H_2O^*t}) + 0.796 \quad (\text{A.156})$$

$$E_{N-H_2O^*s} = 1.076(E_{N^*s} + E_{H_2O^*s}) + 0.788 \quad (\text{A.157})$$

$$E_{N-H_2O^*t} = 1.077(E_{N^*t} + E_{H_2O^*t}) + 0.815 \quad (\text{A.158})$$

$$E_{O-H_2O^*s} = 1.012E_{O^*s} + 0.092 \quad (\text{A.159})$$

$$E_{O-H_2O^*t} = 1.012(E_{O^*t}) + 0.092 \quad (\text{A.160})$$

$$E_{N-O^*s} = 1.155E_{N^*s} + 0.291E_{O^*s} + 1.825 \quad (\text{A.161})$$

$$E_{N-O^*t} = 0.869E_{N^*s} + 0.456E_{O^*s} + 3.092 \quad (\text{A.162})$$

$$E_{NO-O^*s} = 0.932E_{N^*s} + 3.254 \quad (\text{A.163})$$

$$E_{NO-O^*t} = 0.156E_{N^*s} + 0.422E_{O^*s} + 4.735 \quad (\text{A.164})$$

$$E_{NO-N^*s} = 1.392E_{N^*s} + 3.543 \quad (\text{A.165})$$

$$E_{NO-N^*t} = 0.99E_{N^*s} + 4.629 \quad (\text{A.166})$$

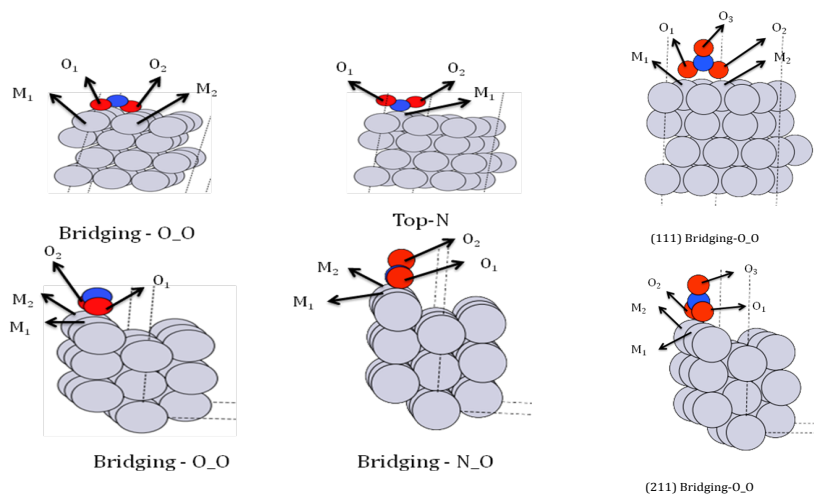


Figure A.2: Geometry of the adsorbed NO_2 , N_2O and NO_3 over transition metal $\text{Pt}\{111\}$ and $\text{Pt}\{211\}$ facets.

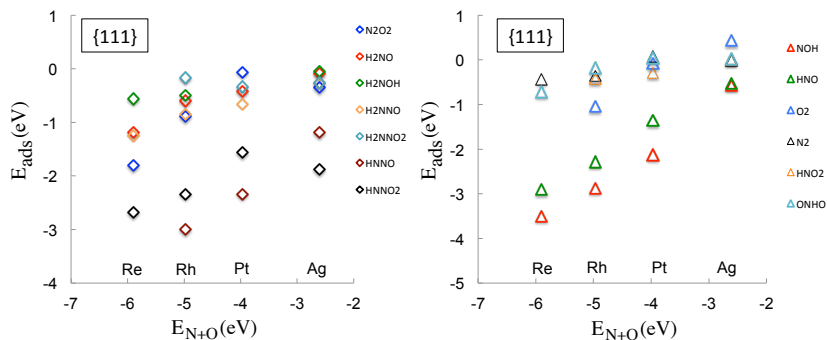


Figure A.3: Adsorption energy of the NO_x -SCR by NH_3 reaction intermediates plotted versus the $(\text{N}+\text{O})$ binding energy for Ag, Pt, Rh and Re $\{111\}$ surfaces. The adsorption energies are calculated relative to their own gas phase energies.

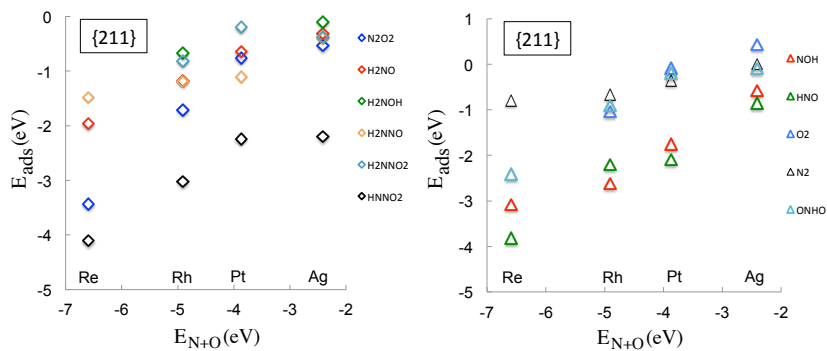


Figure A.4: Adsorption energy of the NO_x-SCR by NH₃ reaction intermediates plotted versus the (N+O) binding energy for Ag, Pt, Rh and Re {211} surfaces. The adsorption energies are calculated relative to their own gas phase energies.

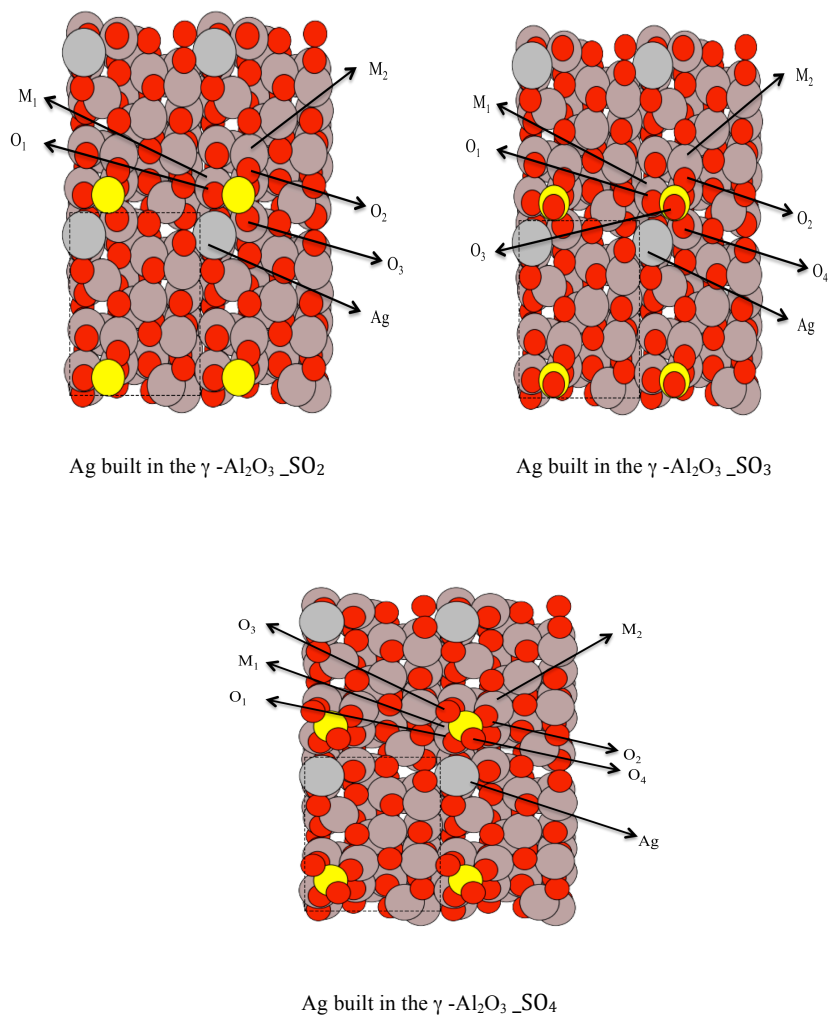


Figure A.5: Geometry of the adsorbed SO₂, SO₃ and SO₄ over the Ag atom built in the γ -Al₂O₃ surface.

Bibliography

- [1] V. Smil. Detonator of the population explosion. *Nature*, 400(29 July):415, 1999.
- [2] B. Lang, R. Joyner, and G. Somorjai. *Surf. Sci.*, 30(2):454, 1972.
- [3] J. K. Nørskov, F. Abild-Pedersen, F. Studt, and T. Bligaard. Density functional theory in surface chemistry and catalysis. *PNAS*, 108:937, 2011.
- [4] J. K. Nørskov, T. Bligaard, J. Rossmeisl, and C. H. Christensen. Towards the computational design of solid catalysts. *Nat. Chem.*, 1:37, 2009.
- [5] M. Evans and M. Polanyi. Inertia and driving force of chemical reactions. *Transactions of the Faraday Society*, 34:11, 1938.
- [6] T. Bligaard, J. K. Nørskov, S Dahl, J Matthiesen, C.H. Christensen, and J. Sehested. The Brønsted–Evans–Polanyi relation and the volcano curve in heterogeneous catalysis. *Journal of Catalysis*, 224:206–217, 2004.
- [7] F. Studt, F. Abild-Pedersen, Q. Wu, A. D. Jensen, B. Temel, J. D. Grunwaldt, and J. K. Nørskov. *J. Catal.*, 293:51–60, 2012.
- [8] S. Linic, J. Jankowiak, and M.A. Barteau. *J. Catal.*, 224:489–493, 2004.
- [9] M.P. Andersson, T. Bligaard, A. Kustov, K.E. Larsen, J. Greeley, T. Johansson, C.H. Christensen, and J.K. Nørskov. *J. Catal.*, 239:501–506, 2006.
- [10] F. Studt, F. Abild-Pedersen, T. Bligaard, R.Z. Sørensen, C.H. Christensen, and J.K. Nørskov. *Science*, 320:320–1322, 2008.
- [11] L. E. Ballentine. *Quantum Mechanics: A Modern Development*. World Scientific Publishing Co. Pte. Ltd., Singapore, 1998.
- [12] R. D Mattuck. *A Guide to Feynman Diagrams in the Many-Body Problem, chapter 0, page 1*. Dover, second edition, 1976.

- [13] G. E. Brown. *Many-Body Problems*. North-Holland, 1972.
- [14] R. G. Parr and W. Yang. *Density-Functional Theory of atoms and molecules*. Oxford Science Publications, 1989.
- [15] Kieron Burke. *THE ABC of DFT*. <http://www.chem.uci.edu/~kieron/dftold2/materials/bookABCDFT/gamma/g1.pdf>, 2007.
- [16] W. Kohn, A. D. Becke, and R. G. Parr. Density functional theory of electronic structure. *J. Phys. Chem.*, 100(31):12974, 1996.
- [17] N. Argaman and G. Mako. Density Functional Theory – an introduction. *American Journal of Physics*, 68:69–79, 2000.
- [18] E. Schrödinger. An Undulatory Theory of the Mechanics of Atoms and Molecules. *Physical Review*, 26(6):1049, 1926.
- [19] M. Born and R. Oppenheimer. Zur Quantentheorie der Molekeln. *Annalen der Physik*, 84(20):457, 1927.
- [20] P. Hohenberg and W. Kohn. Inhomogenous electron gas. *Phys. Rev. B*, 136(3B):B864, 1964.
- [21] W. Kohn and L. J. Sham. Self-consistent equations including exchange and correlation effects. *Phys. Rev.*, 140:A1133, 1965.
- [22] R. M. Martin. *Electronic Structure: Basic Theory and Practical Methods*. Cambridge University Press, 2004.
- [23] D. J. Griffiths. *Introduction to Quantum Mechanics*. Upper Saddle River, New Jersey: Prentice Hall, 1995.
- [24] W. Kohn. Nobel lecture: Electronic structure of matter — wave functions and density functionals. *Rev. Mod. Phys.*, 71:1253, 1999.
- [25] P. A. M. Dirac. Note on exchange phenomena in the Thomas–Fermi atom. *Cambridge Phil. Soc.*, 26(376):385, 1930.
- [26] V. N. Staroverov, G. E. Scuseria, J. M. Tao, and J. P. Perdew. Comparative assessment of a new nonempirical density functional: Molecules and hydrogen-bonded complexes. *J. Chem. Phys.*, 119(23):12129, 2003.
- [27] J. P. Perdew. Unified theory of exchange and correlation beyond the local density approximation. In P. Ziesche and H. Eschrig, editors, *Electronic Structure of Solids '91*, volume 17, page 11, Berlin, 1991. Akademie Verlag.
- [28] J. P. Perdew and W. Yue. Accurate and simple density functional for the electronic exchange energy: Generalized gradient approximation. *Phys. Rev. B*, 33:8800, 1986.
- [29] D. C. Langreth and J. P. Perdew. Theory of nonuniform electronic systems. I. Analysis of the gradient approximation and a generalization that works. *Phys. Rev. B*, 21(12):5469, 1980.

- [30] D. C. Langreth and M. J. Mehl. Beyond the local-density approximation in calculation of ground state electronic properties. *Phys. Rev. B*, 29(4):1809, 1983.
- [31] J. P. Perdew. Density-functional approximation for the correlation energy of the inhomogeneous electron gas. *Phys. Rev. B*, 33(12):8822, 1986.
- [32] J. P. Perdew and S. Kurth. Density functionals for non-relativistic Coulomb systems in the new century. In M. Marques, C. Fiolhais, and M. Marques, editors, *A Primer in Density Functional Theory*, page 1. Springer, 2003.
- [33] A. D. Becke. Density functional calculation of molecular bond energies. *Phys. Rev. B*, 84(8):4524, 1986.
- [34] J. P. Perdew, K. Burke, and M. Ernzerhof. Generalized gradient approximation made simple. *Phys. Rev. Lett.*, 77:3865, 1996.
- [35] E. H. Lieb and S. Oxford. Improved Lower Bound on the Indirect Coulomb Energy. *Int. J. Quantum Chem.*, 19:427, 1981.
- [36] C. Lee, W. Yang, and R. G. Parr. Development of the Colic-Salveti correlation-energy formula into a functional of the electron density. *Phys. Rev. B*, 37:785, 1988.
- [37] J. P. Perdew, K. Burke, and Y. Wang. Generalized gradient approximation for the exchange-correlation hole of a many-electron system. *Phys. Rev. B*, 54:16533, 1996.
- [38] B. Hammer, L. B. Hansen, and J. K. Nørskov. Improved adsorption energetics within density-functional theory using revised Perdew-Burke-Ernzerhof functionals. *Phys. Rev. B*, 59:7413, 1999.
- [39] Y. K. Zhang and W. T. Yang. Comment on "Generalized gradient approximation made simple". *Phys. Rev. Lett.*, 80(4):890, 1998.
- [40] The DACAPO and ASE codes are available as parts of the CAMPOS software: <http://www.camd.dtu.dk/Software>.
- [41] N. W. Ashcroft and N. D. Mermin. *Solid State Physics*. Holt Saunders, Philadelphia, p. 113, 1976.
- [42] H. J. Monkhorst and J. D. Pack. Special points for Brillouin-zone integrations. *Phys. Rev. B*, 13:5188, 1976.
- [43] D. Vanderbilt. Soft self-consistent pseudopotentials in a generalized eigenvalue formalism. *Phys Rev B*, 41:7892–7895, 1990.
- [44] A. D. Becke. Density-functional exchange-energy approximation with correct asymptotic behavior. *Phys. Rev. A*, 38:3098, 1988.
- [45] A. D. Becke. Density-functional thermochemistry. III. The role of exact exchange. *J. Chem. Phys.*, 98:5648, 1993.

- [46] P. J. Stephens, F. J. Devlin, C. F. Chabalowski, and M. J. Frisch. Ab initio calculation of vibrational absorption and circular dichroism spectra using density functional force fields. *J. Phys. Chem.*, 98:11623, 1994.
- [47] I. Chorkendorff and J. W. Niemantsverdriet. *Concepts of Modern Catalysis and Kinetics*. Wiley-VCH, second edition, 2007.
- [48] B. Hammer and J. K. Nørskov. Theoretical surface science and catalysis – calculations and concepts. In B. C. Gates and H. Knözinger, editors, *Impact of Surface Science on Catalysis*, volume 45 of *Advances in Catalysis*, page 71. Academic Press, 2000.
- [49] T. Bligaard and J. K. Nørskov. Heterogeneous Catalysis. In A. Nilsson, L. G. M. Pettersson, and J. K. Nørskov, editors, *Chemical Bonding at Surfaces and Interfaces*, chapter 4. Elsevier, first edition, 2008.
- [50] J. K. Hammer, B. and Nørskov. Why gold is the noblest of all the metals. *Nature*, 376(6537):238–240, 1995.
- [51] B. Hammer and J. K. Nørskov. Electronic factors determining the reactivity of metal surfaces. *Surface Science*, 343:211– 220, 1995.
- [52] M. Mavrikakis, B. Hammer, and J. K. Nørskov. The Effect of Strain on the Reactivity of Metal Surfaces. *Physical Review Letters*, 81:2819, 1999.
- [53] Understanding Catalytic Activity Trends for NO Decomposition and CO Oxidation using Density Functional Theory and Microkinetic Modeling, Ph. D. thesis by Hanne Falsig, Department of Chemistry, DTU, 2010.
- [54] T. Jiang, D. J. Mowbray, S. Dobrin, H. Falsig, B. Hvolbæk, T. Bligaard, and J. K. Nørskov. Trends in CO Oxidation Rates for Metal Nanoparticles and Close-Packed, Stepped, and Kinked Surfaces. *J. Phys. Chem. C*, 113:10548, 2009.
- [55] B. Hvolbæk, T. V. W. Janssens, B. S. Clausen, H. Falsig, C. H. Christensen, and J. K. Nørskov. Catalytic activity of Au nanoparticles. *NANO TODAY*, 2: 14, 2007.
- [56] J. K. Nørskov, T. Bligaard, B. Hvolbæk, F. Abild-Pedersen, I. Chorkendorff, and Claus H. Christensen. The nature of the active site in heterogeneous metal catalysis. *Chem. Soc. Rev.*, 37:2163–2171, 2008.
- [57] T. V. W. Janssens, B. S. Clausen, B. Hvolbæk, H. Falsig, C. H. Christensen, T. Bligaard, and J. K. Nørskov. Insights into the reactivity of supported Au nanoparticles: combining theory and experiments. *Top. Catal.*, 15(1–2):44, 2007.
- [58] B. Hammer, O. H. Nielsen, and J. K. Nørskov. Structure sensitivity in adsorption: CO interaction with stepped and reconstructed Pt surfaces. *Catalysis Letters*, 46:31– 35, 1997.

- [59] A. Logadottir, T. H. Rod, J. K. Nørskov, B. Hammer, S. Dahl, and C. J. H. Jacobsen. The Brønsted-Evans-Polanyi relation and the volcano plot for ammonia synthesis over transition metal catalysts. *Journal of Catalysis*, 197(2):229–231, 2001.
- [60] G Jones, T. Bligaard, F. Abild-Pedersen, and J. K. Nørskov. Using scaling relations to understand trends in the catalytic activity of transition metals. *J. Phys.: Condens. Matter*, 20:64239, 2008.
- [61] N. Brønsted. *Chem. Rev.*, 5(3):231–338, 1928.
- [62] M. G. Evans and N. P. Polanyi. *Trans. Faraday Soc.*, 34(1):11–29, 1938.
- [63] J. K. Nørskov, T. Bligaard, A. Logadottir, S. Bahn, L. B. Hansen, M. Bollinger, H. Bengaard, B. Hammer, Z. Sljivancanin, M. Mavrikakis, Y. Xu, S. Dahl, and C. J. H. Jacobsen. Universality in Heterogeneous Catalysis. *Journal of Catalysis*, 209:275–278, 2002.
- [64] B. Hammer. Coverage dependence of N₂ dissociation at an N, O, or H precovered Ru(0001) surface investigated with density functional theory. *Phys Rev B.*, 63: 205423–205423, 2001.
- [65] R. B. Getman and W. F. Schneider. DFT-Based Coverage-Dependent Model of Pt-Catalyzed NO Oxidation. *ChemCatChem*, 2:1450–1460, 2010.
- [66] C. T. Jr. Goralski and Schneider W. F. Analysis of the Thermodynamic Feasibility of NO_x Decomposition Catalysis to Meet Next Generation Vehicle NO_x Emissions Standards. *Appl. Catal. B*, 37(4):263–267, 2002.
- [67] Q. Ge and M. Neurock. Structure dependence of NO adsorption and dissociation on platinum surfaces. *J. Am. Chem. Soc.*, 126(5):1551–1559, 2004.
- [68] B. Hammer. Structure dependence of NO adsorption and dissociation on platinum surfaces. *Top. Catal.*, 37(1):3–16, 2006.
- [69] J. Rempel, J. Greeley, L. B. Hansen, O. H. Nielsen, J. K. Nørskov, and M. J. Mavrikakis. Step Effects on the Dissociation of NO on Close-Packed Rhodium Surfaces. *J. Phys. Chem. C*, 113(48):20623–20631, 2009.
- [70] J. K. Nørskov, T. Bligaard, A. Logadottir, S. Bahn, L. B. Hansen, M. V. Bollinger, H. S. Bengaard, B. Hammer, Z. Sljivancanin, M. Mavrikakis, Y. Xu, S. Dahl, and C. J. H. Jacobsen. Universality in Heterogeneous Catalysis. *J. Catal.*, 209(2):275, 2002.
- [71] S. Wang, V. Petzold, V. Tripkovic, J. Kleis, J. G. Howalt, E. Skúlason, E. M. Fernández, B. Hvolbæk, G. Jones, A. Toftelund, H. Falsig, , M. Björketun, F. Studt, F. Abild-Pedersen, J. Rossmeisl, J. K. Nørskov, and T. Bligaard. Universal transition state scaling relations for (de)hydrogenation over transition metals. *Phys. Chem. Chem. Phys.*, 13:20760–20765, 2011.

- [72] S. Wang, B. Temel, J. Shen, G. Jones, L. C. Grabow, F. Studt, T. Bligaard, C. H. Abild-Pedersen, F. and Christensen, and J. K. Nørskov. Universal Brønsted-Evans-Polanyi Relations for C–C, C–O, C–N, N–O, N–N, and O–O Dissociation Reactions. *Catal Lett.*, 141:370–373, 2011.
- [73] H. Falsig and J. Shen and T. S. Khan and W. Guo and G. Jones and S. Dahl and T. Bligaard, To be published (2013).
- [74] H. Falsig, T. Bligaard, J. Rass-Hansen, A. L. Kustov, C. H. Christensen, and J. K. Nørskov. Trends in catalytic NO decomposition over transition metal surfaces. *Topics in Catalysis*, 45:117, 2007.
- [75] H. Falsig, T. Bligaard, C. H. Christensen, and J. K. Nørskov. Direct NO decomposition over stepped transition-metal surfaces. *Pure and Applied Chemistry*, 79:1895, 2007.
- [76] T. Bligaard, K. Honkala, A. Logadottir, J. K. Nørskov, S. Dahl, and C. J. H. Jacobsen. On the compensation effect in heterogeneous catalysis. *Journal of Physical Chemistry B*, 107:9325–9331, 2003.
- [77] P. Sabatier. *Ber. Deutsch. Chem. Gesellschaft*, 44:1984, 1911.
- [78] Pascal Granger and Vasile I. Parvulescu. Catalytic NO_x Abatement Systems for Mobile Sources: From Three-Way to Lean Burn after-Treatment Technologies. *Chem. Rev.*, 111:3155–3207, 2011.
- [79] Zhiming Liu and Seong Ihl Woo. Recent Advances in Catalytic DeNO_x Science and Technology. *Catalysis Reviews: Science and Engineering*, 48(1):43–89, 2006.
- [80] Sounak Roy, M.S. Hegde, and Giridhar Madras. Catalysis for NO_x abatement. *Applied Energy*, 86:2283–2297, 2009.
- [81] Kinga Skalska, Jacek S. Miller, and Stanislaw Ledakowicz. Trends in NO_x abatement: A review. *Science of the Total Environment*, 408:3976–3989, 2010.
- [82] H. Falsig, B. Hvolbæk, I. S. Kristensen, T. Jiang, T. Bligaard, C. H. Christensen, and J. K. Nørskov. Trends in the Catalytic CO Oxidation Activity of Nanoparticles. *Angew Chem Int Ed*, 47:4835–4839, 2008.
- [83] T. Zambelli, J. Wintterlin, J. Trost, and G. Ertl. Identification of the ‘Active Sites’ of a Surface-Catalyzed Reaction. *Science*, 273:1688–1690, 1996.
- [84] B. Hammer and J. K. Nørskov. Theoretical Surface Science and Catalysis-Calculations and Concepts. *Advances in Catalysis*, 45:71–128, 2000.
- [85] D. Vanderbilt. Ultrasoft pseudopotential. *Phys Rev B*, 41:7892–7895, 1990.
- [86] H. J. Monkhorst and J. D. Pack. Special points for Brillouin-zone integrations. *Phys Rev B*, 13:5188–5192, 1976.
- [87] NIST Chemistry WebBook, <http://webbook.nist.gov/>.

- [88] E. Ringe, R. P. Van Duyne, and L. D. Marks. Wulff construction for alloy nanoparticles. *Nano Lett.*, 11:3399–3403, 2011.
- [89] A. D. Smeltz, R. B. Getman, W. F. Schneider, and F. H. Ribeiro. Coupled theoretical and experimental analysis of surface coverage effects in Pt-catalyzed NO and O₂ reaction to NO₂ on Pt(111). *Catalysis Today*, 136:84–92, 2008.
- [90] Lars C. Grabow, Britt Hvolbæk, and Jens K. Nørskov. Understanding Trends in Catalytic Activity: The Effect of Adsorbate-Adsorbate Interactions for CO Oxidation Over Transition Metals. *Top Catal*, 53:298–310, 2010.
- [91] Spencer D. Miller and John R. Kitchin. Relating the coverage dependence of oxygen adsorption on Au and Pt fcc(111) surfaces through adsorbate-induced surface electronic structure effects. *Surface Science*, 603:794–801, January 2009.
- [92] Spencer D. Miller, Nilay İnoğlu, and John R. Kitchin. Configurational correlations in the coverage dependent adsorption energies of oxygen atoms on late transition metal fcc(111) surfaces. *J. Chem. Phys.*, 134:104709, 2011.
- [93] V. P. Zhdanov. THE EFFECT OF ADSORBATE-INDUCED SURFACE RECONSTRUCTION ON THE APPARENT ARRHENIUS PARAMETERS FOR DESORPTION. *Progress in Surface Science*, 35:143–157, 1991.
- [94] G. Rupprechter, M. Morkel, H. J. Freund, and R. Hirschl. Sum frequency generation and density functional studies of CO – H interaction and hydrogen bulk dissolution on Pd(111). *Surface Science*, 554:43, 2004.
- [95] S. E. Mason, I. Grinberg, and A. M. Rappe. Adsorbate-Adsorbate Interactions and Chemisorption at Different Coverages Studied by Accurate ab initio Calculations: CO on Transition Metal Surfaces. *J.Phys. Chem. B.*, 110:3816, 2006.
- [96] A. Hellman and K. Honkala. Including lateral interactions into microkinetic models of catalytic reactions. *J. Chem. Phys.*, 127:194704, 2007.
- [97] John R. Kitchin. Correlations in coverage-dependent atomic adsorption energies on Pd(111). *Phys Rev B.*, 79:205412, 2009.
- [98] B. Hammer, L. B. Hansen, and J. K. Nørskov. Improved adsorption energetics within density-functional theory using revised Perdew-Burke-Ernzerhof functionals. *Phys. Rev. B*, 59:7413–7421, 1999.
- [99] M.P. Andersson, F. Abild-Pedersen, I.N. Remediakis, T. Bligaard, G. Jones, J. Engbæk, O. Lytken, S. Horch, J.H. Nielsen, J. Sehested, J.R. Rostrup-Nielsen, J.K. Nørskov, and I. Chorkendorff. *J. Catal.*, 255:6–19, 2008.
- [100] Nilay İnoğlu and John R. Kitchin. Simple model explaining and predicting coverage-dependent atomic adsorption energies on transition metal surfaces. *Phys Rev B.*, 82:045414, 2010.
- [101] L. Diekhoner, H. Mortensen, A. Baurichter, and A. C. Luntz. Coverage dependence of activation barriers: Nitrogen on Ru(0001). *J. Vac. Sci. Technol. A*, 18: 1509–1513, 2000.

- [102] T.C. Bromfield, D.C. Ferre, and J.W. Niemantsverdriet. *ChemPhysChem*, 6: 254–260, 2005.
- [103] H. Orita and Y. Inada. *J. Phys. Chem. B*, 109:22469–22475, 2005.
- [104] C.D. Zeinalipour-Yazdi and R.A. van Santen. *J. Phys. Chem. C*, 116:8721–8730, 2012.
- [105] R. B. Getman, W. F. Schneider, A. D. Smeltz, W. N. Delgass, and F. H. Ribeiro. Oxygen-Coverage Effects on Molecular Dissociations at a Pt Metal Surface. *Physical Review Letters*, 102:076101, 2009.
- [106] Jan Kopyscinski, Tilman J. Schildhauer, and Serge M.A. Biollaz. Production of synthetic natural gas (SNG) from coal and dry biomass – A technology review from 1950 to 2009. *Fuel*, 89:1763, 2010.
- [107] KEVORK HACATOGLU, P. JAMES MCLELLAN, and DAVID B. LAYZELL. Production of Bio-Synthetic Natural Gas in Canada. *Environ. Sci. Technol.*, 44: 2183–2188, 2010.
- [108] E. Perry Murray, T. Tsai, and S. A. Barnett. A direct-methane fuel cell with a ceria-based anode. *NATURE*, 400(12 August):649, 1999.
- [109] Chunshan Song. Fuel processing for low-temperature and high-temperature fuel cells Challenges, and opportunities for sustainable development in the 21st century. *Catalysis Today*, 77:17–49, 2002.
- [110] Velu Subramani and Santosh K. Gangwal. A Review of Recent Literature to Search for an Efficient Catalytic Process for the Conversion of Syngas to Ethanol. *Energy & Fuels*, 22:814–839, 2008.
- [111] Mark E. Dry. The Fischer-Tropsch process: 1950-2000. *Catalysis Today*, 71: 227–241, 2002.
- [112] Hans Schulz. Short history and present trends of Fischer–Tropsch synthesis. *Applied Catalysis A: General*, 186:3–12, 1999.
- [113] Eun Duck Park, Doohwan Lee, and Hyun Chul Lee. Recent progress in selective CO removal in a H₂-rich stream. *Catalysis Today*, 139:280–290, 2009.
- [114] Petar Djinić, Camilla Galletti, Stefania Specchia, and Vito Specchia. CO Methanation Over Ru-Al₂O₃ Catalysts: Effects of Chloride Doping on Reaction Activity and Selectivity. *Top Catal*, 54:1042–1053, 2011.
- [115] M.R. Elahifard, M.P. Jigato, and J.W. Niemantsverdriet. Direct versus Hydrogen-Assisted CO Dissociation on the Fe(100) Surface: a DFT Study. *Chemphyschem*, 13:89–91, 2012.
- [116] J.M. Gracia, F.F. Prinsloo, and J.W. Niemantsverdriet. Mars-van Krevelen-like Mechanism of CO Hydrogenation on an Iron Carbide Surface. *Catal. Lett.*, 133: 257–261, 2009.

- [117] M. Ojeda, A. Li, R. Nabar, A.U. Nilekar, M. Mavrikakis, and E. Iglesia. Kinetically Relevant Steps and H₂/D₂ Isotope Effects in Fischer-Tropsch Synthesis on Fe and Co Catalysts. *J. Phys. Chem. C*, 114:19761–19770, 2010.
- [118] M. Ojeda, R. Nabar, A.U. Nilekar, A. Ishikawa, M. Mavrikakis, and E. Iglesia. CO activation pathways and the mechanism of Fischer–Tropsch synthesis. *J. Catal.*, 272:287–297, 2010.
- [119] R.A. van Santen, M.M. Ghouri, S. Shetty, and E.M.H. Hensen. Structure sensitivity of the Fischer–Tropsch reaction; molecular kinetics simulations. *Catalysis Science & Technology*, 1:891–911, 2011.
- [120] J. K. Nørskov, T. Bligaard, J. Rossmeisl, and C. H. Christensen. Towards the computational design of solid catalysts. *Nature Chemistry*, 1:37, 2009.
- [121] J.S. Hummelshøj, F. Abild-Pedersen, F. Studt, T. Bligaard, and J.K. Nørskov. *Angew Chem Int Edit*, 51:272, 2012.
- [122] CatApp, <http://suncat.slac.stanford.edu/catapp>, 2013.
- [123] D.C.D. da Silva, S. Letichevsky, L.E.P. Borges, and L.G. Appel. *Int. J. Hydrogen Energy*, 37:8923–8928, 2012.
- [124] J. Stýrek J. Rathouský, A. Zukal. *Appl. Catal. A Gen.*, 94:167–179, 1993.
- [125] T.S. Khan and H. Falsig and S. Wang and W. Guo and S. Dahl and T. Bligaard, To be published (2013).
- [126] K. Christmann, O. Schober, G. Ertl, and M. Neumann. *J. Chem. Phys.*, 60: 4528–4540, 1974.
- [127] K. Christmann. *Surf. Sci. Rep.*, 9:1–163, 1988.
- [128] M. Ehsasi and K. Christmann. *Surf. Sci.*, 194:172–198, 1988.
- [129] A. Gross. *J. Chem. Phys.*, 135:174707–174707, 2011.
- [130] A.B. Mhadeshwar, J.R. Kitchin, M.A. Barteau, and D.G. Vlachos. *Catal. Lett.*, 96(1-2):13–22, 2011.
- [131] P. Ferrin, A.U. Nilekar, J. Greeley, M. Mavrikakis, and J. Rossmeisl. Reactivity descriptors for direct methanol fuel cell anode catalysts. *Surf. Sci.*, 602:3424–3431, 2008.
- [132] G. Jones, F. Studt, F. Abild-Pedersen, J.K. Nørskov, and T. Bligaard. Scaling relationships for adsorption energies of C₂ hydrocarbons on transition metal surfaces. *Chem. Eng. Sci.*, 66:6318–6323, 2011.
- [133] F. Abild-Pedersen, J. Greeley, F. Studt, J. Rossmeisl, T.R. Munter, P.G. Moses, E. Skúlason, T. Bligaard, and J.K. Nørskov. Scaling Properties of Adsorption Energies for Hydrogen-Containing Molecules on Transition-Metal Surfaces. *Phys. Rev. Lett.*, 99:016105, 2007.

- [134] A. Michaelides, Z.P. Liu, C.J. Zhang, A. Alavi, D.A. King, and P. Hu. *J. Am. Chem. Soc.*, 125:3704–3705, 2003.
- [135] V. Pallassana and M. Neurock. *J. Catal.*, 191:301–317, 2000.
- [136] J. Sehested, S. Dahl, J. Jacobsen, and J.R. Rostrup-Nielsen. *J. Phys. Chem. B*, 109:2432–2438, 2005.
- [137] A. Haryanto, S. Fernando, N. Murali, and S. Adhikari. *Energy & Fuels*, 19:2098, 2005.
- [138] H.S. Bengaard, J.K. Nørskov, J. Sehested, B.S. Clausen, L.P. Nielsen, A.M. Molenbroek, and J.R. Rostrup-Nielsen. *Journal of Catalysis*, 209:365, 2002.
- [139] S.G. Wang, X.Y. Liao, J. Hu, D.B. Cao, Y.W. Li, J.G. Wang, and H.J. Jiao. *Surf Sci*, 601:1271, 2007.
- [140] S.G. Wang, D.B. Cao, Y.W. Li, J.G. Wang, and H.J. Jiao. *J Phys Chem B*, 110: 9976, 2006.
- [141] D.W. Blaylock, T. Ogura, W.H. Green, and G.J.O. Beran. *The Journal of Physical Chemistry C*, 113:4898, 2009.
- [142] Y. Chen and D.G. Vlachos. *Ind Eng Chem Res*, 51:12244, 2012.
- [143] O.R. Inderwildi, S.J. Jenkins, and D.A. King. *Angew Chem Int Edit*, 47:5253, 2008.
- [144] G. Jones, J.G. Jakobsen, S.S. Shim, J. Kleis, M.P. Andersson, J. Rossmeisl, F. Abild-Pedersen, T. Bligaard, S. Helveg, B. Hinnemann, J.R. Rostrup-Nielsen, I. Chorkendorff, J. Sehested, and J.K. Nørskov. *Journal of Catalysis*, 259:147, 2008.
- [145] T. Bhattacharjee, O.R. Inderwildi, S.J. Jenkins, U. Riedel, and J. Warnatz. *J Phys Chem C*, 112:8751, 2008.
- [146] S. Shetty, A.P.J. Jansen, and R.A. van Santen. *J Am Chem Soc*, 131:12874, 2009.
- [147] J. Sehested. *Catalysis Today*, 111:103, 2006.
- [148] H.F. Rase. *Chemical reactor design for process plants, Vol. 2*. Wiley & Sons, New York, 1900, p. 256.
- [149] D.R. Lide and R.C. Weast. *CRC handbook of chemistry and physics, 68 ed*. CRC Press, Boca Raton, Florida, 1987.
- [150] Chemicool, <http://www.chemicool.com>.
- [151] D.W. Blaylock, Y.-A. Zhu, and W. Green. *Top Catal*, 54:828, 2011.
- [152] L. Wang, D.L. Li, M. Koike, S. Koso, Y. Nakagawa, Y. Xu, and K. Tomishige. *Appl Catal A-Gen*, 392:248, 2011.

- [153] A.C.W. Koh, L. Chen, W. Kee Leong, B.F.G. Johnson, T. Khimyak, and J. Lin. *International Journal of Hydrogen Energy*, 32:725, 2007.
- [154] N.I.I'l'chenko. Catalytic Oxidation of Ammonia. *Russian Chemical Reviews*, 45 (12):2168–2195, 1976.
- [155] Flemming Dannevang. Process for decomposing ammonia in an off-gas. *US Patent*, page 5587134 A, 1996.
- [156] Y. Li and J.N. Armor. Selective NH_3 oxidation to N_2 in a wet stream. *Appl. Catal. B*, 13:131, 1997.
- [157] W.D.Mieher and W. Ho. Thermally activated oxidation of NH_3 on Pt (111) : intermediate species and reaction mechanisms. *Surface Science*, 322:151–167, 1995.
- [158] J.M. Bradley, A. Hopkinson, and D.A. King. A molecular beam study of ammonia adsorption on Pt{100}. *Surface Science*, 371:255–263, 1997.
- [159] A. C. M. van den Broek, J. van Grondelle, and R. A. van Santen. Determination of Surface Coverage of Catalysts: Temperature Programmed Experiments on Platinum and Iridium Sponge Catalysts after Low Temperature Ammonia Oxidation. *Journal of Catalysis*, 185:297–306, 1999.
- [160] B. Afsin, P.R. Davies, A. Pashusky, M.W. Roberts, and D. Vincent. Reaction pathways in the oxydehydrogenation of ammonia at Cu(110) surfaces. *Surface Science*, 284:109–120, 1993.
- [161] A.F. Carley, P.R. Davies, and M.W. Roberts. Oxygen transient states in catalytic oxidation at metal surfaces. *Catalysis Today*, 169:118–124, 2011.
- [162] Albert F. Carley, Philip R. Davies, and M. Wyn Roberts. An STM–XPS study of ammonia oxidation: the molecular architecture of chemisorbed imide ‘strings’ at Cu(110) surfaces. *CHEMICAL COMMUNICATIONS*, 17:1793–1794, 1998.
- [163] Microkinetic Modeling, <https://confluence.slac.stanford.edu/display/SUNCAT/Microkinetic+Modeling>, 2013.
- [164] M. Behrens, F. Studt, I. Kasatkin, S. Kühn, M. Hävecker, F. Abild-Pedersen, S. Zander, F. Girgsdies, P. Kurr, B.-L. Kniep, M. Tovar, R.W. Fischer, J.K. Nørskov, and R. Schlögl. *Science*, 336:893, 2012.
- [165] G. Kresse and J. Furthmüller. Efficiency of ab-initio total energy calculations for metals and semiconductors using a plane-wave basis set. *Comput. Mat. Sci.*, 6:15, 1996.
- [166] J. K. Nørskov, T. Bligaard, A. Logadottir, S. Bahn, L. B. Hansen, M. Bollinger, H. Bengaard, B. Hammer, Z. Sljivancanin, M. Mavrikakis, Y. Xu, S. Dahl, and C. J. H. Jacobsen. Universality in Heterogeneous Catalysis. *Journal of Catalysis*, 209:275–278, 2002.

- [167] T. V. Johnson. Review of diesel emissions and control. *International journal of engine research*, 10(5):275–285, 2009.
- [168] S.Satokawa, J.Shibata, K.Shimizu, S.Atsushi, and T.Hattori. *Appl. Catal. B*, 42: 179–186, 2003.
- [169] R.Burch, J.P.Breen, C.J.Hill, B.Krutzsch, B.Konrad, E.Jobson, L.Cider, K.Eranen, F. Klingstedt, and L.E. Lindfors. *Top. Catal.*, 30-31:19–25, 2004.
- [170] M.Richter, U.Bentrup, R.Eckelt, M.Schneider, M.M.Pohl, and R.Fricke. *Appl. Catal. B*, 51:261–274, 2004.
- [171] M. Richter, R. Fricke, and R. Eckelt. *Catal. Lett.*, 94:115–118, 2004.
- [172] K.-I. Shimizu and A. Satsuma. *Appl. Catal. B*, 77:202–205, 2007.
- [173] D. E. Doronkin, S. Fogel, S. Tamm, L. Olsson, T. S. Khan, T. Bligaard, P. Gabrielsson, and S. Dahl. Study of the “Fast SCR”-like mechanism of H₂-assisted SCR of NO_x with ammonia over Ag/Al₂O₃. *Applied Catalysis B: Environmental*, 113–114:228–236, 2012.
- [174] M. Digne, P. Sautet, P. Raybaud, P. Euzen, and H. Toulhoat. *J. Catal.*, 226: 54–68, 2004.
- [175] H. Sjövall, R. J. Blint, and L. Olsson. Detailed kinetic modeling of NH₃ SCR over Cu-ZSM-5. *Appl. Catal. B*, 92:138–153, 2009.
- [176] Junhua Li, Huazhen Chang, Lei Ma, Jiming Hao, and Ralph T. Yang. Low-temperature selective catalytic reduction of NO_x with NH₃ over metal oxide and zeolite catalysts -A review. *Catalysis Today*, 175:147–156, 2011.
- [177] C. Ciardelli, I. Nova, E. Tronconi, D. Chatterjee, T. Burkhardt, and M. Weibel. NH₃ SCR of NO_x for diesel exhausts aftertreatment: role of NO₂ in catalytic mechanism, unsteady kinetics and monolith converter modelling. *Chemical Engineering Science*, 62:5001–5006, 2007.
- [178] I. Nova, C. Ciardelli, E. Tronconi, D. Chatterjee, and Brigitte Bandl-Konrad. NH₃–NO/NO₂ chemistry over V-based catalysts and its role in the mechanism of the Fast SCR reaction. *Catalysis Today*, 114:3–12, 2006.
- [179] E. Tronconi, I. Nova, C. Ciardelli, D. Chatterjee, and M. Weibel. Redox features in the catalytic mechanism of the “standard” and “fast” NH₃-SCR of NO_x over a V-based catalyst investigated by dynamic methods. *Journal of Catalysis*, 245: 1–10, 2007.
- [180] Sandro Brandenberger, Oliver Kröcher, Arno Tissler, and Roderik Althoff. The State of the Art in Selective Catalytic Reduction of NO_x by Ammonia Using Metal-Exchanged Zeolite Catalysts. *Catalysis Reviews: Science and Engineering*, 50(4):492–531, 2008.
- [181] A. Hellman, I. Panas, and H. Grönbeck. NO₂ dissociation on Ag(111) revisited by theory. *J. Chem. Phys.*, 128:104704, 2008.

- [182] V.A.Kondratenko, U.Bentrup, M.Richter, T.W.Hansen, and E.V.Kondratenko. *Appl. Catal. B*, 84:497–504, 2008.
- [183] A. Hellman and H. Grönbeck. First-Principles Studies of NO_x Chemistry on Ag_n/α-Al₂O₃. *J. Phys. Chem. C*, 113:3674–3682, 2009.
- [184] A. Hellman and H. Grönbeck. Activation of Al₂O₃ by a Long-Ranged Chemical Bond Mechanism. *PHYSICAL REVIEW LETTERS*, 100:116801, 2008.
- [185] J. P. Breen, R. Burch, C. Hardacre, and C. J. Hill. *J. Phys. Chem. B*, 109:4804, 2005.
- [186] H. H. Ingelsten, A. Hellman, H. Kannisto, and H. Grönbeck. Experimental and theoretical characterization of NO_x species on Ag/α-Al₂O₃. *Journal of Molecular Catalysis A*, 314:102–109, 2009.
- [187] H. Gröneck, A. Hellman, and A. Gavrin. Structural, Energetic, and Vibrational Properties of NO_x Adsorption on Ag_n, n = 1-8. *J. Phys. Chem. A*, 111:6062–6067, 2007.
- [188] E. Kondratenko, V. Kondratenko, M. Richter, and R. Fricke. *J. Catal.*, 239: 23–33, 2006.
- [189] P. Sazama, L. Čplek, H. Drobná, Z. Sobalík, J. Dělděček, K. Arve, and B. Wichterlová. *J. Catal.*, 232:302–317, 2005.
- [190] V. Houel, P. Millington, R. Rajaram, and A. Tsolakis. *Appl. Catal. B*, 77:29–34, 2007.
- [191] G. Madia, M. Koebel, M. Elsener, and A. Wokaun. *Ind. Eng. Chem. Res.*, 41: 3512–3517, 2002.
- [192] A. Grossale, I. Nova, E. Tronconi, D. Chatterjee, and M. Weibel. *J. Catal.*, 256: 312–322, 2008.
- [193] K. i. Shimizu, J. Shibata, and A. Satsuma. *J. Catal.*, 239:402–409, 2006.
- [194] J.H. Lee, S.J. Schmiege, and S.H. Oh. *Appl. Catal. A*, 342:78–86, 2008.
- [195] F.C. Meunier and J. Ross. *Appl. Catal. B*, 24:23–32, 2000.
- [196] M. Anstrom, N. Topsøe, and J. A. Dumesic. Density functional theory studies of mechanistic aspects of the SCR reaction on vanadium oxide catalysts. *Journal of Catalysis*, 213:115–125, 2003.
- [197] Ru-Ming Yuan, Gang Fu, Xin Xu, and Hui-Lin Wan. Brønsted-NH₄⁺ mechanism versus nitrite mechanism: new insight into the selective catalytic reduction of NO by NH₃. *Phys. Chem. Chem. Phys.*, 13:453–460, 2011.
- [198] Sezen Soyer, Alper Uzun, Selim Senkan, and Isik Onal. A quantum chemical study of nitric oxide reduction by ammonia (SCR reaction) on V₂O₅ catalyst surface. *Catalysis Today*, 118:268–278, 2006.

- [199] Jun Li and Shuhua Li. A DFT Study toward Understanding the High Activity of Fe-Exchanged Zeolites for the “Fast” Selective Catalytic Reduction of Nitrogen Oxides with Ammonia. *J. Phys. Chem. C*, 112:16938–16944, 2008.
- [200] A. Abe, N. Aoyama, S. Sumiya, N. Kakuta, and K. Yoshida. *Catal. Lett.*, 51: 5–9, 1998.
- [201] P.W. Park and C.L. Boyer. *Appl. Catal. B*, 59:27–34, 2005.
- [202] J.P.Breen, R.Burch, C.Hardacre, C.J.Hill, B.Krutzsch, B.Bandl-Konrad, E.Jobson, L. Cider, P.G. Blakeman, L.J. Peace, M.V. Twigg, M. Preis, and M. Gottschling. *Appl. Catal. B*, 70:36–44, 2007.
- [203] F. Klingstedt, L.-E. Lindfors K. Eränen, S. Andersson, L. Cider, C. Landberg, E. Jobson, L. Eriksson, T. Ilkenhans, and D. Webster. *Top. Catal.*, 30–31:27–30, 2004.
- [204] Q. Ma, Y. Liu, and H. He. *J. Phys. Chem. A*, 112:6630–6635, 2008.
- [205] M.W. Chase Jr. *NIST-JANAF Thermochemical Tables, fourth edition, J. Phys.Chem. Ref. Data, Monograph 9*, pages 1–1951, 1998.
- [206] S. Fogel, D. E.Doronkin, P. Gabrielsson, and S. Dahl. Optimisation of Ag loading and alumina characteristics to give sulphur-tolerant Ag/Al₂O₃ catalyst for H₂-assisted NH₃-SCR of NO_x. *Applied Catalysis B: Environmental*, 125:457–464, 2012.
- [207] A. Sultana, M. Haneda, T. Fujitani, and H. Hamada. *Catal. Lett.*, 114:96–102, 2007.
- [208] K.-I. Shimizu, J.H.Y. Shibata, A. Satsuma, and T. Hattori. *Appl. Catal. B*, 30: 151–162, 2001.
- [209] Q. Wu, H. Gao, and H. He. *J. Phys. Chem. B*, 110:8320–8324, 2006.
- [210] T.C. Brüggemann, D.G. Vlachos, and F.J. Keil. *J. Catal.*, 283:178–191, 2011.
- [211] J.K. Nørskov Á. Logadóttir. *J. Catal.*, 220:273–279, 2003.

Paper I

On the structure sensitivity of direct NO decomposition over low-index transition metal facets

Hanne Falsig, Juan Shen, Tuhin Suvra Khan,
Wei Guo, Glenn Jones, Søren Dahl, and Thomas Bligaard

Topics in Catalysis submitted (2013)

On the structure sensitivity of direct NO decomposition over low-index transition metal facets

Hanne Falsig^{1,2}, Juan Shen², Tuhin Suvra Khan^{1,2}, Wei Guo², Glenn Jones², Søren Dahl³ and Thomas Bligaard^{1,4}

¹*SUNCAT Center for Interface Science and Catalysis, SLAC National Accelerator Laboratory, 2575 Sand Hill Road, Menlo Park, California 94025, USA*

²*Center for Atomic-scale Materials Design, Department of Physics Building 307, Technical University of Denmark, DK-2800 Lyngby, Denmark*

³*Center for Individual Nanoparticle Functionality (CINF), Department of Physics, Building 307, Nano DTU, Technical University of Denmark, DK-2800 Lyngby, Denmark*

⁴*Department of Chemical Engineering, Stanford University, Stanford, CA 94305, USA*

E-mail: bligaard@slac.stanford.edu

Abstract

We study the dissociative chemisorption of NO, O₂, and N₂ over close-packed, stepped, kinked, and open (fcc {111}, {211}, {311}, {532}, {100}, and {110}) transition metal facets using density functional theory (DFT). The offset of the Brønsted-Evans-Polanyi (BEP) relations suggest that the {111} surface is the least reactive, and that the {110} surface is the most reactive. This observation is verified by establishing volcano-relations based on mean-field microkinetic models for each facet, showing that the maximum rate over {110} is 5 orders of magnitude larger than the maximum {111} rate. The ordering of the maximum activity over the facets is: {110} > {100} ~ {532} > {311} ~ {211} > {111}, which is in general agreement with the offset in the BEP relations. We show that the top-point location and shape of the volcano relations are approximately facet-independent. This lends credibility to the approach of analyzing trends in catalytic reactivity over a single low-index facet, and assuming the experimentally observed activity trends are qualitatively well-described by such a single-facet analysis. Our study suggests that a key element for generally obtaining quantitative agreement between theory and experiments is for the simulations to address in detail the propensities of the various types of active sites. Finally, we show that the ordering of NO decomposition rates among metals and facets is essentially unaltered when using BEP- and scaling relations in the microkinetics instead of explicit DFT calculations for each elementary reaction step, and that using a “universal” BEP relation introduces no significant additional qualitative error in trend prediction.

Keywords: NO decomposition; Brønsted-Evans-Polanyi relations; scaling relations; microkinetics; structure sensitivity; sensitivity analysis

Introduction

NO_x in exhaust gases produced during the combustion of fossil and renewable fuels is a major source of air pollution. Increasingly stringent emission requirements for diesel engines require NO_x abatement technologies that are effective under lean-burn conditions to be introduced on a

continuously broader scale. Various technologies such as NO_x traps and selective catalytic reduction (SCR) exist.[1] For small-scale applications, such as for example small passenger vehicles, it would be preferable if a simpler process could be developed, e.g. based on the direct decomposition of NO. In this reaction, the exhaust containing NO is flowed over a heterogeneously catalytic surface, where the NO bond is split, and nitrogen atoms recombine to N₂ while the oxygen atoms recombine to O₂. At low temperatures the decomposition of NO to O₂ and N₂ is spontaneous but kinetically hindered.[2] It is therefore necessary to employ catalysts to accelerate the process.[3,4] The traditionally used three-way catalysts for removing nitrogen oxides from the exhaust of gasoline cars are not efficient at removing nitrogen oxides produced under the lean burn conditions such as in diesel-fueled vehicles.[3] Supported transition metals often serve as catalysts where the metallic part of the catalyst typically is present in the form of nanoparticles on a high surface area support. Utilizing small particles increases the available metal surface area per catalyst metal volume and increases the number of reactive under-coordinated sites.[5] Using very small nanoparticles further potentially provides the opportunity to modulate catalytic activity through so-called ‘finite-size’ effects.[6] On the surface of the nano-particle, different local structures are present which can be characterized as plane surfaces, steps, or kinks which correspond to the faces, edges, and corners of the particle, respectively. The effect of surface structure on the catalytic activity has been widely debated, and it is today well known, based on insights from both experiments and theory, that the catalytic activity can differ many orders of magnitude for different surface structures of the same metal.[7-10]

Depending on the nature of the rate determining elementary steps and the reactive intermediates present under reaction conditions a given reaction may favor one type of site over another and thus show significant structure sensitivity. [11] Examples of two extreme cases are fuel cell electrodes where a plane Pt{111} surface would be favorable for water formation,[12] and the methane steam reforming reaction for which under-coordinated sites are required in order to activate the methane molecule and to facilitate the carbon-oxygen coupling.[13]

The catalytic reactivity of metal surfaces can be described in terms of Brønsted-Evans-Polanyi (BEP) relations,[14-21] which relate the transition state energy and the reaction energy for elementary surface reactions, $E_{TS} = \alpha \Delta E + \beta$. The omnipresence of Brønsted-Evans-Polanyi relations [22,23] means that it is possible to establish selectivity maps and volcano-relations for the trends in catalytic rates for a wide range of reactions over transition metal surfaces.[24,25]

Interestingly, the BEP relations are, for some reactions, found to be structure dependent. This is for example found for the dissociative chemisorption of N-O, O-O, N-N, and C-O, where stepped metal surface facets have lower-lying BEP-lines than the closed-packed surface facets.[26,18,27] This will typically have the consequence that the sites corresponding to the lower-lying BEP-lines are the most relevant to consider as active sites.[26,24,11]

For the direct decomposition of nitric oxide, NO, over transition metals it is found that stepped transition metal surfaces are more active than the closed-packed surfaces.[28,8,29] In ref. [30] the trends in catalytic activity of the {211} transition metal surfaces for the direct NO decomposition were described by combining density functional theory calculations with a simple microkinetic model. The resulting model were found to be in reasonable qualitative agreement with experimental results. That study, however, also showed that even for the most active elemental metals, Pd and Pt, the {211}-facet have a somewhat limited catalytic activity compared to what would be required for a technically feasible solution for a lean-burn passenger vehicle.

We here present a systematic study of the dissociation of a class of diatomic molecules, NO, O₂, and N₂, on different surface facets of transition metals; {111}, {100}, {110}, {211}, {311}, and {532}. For the dissociative chemisorption of NO,

O₂, and N₂, we describe the reactivity going from one metal to the next, and from one surface structure to the next, in terms of BEP relations. Each facet is found to have its own BEP relation. We discuss what causes the structure dependence of the BEP-relations for this class of reactions. We then introduce microkinetic models based on the BEP relations, and use these to model the rate of direct NO decomposition over the various transition metal facets. The results are interpreted in light of the observed effect of surface structure on the catalytic activity. Finally we discuss, how well the catalytic activity for direct NO decomposition is described for the transition metals, when the model is based on scaling compared to the full density functional theory description of the reaction energetics.

Method

Calculation details

Adsorption, transition state, and gas-phase energies were obtained from using the plane wave density functional theory DACAPO code. [31,32] The exchange-correlation (xc)-energy was described by employing the RPBE generalized gradient correction self-consistently.[33] Vanderbilt nonlocal ultrasoft pseudopotentials are used to describe the core electrons.[34] Kohn-Sham one-electron valence states were expanded in a basis of plane waves, which were truncated at a cutoff energy of 340 eV. The Fermi population of the Kohn-Sham state was calculated at electronic temperature of $k_b T = 0.1$ eV, and all energies have been extrapolated to $k_b T = 0$ eV. The surface Brillouin zone was sampled using a Monkhorst-Pack grid.[35] The surface model and k-mesh are shown in **Table 1**.

Surface	k-mesh	unit cell	#atoms
{111}	$8 \times 8 \times 1$	2×2	16
{100}	$8 \times 8 \times 1$	2×2	16
{110}	$8 \times 6 \times 1$	2×2	28
{211}	$8 \times 6 \times 1$	2×1	24
{311}	$8 \times 6 \times 1$	2×2	24
{532}	$6 \times 6 \times 1$	1×1	24

Table 1 Calculation details.

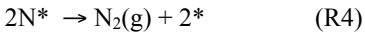
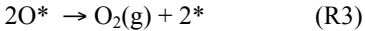
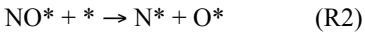
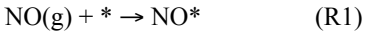
The {111} and {100} surfaces were modeled with a slab thickness of four layers and the two topmost layers were allowed to fully relax, while the {110} surfaces were modeled with a slab thickness of

seven layers and the four topmost layers were allowed to fully relax. For the {211}, {311}, and {532} surfaces the upper half of the atoms in the unit cell were allowed to relax. An inter-slab vacuum separation of at least 10 Å were used for all surfaces. Transition state energies were calculated by increasing the bond length of the diatomic molecule in small steps until a saddle point was reached.

Microkinetic model

In order to link the calculated adsorption energies and activation energies to the catalytic activity, we employ a mean field microkinetic model[36] and solve it under the steady state assumption. We correlate all the relevant adsorption energies and transition state energies in the model with two descriptors, the dissociative chemisorption energies of O₂ and N₂. This way we can explore trends in the catalytic properties as a function of the descriptor variables.[37]

Many complex processes in NO_x chemistry are possible at the transition metal surface, and some of these involve larger species, N_xO_y, with x and y larger than one. Whereas these more complex reactions certainly occur, and the molecular species produced in these have been both measured and could play a key role for both catalyst activity and selectivity, we shall here only consider the following simple elementary reaction steps in the direct NO decomposition:



We limit the study to this small set of elementary reactions since our aim is to study the structure sensitivity of a catalytic cycle rather than establishing the specific mechanism for the potentially rather complex decomposition reaction.

At steady state the reaction rate for the overall reaction is $R = R_1 = R_2 = 2R_3 = 2R_4$, where the rate for each reaction step is given by:

$$R_1 = p_{\text{NO}}\theta_*k_1 - \theta_{\text{NO}}k_{-1}$$

$$R_2 = \theta_{\text{NO}}\theta_*k_2 - \theta_{\text{N}}\theta_{\text{O}}k_{-2}$$

$$R_3 = \theta_{\text{O}}^2k_3 - p_{\text{O}_2}\theta_*^2k_{-3}$$

$$R_4 = \theta_{\text{N}}^2k_4 - p_{\text{N}_2}\theta_*^2k_{-4}$$

θ_{O} , θ_{N} , θ_{NO} , and θ_* are the coverages of O, N, NO and free sites, respectively. The forward rate constant is given by:

$k_i = \nu_i \exp\left(\frac{-(E_{ai} - T\Delta S_{ai} + \Delta \text{ZPE}_{ai})}{k_{\text{B}}T}\right)$ and the backward rate constant from $k_{-i} = k_i/K_i$, where the

ν_i is the prefactor, E_{ai} is the activation energy, ΔZPE_{ai} is the activation zero point energy, ΔS_{ai} is the activation entropy, T is the temperature, k_{B} is Boltzmann's constant, and K_i the equilibrium constant of the elementary step i . Here we assume that the prefactor is given by $\nu_i = k_{\text{B}}T/h$. The activation energy $E_{ai} = E_{\text{TS}} - E_{\text{IS}}$, the activation entropy $\Delta S_{ai} = S_{\text{TS}} - S_{\text{IS}}$, activation zero point energy $\Delta \text{ZPE}_{ai} = \text{ZPE}_{\text{TS}} - \text{ZPE}_{\text{IS}}$, where we use the nomenclature:

E_{TS} : transition state energy,

E_{IS} : initial state energy,

S_{TS} : transition state entropy,

S_{IS} : initial state entropy,

ZPE_{TS} : transition state zero point energy, and

ZPE_{IS} : initial state zero point energy.

To simplify the description of the catalytic trends further, we assume that the entropies of the adsorbed species do not vary significantly between various metals and between the various metal facets. The entropies of the adsorbed and transition state species calculated using standard normal-mode analysis on the Rh{111} surface are thus used for all the metals and facets. The entropies of the gas phase species are taken from ref. [38]. The coverage of the surface intermediates, θ_{O} , θ_{N} , and θ_{NO} are obtained by solving the rate equations at steady state, and using the site conservation rule that the total sum of coverages of free sites and adsorbed intermediates is equal to 1.[36] Within this model there are seven independent parameters determining the rate and equilibrium constants kinetics, which are the adsorption energies of NO, O, and N, and the transition state energies of the 4 elementary reactions (R1)-(R4).

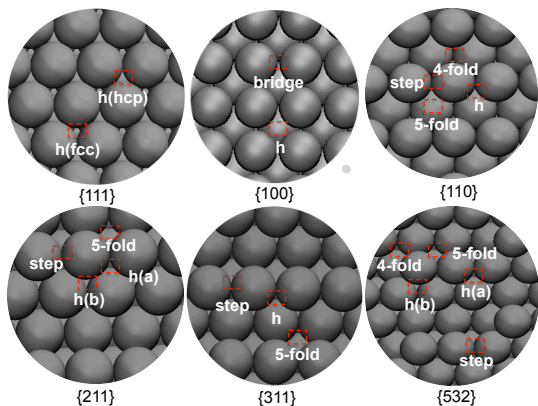


Fig.1 Schematics of the surface structure of {111}, {100}, {110}, {211}, {311}, and {532} facets (for details see the supplementary online material).

Results and discussion

For a number of transition metals, ranging from the nominally noble Au, Ag, Cu to the more reactive Pd, Pt, Rh, Co, Ru, Ni, and Re we have calculated the adsorption energies of N, O, and NO, and the transition state energies for the dissociations of NO, O₂, and N₂ over the fcc {111}, {100}, {110}, {211}, {311}, and {532} surface facets. For each metal and each surface facet we have probed the high symmetry surface sites depicted in **Fig. 1**.

The {111} and {100} facets are both closed-packed facets, where the {100} is more open. {110}, {211}, and {311} are all different kinds of stepped surfaces,

while the {532} facet has both steps and kinks.

Brønsted-Evans-Polanyi for N₂, O₂, and NO dissociation

In **Fig. 2** we present the universal (molecule independent) BEP-lines for the dissociative chemisorption of NO, O₂, and N₂ over the different metal facets. The transition state energy, E_{ts} , and the reaction energy, E_{diss} , for the dissociative chemisorption, $AB(g) + 2* = A* + B*$, are obtained from:

$$E_{ts} = E_{ts/slab} - E_{slab} - E_{gas}$$

$$E_{diss} = E_{A/slab} + E_{B/slab} - 2 E_{slab} - E_{gas}$$

where $E_{x/slab}$, E_{slab} , and E_{gas} are the energies of the adsorbate-surface system, the clean surface, and the molecular precursor in the gas phase, respectively. The linearity of the BEP-line (and its slope of almost one) has been explained by noting that the transition state geometry *in general* has final state character.[16,18] At first glance NO, N₂, and O₂ fall on the same universal line,[18] however, as seen in **Table 2**, where the fitted parameters for both the individual reactant dependent and the universal BEP-lines are given for each surface facet, there is considerable ‘fine structure’ to the universal behavior.[19]

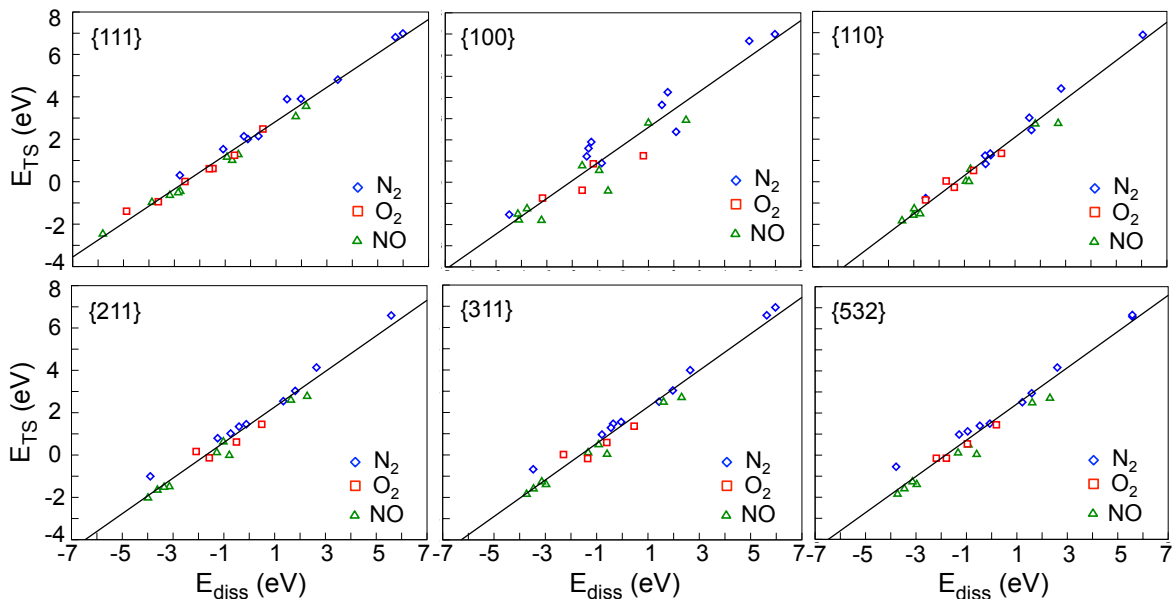


Fig. 2 Universal (molecule-independent) Brønsted-Evans-Polanyi relations for 6 different low-index fcc facets. The transition state potential energy is shown for various transition metal surfaces as a function of the dissociative chemisorption energy for the given species (N_2 , O_2 , and NO) for a range of transition metal facets. The solid lines represent the (universal) best linear fits to points for all three molecules, simultaneously.

Table 2 The fitted parameters for Brønsted-Evans-Polanyi relations for NO , O_2 , and N_2 dissociation.

Reaction	Slope (α)	Constant (β) (eV)	RMSE (eV)
{111}			
$\text{NO(g)} + 2^* \rightarrow \text{N}^* + \text{O}^*$	0.74 ± 0.02	1.74 ± 0.06	0.15
$\text{O}_2(\text{g}) + 2^* \rightarrow 2\text{O}^*$	0.71 ± 0.05	1.84 ± 0.13	0.22
$\text{N}_2(\text{g}) + 2^* \rightarrow 2\text{N}^*$	0.78 ± 0.03	2.32 ± 0.09	0.25
Universal	0.80 ± 0.02	2.05 ± 0.06	0.30
{100}			
$\text{NO(g)} + 2^* \rightarrow \text{N}^* + \text{O}^*$	0.73 ± 0.10	1.26 ± 0.28	0.69
$\text{O}_2(\text{g}) + 2^* \rightarrow 2\text{O}^*$	0.53 ± 0.18	0.93 ± 0.35	0.51
$\text{N}_2(\text{g}) + 2^* \rightarrow 2\text{N}^*$	0.80 ± 0.07	2.25 ± 0.23	0.71
Universal	0.84 ± 0.06	1.75 ± 0.17	0.79
{110}			
$\text{NO(g)} + 2^* \rightarrow \text{N}^* + \text{O}^*$	0.80 ± 0.04	0.90 ± 0.10	0.27
$\text{O}_2(\text{g}) + 2^* \rightarrow 2\text{O}^*$	0.71 ± 0.10	0.98 ± 0.15	0.22
$\text{N}_2(\text{g}) + 2^* \rightarrow 2\text{N}^*$	0.93 ± 0.04	1.33 ± 0.11	0.30

Universal	0.90±0.03	1.19±0.07	0.34
{211}			
NO(g) + 2* → N* + O*	0.79±0.04	1.09±0.10	0.25
O ₂ (g) + 2* → 2O*	0.55±0.16	1.03±0.22	0.32
N ₂ (g) + 2* → 2N*	0.81±0.04	1.76±0.09	0.27
Universal	0.84±0.04	1.43 ± 0.09	0.40
{532}			
NO(g) + 2* → N* + O*	0.81±0.04	1.24±0.10	0.23
O ₂ (g) + 2* → 2O*	0.71±0.08	1.26±0.12	0.15
N ₂ (g) + 2* → 2N*	0.80±0.04	1.93±0.11	0.32
Universal	0.86±0.03	1.57±0.09	0.39
{311}			
NO(g) + 2* → N* + O*	0.77±0.04	1.01±0.10	0.24
O ₂ (g) + 2* → 2O*	0.53±0.18	0.95±0.25	0.37
N ₂ (g) + 2* → 2N*	0.83±0.03	1.72±0.10	0.28
Universal	0.86±0.03	1.40±0.08	0.42

This is highlighted, in particular for the plot corresponding to the BEP-line for N₂ dissociation, where for most facets it is found to lie several tenths of eVs above the lines for NO and O₂ dissociation. That is, for the same reaction energy, it costs several tenths of eVs more to dissociate N₂ than NO, and O₂. This probably reflects the bonding in N₂ is stronger than the bonding in both NO and O₂. The slopes for N₂ and NO are approximately 0.8, which reflects the final state character of the transition state. The fitted BEP-line for O₂ dissociation is based on fewer data points, as there is no barrier for this reaction on the more reactive metals and facets (i.e. the reaction proceeds with no barrier even from its molecular precursor state of adsorbed O₂). The universal BEP-relation for a given facet is therefore an average between points that better fit three distinct molecule-dependent lines. However, it is noteworthy that the root-mean-square error (RMSE) is only slightly higher for the universal BEP-line than for the reactant dependent BEP-lines for any given facet. We will discuss in a later section the error one introduces in the description of the catalytic activity by employing the universal vs. the reactant dependent BEP-line for describing the

transition state energies in a microkinetic model.

We now turn to discuss the effect of surface structure on the BEP-line. It has been shown,[18] that the stepped {211} facet of transition metals has a lower lying BEP-line than the close-packed facet for this class of reactions. It is known that this variation is due to a combination of electronic and geometrical effects, and the BEP-lines establish a natural framework for addressing the decomposition of electronic and geometrical effects.[11] In **Fig. 3** the BEP-relations for all the studied facets are plotted together. It is seen that the surface structure of the metal significantly affects the position of the BEP-lines, and we find that the BEP-lines for all the stepped, kinked, and open facets lie at least 0.5 eV below the line for the close-packed {111} facet. The reactivity at optimal descriptor values (at the peak of the activity volcano) is then traditionally expected to increase when going from the close-packed facets to any of the stepped or kinked facets because their BEP-lines are lower-lying.[18,24,11] Based on the positioning of the BEP-lines in Figure 3, we could thus expect that the {111}-facet is the least catalytically active, and that the {110}-facet is the

most active facet for direct NO decomposition. We shall subsequently see that these observations hold when we make a full microkinetic analysis. More specifically we would expect that the ordering of activity of the various facets are given as: $\{110\} > \{311\} > \{211\} > \{532\} > \{100\} > \{111\}$. The underlying assumption that suggests ordering the reactivity according to the relative position of the BEP-lines is that there are only two significant kinetic parameters, one related to reactant activation and one related to product formation and desorption, that these define two kinetically competing regimes, and that these two significant kinetic parameters are linearly dependent on the same descriptor, such as for example a dissociative chemisorption energy of a key reactant.[24] The two dominant kinetic regimes are then describing the left and the right leg of a one-dimensional volcano relation for the rate as a function of the descriptor value. One regime is dominated by surface poisoning and the other regime is dominated by the activation barrier for the key reactant. As the governing BEP-line is lowered, the barrier becomes lower at a given surface poisoning, and the rate at the top of the volcano must therefore increase. When there are more than two kinetically important parameters, the picture is not necessarily this simple. For the present reaction which involves three adsorption energies and four activation barriers we shall see below, that whereas the qualitative argument holds that the open, stepped, and kinked facets have lower-lying BEP-lines and higher maximum rates, the ordering is not exactly given by the position of the BEP-lines.

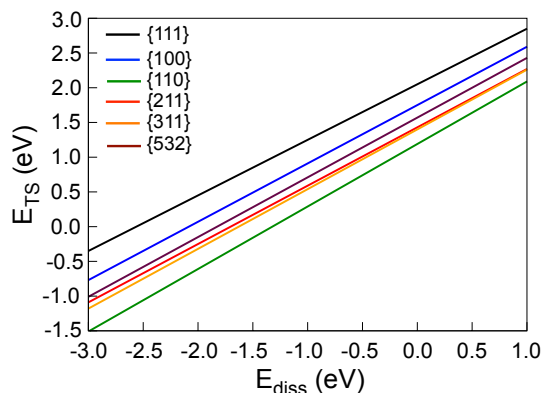


Fig. 3 The fitted universal BEP-lines for the various surface facets.

Catalytic Activity

Having established the molecule-dependent BEP-lines for the various facets, we shall now study the effects of surface structure on the catalytic activity for the direct NO decomposition. To do this, we use the microkinetic model described above, and we use scaling relationships to reduce the number of independent parameters required to describe the catalytic activity.[39,30,40] The adsorption energy of NO is described as a linear function of the N_2 dissociative chemisorption energy, and we assume there is only an entropic barrier for the adsorption of NO on the surface in the elementary reaction (R1). The transition state energies for elementary steps 2, 3, and 4 are described through the dissociative chemisorption energies of N_2 and O_2 , using the reactant dependent BEP-relations in **Table 2**, and that the dissociative chemisorption energy of NO can be written in terms of the dissociative chemisorption energies of N_2 and O_2 . Hence, the catalytic activity can now be described solely on the basis of two descriptors, the dissociative chemisorption energies of N_2 and O_2 . [30,40]

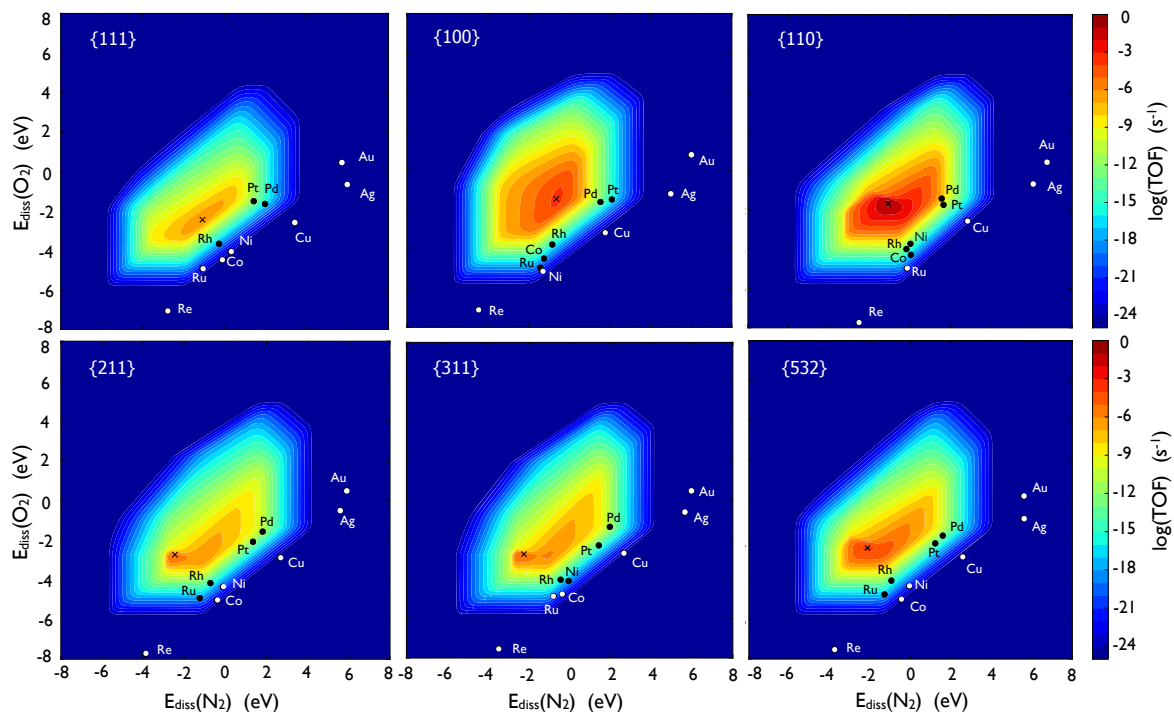


Fig. 4 The NO decomposition rate as a function of the descriptors ($E_{\text{diss}}(\text{N}_2)$, $E_{\text{diss}}(\text{O}_2)$) as predicted by a mean-field microkinetic model at a temperature of 700K. The partial pressures are $p_{\text{NO}} = 0.001$ bar, $p_{\text{N}_2} = 0.7$ bar, and $p_{\text{O}_2} = 0.1$ bar.

In **Fig. 4** the volcano curves for direct decomposition of NO on the various facets are shown under lean-burn conditions, along with the location of the transition metals on the overall volcano. First, we find that the maximum in catalytic activity increases significantly going from the closed-packed {111} facet to the open {110} facet. The rate at the top of the {110} volcano is at least 4 orders of magnitude higher for NO decomposition than the close-packed {111} surface. The {110} is the most active facet followed by the {100} and {532} facets. The activity at the top of the volcano for the stepped facets {211} and {311} are only 1 order of magnitude higher than the close-packed {111} facet. The reactivity trend for direct NO decomposition based on microkinetics can thus be written as $\{111\} < \{211\} \sim \{311\} < \{532\} \sim \{100\} < \{110\}$. Though the {110} is the most active facet, and the {111} is the least active facet as predicted by the relative position of the BEP-lines, the ordering of the other facets of intermediate reactivity is rather different from what would be predicted solely on the basis of the offset in the BEP-relations. Most

notably the {100} facet is remarkably reactive, and the improvement in rate of the {211} and {311} facets over the rate of the {111} is remarkably modest. This shows that whereas the relative positions of the BEP-relations do influence the kinetics, a microkinetic is essential for creating insight into the relative rates of two different facets. Over the {110} facet the maximum rate (at optimal descriptor values) is on the order of 1s^{-1} . This rate is so high that it suggests that just the right choice of transition metal (alloy) could become useful as a technical catalyst if it could be prepared with high enough density of highly under-coordinated surface sites such as those present on the {110} facet. However, it is clear that the elemental transition metals considered in the present study still fall short of achieving such significant rates. Pd is seen to be the most active {110} catalyst with an activity approximately 8 orders of magnitude lower than the rate at the top of the {110} volcano. Going from the close-packed {111}-facet to the more under-coordinated facets, the activity of given metals closest to the volcano top generally increases. The

Pd{110} surface is e.g. more than a million times more active for direct NO decomposition than a Pd{111} surface. Due to the scaling between the adsorption energies for adsorption of N and O, the metals fall on a line, and to the right of the volcano maximum.[30,40] The adsorption energy of N relative to gas-phase N_2 on the transition metals is simply too weak compared to that for O relative to O_2 . Most of the more reactive transition metals are thus poisoned with oxygen under the given reaction conditions. This is observed for the {111} facet in **Fig. 5**, where it can be seen that the reactive metals have a coverage of oxygen close to one monolayer and a coverage of nitrogen close to zero. The nobler metals are not poisoned by oxygen (except for Cu), but only Pt and Pd, which are the most active {111} catalysts, have considerable coverage of NO and N.

Reaction rate sensitivity

In the analysis above, we have employed the reactant dependent BEP-relations to describe the transition state energies for the elementary steps and the adsorbate scaling between NO and N adsorption, and we thereby limited the number of independent variables describing the kinetics from seven to two.

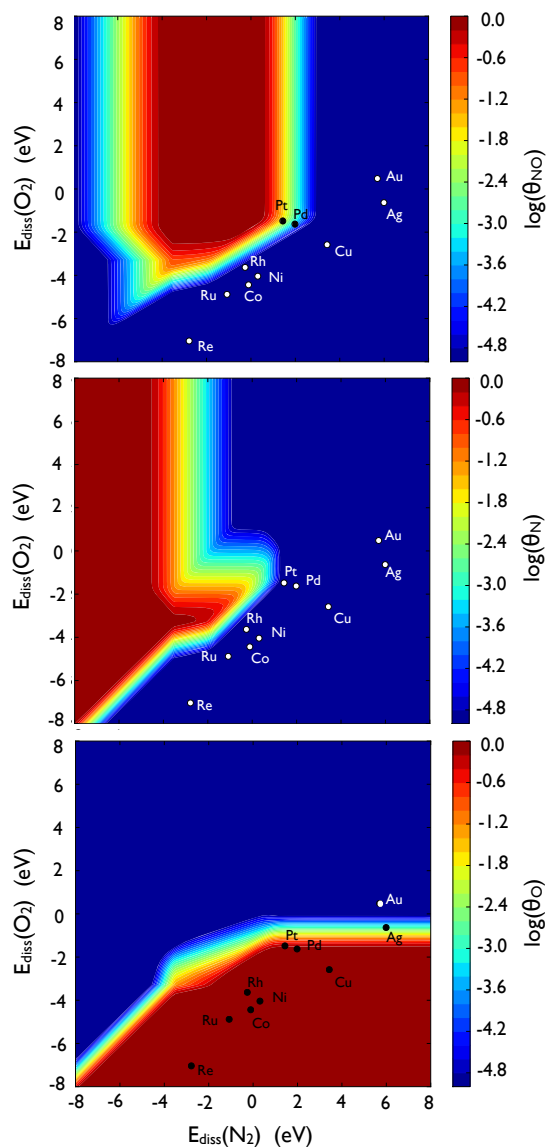


Fig. 5 The coverage of the surface intermediates, NO, N and O, versus $E_{\text{diss}}(N_2)$ and $E_{\text{diss}}(O_2)$ for the {111} facet.

One key question is then how well the trends in catalytic activity are represented in the reduced dimensionality model compared to a full description with explicit density functional theory calculations for all kinetic parameters (adsorption energies and activation barriers), and how much additional error is introduced by using universal (adsorbate-independent) BEP-relations instead of the BEP-relations for the individual adsorbates.

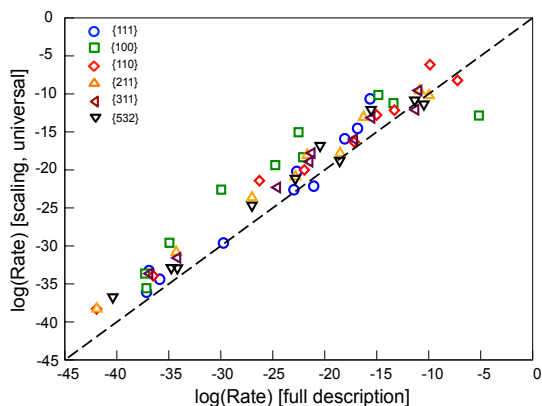


Fig. 6 The rate for direct NO decomposition obtained from using the universal BEP-relations versus the rate obtained from using explicit density functional theory calculations for all adsorption energies and activation barriers.

Fig. 6 shows the rate for microkinetic model of direct NO decomposition over the transition metals obtained by using the universal BEP-relation as a function of the rate obtained from a full density functional theory description of the energetics. The rate obtained using the universal BEP-relation are several orders of magnitude higher than the full description rates for many of the metals. However, if one is interested in describing the trends in the catalytic activity the simple universal description is, for most facets, accurate enough to order the metal's reactivities correctly.

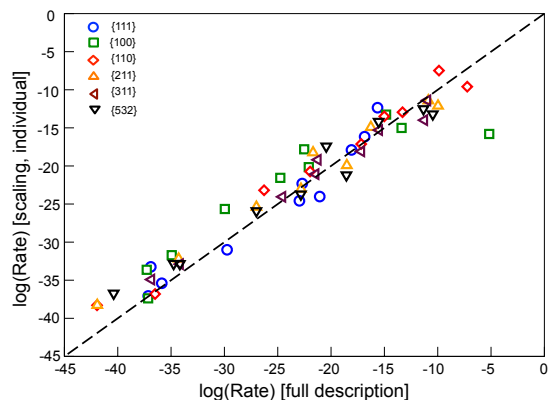


Fig. 7 The rate for NO decomposition obtained from using the reactant dependent BEP relations for the individual elementary steps versus the rate obtained from using the density functional theory energies.

In **Fig. 7** the rate for direct NO decomposition on the transition metals obtained from using the individual reactant dependent BEP-relations is

presented. The rate for the metals is now described somewhat better than the universal BEP-relation approach. For all surface structures, except the {100}-facet, the trend in catalytic activity of the transition metals is in agreement with the full density functional theory description. Interestingly, the full description predicts Pt{100} to be the metal-facet with the highest NO decomposition rate of $\sim 10^{-6} \text{ s}^{-1}$ this rate is underestimated many orders of magnitude by the microkinetic model defined in terms of the BEP-relations. However, the qualitative ordering of the metals on a given facet is rather good when described in terms of the individual BEP-relations, though not significantly better than the ordering obtained from the universal BEP-relations.

Conclusion

We have presented the BEP-relations for the dissociations of NO, O₂, and N₂ over close-packed, open, stepped, and kinked facets of transition metals. We have shown that the BEP-lines for these dissociation reactions varies for with the exposed facet of the catalyst. It has also been shown that the transition state energy for a given transition metal decreases by the same 'universal constant' of approximately $\sim 0.9 \text{ eV}$, when going from the close-packed {111} facet to any of the other (more under-coordinated) facets considered in the present study. We showed that going from a {111} facet to a more open or under-coordinated surface facet the catalytic activity increases 1-5 orders of magnitude in general agreement with lower-lying BEP-lines corresponding to a more active volcano top-point, but microkinetic modeling is necessary in order to find the correct ordering of activity of the different facets. We have shown that the {110} facet of the most active metals, Pd and Pt, was more than a million times more active than the corresponding {111} metal facets, and that there is considerable room for further improvements if one can break the scaling between the oxygen and nitrogen chemisorption energies of the pure elemental metals (for example by going to alloys). This lends some hope that a transition metal alloy catalyst for direct NO decomposition could potentially be found if one could simultaneously create a high density of under-coordinated sites under reaction conditions, and break the oxygen-nitrogen scaling that the elemental metals follow.

Acknowledgement

The authors thank Professor J.K. Nørskov for many helpful discussions on the present study and for the privilege of having him as a mentor during the early stages of our research careers.

References

1. Liu Z, Ihl Woo S (2006) *Catalysis Reviews* 48:43-89
2. Glick HS, Klein JJ, Squire W (1957) *J Chem Phys* 27:850-857
3. Parvulescu VI, Grange P, Delmon B (1998) *Catal Today* 46:233-316
4. Garin F (2001) *Appl Catal A-Gen* 222:183-219
5. Lopez N, Janssens TVW, Clausen BS, Xu Y, Mavrikakis M, Bligaard T, Nørskov JK (2004) *J Catal* 223 (1):232-235
6. Li L, Larsen AH, Romero NA, Morozov VA, Glinsvad C, Abild-Pedersen F, Greeley J, Jacobsen KW, Nørskov JK (2013) *J Phys Chem Lett* 4 (1):222-226
7. Somorjai GA, Joyner RW, Lang B (1972) *Proceedings of the Royal Society of London A* 331:335-346
8. Zambelli T, Winterlin J, Trost J, Ertl G (1996) *Science* 273:1688-1690
9. Dahl S, Logadottir A, Egeberg RC, Larsen JH, Chorkendorff I, Törnqvist E, Nørskov JK (1999) *Physical Review Letters* 83 (9):1814-1817
10. Jiang T, Mowbray DJ, Dobrin S, Falsig H, Hvolbæk B, Bligaard T, Nørskov JK (2009) *J Phys Chem C* 113 (24):10548-10553
11. Nørskov JK, Bligaard T, Hvolbæk B, Abild-Pedersen F, Chorkendorff I, Christensen CH (2008) *Chem Soc Rev* 37 (10):2163-2171
12. Nørskov JK, Rossmeisl J, Logadottir A, Lindqvist L, Kitchin JR, Bligaard T, Jonsson H (2004) *J Phys Chem B* 108 (46):17886-17892
13. Jones G, Jakobsen JG, Shim SS, Kleis J, Andersson MP, Rossmeisl J, Abild-Pedersen F, Bligaard T, Helveg S, Hinnemann B, Rostrup-Nielsen JR, Chorkendorff I, Sehested J, Nørskov JK (2008) *J Catal* 259 (1):147-160
14. Evans MG, Polanyi M (1938) *Transactions of the Faraday Society* 34:11
15. Pallassana V, Neurock M (2000) *J Catal* 191 (2):301-317
16. Liu ZP, Hu P (2001) *J Chem Phys* 115 (11):4977-4980
17. Logadottir A, Rod TH, Nørskov JK, Hammer B, Dahl S, Jacobsen CJH (2001) *J Catal* 197 (2):229-231
18. Nørskov JK, Bligaard T, Logadottir A, Bahn S, Hansen LB, Bollinger M, Bengaard H, Hammer B, Sljivancanin Z, Mavrikakis M, Xu Y, Dahl S, Jacobsen CJH (2002) *J Catal* 209 (2):275-278
19. Michaelides A, Liu ZP, Zhang CJ, Alavi A, King DA, Hu P (2003) *J Am Chem Soc* 125 (13):3704-3705
20. Andersin J, Lopez N, Honkala K (2009) *J Phys Chem C* 113 (19):8278-8286
21. Loffreda D, Delbecq F, Vigne F, Sautet P (2009) *Angew Chem-Int Edit* 48 (47):8978-8980
22. Wang S, Temel B, Shen J, Jones G, Grabow LC, Studt F, Bligaard T, Abild-Pedersen F, Christensen CH, Nørskov JK (2011) *Catal Lett* 141 (3):370-373
23. Wang S, Petzold V, Tripkovic V, Kleis J, Howalt JG, Skulason E, Fernandez EM, Hvolbæk B, Jones G, Toftlund A, Falsig H, Björketun M, Studt F, Abild-Pedersen F, Rossmeisl J, Nørskov JK, Bligaard T (2011) *Phys Chem Chem Phys* 13 (46):20760-20765
24. Bligaard T, Nørskov JK, Dahl S, Matthiesen J, Christensen CH, Sehested J (2004) *J Catal* 224 (1):206-217
25. Nørskov JK, Bligaard T, Rossmeisl J, Christensen CH (2009) *Nat Chem* 1 (1):37-46
26. Dahl S, Logadottir A, Jacobsen CJH, Nørskov JK (2001) *Appl Catal A-Gen* 222 (1-2):19-29
27. Vang RT, Honkala K, Dahl S, Vestergaard EK, Schnadt J, Lægsgaard E, Clausen BS, Nørskov JK, Besenbacher F (2005) *Nat Mater* 4 (2):160-162
28. Wolf RM, Bakker JW, Nieuwenhuys BE (1991) *Surface Science* 246:135-140
29. Rempel J, Greeley J, Hansen LB, Nielsen OH, Nørskov JK, Mavrikakis M (2009) *J Phys Chem C* 113 (48):20623-20631
30. Falsig H, Bligaard T, Rass-Hansen J, Kustov AL, Christensen CH, Nørskov JK (2007) *Top Catal* 45 (1-4):117-120
31. Bahn, Sr., Jacobsen KW (2002) *Comput Sci Eng* 4 (3):56-66
32. <http://wiki.fysik.dtu.dk/dacapo/>
33. Hammer B, Hansen LB, Nørskov JK (1999) *Phys Rev B* 59 (11):7413-7421
34. Vanderbilt D (1990) *Phys Rev B* 41 (11):7892-7895
35. Monkhorst HJ, Pack JD (1976) *Phys Rev B* 13 (12):5188-5192
36. Dumesic JA, Rudd DF, Aparicio LM, Rekoske JE, Treviño AA (1993) *The microkinetics of heterogeneous catalysis*. ACS Professional Reference Book. American Chemical Society, Washington, D.C.
37. Balandin AA (1958) *Advances in Catalysis* 10:96-129
38. <http://webbook.nist.gov/>
39. Abild-Pedersen F, Greeley J, Studt F, Rossmeisl J, Munter TR, Moses PG, Skulason E, Bligaard T, Nørskov JK (2007) *Physical Review Letters* 99 (1)
40. Falsig H, Bligaard T, Christensen CH, Nørskov JK (2007) *Pure Appl Chem* 79 (11):1895-1903

Paper II

Parameterization of a Model for Adsorbate-Adsorbate Interactions

Tuhin Suvra Khan, Hanne Falsig, Shengguang Wang, Wei Guo, Søren Dahl, and Thomas Bligaard

To be submitted (2013)

Parameterization of a Model for Adsorbate-Adsorbate Interactions

Tuhin Suvra Khan,^{1,2} Hanne Falsig,^{1,2} Shengguang Wang,¹ Wei Guo,¹ Søren Dahl⁴,
and Thomas Bligaard^{2,3}

¹Center for Atomistic-scale Materials Design (CAMD), Department of Physics, Building
307, Nano DTU, Technical University of Denmark, DK-2800 Kgs. Lyngby, Denmark

²SUNCAT Center for Interface Science and Catalysis, SLAC National
Accelerator Laboratory, 2575 Sand Hill Road, Menlo Park, CA 94025, USA

³Department of Chemical Engineering, Stanford University, Stanford, CA 94305, USA and

⁴Center for Individual Nanoparticle Functionality (CINF), Department of Physics, Building
307, Nano DTU, Technical University of Denmark, DK-2800 Kgs. Lyngby, Denmark

The lateral interaction between atoms and molecules adsorbed on the surface of a transition metal affects both the adsorption energies of the surface species and also the transition state energies for surface reactions. A simple model for obtaining the effect of such interactions on adsorption energies is proposed, where the adsorption energy varies linearly with the coverage of species at the surface. The model is parameterized using the DFT calculated adsorption energies at different coverages for a number of atoms and molecules on the most stable closed packed facet of different transition metals in their most favorable crystal structure.

I. INTRODUCTION

Adsorbate-adsorbate interactions between reaction intermediates adsorbed to the surface of a catalyst can significantly change the adsorption energy of a given reaction intermediate.^{1,2} A model to describe such interactions is therefore important in order to describe the catalytic reactivity, the surface structure of the catalyst under reaction conditions, the temperature of adsorption/desorption, and many other chemical and physical processes.³ For a large range of coverages, it has been shown that the adsorption energy of oxygen on the closed-packed facets of the transition metals, scales linearly with coverage for coverages above ≈ 0.2 ML.^{2,4} In Figure 1 (top), this is shown for oxygen at coverages between $\frac{1}{4}$ - 1 ML for a range of transition metals. Here the average adsorption energy of oxygen is plotted versus the coverage of oxygen on the surface. Kitchin et al. also described that the interaction between the adsorbed oxygen atoms was different on Au compared to Pt.³ We also observe that the change in adsorption energy with coverage is metal dependent, since the slope of the fitted lines changes from one metal to the next. In Figure 1(bottom) the linear dependence of the adsorption energy with surface coverage is shown for a range of atoms and molecules adsorbed on Rh{111}. Here it is seen, that not only is the change in adsorption energy metal dependent, but also adsorbate dependent. Since the adsorption energy changes significantly with coverage, it is most probably crucial to include such effects in a theoretical description of catalytic reactions and trends in catalytic activity. Recently Grabow et al.² proposed an interaction model, and combined it with a simple mean field kinetic model.⁵ For the catalytic CO oxidation reaction on the transition metals, it was shown that including the description of the adsorbate-adsorbate interactions, the traditionally ‘too’ reactive metals became significantly more active, and almost as

active as the most active catalyst, Pd.

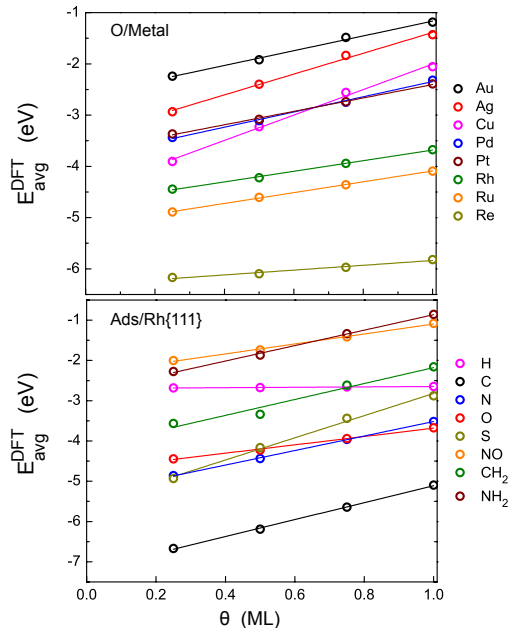


FIG. 1. Linear variation of average adsorption energy with coverage for (top) O adsorption on the closed-packed facet of the following transition metals: Au, Ag, Cu, Pd, Pt, Rh, Ru and Re, (bottom) H, C, N, O, S, NO, CH₂ and NH₂ adsorption on the Rh{111} surface.

^a only the most favorable crystal structure of the metals are studied.

A linear interaction model was first introduced by V.P.

Zhdanov to study the effect of the adsorbate-induced surface reconstruction on the apparent Arrhenius parameters for desorption processes.⁶ Rupprechter et al.⁷ studied the adsorbate-adsorbate interactions for the CO+H system on Pd{111}. They explained the fact that it is neither possible to dissociate H₂ on a CO covered surface, nor adsorb CO on a H covered surface, due to a strong repulsive interaction between H and CO. Mason et al.⁸ explained the effect of adsorbate-adsorbate interactions on adsorption energy on different transition metals and identified factors influencing the interaction. A. Hellman and K. Honkala⁹ described lateral interactions between adsorbents by a simple mean field model. By applying this model for the NH₃ synthesis on Ru{0001} step surface, they showed that compared to the highly sophisticated Monte Carlo simulations the simple mean field interaction model describes the adsorbate-adsorbate interactions reasonably well.

Here we propose a new interaction model, where the adsorption energy varies linearly with the coverage of the surface species. From density functional theory calculations, we obtain interaction parameters for both the self-interaction parameters between the same surface species and the cross-interaction parameters for interactions between two different surface species. The number of parameters in a full description of the interactions varies as $N_{surface} \times N_{sp}(N_{sp} + 1)/2$, where N_{sp} is the number of adsorbed species and $N_{surface}$ is the number of surfaces. In order to make the linear interaction model more useful and applicable to eg. catalysis, we show how the number of parameters can be reduced. First by showing how the cross-interaction parameters can be obtained from self-interaction parameters. Second by proposing 2 submodels : i) An interaction model, where the interaction parameters obtained for one metal can be applied for description of interaction on all the considered transition metals ii) a scaling based model, where we use scaling between adsorbate-adsorbate interaction parameters and adsorption energies to describe the interaction on different metals. As it has been shown earlier^{2,3} that before some threshold coverage the adsorption energy remains nearly constant we propose a piecewise interaction model where the adsorption energy is kept constant until the threshold coverage and then increases with the coverage of the surface species for a single adsorbate system. We discuss the precision and usefulness of each of the different adsorbate-adsorbate interaction models separately. We then discuss the limitations of the proposed models, and finally for the direct decomposition of NO, we show what effect the inclusion of a description of the interactions in the kinetic model, has on the catalytic activity.

II. METHOD

We propose an interaction model, where the total adsorption energy per surface site varies quadratically with

coverage:

$$E_T(\underline{\theta}) = \underline{E}^0 \underline{\theta} + \frac{1}{2} \underline{\theta}^T \underline{\epsilon} \underline{\theta}, \quad (1)$$

where E^0 is the differential adsorption energy at zero coverage, and $\underline{\epsilon}$ is the i times i dimensional interaction matrix, with the interaction parameters for interactions between the i different species. In the matrix the interaction parameters, $\epsilon_{ij} = \epsilon_{ji}$.

The average adsorption energy, $E_{avg}(\theta)$, is defined as the total adsorption energy per surface site divided by the sum of the coverages:

$$E_{avg}(\underline{\theta}) = \frac{E_T(\underline{\theta})}{\sum \theta} = \frac{\underline{E}^0 \underline{\theta} + \frac{1}{2} \underline{\theta}^T \underline{\epsilon} \underline{\theta}}{\sum \theta} \quad (2)$$

For a single adsorbate system it has the form:

$$E_{avg}(\theta_i) = \frac{E_T(\theta_i)}{\theta_i} = E_i^0 + \frac{1}{2} \epsilon_{ii} \theta_i \quad (3)$$

The self-interaction parameters, ϵ_{ii} , can be obtained by calculating the average adsorption energy at two different coverages with density functional theory:

$$\epsilon_{ii} = \frac{2(E_{avg}(\theta_1) - E_{avg}(\theta_2))}{(\theta_1 - \theta_2)} \quad (4)$$

The cross-interaction terms, ϵ_{ij} , are obtained from a system, where the adsorbates, i and j , are co-adsorbed and have the coverages θ_i and θ_j respectively with average co-adsorption energy $E_{avg}(\theta_i, \theta_j)$ as,

$$\begin{aligned} \epsilon_{ij} = & \frac{(\theta_i + \theta_j)E_{avg}(\theta_i, \theta_j) - E_i^0 \theta_i - E_j^0 \theta_j}{\theta_i \theta_j} \\ & - \frac{\frac{1}{2}(\epsilon_{ii} \theta_i^2 + \epsilon_{jj} \theta_j^2)}{\theta_i \theta_j} \end{aligned} \quad (5)$$

In catalysis we are often interested in the adsorption energy of the species taking part in a reaction has for a given coverage, this is the differential adsorption energy. The differential adsorption energy, $E_{diff}(\theta)$, can be obtained from $E_T(\theta)$ as,

$$E_{diff}^i(\underline{\theta}) = \frac{dE_T(\underline{\theta})}{d\theta_i} \quad (6)$$

So one can express the differential adsorption energy, when only one specific adsorbate is adsorbed with coverage θ_i as,

$$E_{diff}^i(\theta_i) = \frac{dE_T(\theta_i)}{d\theta_i} = E_i^0 + \epsilon_{ii} \theta_i \quad (7)$$

When multiple species are adsorbed we can express the differential adsorption energy as,

$$E_{diff}^i(\underline{\theta}) = \frac{dE_T(\underline{\theta})}{d\theta_i} = E_i^0 + \sum_j \epsilon_{ij} \theta_j \quad (8)$$

III. COMPUTATIONAL DETAILS

The plane wave DFT code, DACAPO, was used to calculate adsorption and gas phase energies.¹⁰ Kohn-Sham one-electron valence states were expanded in a plane-wave basis. A plane wave cutoff of 340.15 eV and a density wave cutoff of 680 eV were used for the calculation. The core electrons were described by Vanderbilt ultrasoft pseudopotentials.¹¹ RBPE was used to describe the exchange-correlation energy.¹² Fermi population of the Kohn-Sham states was calculated at $k_B T = 0.1$ eV. All energies are extrapolated to $k_B T = 0$ eV. The convergence limit was set as a maximum change in the force constant of 0.03 eV.

The most stable closed-packed surface of the metals in their favorable crystal structure were modeled by a 2×2 surface cell, with a slab thickness of 4 layers, where the two topmost layers were allowed to relax. A $8 \times 8 \times 1$ Monkhorst-Pack k-point¹³ sampling in the irreducible Brillouin zone was used. Adsorption energies for the individual species have been calculated at $\frac{1}{4}$ ML, $\frac{1}{2}$ ML, $\frac{3}{4}$ ML and 1 ML coverage for the most stable adsorption site at low coverage. For the determination of the cross-interaction terms, calculations were performed with coverage $\frac{1}{2}$ ML of each of the involved adsorbates. Finally, for the low coverage adsorption energy calculations on the transition metals, we used 3×3 and 4×4 unit cells, with $6 \times 6 \times 1$ and $4 \times 4 \times 1$ k-point sampling respectively.

IV. RESULT AND DISCUSSION

Catalytic trend studies are often performed without describing the coverage effect on the adsorption energy of the reaction intermediates. Often the adsorption energy calculated at $\frac{1}{4}$ ML coverage is assumed to be representative for the adsorption energy at any coverage. In Figure 2 the average adsorption energy on transition metals for a number of different atoms and molecules at surface coverage $\frac{1}{4}$, $\frac{1}{2}$, $\frac{3}{4}$, and 1 ML is plotted versus the adsorption energy at $\frac{1}{4}$ ML coverage. Clearly the adsorption energy changes significantly with coverage, and this can affect the catalytic rate of a given reaction, and most probably also the activity trends when going from one metal to the next.

The linear interaction model has been parametrized for a number of atoms and molecules adsorbed on transition metal surfaces. The self-interaction parameter for interactions between adsorbates of the same species have been obtained using equation (4) and the DFT calculated adsorption energies at $\frac{1}{4}$ ML and 1 ML. And the cross-interaction parameter for the interaction between different adsorbates have been obtained using (5) and the $\frac{1}{2}$ ML + $\frac{1}{2}$ ML coverage calculation. The adsorption geometries for used in the parametrization of the interaction model are illustrated for O (and N) adsorption on Rh(111) in 3. The interaction parameters are given in supplementary material.

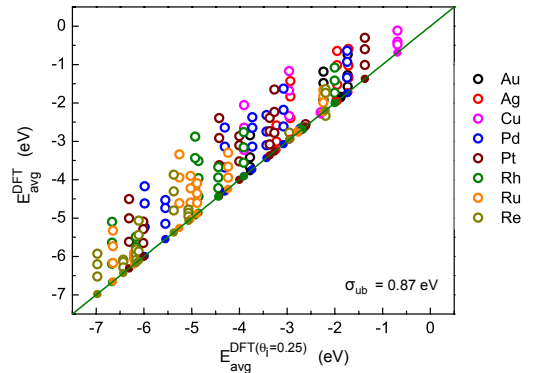


FIG. 2. Parity plot of the average adsorption energy from DFT at $\frac{1}{4}$ ML, $\frac{1}{2}$ ML, $\frac{3}{4}$ ML and 1 ML surface coverage versus the adsorption energy from DFT at $\frac{1}{4}$ ML coverage. The filled circles are for $\frac{1}{4}$ ML coverage. The studied adsorbents are: H, C, N, O, S, CH, NH and NO.

^a to be consistent with number of data points, for Au, Ag and Cu the adsorbents only for those we could obtain the interaction parameters in table I in supplementary material are included. Same in Figure 4, 9, 11, 14 and 15

We first discuss the results obtained from the description of the coverage dependent adsorption energy using the full linear interaction model.

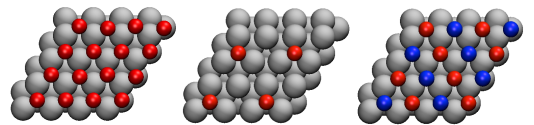


FIG. 3. Adsorption geometries of O at $\frac{1}{4}$ ML and 1 ML coverage and co-adsorbed N and O at $(\frac{1}{2} + \frac{1}{2})$ ML on Rh{111} metal surface. Oxygen and nitrogen atoms are denoted with red and blue color respectively.

A. The full linear interaction model

In Figure 4 we apply the full interaction model to predict the average adsorption energy at coverages $\frac{1}{4}$, $\frac{1}{2}$, $\frac{3}{4}$ and 1 ML. The adsorption energies are obtained using eq. 3, where an interaction parameter has been calculated for each adsorbate on each metal. The linear interaction model effectively predicts the DFT calculated adsorption energy for any of the studied adsorbates, at surface coverages between $\frac{1}{4}$ -1 ML. Since the interaction parameters are obtained from the slope of the fitted line through the DFT energies at $\frac{1}{4}$ ML and 1 ML, the average adsorption energies from the full linear interaction model will be exactly the DFT energies at these coverages. The unbiased

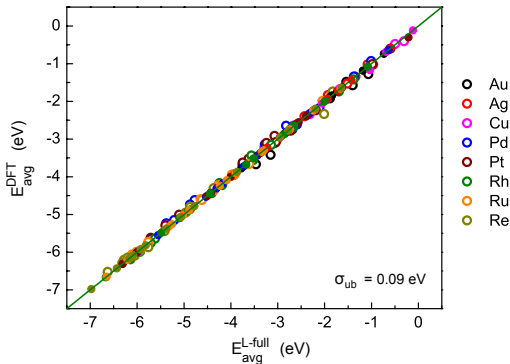


FIG. 4. Parity plot of the average adsorption energy from DFT at $\frac{1}{4}$ ML, $\frac{1}{2}$ ML, $\frac{3}{4}$ ML and 1 ML surface coverage versus the adsorption energy obtained using the full interaction model at those corresponding surface coverages. The filled circles are for $\frac{1}{4}$ ML and 1 ML coverage. The studied adsorbents are: H, C, N, O, S, CH, NH and NO.

standard deviation (the RMSE, where the modeled energies at $\frac{1}{4}$ ML and 1 ML have not been included) on the average adsorption energy is 0.09 eV. The full linear interaction model thus gives a very accurate description of the coverage dependent adsorption energy for a large region of coverages and a far more accurate description than neglecting lateral interactions. The full linear interaction model is very useful, when we are interested in simple catalytic model systems, that is a few reaction intermediates, over a few specific surfaces. However obtaining the interaction parameters for larger systems is heavy, since the number of parameters increases rapidly with number of adsorbates and metal surfaces. We now seek to reduce the number of independent parameters to make the model more applicable to catalysis in general.

B. Obtaining the cross-interaction terms from the self-interaction terms

In Figure 5 the DFT calculated adsorption energy for co-adsorption of two different species at $\frac{1}{2}$ ML coverage each is plotted versus the average of the adsorption energy of the two species at $\frac{1}{4}$ ML coverage. Clearly interactions between adsorbates of different species are significant.

We propose two ways of parametrizing the cross-interaction parameter for interaction between adsorbate i and adsorbate j , from their respective self-interaction parameters, ϵ_{ii} , and ϵ_{jj} :

$$\epsilon_{ij}^{AM} = \frac{1}{2}(\epsilon_{ii} + \epsilon_{jj}) \quad (9)$$

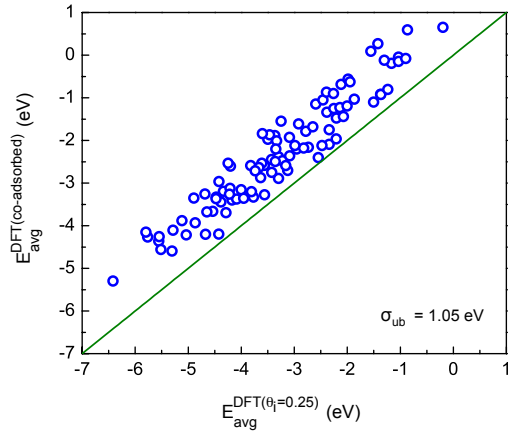


FIG. 5. Parity plot of average adsorption energy from DFT for co-adsorbed H, C, N, O, S, CH, CH₂, CO, NH, NH₂, NO, N₂, N₂O, OH and SH on Rh{111} versus adsorption energy calculated using the average of the DFT calculated adsorption energy at $\frac{1}{4}$ ML coverage of those two corresponding species.

^a For plotting the co-adsorbate systems, where co-adsorption with $\frac{1}{2}$ ML + $\frac{1}{2}$ ML coverage of the corresponding adsorbates are not stable, were excluded, see table II in supplementary material. Same with Figure 6 and 7.

$$\epsilon_{ij}^{GM} = \sqrt{(\epsilon_{ii} \times \epsilon_{jj})} \quad (10)$$

Eq. 9 is the arithmetic mean, (AM), and eq. 10 the geometric mean (GM), of the self-interaction parameters. In Figure 6 and 7, we show for rhodium, how well the coverage dependent adsorption energy is described for co-adsorbed systems, where the cross-interaction parameters have been obtained from the arithmetic mean and the geometric mean, respectively.

By using the geometric mean (GM) to obtain the cross-interaction parameters, the RMSE on the prediction of the adsorption energy for co-adsorbed species is 0.22 eV, whereas the use of the arithmetic mean, gives a slightly higher RMSE, namely 0.26 eV. With a relatively small error, we can now reduce the number of independent parameters from $N_{sp}(N_{sp} + 1)/2 \times N_{surface}$ to only $N_{sp} \times N_{surface}$ by using the parametrization for cross-interaction parameters.

C. The linear interaction model based on the interaction parameters from Rhodium

In Figure 8 we have plotted the interaction parameters obtained for a number of different adsorbates on the different metals versus the interaction parameters obtained for rhodium. Clearly there is a large variation in the in-

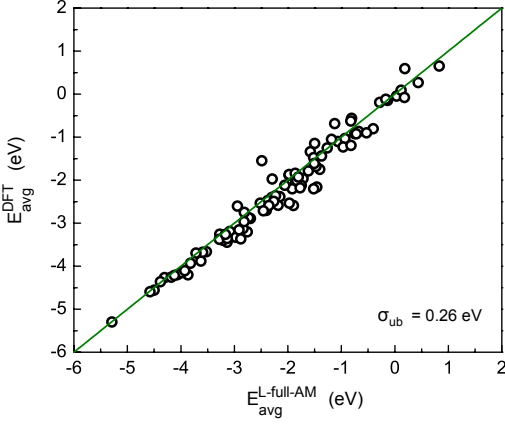


FIG. 6. Parity plot of average adsorption energy from DFT of co-adsorbed H, C, N, O, S, CH, CH₂, CO, NH, NH₂, NO, N₂, N₂O, OH and SH on Rh{111} versus the adsorption energy calculated using the interaction model, with the cross-interaction parameters are obtained from the arithmetic mean of the self-interaction parameters.

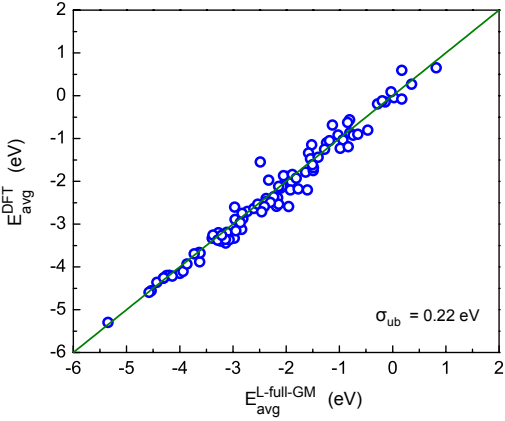


FIG. 7. Parity plot of average adsorption energy from DFT of co-adsorbed H, C, N, O, S, CH, CH₂, CO, NH, NH₂, NO, N₂, N₂O, OH and SH on Rh{111} versus the adsorption energy calculated using the interaction model, with the cross-interaction parameters are obtained from the geometric mean of the self-interaction parameters.

teraction parameters among the transition metals, however using the interaction parameters for Rh gives an average description of the adsorbate-adsorbate interactions. Therefore we propose a simple sub-model, where we use the interaction parameters obtained for the adsorption of the different species on rhodium, to describe

the interactions on all the (considered) transition metals.

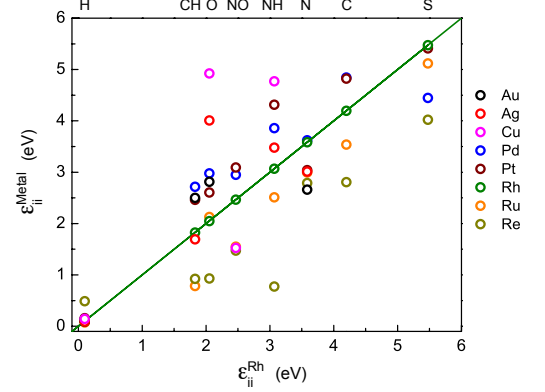


FIG. 8. Plot for adsorbate-adsorbate interaction parameter for H, C, N, O, S, CH, NH and NO on the closed packed facet of Au, Ag, Cu, Pd, Pt, Ru and Re with respect to the adsorbate-adsorbate interaction parameter for Rh{111}.

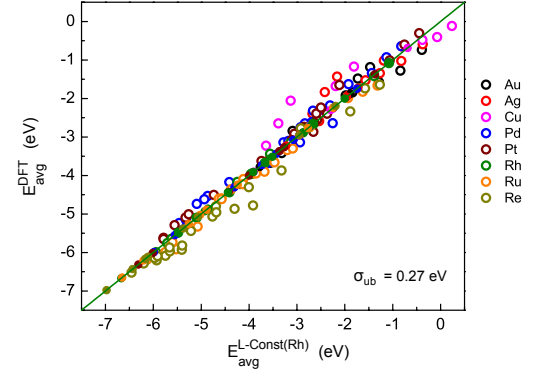


FIG. 9. Parity plot of the average adsorption energy from DFT at $\frac{1}{4}$ ML, $\frac{1}{2}$ ML, $\frac{3}{4}$ ML and 1 ML surface coverage versus the adsorption energy obtained using the interaction model based on the interaction parameters of Rh from table ??, at those corresponding surface coverages. The filled circles are for $\frac{1}{4}$ ML coverage on all the metals and 1 ML coverage on Rh only. The studied adsorbents are: H, C, N, O, S, CH, NH and NO.

In Figure 9 the adsorption energy calculated by DFT is plotted versus the coverage dependent adsorption energy obtained from this sub-model for a given coverage. We can see that even by using this simple model one can predict the coverage dependent adsorption energy with good accuracy for all the metals for a large range of coverages. In comparison to neglecting the effect of interaction on the adsorption energies, this simple model certainly gives

more accurate description of the adsorption energies as we reduce the unbiased standard deviation from 0.87 eV in Figure 4 to 0.27 eV using this model. We therefore propose this model as a very simple and extremely effective sub-model to describe the coverage dependent adsorption energy.

D. A scaling based model

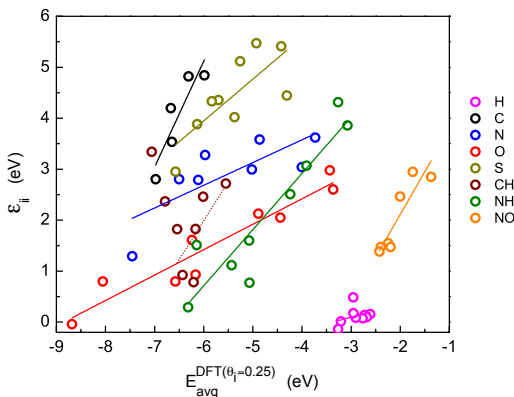


FIG. 10. Plot for adsorbate-adsorbate interaction parameter for H, C, N, O, S, CH, NH and NO on the closed packed facet of Pd, Pt, Rh, Ru, Re, Mo, W, Sc and Ti with respect to the adsorption energy of the corresponding adsorbates at $\frac{1}{4}$ ML coverage on the above transition metal surfaces.

^a the interaction parameter versus adsorption energy scaling do not hold for CH on W and Ti. We only can use the scaling up-to Mo, plotted in dotted lines.

Though the rhodium interaction model effectively describes the change in adsorption energy with coverage for the transition metals, we find that the adsorbate-adsorbate interaction on the less reactive metals, Pd and Pt, is in general stronger and on more reactive metals (Ru and Re) in general weaker than those on Rh, as seen in Figure 8. The interaction parameters for the noble metals are scattered on both sides of the Rh-line and do not seem to follow any general trend. The d-band model proposed by Hammer and Nørskov^{14–18} correlates the systematic change in the adsorption energy along any metal series to the position of the d-band center of the metal surface. Kitchin et al.^{3,4,19,20} showed that the d-band width of the surface metal atoms increases, together with a downshift of the d-band center, for increasing surface coverage. The change in the adsorption energy with coverage thus also follows the Hammer-Nørskov d-band model.

In Figure 10 it is seen that the adsorbate-adsorbate interaction parameter scales linearly with the adsorption energy. The interaction among the adsorbates thus de-

creases going from less to more reactive transition metals. In order to establish this systematic trend calculations of the interaction parameters for the adsorbates on Mo, W, Sc and Ti have been included. The scaling is surprisingly good for most adsorbates, however for CH on W and Ti the scaling does not hold and we suggest using the scaling for CH for less reactive metals than Mo (plotted in dotted lines in Figure 10). Also the interaction parameters for the noble metals do not follow the scaling. For these metals we found from fitting the scaled interaction parameters of Rh, Pd, Pt and Cu to the interaction parameters for the noble metals, that the interaction parameters for Pd gives the most accurate description of interactions on the noble metals. suggest a cut-off adsorption energy after which the interaction parameter remains constant. In order to obtain this cut-off the scaled interaction parameters for Rh, Pt, Pd and Cu were fitted to the interaction parameters for the noble metals. We found the scaled Pd interaction parameters to describe the interactions on the noble metals the best (to make this cutoff more general, a metal-specific adsorption energy is suggested here instead of some best fitted arbitrary adsorption energy).

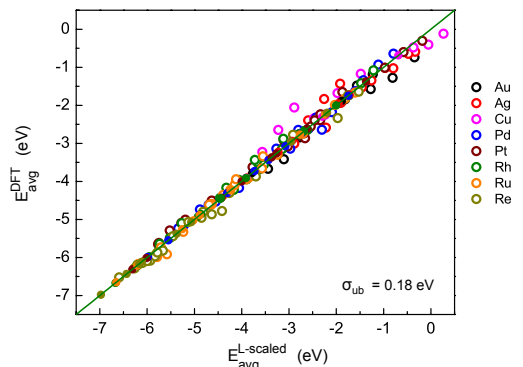


FIG. 11. Parity plot of the average adsorption energy from DFT at $\frac{1}{4}$ ML, $\frac{1}{2}$ ML, $\frac{3}{4}$ ML and 1 ML surface coverage versus the adsorption energy obtained using the interaction model based on the interaction parameters and adsorption energy scaled interaction parameters, at those corresponding surface coverages. The filled circles are for $\frac{1}{4}$ ML coverage. The studied adsorbents are: H, C, N, O, S, CH, NH and NO.

In Figure 11 the adsorption energy calculated with DFT is plotted versus the coverage dependent adsorption energy obtained from this scaling based linear interaction model. The unbiased standard deviation is 0.18 eV for the studied systems. As expected this model describes the adsorption energy more precisely than the Rh interaction model.

From scaling of the interaction parameters to the adsorption energy, we are now able to include the systematic change in the adsorbate-adsorbate interaction parameter for a complete adsorption energy range of inter-

ested metals to get a full descriptive adsorbate-adsorbate interaction model applicable to micro-kinetic modeling.

V. PIECEWISE INTERACTION MODEL

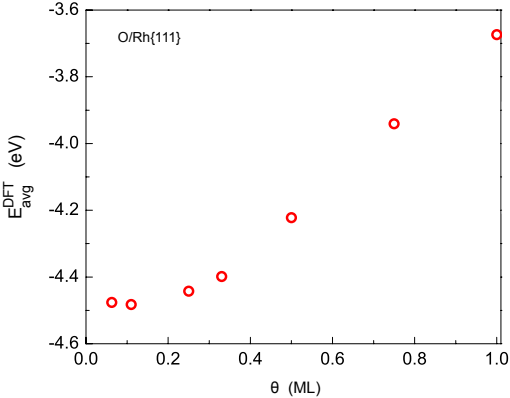


FIG. 12. Variation in the average adsorption energy for O adsorption with surface coverage for the full coverage range on Rh{111} facet.

Up until now we have used a linear interaction model to describe the coverage dependent adsorption energy in the $\frac{1}{4}$ - 1 ML coverage range. In Figure ?? and also in work by Grabow et al.² and Kitchin et al.³, it has been shown that below some threshold coverage θ^0 , the change in the adsorption energy with coverage is negligible. To correct our linear interaction model in the low coverage regime, I have proposed a piecewise interaction model, where the differential adsorption energy remains constant below the threshold coverage θ^0 and changes linearly with coverage after θ^0 . For coverages above the threshold coverage θ^0 , the linear and the piecewise interaction models are the same for single adsorbate system. This piecewise interaction model is similar to the one proposed by Grabow et al.². However our proposed piecewise interaction model uses a universal threshold coverage and hence can be used for systems with multiple adsorbates.

The equation for the differential adsorption energy $E_{diff}(\theta)$ can be written as,

$$E_{diff}^i(\theta) = E^0, \text{ when } |\theta| \leq \theta^0 \\ = E^0 + f \left(\frac{|\theta| - \theta^0}{\theta} \right), \text{ when } |\theta| > \theta^0 \quad (11)$$

where E^0 is the adsorption energy at coverage θ^0 , $|\theta| = \sum_i \theta_i$ where θ_i are the elements in θ , $f = \frac{(|\theta| - \theta^0)}{\theta}$ and $\underline{\epsilon}$ is the interaction matrix. In the matrix the interaction parameters, $\epsilon_{ij} = \epsilon_{ji}$. The cross-interaction parameters (ϵ_{ij}) will be obtained as the geometric mean of the corresponding self interaction parameters.

One can now express the differential adsorption energy for a single adsorbate with coverage θ_i as,

$$E_{diff}^i(\theta_i) = E_i^0, \text{ when } \theta_i \leq \theta^0 \\ = E_i^0 + \epsilon_{ii} (\theta_i - \theta^0), \text{ when } \theta_i > \theta^0 \quad (12)$$

For multiple adsorbates the differential adsorption energy can be expressed as,

$$E_{diff}^i(\theta) = E_i^0, \text{ when } \theta_i \leq \theta^0 \\ = E_i^0 + \sum_j f \epsilon_{ij} \theta_j, \text{ when } |\theta| > \theta^0 \quad (13)$$

In previous study by Grabow et al.² we have seen that the threshold coverage is very much dependent on the metal surfaces and also on the adsorbates. In order to determine a general threshold coverage I have calculated the average adsorption energy for a range of adsorbates on the transition metals at different low coverages.

For a single adsorbate system the average adsorption energy has the form:

$$E_{avg}(\theta_i) = E_i^0, \text{ when } \theta_i \leq \theta^0 \\ = E_i^0 + \frac{1}{2} \epsilon_{ii} (\theta_i - \theta^0), \text{ when } \theta_i > \theta^0 \quad (14)$$

In order to obtain the threshold coverage, I have calculated adsorption energies at coverages $\frac{1}{16}$ ML, $\frac{1}{9}$ ML, $\frac{1}{4}$ ML, $\frac{1}{3}$ ML and $\frac{1}{2}$ ML. For the condition, when the threshold coverage θ^0 is lower than 0.25 ML, the self-interaction parameters, ϵ_{ii} remains the same as the one obtained from the linear interaction model, using equation (4). However, when the threshold coverage θ^0 is higher than 0.25 ML, the self-interaction parameters, ϵ_{ii} , are obtained from equation:

$$\epsilon_{ii} = \frac{2 \left(E_{avg}(\theta = 1) - E_{avg}(\theta = 0.25) \right)}{(1 - \theta^0)} \quad (15)$$

As the $\theta^0 < 0.25$ ML, the adsorption energy at θ^0 should be equal to the adsorption energy calculated at 0.25 ML, i.e $E_{avg}(\theta^0) = E_{avg}(\theta = 0.25)$.

In previous study by Grabow et al.² we have seen that the threshold coverage is very much dependent on the metal surfaces and also on the adsorbates. In order to determine a general threshold coverage we calculated the average adsorption energy for a range of adsorbates on the transition metals at different low coverages. In Figure 13 the RMSE of the fitted piecewise interaction model is plotted versus the threshold coverage. Though according to a mean field model the threshold coverage was expected to be $\frac{1}{3}$ ML, we found that the threshold coverage with lowest RMSE for the systems studied here is 0.22 ML.

In Figure 14 and 15 we compare the estimated adsorption energies using the linear interaction model and the piecewise interaction model, respectively. The linear interaction model predicts a lower adsorption energy than

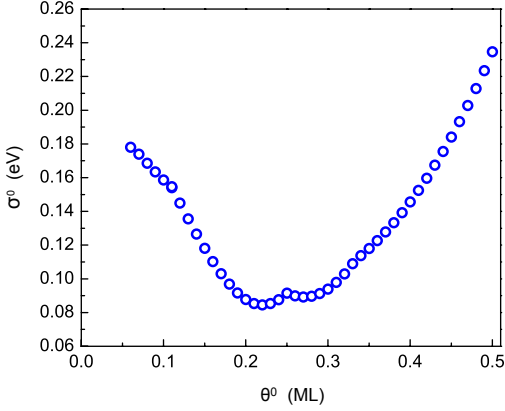


FIG. 13. The RMSE of the fitted piecewise interaction model versus the threshold coverage. The studied adsorbates: C, N, O, S, CH, NH and NO; metals: Au, Ag, Cu, Pd, Pt, Rh, Ru and Re and coverages are: $\frac{1}{16}$ ML, $\frac{1}{9}$ ML, $\frac{1}{4}$ ML, $\frac{1}{3}$ ML and $\frac{1}{2}$ ML.

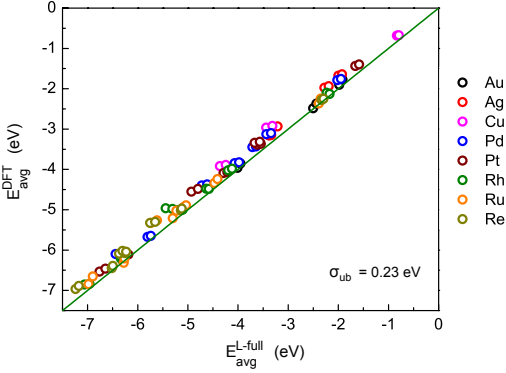


FIG. 14. Parity plot of the average adsorption energy from DFT at $\frac{1}{16}$ ML and $\frac{1}{9}$ ML surface coverage versus the adsorption energy obtained using the full interaction model, at those corresponding surface coverages. The studied adsorbents are: C, N, O, S, CH, NH and NO.

the actual DFT adsorption energy in the low coverage regime for most of the species. The piecewise interaction model is clearly better and predict the adsorption energy with good accuracy in the low coverage regime. The unbiased standard deviations for the linear and piecewise model are 0.23 eV and 0.08 eV respectively.

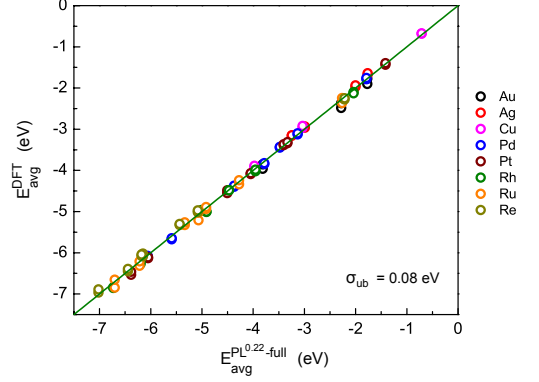


FIG. 15. Parity plot of the average adsorption energy from DFT at $\frac{1}{16}$ ML and $\frac{1}{9}$ ML surface coverage versus the adsorption energy obtained using the piecewise full interaction model with 0.22 as the threshold coverage, at those corresponding surface coverages. The studied adsorbents are: C, N, O, S, CH, NH and NO.

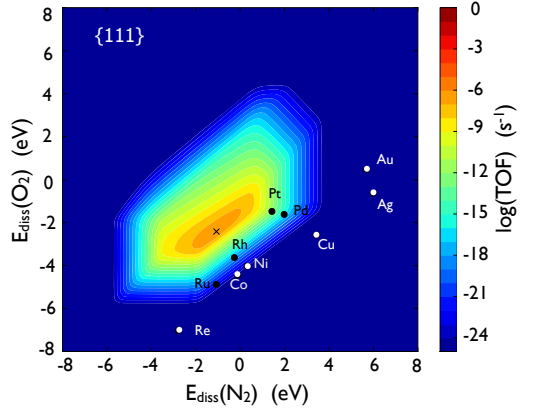


FIG. 16. Volcano curve for direct NO decomposition on transition metals with no adsorbate-adsorbate interactions

VI. THE DIRECT NO DECOMPOSITION: AN EXAMPLE

We take the direct NO decomposition as an example to illustrate the effect of adsorbate-adsorbate interaction in catalytic activity by including the interaction models in the microkinetic modeling. The reaction mechanism, scaling relations and formulation of the microkinetic model for the direct NO decomposition is described by Falsig et al.²¹. In Figure 16 the rate for the direct decomposition of NO is calculated using the non-interacting mean field model.²¹

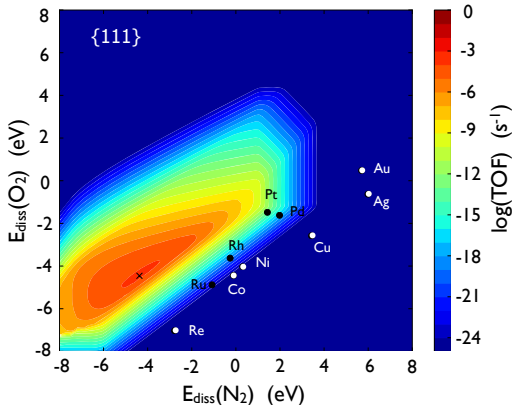


FIG. 17. Volcano curve for direct NO decomposition on transition metals using the Rhodium model to describe adsorbate-adsorbate interactions

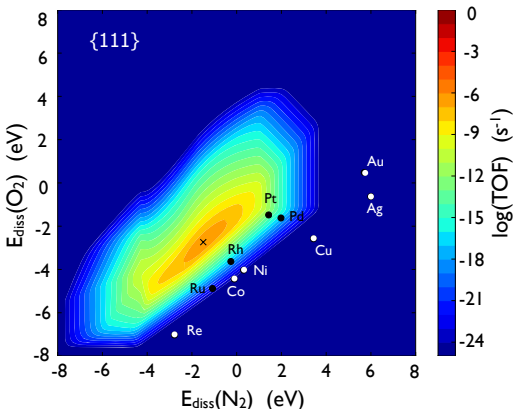


FIG. 18. Volcano curve for direct NO decomposition on transition metals using the scaled piecewise interaction model to describe adsorbate-adsorbate interactions

Here we apply two different sub-models to investigate the effect of adsorbate-adsorbate interaction on catalytic activity, namely the simplest description, rhodium interaction model and the most useful, scaling based piecewise interaction model. It has been shown previously that the TS-scaling relation calculated at low coverage also holds for higher coverages.^{22–24} The scaling relations from article²¹ therefore are also applied here. We start out with the interaction model ‘L-Const(Rh)-GM’. This linear interaction model is based on the interaction parameters for rhodium and they remains constant for the whole adsorption energy range. The cross-interaction parameters are obtained from the geometric mean of the self-interaction parameters.

In Figure 17 the catalytic activity is calculated using this rhodium interaction sub-model to include the coverage dependent adsorption energy in the microkinetic model. Due to the inclusion of the adsorbate-adsorbate interaction, the reactive metals are now less poisoned and regains some of their lost activity. The reactive metals are visibly more active here compared to the previous non-interacting mean field description shown in Figure 16. The inclusion of the interaction lifts up the lower left side of the volcano and makes it more flat. The right side of the volcano is not affected much and remains nearly the same. The maximum rate for the direct NO decomposition changes appreciably and it is $\sim 10^3$ times higher than the maximum rate in Figure 16. Pt is still the two catalyst, and catalytic rate for Pt is similar to the catalytic rate for Pt obtained with non-interacting mean field description. The increment in catalytic rate is more prominent for the reactive metals.

After the simplest rhodium interaction parameters for all the metals in the first sub-model in Figure 17, we took our most promising interaction model the ‘PW^{0.22}-scaled-GM’ for this study. This a piecewise interaction model based on the scaled interaction model. The interaction parameters for adsorption energy up-to Pd adsorption energy are obtained using the ϵ vs E_{ads} linear scaling and for adsorption energies above Pd we use the same interaction parameter obtained for Pd. The cross-interaction parameters are obtained as the geometric mean of the self-interaction parameters. The threshold coverage is 0.22 ML.

Due to the use of constant rhodium interaction parameters for all the metals in the first sub-model in Figure 17, the effect of adsorption-adsorption interaction is visible all the way down to the very reactive metals and it have a very wide adsorption energy regime within which the catalytic decomposition is feasible. But as the interaction parameters in practice are smaller for the more reactive metals, we overestimate the effect of adsorbate-adsorbate interaction when we use the rhodium interaction model. The scaling based interaction model takes into account these changes in the interaction parameters with the adsorption energy and provide more accurate catalytic rates for the direct decomposition of NO in Figure 18. From Figure 16 and 18 we can clearly see that though the inclusion of a right adsorbate-adsorbate interaction model ‘PW^{0.22}-scaled-GM’, increases the catalytic rates for the reactive metals, the effect is not as prominent as using the rhodium interaction model and the shape of the volcano curve remains nearly unchanged. In Figure 18 the inclusion of the adsorbate-adsorbate interaction also widens the catalytic active area, but the maximum rate for the direct decomposition of NO at the top of the volcano and also the catalytic rate for our best metal Pt remains unchanged from the non-interacting mean field model in Figure 16. The inclusion of the adsorbate-adsorbate interaction do not change the catalytic trends among the transition metals.

VII. CONCLUSION

We have presented parametrization of a simple linear interaction model to describe the coverage dependent adsorption energy. To make the interaction model useful for catalytic trends study we reduce the number of independent interaction parameter first by introducing two ways of obtaining the cross-interaction parameters, from the geometric mean or the arithmetic mean the self interaction parameters and then by proposing two simple sub-models. The geometric mean method is slightly better than the arithmetic mean method. The rhodium based sub-model is proposed as one of the simplest interaction model, where interaction parameters for rhodium are used for all the metals. This rhodium interaction model suggested to be used as an first step to study the effect of adsorbate-adsorbate interaction in the catalytic trend study before moving to more complicated interaction models. While using the rhodium interaction model we observe that there is a large variation in the interaction parameter among the transition metals and the interaction parameter among the transition metals decreases linearly with increase in the adsorption energy of that adsorbate on those metals. A scaling based interaction model is proposed where we included the systematic change in the interaction parameter among the different transition metals by using the linear scaling between the interaction parameter and adsorption energy of that adsorbates calculated at low coverage. The noble metals, Au, Ag and Cu however do not follow this general trend and for them it is suggested to use interaction parameters obtained for Pd. The scaling based model can be used in a consistent manner in the microkinetic model for catalytic trend study to incorporate the coverage dependent adsorption energy in theoretical catalyst modeling. To correct the low coverage region, where the adsorption remains constant until some threshold coverage we proposed a piecewise interaction model, where the adsorption energy remains constant up-to the threshold coverage and then it changes linearly. The op-

timum threshold coverage for the systems studied here was found to be 0.22 ML. With all these different proposed models, considering their limitations, precision and applicability we propose two of the most useful lateral interaction sub-model for catalytic trend study, the simplest, ‘L-Const(Rh)-GM’, a rhodium based interaction model and the most useful, ‘PW^{0.22}-scaled-GM’, a scaling based piecewise interaction model.

We studied the effect of introduction of the adsorbate-adsorbate interaction in catalytic trend study using the above two interaction model taking direct decomposition of NO as an example. We showed that when we choose the rhodium interaction model, we overestimate the amount of interaction for the reactive metals and the lower-left side of the volcano become highly reactive all the way down for the most reactive transition metals. One always should also be careful about choosing a interaction model and always keep in mind its accuracy and limitations. We also showed that inclusion of a correct interaction model also have distinct effect on the catalytic rates for the reactive metals and increases the catalytic rates for the left side of the volcano, the effect is not dramatic. The catalytic rate at the top of the volcano and also the best catalyst remains the same in both models. Though the introduction of the lateral interaction have very little effect at the top of the volcano it widens the adsorption energy range where the catalytic activity for the reaction is appreciable and thus gives us possibility of having more choices in our search for the best catalyst.

ACKNOWLEDGMENTS

The Authors thank the Strategic research council of Denmark for support through grant 09-067233, the support form office of Basic Energy Sciences of the U.S. Department of Energy to the SUNCAT Center for Interface Science and Catalysis at SLAC/Stanford, support from Center for Atomic-scale Materials Design at DTU, CASE and Danish Center for Scientific Computing are gratefully acknowledged.

-
- ¹ A.D. Smeltz, R.B. Getman, W.F. Schneider, F.H. Ribeiro, *Catalysis Today* **136**, 84 (2008)
 - ² L.C. Grabow, B. Hvolbæk, J.K. Nørskov, *Top Catal* **53**, 298 (2010)
 - ³ S.D. Miller, J.R. Kitchin, *Surface Science* **603**, 794 (2009)
 - ⁴ S.D. Miller, N. İnoğlu, J.R. Kitchin, *J. Chem. Phys.* **134**, 104709 (2011)
 - ⁵ H. Falsig, B. Hvolbæk, I.S. Kristensen, T. Jiang, T. Bligaard, C.H. Christensen, J.K. Nørskov, *Angew Chem Int Ed* **47**, 4835 (2008)
 - ⁶ V.P. Zhdanov, *Progress in Surface Science* **35**, 143 (1991)
 - ⁷ G. Rupprechter, M. Morkel, H.J. Freund, R. Hirschl, *Surface Science* **554**, 43 (2004)
 - ⁸ S.E. Mason, I. Grinberg, A.M. Rappe, *J.Phys. Chem. B.* **110**, 3816 (2006)
 - ⁹ A. Hellman, K. Honkala, *J. Chem. Phys.* **127**, 194704 (2007)
 - ¹⁰ <https://wiki.fysik.dtu.dk/ase/ase/calculators/jacapo.html>
 - ¹¹ D. Vanderbilt, *Phys Rev B.* **41**, 7892 (1990)
 - ¹² B. Hammer, L.B. Hansen, J.K. Nørskov, *Phys. Rev. B* **59**, 7413 (1999)
 - ¹³ H.J. Monkhorst, J.D. Pack, *Phys Rev B.* **13**, 5188 (1976)
 - ¹⁴ B. Hammer, J.K. Nørskov, *Surface Science* **343**, 211 (1995)
 - ¹⁵ A. Nilsson, L.G.M. Pettersson, B. Hammer, T. Bligaard, C.H. Christensen, J.K. Nørskov, *Catalysis Letters* **100**, 111

- (2005)
- ¹⁶ A. Ruban, B. Hammer, P. Stoltze, H.L. Skriver, J.K. Nørskov, *Journal of Molecular Catalysis A: Chemical* **115**, 421 (1997)
- ¹⁷ B. Hammer, O.H. Nielsen, J.K. Nørskov, *Catalysis Letters* **46**, 31 (1997)
- ¹⁸ B. Hammer, J.K. Nørskov, *Advances in Catalysis* **45**, 71 (2000)
- ¹⁹ J.R. Kitchin, *Phys Rev B*. **79**, 205412 (2009)
- ²⁰ N. İnoğlu, J.R. Kitchin, *Phys Rev B*. **82**, 045414 (2010)
- ²¹ H. Falsig, J. Shen, W. Guo, G. Jones, T. S. Khan, S. Dahl, J. K. Nørskov, T. Bligaard, To be published (2013)
- ²² J.K. Nørskov, T. Bligaard, A. Logadottir, S. Bahn, L.B. Hansen, M. Bollinger, H. Bengaard, B. Hammer, Z. Sljivancanin, M. Mavrikakis, Y. Xu, S. Dahl, C.J.H. Jacobsen, *Journal of Catalysis* **209**, 275 (2002)
- ²³ B. Hammer, *Phys Rev B*. **63**, 205423 (2001)
- ²⁴ L. Diekhoner, H. Mortensen, A. Baurichter, A.C. Luntz, *J. Vac. Sci. Technol. A* **18**, 1509 (2000)

Paper III

On the Effect of Coverage Dependent Adsorbate-Adsorbate Interactions for CO Methanation on Transition Metal Surfaces

Adam C. Lausche, Andrew J. Medford, [Tuhin Suvra Khan](#), Yue Xu, Thomas Bligaard, Frank Abild-Pedersen, Jens K. Nørskov, and Felix Studt

submitted (2013)

On the Effect of Coverage Dependent Adsorbate-Adsorbate Interactions for CO Methanation on Transition Metal Surfaces

Adam C. Lausche,^{a,b} Andrew J. Medford,^b Tuhin Suvra Khan,^{a,c} Yue Xu,^{a,d} Thomas Bligaard,^{a,b} Frank Abild-Pedersen,^a Jens K. Nørskov,^{a,b} and Felix Studt^{a*}

^a SUNCAT Center for Interface Science and Catalysis, SLAC National Accelerator Laboratory, Menlo Park, CA, United States

^b Department of Chemical Engineering, Stanford University, Stanford, CA, United States

^c Center for Atomistic-scale Materials Design (CAMD), Department of Physics, Technical University of Denmark, Lyngby, Denmark

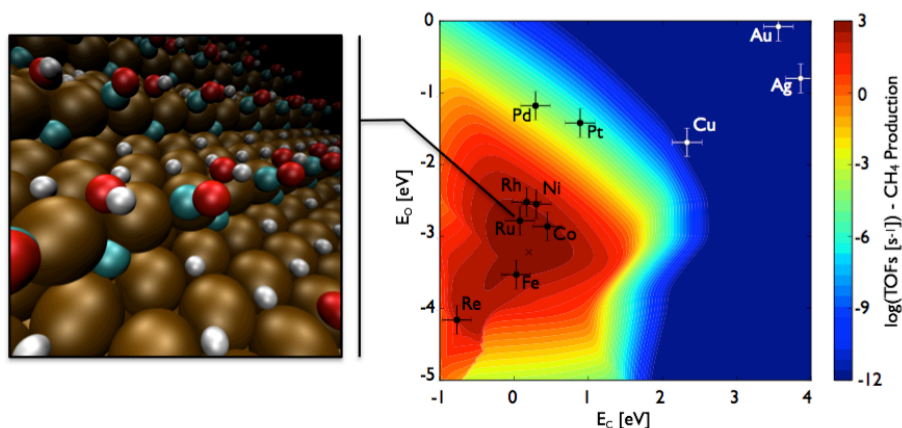
^d State Key Laboratory of Chemical Engineering, East China University of Science and Technology, Shanghai, China

* Corresponding author: studt@slac.stanford.edu

phone: 001 650 926-3668

address: 2575 Sand Hill Road, MS 31, Menlo Park, CA 94025, USA

Graphical Abstract



Abstract

Heterogeneously catalyzed reactions involving the dissociation of strongly bonded molecules typically need quite reactive catalysts with high coverages of intermediate molecules. Methanation of carbon monoxide is one example, where C-O dissociation has been reported to take place on step sites with a high coverage of CO. At these high coverages, reaction intermediates experience interaction effects that typically reduce their adsorption energies. Herein the effect of these interactions on the activities of transition metals for CO methanation is investigated.

For transition metals that have low coverages of reactants, the effect is minimal. But for materials with high coverages under reaction conditions, rates can change by several orders of magnitude. Nevertheless, the position of the maximum of the activity volcano does not shift significantly, and the rates at the maximum are only slightly perturbed by adsorbate-adsorbate interactions. In order to accurately describe selectivities, however, adsorbate-adsorbate interactions will likely need to be included.

Highlights:

- Trends in catalytic activity for CO methanation are examined for transition metal surfaces
- We model adsorbate-adsorbate interactions between methanation intermediates on multiple sites
- DFT and microkinetic modeling predict the CO methanation rates of transition metals
- Trends in methanation rates are preserved when interaction effects are included
- Interactions were found to increase the rates of the most reactive metals

Keywords: CO methanation; coverage effects; adsorbate-adsorbate interactions; heterogeneous catalysis; scaling relations; density functional theory

I. Introduction

Advances in electronic structure theory have made it possible to calculate the adsorption energies and activation barriers of reaction intermediates on transition-metal surfaces with sufficient accuracy for the estimation of surface reaction kinetics [1, 2]. There have already been several examples where catalytic reactions have been modeled successfully based on density functional theory calculations [3-6]. Trends in the kinetics of transition metal surfaces across the transition metal series have been expressed in terms of changes in adsorption and transition-state energies, as successfully explained by the d-band model [7]. While in principle there are many different parameters that affect the kinetics of a given reaction, correlations between various adsorption energies [8-10] and transition-state energies [11-16] have made it possible in several cases to reduce the number of variables that determine the kinetics of a catalytic reaction to one or two [1, 8, 17, 18]. The rates and selectivities usually follow a volcano-shaped curve, where the optimal catalysts bind the intermediates neither too strongly nor too weakly. Establishing suitable descriptors and combining these with microkinetic modeling allows for the determination of the optimal descriptor values defining the maximum in catalytic activity, which opens the possibility of a directed search for new catalytic materials. Already several examples of the computational discovery of new catalyst leads have been reported using this approach [6, 19-22].

The simplest microkinetic models assume that there are no adsorbate-adsorbate interactions. At temperatures where the surface mobilities of reaction intermediates

are high and coverages are low, the kinetic model can be solved using a mean field approach. For situations with high surface coverages of intermediates, however, adsorbate-adsorbate interactions cannot necessarily be neglected and the kinetic problem becomes substantially more complex. While it is often found that optimal catalytic rates are associated with surfaces where the coverage of a key reactant is approximately 0.5 ML [13], this may not be true for more complex reactions where multiple surface intermediates interact with each other. One example of this type of reaction is the conversion of synthesis gas (a mixture of CO and H₂) to hydrocarbons in the so-called Fischer-Tropsch process. In order to have a significant rate for carbon-carbon coupling, the coverages of carbon on the surface would need to be sufficiently high, so that adsorbate-adsorbate interactions may play a significant role in this type of reaction [23-25].

In order to investigate the effect of surface coverage on the reaction rates, we use the production of CH₄ from CO and H₂ as a test reaction. We shall assume throughout this analysis that the reaction takes place at the steps of the catalyst surface, since this is the only site where C-O bond splitting proceeds efficiently for the best catalysts for this process [26]. Reaction intermediates for CO methanation can adsorb on different sites of the stepped surface as shown in Figure 1. These are on-top of the step (Figure 1a), in the four-fold hollow beneath the step (Figure 1b), and on terrace sites (Figure 1c) [26]. This complex reaction network makes CO methanation a challenging reaction to model and an attractive test case for the analysis of the effects of adsorbate-adsorbate interactions on its kinetics. We will investigate the adsorption energies of the reaction intermediates on the different facets (on-top, four-fold, and terrace) as a function of coverage, and model interactions between intermediates that are adsorbed on the different facets of the catalyst. We will assume a simple model of adsorbate-adsorbate interactions and show how catalytic trends are changed when we take those into account.

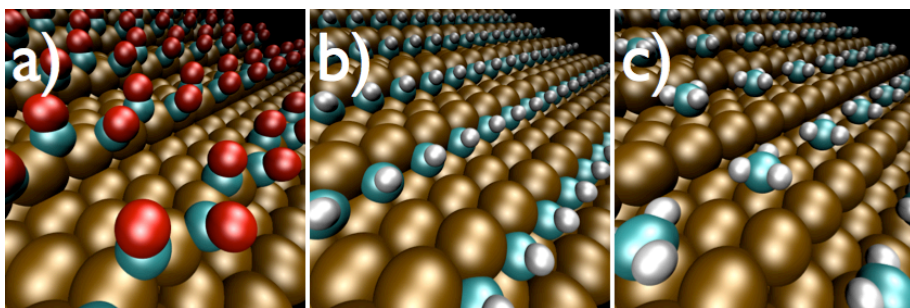


Figure 1 – Adsorption for reaction intermediates on the a) on-top (illustrated by CO*), b) four-fold (illustrated by CH*), and c) terrace sites (illustrated by CH₃*) on the (211) surface of Rh.

II. Methods

Self-consistent, periodic density functional theory (DFT) calculations were performed using the Dacapo code [27], which describes the valence electrons using a plane-wave implementation and represents the ionic cores using Vanderbilt ultrasoft pseudopotentials. A kinetic energy cutoff of 340 eV and a density cutoff of 500 eV were used. DFT calculations were performed using the RPBE functional, which uses a generalized gradient approximation [28]. The self-consistent electron density was determined by iterative diagonalization of the Kohn-Sham Hamiltonian, with the occupation of the Kohn-Sham states being smeared according to a Fermi-Dirac distribution with a smearing factor of $k_B T = 0.1$ eV [29]. All energies were extrapolated to $k_B T = 0$ eV. Sampling of the Brillouin zone was done using a $4 \times 4 \times 1$ Monkhorst-Pack k-point set. Stepped (211) surfaces of Ag, Cu, Pd, Pt, Rh, and Ru were modeled as nine-layer slabs (corresponding to three layers in the (111) direction) with (1×3) unit cells. A vacuum of 15 Å separated successive slabs. All adsorbates and the top two layers were allowed to relax, while the bottom two layers were kept fixed in their bulk truncated positions.

In order to investigate the effect of adsorbate-adsorbate interactions on the adsorption energies of reaction intermediates, adsorption energies were calculated at coverages of $\frac{1}{4}$ ML, $\frac{1}{3}$ ML, $\frac{1}{2}$ ML, $\frac{2}{3}$ ML, $\frac{3}{4}$ ML, and 1 ML in the adsorption sites where the intermediates were most stable at $\frac{1}{4}$ ML coverage. A 1 ML coverage for the 211 surface is defined as one adsorbate per atom along the step. These calculations were performed on (1×2) (for $\frac{1}{2}$ ML and 1 ML), (1×3) (for $\frac{1}{3}$ ML and $\frac{2}{3}$ ML), and (1×4) (for $\frac{1}{4}$ ML and $\frac{3}{4}$ ML) model slabs. As described elsewhere, the adsorbate-adsorbate interaction effects were fitted using a piecewise continuous interaction model, similar to those reported in the literature [30, 31]. This model describes the total adsorption energy per site as a function of coverage. It is observed that differential adsorption energies are constant when the coverage is below a threshold coverage and is linear with coverage above that threshold. The differential adsorption energy for a single adsorbate as a function of coverage takes the form:

$$E_i(\theta_i) = E_i^0 \quad \text{when } \theta_i \leq \theta_0 \quad \text{Equation 1a}$$

$$E_i(\theta_i) = E_i^0 + \varepsilon(\theta_i - \theta_0) \quad \text{when } \theta_i > \theta_0 \quad \text{Equation 1b}$$

where E_i is the adsorption energy of adsorbate i at coverage θ_i , E_i^0 is the adsorption energy below a threshold coverage θ_0 , and ε is the self-interaction parameter, which is the slope of the adsorption energy above the threshold coverage:

$$\varepsilon = \frac{dE_i}{d\theta_i} \quad \text{Equation 2}$$

For a reaction with multiple adsorbates, the model is expressed as:

$$E_i(\theta_i) = E_i^0 \quad \text{when } |\theta| \leq \theta_0 \quad \text{Equation 3a}$$

$$E_i(\theta_i) = E_i^0 + \sum_j f \varepsilon_{ij} \theta_j \quad \text{when } |\theta| > \theta_0 \quad \text{Equation 3b}$$

where $|\theta|$ is the sum of the coverages of all the adsorbates, $f = (|\theta| - \theta_0)/|\theta|$, and ε_{ij} is the cross-interaction parameter between species i and j , which is calculated as the geometric average of the self-interaction parameters for species i and j :

$$\varepsilon_{ij} = (\varepsilon_{ii} * \varepsilon_{jj})^{1/2} \quad \text{Equation 4}$$

The methanation reaction was assumed to involve four reaction sites (i.e., on-top of the step, the four-fold hollow beneath the step, the terrace, and a hydrogen adsorption site). CO*, OH*, and O* adsorbed on the top row of the step (the “on-top” site), either bridged between the top row atoms or behind them in the three-fold hollow site. C* and CH* adsorbed in the four-fold hollow between the atoms of the bottom row. And CH₂* and CH₃* adsorbed on the terrace in either the on-top or three-fold hollow positions. It has been both experimentally and theoretically shown that hydrogen has negligible interactions with itself and other adsorbates on many surfaces [32-37]. As such, the use of a “hard-sphere” model, where one adsorbate occupies a site to the exclusion of other adsorbates, may not be appropriate for describing the coverage of hydrogen in the microkinetic model. In most cases, a reaction intermediate adsorbed on a particular catalytic site sterically hinders the adsorption of other intermediates with the same characteristic length on that same site. In cases where adsorbates have significantly different characteristic lengths, however, such a “hard-sphere” model may not accurately describe the co-adsorption of such intermediates. We propose that the adsorption of hydrogen in the presence of CO methanation intermediates represents such a case. One strategy for modeling this behavior is to assert that hydrogen adsorbs on a separate set of terrace sites, which is superimposed on the original terrace. Thus, the coverage of hydrogen may approach 1, even while other terrace adsorbates are present in relatively high coverages.

Interactions between adsorbates on the on-top, four-fold, and terrace sites were expressed as:

$$E_i(\theta_i) = E_i^0 \quad \text{when } |\theta| \leq \theta_0 \quad \text{Equation 5a}$$

$$E_i(\theta_i) = E_i^0 + \sum_j f \varepsilon_{ij} \theta_j \quad \text{when } |\theta| > \theta_0 \quad \text{Equation 5b}$$

where $f = (|\theta| - \theta_0)/|\theta|$, and $|\theta|$ is the sum of coverages of adsorbates on the step and terrace sites. For example, interactions between adsorbates on the terrace (CH₂* and CH₃*) are scaled by the sum of the coverages of those adsorbates. Likewise, interactions between adsorbates on the on-top and four-fold sites (CO*, OH*, O*, C* and CH*) are scaled by the sum of the coverages of these adsorbates. It should be noted that since this involves interactions between two sites, the maximum value for $|\theta|$ for the step is 2.

In order to describe the discontinuity at the threshold coverage θ_0 , the model described above (Equation 5) was modified slightly to make it piecewise continuous and differentiable over the whole coverage range:

$$E_i(\theta_i) = E_i^0 \quad \text{when } |\theta| \leq \theta_0 - \frac{\varepsilon_{ij}}{4} \quad \text{Equation 6a}$$

$$E_i(\theta_i) = E_i^0 + (|\theta| - \theta_0 + \varepsilon_{ij}/4)^2 * \left(\frac{\theta_i}{|\theta|}\right) \quad \text{when } \theta_0 - \frac{\varepsilon_{ij}}{4} < |\theta| \leq \theta_0 + \frac{\varepsilon_{ij}}{4} \quad \text{Eqn 6b}$$

$$E_i(\theta_i) = E_i^0 + \sum_j f_k \varepsilon_{ij} \theta_j \quad \text{when } |\theta| > \theta_0 + \frac{\varepsilon_{ij}}{4} \quad \text{Equation 6c}$$

As described elsewhere, the adsorption energies of all reaction intermediates considered here can be scaled with the binding energies of carbon (ΔE_C) and oxygen (ΔE_O) [8-10]. Further details about the scaling used herein can be found in the Supplementary Material. Transition state energies for each elementary reaction step are scaled with the energies of the reaction products (see Supplementary Material for further details) [1, 11-16].

Transition state energies for reactions on the (111) terrace (H-H, CH₂-H, CH₃-H) and (211) step (C-H, CH-H, H-OH, and O-H) on Ag, Cu, Pd, Pt, and Rh were taken from the literature [15, 38]. A number of CO dissociation pathways have been proposed in

the literature for CO dissociation, including direct ($\text{CO}^* \leftrightarrow \text{C}^* + \text{O}^*$),

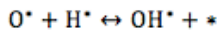
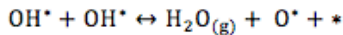
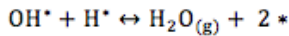
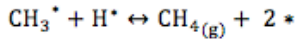
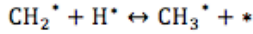
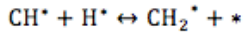
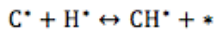
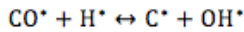
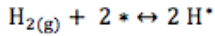
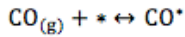
$\text{COH}^* (\text{CO}^* + \text{H}^* \leftrightarrow \text{COH}^* \leftrightarrow \text{C}^* + \text{OH}^*)$, $\text{CHO}^* (\text{CO}^* + \text{H}^* \leftrightarrow \text{CHO}^* \leftrightarrow \text{CH}^* + \text{O}^*)$, and

hydrogen-assisted one-step CO dissociation ($\text{CO}^* + \text{H}^* \leftrightarrow \text{C}^* + \text{OH}^*$) [26, 39-43]. As has been shown earlier, the dominant C-O splitting pathway for Ni is a hydrogen-assisted CO dissociation [26]. In order to justify this approach throughout the range of carbon and oxygen binding energies considered here, however, we incorporated the alternative CO splitting pathways suggested above into the microkinetic model. It was found that these additional pathways made insignificant contributions to the total rate due to their prohibitively high reaction barriers (see Figure S4, Supplemental Material).

Transition state energies for the C-O-H and TS O-H-OH reactions were calculated using the fixed bond length (FBL) method (transition state energies can be found in the Supplementary Material). The transition state energies for C-O-H bond breaking are calculated with a CO* coverage of 1 along the step, since it has been shown earlier that C-OH dissociation has the lowest activation barrier at 1 ML CO* coverages. This is due to the fact that in this case the transition state energy is not decreased as much as the initial state (adsorbed CO*) by the adsorbate-adsorbate interactions caused by 1 ML of CO* [21, 26]. C-OH bond splitting does hence proceed on a BEP line calculated for high CO* coverage that is lower in energy than the corresponding low coverage BEP line (see Figure S3a). Since high CO coverages along the step occur for all metals close to/or on top of the volcano, the high coverage BEP is used throughout. An activity volcano constructed using the BEP line in the low coverage limit is shown in the Supplementary Material (Figure S3). In such a scenario, the activity volcano has its top at much more reactive metals, which highlights the importance of using an appropriate description of the C-OH bond splitting barrier. Since high coverage of CO* is included in the BEP line, double counting of adsorbate-adsorbate interactions has to be avoided. Section 3 of the Supplementary Material explains how this is achieved in the current model.

Zero point energies, entropies and internal energies of adsorbed intermediates on the Cu(211) surface were calculated from the vibrational frequencies using the harmonic oscillator approximation, and were assumed to be constant for all surfaces.

The microkinetic model, therefore, consists of the following elementary steps, similar to that reported elsewhere [1, 13, 21]:



We solved the microkinetic model to determine the predicted rates and coverages for the (211) surface using a self-consistent mean field approach. Since adsorbate-adsorbate interactions in the model outlined above only depend on the average occupation of a given intermediate, it is possible to use coverages as the variables. Given the approximations in the adsorbate-adsorbate interaction model, the basic assumption behind the mean field approach we took is that every site is randomly occupied with a probability given by the average coverage. For this to be a good approximation, two requirements must be met. First, the surface diffusion of adsorbed reaction intermediates needs to be fast. This is not a problem for the surfaces and temperatures considered here. Typical diffusion barriers for the species we treated are 0.5 eV [44]. The second requirement is that there is no island formation. For cases with a single adsorbed species, island formation is never observed when the differential adsorption energy as a function of coverage is monotonically increasing (i.e., self-interaction is non-attractive), as is the case for all the reaction intermediates considered here. There are known cases in the literature, however, where island formation occurs and it should be noted that the mean-field model would not give reasonable results for these instances. For two or more species the tendency towards island formation depends on the relationship between the self-interaction of each adsorbate and the strength of the interaction between different adsorbates at a given temperature. In our case the main adsorbates are CO^* , C^* , CH^* , and O^* , which react with H^* . Due to the low interactions that H^* has

with other adsorbates [28, 31], our model assumes it adsorbs on a separate site. In such a case, the formation of islands is trivially precluded.

Steady-state solutions of the microkinetic model were found using a multi-dimensional Newton's method algorithm as implemented in the findroot function from the python mpmath library for arbitrary-precision arithmetic modeling (the stiffness of the equations required up to 100 decimals of precision) [45]. These solutions were obtained for reaction conditions typical of reactor operation ($T = 523$ K, $P = 1$ bar, 1% CO, 97% H_2 , 1% CH_4 , and 1% H_2O) under differential conditions (corresponding to 10^{-9} % approach to equilibrium) [46, 47].

III. Results and Discussion

The effect of coverage on the adsorption energies of CO, C, OH, and O on the (211) surfaces of Pt, Pd, Rh, and Ru for coverages ranging from 0.25 – 1.0 ML is shown in Figure 2. In this figure the adsorption energies predicted by the model are compared to those from the full DFT calculations, and the quality of the model can be judged directly. Clearly the model is always qualitatively correct and in most cases it is semi-quantitative.

It was found that the adsorption energies for intermediates on the on-top and four-fold sites are relatively constant for coverages less than 0.5 ML, in general agreement with other theoretical studies [30, 48-50]. This result is somewhat different as compared to the (111) facet, where adsorbate-adsorbate interactions start to become significant at coverages above 0.25 ML [30]. Above the threshold coverage of 0.5 ML, the adsorption energies decrease linearly with coverage. The magnitude of these interactions ranges from 0.1 to 0.7 eV at 1 ML coverage for the different intermediates. One surface that has been investigated in detail is Rh(111) [31]. A comparison of the adsorbate-adsorbate interactions on the Rh(211) and Rh(111) surfaces indicates that interactions on the (211) surface are typically smaller than those on the (111) surface (see Table 1). The differences between the interaction parameters on the two surfaces can be explained by the geometry of the (211) step, where there are no direct neighbors below a coverage of 0.5 ML and a maximum of two neighbors at a coverage of 1. As can be seen from Table 1, the self-interaction parameter for hydrogen is essentially zero for most metals, which is consistent with earlier reports [32]. The interaction parameters were observed to be larger for metals with lower carbon and oxygen binding energies (e.g., Pd and Pt), as compared to stronger binding metals (e.g., Ru and Rh) as has been observed for the (111) surface [31]. In order to include these variations in the interaction model, the interaction parameters were scaled with the carbon and oxygen binding energies (values are given in Table S14). Details regarding the scaling relations for these interaction parameters are given in the Supplemental Material.

Table 1 – Adsorbate-adsorbate self-interaction parameters (ε_{ii}) for the (211) surfaces of Pd, Pt, Rh, and Ru. All energies are in eV. Data for the Rh(111) surface is taken from reference [31].

Adsorbate	Pd(211)	Pt(211)	Ru(211)	Rh(211)	Rh(111)
CH*	0.94	0.75	0.42	0.57	0.92
C*	1.34	0.81	0.65	0.63	2.10
CO*	0.66	0.52	0.21	0.17	1.27
OH*	0.85	0.82	0.50	0.53	0.60
O*	0.91	0.91	1.02	1.13	1.03
H*	0.02	0.05	0.18	-0.04	0.05

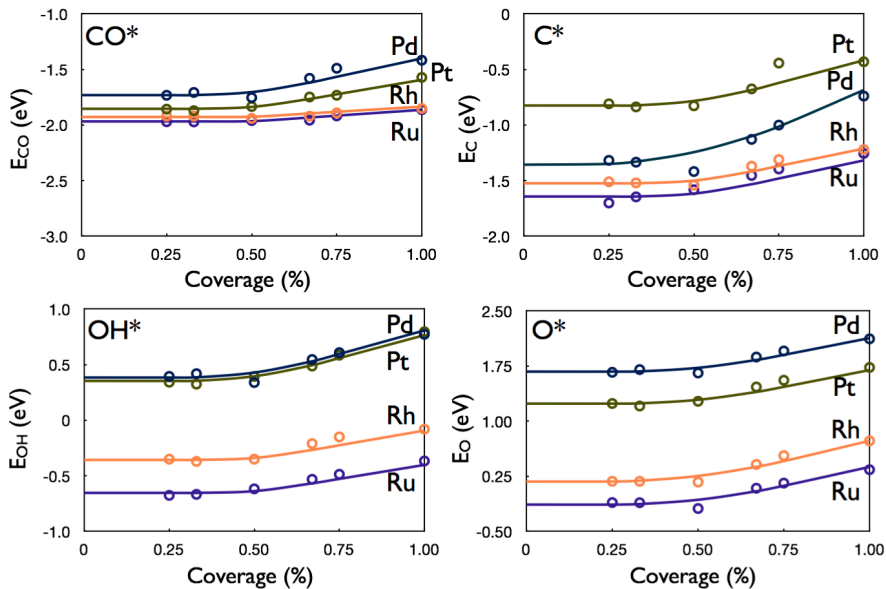


Figure 2 – Adsorption energies of CO, C, OH, and O for the stepped (211) surfaces of Pd, Pt, Rh, and Ru as a function of coverage. All adsorption energies are given relative to CO, H₂O and H₂ in the gas phase. Adsorption sites for CO*, OH* and O* are on-top of the step, while C* is adsorbed in the four-fold hollow site at the base of the step. The best-fit line is obtained from the adsorbate-adsorbate interaction model (see Methods section, Equation 6).

We further include all cross interactions between the adsorbed reaction intermediates in our model. In addition to cross interaction of intermediates adsorbed on the same type of site, we include cross interactions between adsorbates

on the on-top, four-fold, and terrace sites. All cross interactions can be described by the sum of coverages on the on-top, four-fold, and terrace sites when calculating the interaction effects in Equation 6 with a threshold coverage of 0.5 ML. Figure 3 shows a comparison of all possible cross-interactions of CO*, OH*, O*, and C* on the 211 surfaces, as predicted by the interaction model versus those obtained by full DFT calculations. As can be seen, the predictions obtained with this simple model are reasonable, with an average error of 0.3 eV and a maximum error of 0.9 eV.

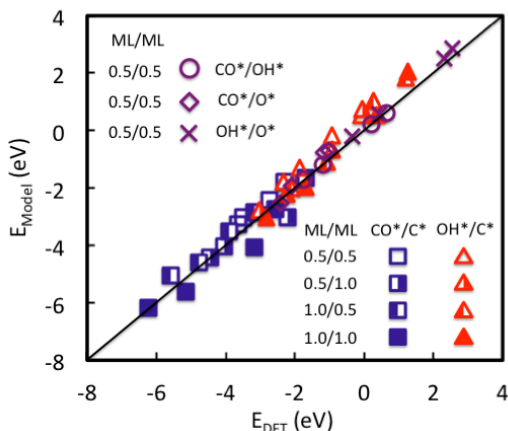


Figure 3 – Comparison of adsorption energies of C*, CO*, OH*, O* on the stepped (211) surfaces of Pd, Pt, Rh, and Ru with coverages of 0.5 and 1.0 ML. Energies predicted by the adsorbate-adsorbate interaction model (y-axis) are compared to those derived from the full DFT calculations (x-axis). All adsorption energies are given relative to CO, H₂O and H₂ in the gas phase. CO*, OH* and O* are adsorbed on the on-top site, while C* is adsorbed in the four-fold site. Circles, routes and stars represent adsorption on the ontop sites. Squares and triangles represent cross interactions between adsorbates on the on-top and four-fold sites. The average error between model and DFT-calculated values was 0.3 eV, and the maximum error was 0.9 eV.

In the first part we introduced a model that describes adsorbate-adsorbate interactions in simple terms. In the second part of the paper we will now analyze their influence on the surface coverages of reaction intermediates and reaction energetics, as well as the predicted reaction rates. As described in earlier studies [1, 8, 17, 18], we employ scaling relations between adsorbates [8-10] and transition-state energies [11-16] in order to describe the methanation reaction by only two parameters, the binding energies of carbon (ΔE_{C}) and oxygen (ΔE_{O}). These scaling relations have been proven extremely useful in the description of trends and are extensively described in earlier work [9]. The use of these scaling relations allows for the description of reaction parameters as a function of ΔE_{C} and ΔE_{O} . Previous models of CO methanation have involved assumptions about the rate-determining step (either C-O dissociation, OH_x, or CH_x hydrogenation) [13, 21, 26]. Herein,

however, we make use of a full microkinetic model, where all elementary reaction steps are treated as being potentially rate determining.

Figures 4 and 5 show the coverages of CH^* , C^* , O^* and CO^* as a function of ΔE_{C} and ΔE_{O} as calculated by microkinetic modeling for both scenarios, with and without adsorbate-adsorbate interactions at typical methanation reaction conditions. Note that C^* and CH^* bind most favorably to the four-fold site, while O^* and CO^* compete for on-top adsorption. As can be seen from Figures 4 and 5, C^* and O^* cover the surfaces of metals that have high carbon and oxygen binding energies, respectively. For example, metals like Re and Fe bind oxygen very strongly, so that their surface steps sites are primarily covered with O^* . Metals with more moderate oxygen binding energies (e.g., Ru, Rh, Ni, Co, Pd and Pt) are primarily covered with CO^* on the on-top site. For transition metals that are most active in the methanation reaction, the coverages of CO^* , O^* , CH^* , and C^* are somewhat in the area of 0.5 ML on the on-top and four-fold sites. For very strong oxygen and carbon binding energies there is the possibility of adsorbate induced surface reconstruction. These reconstructions and their effect on predicted rates are, however, not within the focus of this paper.

The inclusion of adsorbate-adsorbate interactions does not change this picture qualitatively. The onset binding energy where surfaces start to become covered with adsorbates is relatively unchanged; the increase in adsorbate coverages, however, is more gradual with a relatively smooth increase from 0 to 1 ML. This effect can most clearly be seen in the coverage of CO^* on the on-top site. Without the consideration of adsorbate-adsorbate interactions the coverage of CO changes from 0.01 ML to 0.99 ML in 0.8 eV of carbon binding energy (Figure 4b). When adsorbate-adsorbate interactions are included, however, the CO coverage increases from 0.01 ML to 0.99 ML in 1.4 eV, almost twice that range (Figure 4e). We note that Fig. 5f clearly shows the dividing line between the metals that only form methane (low CH_x coverage) and those that form higher hydrocarbons (higher CH_x coverage). In the group Ni, Co, Rh, Ru and Fe, Ni is furthest away from the high CH_x coverage regime while Ru, Co and Fe are further into the high coverage region. The rate-determining step (RDS) for CO methanation varied closely with the coverages of the reaction intermediates. For materials with relatively weak carbon and oxygen binding energies, the RDS was the dissociation of CO. Materials with strong carbon energies, however, were limited by the rate of CH_4 desorption. Likewise, materials with strong oxygen binding energies were limited by the rate of H_2O desorption. These trends were unaffected by the inclusion of interaction effects.

The energies of the transition states for the elementary reactions steps scale with the energies of the reaction products at low coverages [1, 11-16]; here we assume that this relationship holds true at high coverages as well. As has been discussed in the experimental section, this is actually not true for the activation barrier of the C-OH splitting step. Here the BEP line for the high coverage regime is significantly lower as compared to the low coverage regime. Inclusion of the correct BEP line at high coverages is essential if one wants to yield the correct activity volcano (an

activity volcano using a low coverage BEP line is shown in Figure S3 of the Supplementary Material). Apart from the splitting of the C-OH bond, however, all of the other steps are simple hydrogenation reactions. Since the adsorbate-adsorbate interactions for hydrogen are negligible to a first order, we assume here that all hydrogenation steps simply follow the low coverage BEP line. This might be an oversimplification and future studies need to be conducted to address this issue.

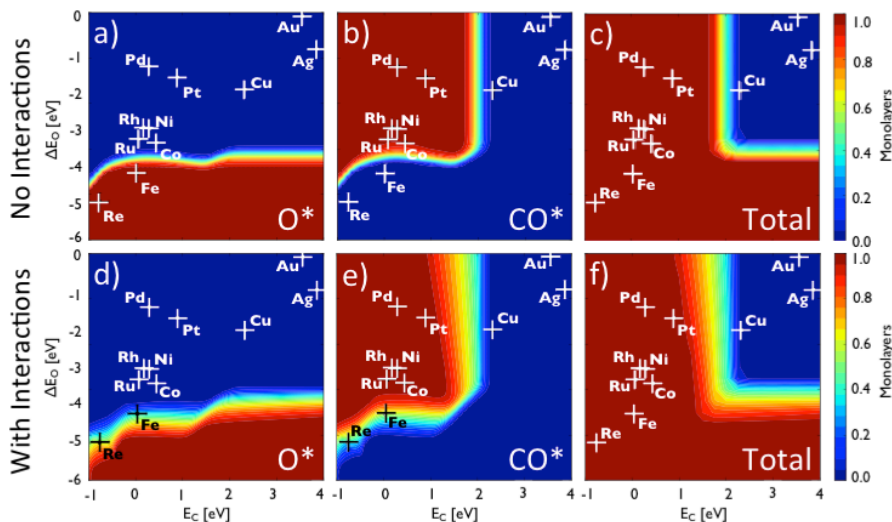


Figure 4 – Coverages of O*, CO*, and the total coverage on the on-top site as a function of the carbon (ΔE_c) and oxygen (ΔE_o) binding energies as obtained by the solutions to the microkinetic model without (a-c) and with (d-f) adsorbate-adsorbate interactions. The carbon and oxygen binding energies for the (211) surfaces of selected transition metals are depicted. Reaction conditions are 523 K and 1 bar with a gas composition of 1% CO, 97% H₂, 1% CH₄, and 1% H₂O, corresponding to 10⁻⁹ % approach to equilibrium.

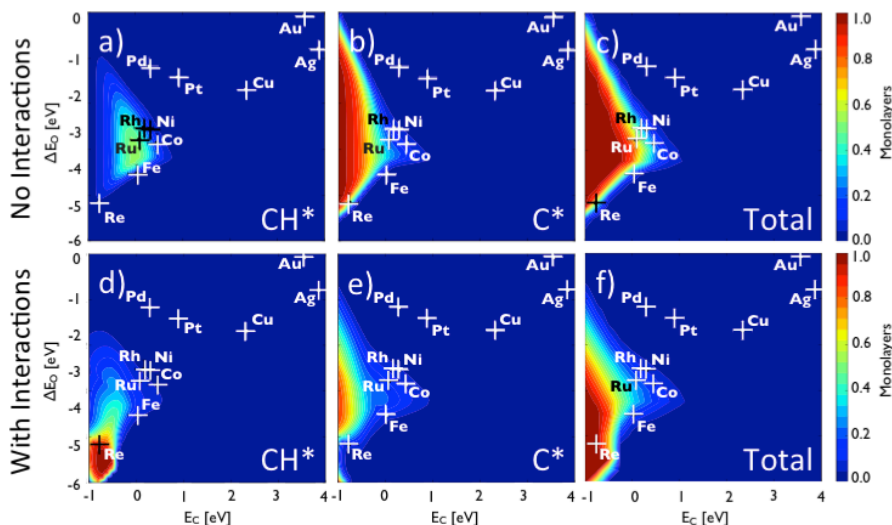


Figure 5 – Coverages of CH^* , C^* , and the total coverage on the four-fold site as a function of the carbon (ΔE_c) and oxygen (ΔE_o) binding energies as obtained by the solutions to the microkinetic model without (a-c) and with (d-f) adsorbate-adsorbate interactions. The carbon and oxygen binding energies for the (211) surfaces of selected transition metals are depicted. Reaction conditions are 523 K and 1 bar with a gas composition of 1% CO , 97% H_2 , 1% CH_4 , and 1% H_2O , corresponding to 10^{-9} % approach to equilibrium.

The theoretical activity volcanoes for the (211) surface also reflect the effects of adsorbate-adsorbate interactions for CO methanation, as illustrated in Figures 6a and 6b for the cases of methanation without and with interactions, respectively. A comparison of these predicted rates is shown in Figure 6c. Both models with and without interaction effects predict Ru and Co to be the most active metals, while rates for Rh, Ni, and Fe are predicted to be moderately active, in agreement with earlier theoretical [13, 21, 26] and experimental [46, 51] studies. The turnover frequencies are for the stepped (211) surfaces, which usually constitute about 5% of the total catalyst surface area. The volcano with adsorbate-adsorbate interactions is different from the one without interactions in that it extends to the more reactive metal surfaces by falling off less steeply at strong carbon and oxygen binding energies. But the general features of the volcano, including the position of the maximum, are essentially unchanged. The weak-binding region ($\Delta E_c > 2$ eV, $\Delta E_o > -3$ eV), where coverages of all intermediates are close to zero and well below the threshold of 0.5 ML, is essentially unchanged, as there are no adsorbate-adsorbate interactions.

The differences in predicted rates illustrated in Figure 6c could be understood in the following way. An increase in surface coverages above the threshold coverage ($|\theta| > 0.5$) results in a decrease in the binding energies of intermediates and their corresponding transition state energies. High coverages of reaction intermediates are observed in regions of the volcano where desorption of the products is the rate-determining step. A decrease in chemisorption energies in these regions leads to a decrease in these desorption barriers and hence increases the predicted rates. Since these effects are typically observed at coverages higher than 0.5 ML, adsorbate-adsorbate interactions only affected the strong-binding leg of the volcano, which shifted upwards in rate. This was observed for the regions where C* and O* removal are the rate-determining steps, i.e. at high carbon and high oxygen binding energies, respectively. But the effect on the top of the volcano, where adsorbate coverages are approximately 0.5 ML, was minimal. For example, the predicted rates for a metal near the top of the volcano, like Ru, increased by only 6% when adsorbate-adsorbate interactions were included. In contrast, for a metal on the strong-binding region, like Fe, the predicted rates increased by nearly two orders of magnitude. Similar trends have been observed for CO oxidation and NO decomposition [30, 31].

We did, however, observe decreases in the predicted rates for the region of low carbon and high oxygen binding energies ($\Delta E_C > 2$ eV, $\Delta E_O < -3$ eV) upon inclusion of interaction effects, which was rather unexpected (Figure 6c). Due to the high oxygen binding energies, the oxygen coverages are high, leading to a decrease in chemisorption energies of all intermediates. This would make oxygen removal easier, and hence one would expect to see an increase the water desorption rate. Due to the relatively low carbon binding energies, however, the rate-determining step in this region is breaking of the C-OH bond, which is decreased upon inclusion of adsorbate-adsorbate interactions. Consequently, the overall rate decreases in this region when adsorbate-adsorbate interactions are incorporated in the volcano.

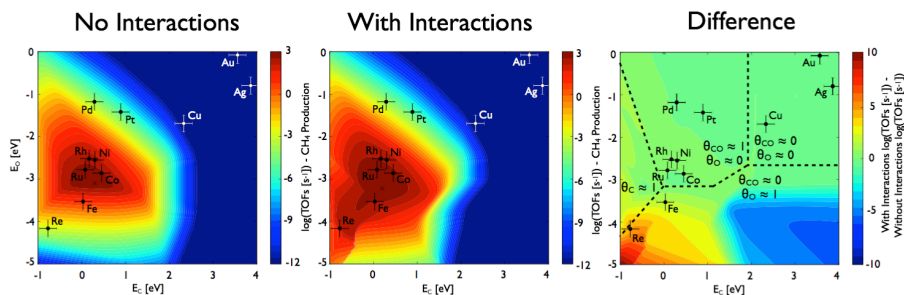


Figure 6 – Theoretical activity volcanoes for the production of methane from CO and H₂ without (a) and with (b) the inclusion of adsorbate-adsorbate interactions, as well as (c) the difference in rates between the two scenarios. Turnover frequencies for the 211 surfaces are plotted a function of the carbon (ΔE_C) and oxygen (ΔE_O) binding energies as obtained by the solutions to the microkinetic model. The carbon and oxygen binding energies for the (211) surfaces of selected transition metals are

depicted. Reaction conditions are 523 K and 1 bar with a gas composition of 1% CO, 97% H₂, 1% CH₄, and 1% H₂O, a 10⁻⁹ % approach to equilibrium.

IV. Summary

In summary, we analyzed the influence of adsorbate-adsorbate interactions on the reactivity trends of transition metal surfaces as expressed by the volcano curve. Taking CO methanation as an example, we calculated adsorbate-adsorbate interactions between the reaction intermediates on the different sites of the stepped (211) facet. The interactions were found to become significant above coverages of 0.5 ML, while the effects were negligible below this threshold coverage. This threshold coverage is slightly higher than that found for the close-packed (111) facet, which can be attributed to the fact that there is a maximum of two neighbors along the step as opposed to 6 on the (111) facet. Importantly, these interactions were found to scale with the adsorption strength of the intermediates, where stronger adsorption leads to weaker interactions. In order to study the influence of these interactions on predicted reaction rates, we incorporated them into a microkinetic model developed earlier, which already used a BEP line for the C-OH splitting reaction at high CO coverages in order to describe the maximum of the volcano correctly. Further inclusion of adsorbate-adsorbate interactions, however, primarily increased the CO methanation rates of those materials that have high coverages of reaction intermediates, as one would expect. Importantly, the turnover frequencies of reactive metals with a high surface coverage of intermediates are underestimated by several orders of magnitude when adsorbate-adsorbate interactions are not included. The general shape of the volcano, including the position of the volcano peak, however, are essentially unchanged. This can be attributed to the fact that coverages near the top of the volcano are about 0.5 ML, and subsequently increase for more reactive metals. This finding supports the use of the mean field model without interaction effects in cases of simple reaction schemes, such as the methanation reaction, since the general trends are essentially unchanged when compared to the full treatment of interaction effects. For more complicated reaction schemes that involve multiple possible reaction products, such as Fischer-Tropsch synthesis, however, the inclusion of adsorbate-adsorbate interactions would likely play an important role in predicted product selectivities of a given catalyst surface. We have shown that coverages of reaction intermediates that strongly affect Fischer-Tropsch selectivity can be greatly influenced by adsorbate-adsorbate interactions, especially on metals with high adsorption energies for those intermediates. We therefore suggest that their inclusion is essential when selectivities of reactions that require high surface coverages are investigated.

Acknowledgements

Support from the U.S. Department of Energy (DOE), Office of Basic Energy Sciences to the SUNCAT Center for Interface Science and Catalysis is gratefully acknowledged.

References

- [1] J.K. Nørskov, F. Abild-Pedersen, F. Studt, T. Bligaard, *Proc. Natl. Acad. Sci. USA* 108 (2011) 937-943.
- [2] J.K. Nørskov, T. Bligaard, J. Rossmeisl, C.H. Christensen, *Nat. Chem.* 1 (2009) 37-46.
- [3] K. Reuter, D. Frenkel, M. Scheffler, *Phys. Rev. Lett.* 93 (2004) 116105.
- [4] K. Honkala, A. Hellman, I.N. Remediakis, A. Logadottir, A. Carlsson, S. Dahl, C.H. Christensen, J.K. Nørskov, *Science* 307 (2005) 555-558.
- [5] S. Kondo, J. Greeley, M.A. Sanchez-Castillo, S.T. Evans, A.A. Gokhale, J.A. Dumesic, M. Mavrikakis, *Top. Catal.* 37 (2006) 17-28.
- [6] F. Studt, F. Abild-Pedersen, Q. Wu, A.D. Jensen, B. Temel, J.-D. Grunwaldt, J.K. Nørskov, *J. Catal.* 293 (2012) 51-60.
- [7] B. Hammer, J.K. Nørskov, *Nature* 376 (1995) 238-240.
- [8] P. Ferrin, A.U. Nilekar, J. Greeley, M. Mavrikakis, J. Rossmeisl, *Surf. Sci.* 602 (2008) 3424-3431.
- [9] F. Abild-Pedersen, J. Greeley, F. Studt, J. Rossmeisl, T.R. Munter, P.G. Moses, E. Skúlason, T. Bligaard, J.K. Nørskov, *Phys. Rev. Lett.* 99 (2007) 016105.
- [10] G. Jones, F. Studt, F. Abild-Pedersen, J.K. Nørskov, T. Bligaard, *Chem. Eng. Sci.* 66 (2011) 6318-6323.
- [11] J.K. Nørskov, T. Bligaard, A. Logadottir, S. Bahn, L.B. Hansen, M. Bollinger, H. Bengaard, B. Hammer, Z. Sljivancanin, M. Mavrikakis, Y. Xu, S. Dahl, C.J.H. Jacobsen, *J. Catal.* 209 (2002) 275-278.
- [12] A. Michaelides, Z.P. Liu, C.J. Zhang, A. Alavi, D.A. King, P. Hu, *J. Am. Chem. Soc.* 125 (2003) 3704-3705.
- [13] T. Bligaard, J.K. Nørskov, S. Dahl, J. Matthiesen, C.H. Christensen, J. Sehested, *J. Catal.* 224 (2004) 206-217.
- [14] V. Pallassana, M. Neurock, *J. Catal.* 191 (2000) 301-317.
- [15] S. Wang, V. Petzold, V. Tripkovic, J. Kleis, J.G. Howalt, E. Skúlason, E.M. Fernández, B. Hvolbæk, G. Jones, A. Toftelund, H. Falsig, M.E. Björketun, F. Studt, F. Abild-Pedersen, J. Rossmeisl, J.K. Nørskov, T. Bligaard, *Phys. Chem. Chem. Phys.* 13 (2011) 20760-20765.
- [16] S. Wang, B. Temel, J. Shen, G. Jones, L.C. Grabow, F. Studt, T. Bligaard, F. Abild-Pedersen, C.H. Christensen, J.K. Nørskov, *Catal. Lett.* 141 (2011) 370-373.
- [17] L.C. Grabow, F. Studt, F. Abild-Pedersen, V. Petzold, J. Kleis, T. Bligaard, J.K. Nørskov, *Angew. Chem. Int. Ed.* 50 (2011) 4601-4605.
- [18] A.C. Lausche, J.S. Hummelshøj, F. Abild-Pedersen, F. Studt, J.K. Nørskov, *J. Catal.* 291 (2012) 133-137.
- [19] J. Greeley, M. Mavrikakis, *J. Am. Chem. Soc.* 126 (2004) 3910-3919.
- [20] S. Linic, J. Jankowiak, M.A. Barteau, *J. Catal.* 224 (2004) 489-493.

- [21] M.P. Andersson, T. Bligaard, A. Kustov, K.E. Larsen, J. Greeley, T. Johannessen, C.H. Christensen, J.K. Nørskov, *J. Catal.* 239 (2006) 501-506.
- [22] F. Studt, F. Abild-Pedersen, T. Bligaard, R.Z. Sorensen, C.H. Christensen, J.K. Nørskov, *Science* 320 (2008) 1320-1322.
- [23] T.C. Bromfield, D.C. Ferre, J.W. Niemantsverdriet, *ChemPhysChem* 6 (2005) 254-260.
- [24] H. Orita, Y. Inada, *J. Phys. Chem. B* 109 (2005) 22469-22475.
- [25] C.D. Zeinalipour-Yazdi, R.A. van Santen, *J. Phys. Chem. C* 116 (2012) 8721-8730.
- [26] M.P. Andersson, F. Abild-Pedersen, I.N. Remediakis, T. Bligaard, G. Jones, J. Engbæk, O. Lytken, S. Horch, J.H. Nielsen, J. Sehested, J.R. Rostrup-Nielsen, J.K. Nørskov, I. Chorkendorff, *J. Catal.* 255 (2008) 6-19.
- [27] The Dacapo Plane Wave/Pseudopotential Code is Available as Open Source Software. , <http://wiki.fysik.dtu.dk/dacapo>.
- [28] B. Hammer, L.B. Hansen, J.K. Nørskov, *Physical Review B: Condensed Matter Material Physics* 59 (1999) 7413-7421.
- [29] G. Kresse, J. Furthmuller, *Comp Mater Sci* 6 (1996) 15-50.
- [30] L.C. Grabow, B. Hvolbæk, J.K. Nørskov, *Top. Catal.* 53 (2010) 298-310.
- [31] T.S. Khan, H. Falsig, S. Wang, W. Guo, S. Dahl, T. Bligaard, To be published (2013).
- [32] B. Hammer, *Phys Rev B* 63 (2001) 205423.
- [33] K. Christmann, O. Schober, G. Ertl, M. Neumann, *J. Chem. Phys.* 60 (1974) 4528-4540.
- [34] K. Christmann, *Surf. Sci. Rep.* 9 (1988) 1-163.
- [35] M. Ehsasi, K. Christmann, *Surf. Sci.* 194 (1988) 172-198.
- [36] A. Gross, *J. Chem. Phys.* 135 (2011) 174707-174707.
- [37] A.B. Mhadeshwar, J.R. Kitchin, M.A. Barteau, D.G. Vlachos, *Catal. Lett.* 96 (2004).
- [38] J.S. Hummelshøj, F. Abild-Pedersen, F. Studt, T. Bligaard, J.K. Nørskov, *Angew. Chem. Int. Ed.* 51 (2012) 272-274.
- [39] M.R. Elahifard, M.P. Jigato, J.W. Niemantsverdriet, *Chemphyschem* 13 (2012) 89-91.
- [40] J.M. Gracia, F.F. Prinsloo, J.W. Niemantsverdriet, *Catal. Lett.* 133 (2009) 257-261.
- [41] M. Ojeda, A. Li, R. Nabar, A.U. Nilekar, M. Mavrikakis, E. Iglesia, *J. Phys. Chem. C* 114 (2010) 19761-19770.
- [42] M. Ojeda, R. Nabar, A.U. Nilekar, A. Ishikawa, M. Mavrikakis, E. Iglesia, *J. Catal.* 272 (2010) 287-297.
- [43] R.A. van Santen, M.M. Ghouri, S. Shetty, E.M.H. Hensen, *Catalysis Science & Technology* 1 (2011) 891-911.
- [44] A.U. Nilekar, J. Greeley, M. Mavrikakis, *Angew. Chem. Int. Ed.* 45 (2006).
- [45] F. Johansson, mpmath: a Python library for arbitrary-precision floating-point arithmetic, 0.14 ed., <http://code.google.com/p/mpmath/>, 2010.
- [46] D.C.D. da Silva, S. Letichevsky, L.E.P. Borges, L.G. Appel, *Int. J. Hydrogen Energy* 37 (2012) 8923-8928.
- [47] J. Rathouský, A. Zukal, J. Stárek, *Appl. Catal. A Gen.* 94 (1993) 167-179.

- [48] O.R. Inderwildi, D. Lebiedz, O. Deutschmann, J. Warnatz, J. Chem. Phys. 122 (2005) 034710.
- [49] O.R. Inderwildi, D. Lebiedz, O. Deutschmann, J. Warnatz, J. Chem. Phys. 122 (2005) 154702.
- [50] C. Stampfl, H.J. Kreuzer, S.H. Payne, H. Pfnur, M. Scheffler, Phys. Rev. Lett. 83 (1999) 2993-2996.
- [51] J. Sehested, S. Dahl, J. Jacobsen, J.R. Rostrup-Nielsen, J. Phys. Chem. B 109 (2005) 2432-2438.

Paper IV

In silico Search for Novel Methane Steam Reforming Catalysts

Yue Xu, Adam C. Lausche, Shengguang Wang, Tuhin Suvra Khan, Frank Abild-Pedersen, Felix Studt, Jens K. Nørskov and Thomas Bligaard

submitted (2013)

In silico Search for Novel Methane Steam Reforming Catalysts

Yue Xu^{1,2}, Adam C. Lausche^{1,3}, Shengguang Wang⁴, Tuhin S. Khan^{1,5}, Frank Abild-Pedersen¹, Felix Studt¹, Jens K. Nørskov^{1,3}, and Thomas Bligaard^{1,3,*}

¹ SUNCAT Center for Interface Science and Catalysis, SLAC National Accelerator Laboratory, Menlo Park, CA 94025, U.S.A.

² State Key Laboratory of Chemical Engineering, East China University of Science and Technology, Shanghai, China

³ Department of Chemical Engineering, Stanford University, Stanford, CA 94305, U.S.A.

⁴ Department of Chemical and Biomolecular Engineering, University of Delaware, Newark, DE 19716, U.S.A.

⁵ Center for Atomic-scale Materials Design, Department of Physics, Building 307, Technical University of Denmark, DK-2800 Kgs. Lyngby, Denmark

E-mail: bligaard@slac.stanford.edu

PACS: 71.15.Mb, 71.15.Nc, 71.20.Be, 81.05.Zx, 82.20.Db, 82.20.Tr, 88.20.fs, 88.30.g



Online supplementary data available from stacks.iop.org/NJP/XYZ....

Abstract

This paper demonstrates a method for screening transition metal and metal alloy catalysts based on their predicted rates and stabilities for a given catalytic reaction. This method involves combining reaction and activation energies (available to the public via a web-based application “*CatApp*”) with a microkinetic modeling technique to predict the rates and selectivities of a prospective material. This paper illustrates this screening technique using the steam reforming of methane to carbon monoxide and hydrogen as a test reaction. While catalysts are already commercially available for this process, the method demonstrated in this paper is very general and could be applied to a wide range of catalytic reactions. Following the steps outlined herein, such an analysis could potentially enable researchers to understand reaction mechanisms on a fundamental level and, on this basis, develop leads for new metal alloy catalysts.

Keywords:

Methane, steam reforming, syngas, scaling relations, BEP-relations, heterogeneous catalysis, density functional theory, catalysis informatics, computational materials discovery

1 Introduction

One of the ultimate goals in catalysis research is to help accelerate the search for novel active and selective catalysts for heterogeneous reactions [1]. Central to achieving this goal is a molecular level understanding of the interactions between the surface of a catalyst and the intermediates and transition states of a given reaction. Recent advances in electronic structure theory have made it possible to carry out reactions “*in silico*” on large numbers of heterogeneous catalysts, and then screen these to find leads for new materials with high predicted rate, selectivity, and stability. This method involves finding correlations between the energetics of the relevant reaction barriers and adsorption energies, finding appropriate descriptors for these correlations, and then utilizing these descriptors to simulate reaction kinetics in the reduced-dimensional descriptor space [2-5]. This approach has already assisted researchers in finding promising catalyst leads for heterogeneously catalyzed reactions [2, 6-9] and lends hope that a mapping of the catalyst genome could lead to general catalyst design strategies, where atomic-scale simulations would play a key role in an integrated approach to catalyst search.[10]

In the present study we use the steam reforming of methane as a test reaction for demonstrating the utility of this strategy. CH₄ steam reforming is one of the most commonly used processes for the inexpensive production of H₂ and synthesis gas [11]. A number of transition metals have been reported to be active for this reaction. The highest CH₄ steam reforming rates have been observed for Rh and Ru-based catalysts, with Ni, Pt, Ir, and Pd also showing high rates.[12-16] Commercial catalysts are typically formulated using Ni as the active phase, since it is the least expensive of these metals.[17] The Ni-catalyst is also very active for the steam and dry reforming of other reactants.[18, 19] High reactor temperatures are required to achieve a high CH₄ conversion (from 750 °C to 1000 °C), because the reaction is strongly endothermic (Equation 1). Furthermore, high steam-to-carbon ratios (H₂O/CH₄ > 3) are often needed to prevent catalyst deactivation through the deposition of graphitic carbon, which increases the capital and operating costs for H₂ generation.



While the steam reforming of CH₄ using Ni-based catalysts is a relatively mature technology, important challenges still remain and are the subject of active research. Among these are the areas of improving catalyst rates while increasing the resistance to catalyst deactivation via sulfur poisoning, carbon formation and sintering [17, 20]. One strategy in particular that has been investigated for increasing catalyst resistance to deactivation is through alloying the active metal (e.g., Ni), with another metal (e.g., Sn [21], Au [22, 23], Ag [24], Ru [25, 26]). Typically these experiments have resulted in an improvement in the long-term stability of the catalyst, albeit with a sacrifice in catalytic reaction rates.

In order to develop materials with high rates and stabilities under reaction conditions, it is essential to develop a better understanding of the steam reforming reaction mechanism. Previous studies, both experimental and theoretical, have proposed a range of reaction pathways for CH₄ steam reforming. Early theoretical work by Bengaard et al., for example, indicated that the rate-determining step for CH₄ steam reforming on Ni(111) and Ni(211) surfaces involves the breaking of the initial C-H bond of CH₄ [27]. They also reported that the CO formation proceeds through a direct C-O combination pathway. Other researchers suggest that CH₄ reforming on a Ni(111) surface, however, may involve a hydrogen insertion pathway involving CHO*, as opposed to the direct C-O formation pathway [28-30]. Experiments by Wei and Iglesia show that at high temperatures (823 – 1023 K) the rate-limiting step in both steam and dry reforming of CH₄ is the activation of the first C-H bond [31]. At somewhat lower temperatures (below 773 K), however, it has been suggested that the CO formation may proceed through a hydrogen insertion mechanism involving COH* [16]. Moreover, a study by Bhattacharjee et al. is consistent with experimental results suggesting that on a Rh(211) surface at high temperatures the formation of CO proceeds through the direct C-O combination pathway. At lower temperatures, however, a hydrogen insertion mechanisms involving COH* may be favorable [32]. Shetty et al. studied both the direct and H-assisted pathway for CO formation on Ru(1121), showing that the direct CO formation pathway has a lower overall barrier [33]. Chen et al. studied the steam reforming pathways on Pt(111) and Pt(211), indicating that COH pathway is important for CO production [34]. Research by Inderwildi et al. suggests that CHO* pathway is thermodynamically more favorable on Ru(0001), Pt(111), and Pd(111) surfaces.[35]

As described elsewhere, microkinetic modeling calculations can incorporate multiple reaction routes, so it is unnecessary to know beforehand which pathways may become dominant under a given set of conditions [4, 36]. By solving the model we can obtain reaction rates for each route and thus predict which elementary steps may become rate determining for different surfaces and under different reaction conditions. In a number of studies this method has been used to gain insight into heterogeneously catalyzed reactions.[3, 4, 37-39] Herein we consider three potential CO formation pathways: direct formation via C* and O*, as well as hydrogen insertion pathways involving CHO* or COH*. In principle many different parameters may affect the reaction rates and selectivities of a given catalyst. Nevertheless, it has been reported that correlations between various adsorption [40-42] and transition-state energies [27, 43-45] offer the possibility to reduce the number of these parameters to one or two [3, 4, 41]. In this paper, we coupled the microkinetic model with a descriptor-based approach in order to predict reaction rates in terms of just two parameters (i.e., the adsorption energies of atomic carbon and oxygen) [16]. Using this model, we screened a large number of transition metal alloys based on their predicted rates and stabilities for CH₄ steam reforming.

2 Methods

In order to develop catalyst leads for the steam reforming of CH₄, a three-step approach was employed. First, a microkinetic model of the elementary reactions considered was developed. Second, energies of reaction intermediates were scaled with descriptors and incorporated to the microkinetic model. Third, using the results of this model, a large number of transition metal alloys were screened based on their predicted rates and stabilities under reaction conditions.

2.1 Microkinetic model method

This microkinetic model consisted of the following reaction steps for CH₄ and H₂O dehydrogenation, as well as several possible pathways for CO formation via C*, CHO*, and COH* intermediates:



The parameterization of the microkinetic model was performed as described in literature [4, 8, 16], and can be found in Section 2 of the Supplementary Material.

In the microkinetic model, adsorbates may be adsorbed on one of four different sites: the “step” (*s) site corresponds to the upper part of a (211) step site. The “four-fold” (*f) site corresponds to the lower four-fold site of a (211) step. The “terrace” (*t) corresponds to a (211) terrace site. In addition, hydrogen is adsorbed in a special “hydrogen reservoir” site (*h) which has the same energetics as a three-fold hollow site at steps.

Interactions between adsorbates were also considered in the microkinetic model. Adsorption energies are described as a function of coverage using the model reported elsewhere [1, 36, 46, 47]. Adsorption energies for the individual intermediates are calculated at ¼ ML, ½ ML, ¾ ML and 1 ML coverages for the lowest-energy adsorption site at low (¼ ML) coverage. A brief summary of the interaction model, including the interaction parameters used in the microkinetic model, which can be found in Section 3 of the Supplementary Material.

Steady-state numerical solutions to the microkinetic model were calculated for one laboratory scale reactor conditions studied in the earlier work [16] and two model industrial reaction conditions, which were designed to simulate the inlet and outlet conditions of a typical steam reforming reactor designed to generate H₂ for ammonia synthesis [48]. The temperatures, pressures, and gas compositions of these three conditions are described in Table 1.

Table 1. The conditions in steam reforming reactor (as described in Ref. [16, 48]).

Conditions	Lab scale	Inlet-low	Outlet-high
T (K)	773	638	1066
P (bar)	1	14.3	12.2
Conversion (%)	29 ^a	0.3 ^b	50 ^c
H ₂ O (mol. %)	40	83.1	65.8
H ₂ (mol. %)	15	1.9	25.0
CH ₄ (mol. %)	40	14.5	2.4
N ₂ (mol. %)	0	0.4	0.3
CO (mol. %)	5	0.1	6.5

^{a,b,c} Conversions are respect to their equilibrium conversions.

2.2 Scaling method

As described in previous studies, binding energies of reaction intermediates can be scaled with the binding energies of carbon (E_C) and oxygen (E_O) [40-42]. Similarly, the transition state energies for the various reaction steps can be scaled with the energies of the reaction products [4, 43-45, 49]. DFT-calculated energies for the various reaction intermediates and transition states were accessed from *CatApp*, a web application that stores energetic information for elementary coupling reaction on transition metal surfaces [50],¹ and can be found in Section 1 of the Supplementary Material, along with the fitting parameters of all the scaling relations. Energies are given relative to the gas-phase energies of CH₄, H₂O and H₂.

The DFT-calculated adsorption energies of surface intermediates and transition states for on the stepped (211) surfaces of Ag, Cu, Pd, Pt, and Rh were accessed via *CatApp* [50, 51]. Transition state energies for reactions (7) and (9) were calculated using the fixed bond length (FBL) method in this work. Self-consistent, periodic density functional theory (DFT) calculations for the surface intermediates and transition states were performed using the Dacapo plane wave code², which represents the ionic cores using Vanderbilt ultrasoft pseudopotentials. Calculations were performed using the RPBE exchange-correlation functional [52], which uses a generalized gradient approximation, with a kinetic energy cutoff of 340 eV and a density cutoff of 500 eV. Self-consistent electron densities were determined by

¹ The CatApp is available for free at: <http://suncat.slac.stanford.edu/catapp>

² The Dacapo plane wave pseudopotential code is available as Open Source Software, <http://wiki.fysik.dtu.dk/dacapo>

iterative diagonalization of the Kohn-Sham Hamiltonian, where the occupation of the Kohn-Sham states were smeared according to a Fermi-Dirac distribution with a smearing factor of $k_B T = 0.1$ eV [53]. Energies were extrapolated to $k_B T = 0$ eV. Stepped (211) surfaces were represented with nine-layered slabs (which correspond to three layers in the (111) direction) with (1×3) unit cells. All adsorbates and the top two layers were allowed to relax, while the remaining layers were kept fixed in their bulk-truncated positions. Brillouin zones were sampled using Monkhorst-Pack k-point meshes of $3 \times 3 \times 1$. Successive slabs were separated with a vacuum of 15 Å.

Zero-point energies, entropies and internal energies of adsorbed intermediates were included due to the relatively high reaction temperatures. These values were calculated using the harmonic oscillator approximation from their vibrational frequencies on the Rh(211) surface (Table S.5 of the Supplementary Material), and were assumed to be constant on all surfaces.

2.3 Alloy screening method

Based on this microkinetic model, a large number of transition metal alloys were screened based on their predicted rates, costs, and stabilities for CH₄ steam reforming. Specifically, we thus imposed the following screening criteria for A₃B and AB transition metal alloys, as depicted in Fig. 1:

- (1) The candidate bulk alloy should be stable or close to stable with respect to its bulk pure metal constituents.
- (2) The candidate bulk alloy should be stable or almost stable against oxidation at the given reaction conditions.
- (3) The candidate should not contain expensive metal constituents.
- (4) The candidate should be reasonably active under the given reaction conditions.

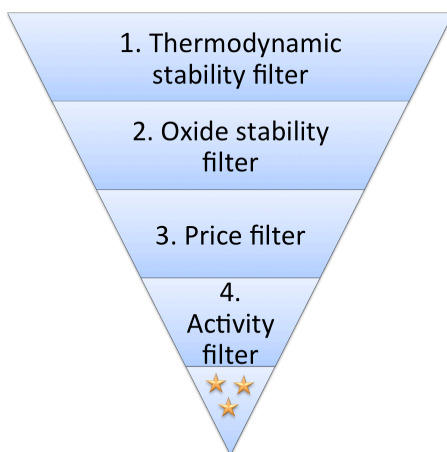


Figure 1. Schematic for searching transition metal alloy catalysts based on their predicted rates, costs, and stabilities for steam reforming.

2.3.1 Thermodynamic stability filter

The ability of two elemental metals to form a stable intermetallic compound is described by the alloy's formation energy, E_f . As a simple model for the stability of the binary intermetallic compounds, the formation energies of the binary alloys of the form A_3B and AB in simple FCC (face-centered cubic)-like crystal structures were calculated using DFT. The formation energy of these simple alloys is then used to predict the ability of the metals to form stable intermetallic compounds with each other. The formation energy of a given alloy was defined as:

$$E_f = E_{\text{alloy}} - N_A E_{A(\text{bulk})} - N_B E_{B(\text{bulk})} \quad (\text{Eq. 1})$$

where E_f is the formation energy, E_{alloy} is the DFT-calculated energy of the metal alloy, and N_i and $E_{i(\text{bulk})}$ are the molar ratios and the DFT-calculated energies, respectively, of the individual metal, i . According to this definition, the more negative the value, the more stable the alloy. For the purposes of the present analysis, only alloys with formation energy less than +0.2 eV per unit cell were considered to be potentially stable. A complete list of the investigated alloys, as well as their formation energies, is given in Table S.8 of the Supplementary Material.

2.3.2 Oxidation stability filter

In order to mitigate catalyst deactivation due to coking and achieve an improved high CH_4 conversion, a high steam-to-carbon ratio is used under industrial conditions. With high H_2O partial pressure, however, metals and metal alloys may deactivate via the formation of an inactive bulk metal oxide. Candidate alloys, therefore, must be evaluated in terms of their stability with respect to oxidation.

In order to estimate the stability of a given candidate alloy (A_xB_y) against oxidation, we calculated the Gibbs free energy of oxidation for each of the constituent metal atoms under reaction conditions. Then we compared those energies with the formation energy of the alloy as a whole using the equation:

$$\Delta G_{\text{oxide}}^{\text{alloy}} = -E_f + x\Delta G_{A-\text{oxide}} + y\Delta G_{B-\text{oxide}}$$

where ΔE_f is the energy of formation, $\Delta G_{A-\text{oxide}}$ and $\Delta G_{B-\text{oxide}}$ are the energies of oxidation of metal A and B, respectively, and $G_{\text{oxide}}^{\text{alloy}}$ is the energy of oxidation of the alloy. The energy of oxidation for metal M, which has a ground state oxide M_mO_n , was calculated using the equation:

$$\Delta G_{M-\text{oxide}} = \Delta H_{\text{reaction}}^0 - T\Delta S_{\text{reaction}}^0 - \frac{n}{m}RT \ln \left(\frac{P_{\text{H}_2\text{O}}}{P_{\text{H}_2}} \right)$$

where $\Delta H_{reaction}^0$ and $\Delta S_{reaction}^0$ are calculated using reference values from literature [54]. A detailed description of the method used here, as well as several example calculations, are given in Section 4 of the Supplementary Material.

2.3.3 Cost and activity filters

In order to be relevant on an industrial scale, it is often necessary to limit the use of expensive noble metals. Therefore, we used a simple interpolation method to estimate the cost of the various transition metal alloys, assuming that the cost is independent of the preparation method but depends solely on the cost of the constituted metals. In order to exclude alloys containing noble metals (e.g., Pt, Pd, Ir, Ru, Rh, Os, and Au), we considered that alloys with predicted costs larger than \$5000 kg⁻¹ should be excluded. Reference prices of pure metals were taken from chemicool³, and can be found in Table S.7 of the *Supplementary Material*. Alloys were also screened based on their predicted rates for CH₄ steam reforming. In order to concentrate on those alloys that have the highest predicted rates, we screened them based on turnover frequencies larger than 10⁻⁴ s⁻¹ and 10⁻² s⁻¹ for the inlet and outlet reactor conditions, respectively. The predicted costs and rates of all thermodynamically stable alloys are given in Table S.8 of the *Supplementary Material*.

3. Results and discussion

3.1 Microkinetic model

The reaction energetics for CH₄ steam reforming on a stepped Rh(211) surface are given in Fig. 2. Three reaction paths for the formation of CO* are depicted – the direct C-O formation pathway, as well as two hydrogen insertion pathways involving CHO* and COH*. The highest barriers for steam reforming on a Rh(211) surface (Fig. 2) are those for the formation of CO*. This is consistent with earlier work that suggested the formation of C-O as the rate-limiting step at low temperatures [16]. Similarly, it has been suggested that, while the direct formation of CO* from C* and O* is the main pathway, CO* formation from COH* and CHO* can also be significant at lower temperatures [55]. From the free energy pathway shown in Fig. 2b, however, it is difficult to elucidate which CO formation pathway will be the dominant.

³ www.chemicool.com accessed on February 1, 2013.

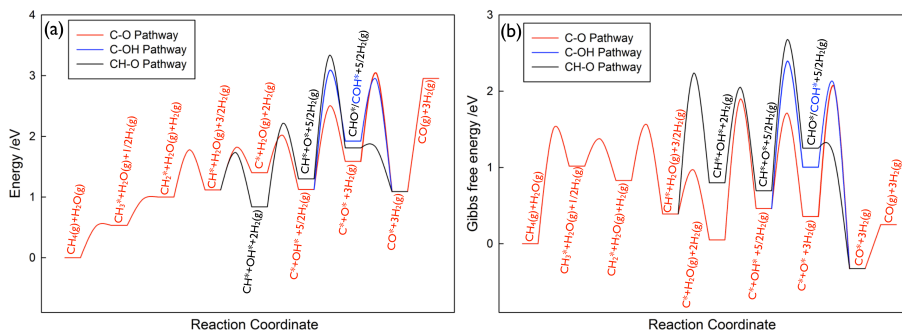


Figure 2– (a) Potential energy diagram for CH_4 steam reforming to $\text{CO}_{(\text{g})}$ and $\text{H}_{2(\text{g})}$ on a Rh(211) surface; (b) Free energy diagram for CH_4 steam reforming to $\text{CO}_{(\text{g})}$ and $\text{H}_{2(\text{g})}$ on a Rh(211) surface. Reaction conditions are: $T = 773 \text{ K}$, $P = 1 \text{ bar}$, with a gas composition of 40% CH_4 , 40% H_2O , 5% CO and 15% H_2 (corresponding to 29% approach to equilibrium). Three pathways are depicted in red, black, and blue for the formation of $\text{CO}_{(\text{g})}$ via $\text{C}^* + \text{O}^*$, $\text{C}^* + \text{OH}^*$, and $\text{CH}^* + \text{O}^*$, respectively. The main pathway is depicted in red. Values for the adsorption energies of reaction intermediates were taken from CatApp [50, 56].

Combining scaling relations with microkinetic model is one strategy for developing a more general picture of catalyst reactivity in terms of theoretical activity volcanoes. For example, Fig. 3 shows the predicted CH_4 steam reforming rates as a function of E_{c} and E_{o} , as calculated by microkinetic modeling, with and without adsorbate-adsorbate interactions, for reaction conditions similar to a laboratory scale CH_4 steam reforming reactor. The highest rates are predicted for transition metals such as Rh, Ru, Ni and Ir, while lower rates are predicted for Pd and Pt. These results are consistent with previous experimental work under same reaction conditions, showing that catalysts involving Rh, Ru, Ni, Ir, Pd, and Pt are active for steam reforming [13, 16, 19]. These results are also very similar to the previously volcano plots [16], where the dissociative adsorption of CH_4 and the direct formation of CO^* from C^* and O^* are assumed to be competing as rate determining steps.

The overall shape of the activity volcano is better understood in terms of the coverages of C^* , O^* and CO^* , as depicted in Fig. 4. Note that adsorbed carbon (C^*) bonds on the four-fold sites of the stepped surface, while CO^* and O^* are bonded more strongly on the on-top steps sites [47]. Based on a comparison of Fig. 3 and 4, it is evident that the most active transition metals have coverages of these strongly bonded intermediates somewhat in the area of 0.5 monolayers (ML) on the on-top and four-fold sites. As discussed elsewhere, interactions between adsorbates can influence their adsorption energies at coverages above a certain threshold (0.25 – 0.5 ML) [46, 47, 57], which potentially can affect the predicted rates. Therefore, we used an interaction model similar to that reported earlier to describe interactions between adsorbed reaction intermediates [46, 47]. The fitted interaction

parameters are calculated on Pd, Pt, Rh and Ru and scaled with the sum of C* and O* adsorption energies, as described in Section 3 of the Supplementary Material.

As shown in Fig. 3c, the inclusion of adsorbate-adsorbate interactions only affects regions of the activity volcano where coverages of reaction intermediates exceed 0.5 ML. The predicted rates in the upper right section are hence unaffected since their coverages do not exceed this threshold. Similarly, the overall shape of the volcano, as well as the position of the maximum rates, are essentially unaffected. The volcano with adsorbate-adsorbate interactions differs from the one without interactions primarily in that it increases or decreases the predicted rates of the most strongly binding metals. The lower right section of the volcano, as well as the peak, are predicted to have lower rates due to increased barriers for C-O formation. High coverages of adsorbed oxygen lower the adsorption energies of both C* and O*, which increases the activation barrier for CO production. At high carbon binding energies, however, inclusion of interaction effects causes the predicted rates to increase. High coverages of C* and O* (left side in the volcano plot) lower the adsorption energies of the reaction intermediates, which increases the concentration of free sites available for the reaction.

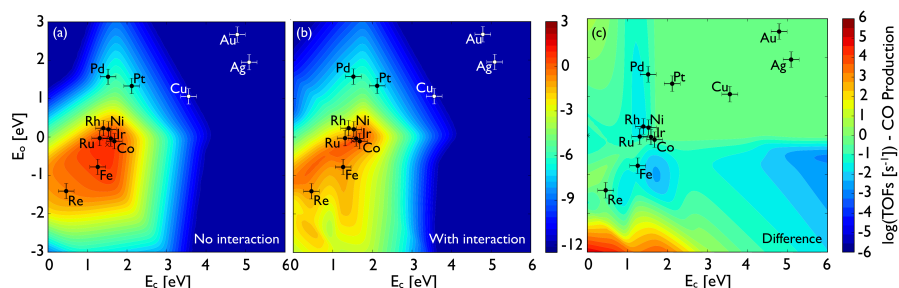


Figure 3 - Calculated turnover frequencies (TOFs) for CH₄ steam reforming to CO and H₂ (a) without adsorbate-adsorbate interactions; (b) with adsorbate-adsorbate interactions and (c) differences of the reaction rates between models with and without adsorbate-adsorbate interaction. The carbon and oxygen binding energies for the stepped (211) surfaces of selected transition metals are depicted. The error bars indicate an estimated error of 0.2 eV for E_c and E_o. Reaction conditions are: T = 773 K, P = 1 bar, with a gas composition of 40% CH₄, 40% H₂O, 5% CO and 15% H₂ (corresponding to 29% approach to equilibrium).

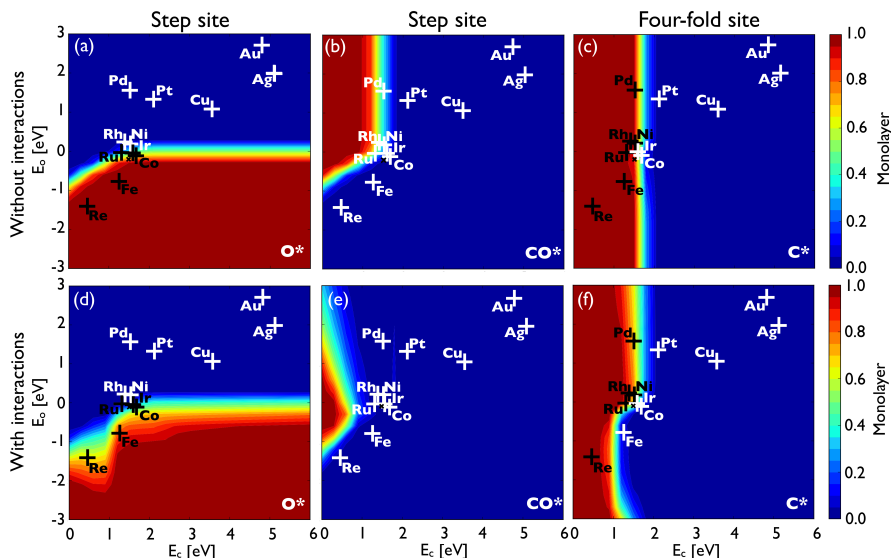


Figure 4 - Coverages of O^* , CO^* , and C^* as a function of the carbon (E_c) and oxygen (E_o) binding energies as obtained by the solutions of the microkinetic model without (a-c) and with (d-f) adsorbate-adsorbate interactions. Reaction conditions are: $T = 773$ K, $P = 1$ bar, with a gas composition of 40% CH_4 , 40% H_2O , 5% CO and 15% H_2 (corresponding to 29% approach to equilibrium).

By incorporating multiple reaction paths for CO formation, microkinetic modeling can also determine which path is likely to be the most important under the given reaction conditions. Based on the predicted reaction rates for each of the three CO formation paths (Fig. 5), the direct formation of CO from C-O coupling has the highest predicted rates at the top of the volcano, as compared to the hydrogen-assisted routes for involving COH^* and CHO^* . This result is consistent with the theoretical work on metal (211) surfaces, which are conducted by Bengaard [27], Shetty [33] and Bhattacharjee [32], but contradictory to the results reported by Inderwildi [58], Wang [28, 29] and Blaylock [30] on flat surfaces. There might be two reasons for the disparateness. First, our scaling relations are obtained using energies calculated on stepped metal (211) surfaces. Generally the steps are more reactive than flat (111) surfaces for dissociation reactions, while whether the steps could promote bond formation depends on the individual reaction as well as the particular metal [59]. Therefore, the different structure sensitivity of elementary reactions maybe one of the reasons for different results of the primary pathways. Second, most of the work on the reaction mechanism only considered the potential energy of each pathway, neglecting temperature and coverage effects. From Fig. 2 we can see that the free energy barrier for activating gas-phase species are higher due to the significant loss of entropy at high temperatures. As depicted in Fig. 4, C^* is one of the dominant species on the surface, the coverage of C^* might be 2-4 orders

of magnitude larger than CH^* in the active area. Even if the activation barrier might be a little lower for CH-O pathway, the rate for direct CO formation pathway could still be significantly higher.

For less active metals, however, such as Pt and Pd , the hydrogen-assisted route involving COH^* will likely also be important because coverage effects only play a minor role as compared to the activation barrier, in accordance with earlier work by Chen [34] and Inderwildi [35]. We also analysed the reaction pathways for CO formation under two industrial conditions, and the result that direct C-O coupling is the main route still holds.

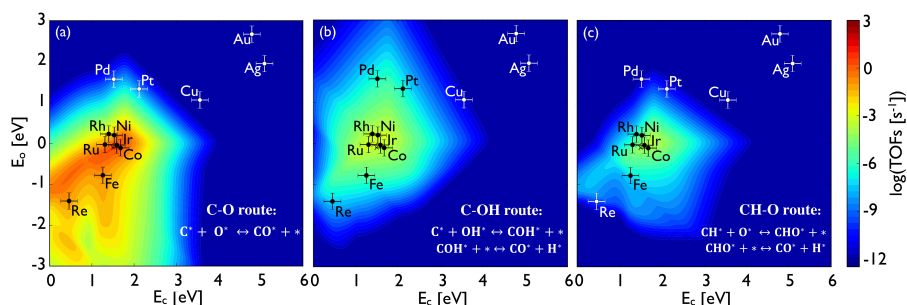


Figure 5 - Three routes for CO^* formation: (a) direct C-O coupling, (b) COH^* decomposition and (c) CHO^* decomposition. Reaction conditions are: $T = 773 \text{ K}$, $P = 1 \text{ bar}$, with a gas composition of 40% CH_4 , 40% H_2O , 5% CO , and 15% H_2 (corresponding to 29% approach to equilibrium).

Finally, the microkinetic model also provides a way to predict changes in rates as a function of changing gas compositions, similar to what might be experienced in a packed bed reactor with changing temperatures and extents of conversion. In Fig. 6, the predicted rates (including interaction effects) for catalysts for the inlet and outlet conditions of such a reactor are given. While the overall shape of the volcano is conserved, it is evident that higher rates are predicted for the reactor outlet, primarily due to the increase in reactor temperature (since the reaction is endothermic).

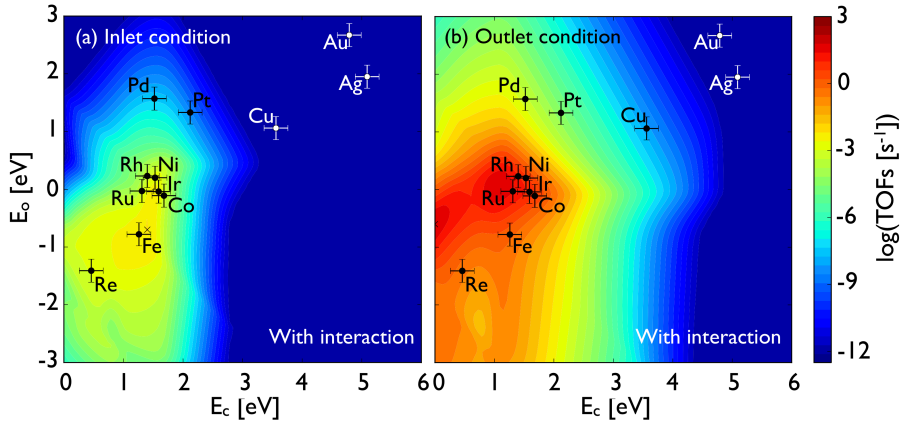


Figure 6 - Calculated turnover frequencies (TOFs) for CO production (calculated in the microkinetic model with interaction between adsorbates considered) under industrial (a) inlet conditions: $T = 638$ K, $P = 14.3$ bar, with a gas composition of 14.5% CH_4 , 83.1% H_2O , 0.1% CO , 0.4% N_2 , and 1.9% H_2 (corresponding to 0.3% approach to equilibrium); and (b) outlet conditions: $T = 1066$ K, $P = 12.2$ bar, with a gas composition of 2.4% CH_4 , 65.8% H_2O , 6.5% CO , 0.3% N_2 , and 25% H_2 (corresponding to 50% approach to equilibrium); for CH_4 steam reforming as a function of C and O binding energies.

3.2 Alloy Screening

3.2.1 Thermodynamic and oxidation filters

Having established a volcano shaped relationship for methane steam reforming as a function of two descriptors, we will now proceed to screen a large number of transition metal alloys with respect to their predicted rates, stability, and cost. Alloys with compositions of A_3B and AB (where A and B are transition metals) were considered. The full list of alloys is given in Section 4 of the Supplementary Material. Using DFT, the formation energies of these alloys were calculated in connection with an earlier study of methanol formation.[8] We here consider those alloys with formation energy less than 0.2 eV per unit cell to be “potentially” stable. The carbon and oxygen adsorption energies on the stepped (211) surfaces of these thermodynamically stable alloy materials were also calculated using DFT in the study by Studt et al.,[8] and are available through the CatApp.[50] As depicted in Fig. 7, we used the activity volcanoes from the previous section to predict the CH_4 steam reforming rates of these materials. We also assessed the stabilities of these alloys in terms of their predicted energies of oxidation. For screening purposes, we divided the alloys into three categories of predicted stability: 1) alloys that are predicted to be very stable ($\Delta G_{\text{oxide}}^{\text{alloy}} > 0.05\text{eV}$), 2) alloys of intermediate stability ($-0.05\text{ eV} < \Delta G_{\text{oxide}}^{\text{alloy}} < 0.05\text{eV}$), and 3) alloys that are predicted to oxidize under reaction conditions ($\Delta G_{\text{oxide}}^{\text{alloy}} < -0.05\text{eV}$). These predicted stabilities are illustrated in Fig. 7a, where it is evident that many of the alloys can be oxidized under inlet conditions. As

expected, the majority of the alloys that are predicted to be resistant to deactivation via bulk oxidation are located at the upper right portion of the volcano – that is, they have relatively low binding energies of carbon and oxygen.

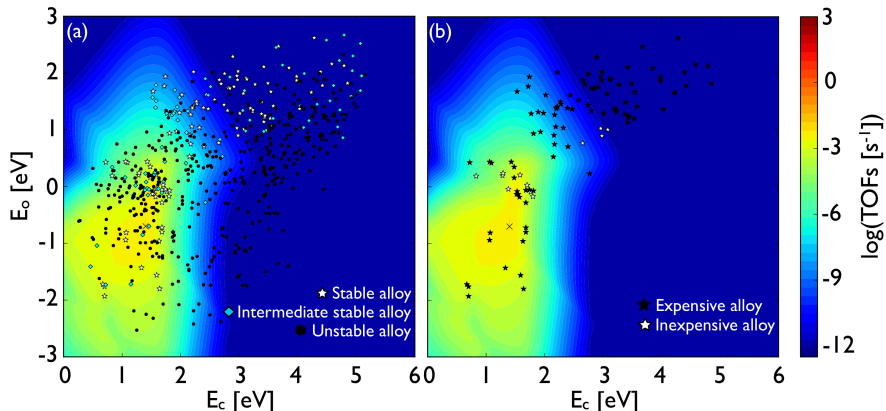


Figure 7 - Theoretical activity volcanoes for the production of CO under industrial inlet conditions: $T = 638$ K, $P = 14.3$ bar, with a gas composition of 14.5% CH_4 , 83.1% H_2O , 0.1% CO , 0.4% N_2 and 1.9% H_2 (corresponding to 0.3% approach to equilibrium). (a) Alloys are divided into three categories based on their predicted stabilities with respect to oxidation: 1) alloys with high stability (white stars), 2) alloys with intermediate stability (cyan diamonds), and 3) alloys with low stability (black circles). Alloy labels are omitted for clarity. (b) Alloys are divided into two categories based on the material costs of their component metals [chemicool.com]: 1) expensive alloys (black star, cost $\geq \$5000 \text{ kg}^{-1}$, and 2) inexpensive alloys (white stars $< \$5000 \text{ kg}^{-1}$).

3.2.2 Price and activity filters

One of the main drivers of new catalyst development is the desire to reduce the use of rare and expensive metals. As depicted in Fig. 7b, we screened potential alloy formulations based on the costs of their component metals. Alloys with estimated costs less than $\$5000 \text{ kg}^{-1}$ are denoted in the volcano plot using white stars, while more expensive alloys are denoted using black stars. This cutoff value of $\$5000 \text{ kg}^{-1}$ was chosen to eliminate alloys containing metals that are relatively expensive (e.g., Pt, Pd, Rh, Ru, Os, Au, Ir). The remaining alloys, as depicted in Fig. 8, are the most interesting candidates for CH_4 steam reforming – since they are predicted to be stable under reaction conditions, formed from earth abundant materials, and have high predicted reaction rates.

It can be seen from Fig. 8 that most of the active, stable and inexpensive binary alloys contain Ni, Fe, and Co in the A_3B composition. It is also observed that the inlet conditions are more demanding in terms of stability than the outlet condition. This is reasonable because at the inlet the partial pressure of H_2O is significantly higher, and the temperature lower, both of which tend to stabilize oxide formation. For all

metals their oxides becomes less stable when the temperature increases. Two different (211)-like surface structure terminations are possible for the A_3B -type alloy, as shown in Fig. S3 of the Supplementary Material. Both terminations are considered in the activity filtering process. Of all screened alloys, only the Ni_3Fe and Co_3Ni are suggested to be active for both terminations, further supporting that they might be good candidates for steam reforming reactions. Some experimental results also support our predictions. Wang et al. tested the catalytic performance of $Ni-Fe/Al_2O_3$ catalysts in the steam reforming of tar, showing both high activity and stability of the $Ni-Fe$ alloy [60]. Koh et al. investigated a series of $Ni-Co$ catalysts in partial oxidation of CH_4 to CO , indicating that $Ni-Co$ catalysts have high activity and selectivity and are relatively resistant to coking [61]. Other materials, such as $Ni-Ge$ and $Ni-Ga$, have not been investigated previously, and are therefore interesting candidates for CH_4 steam reforming.

Although some of the alloys are located close to the top of the volcano, they might experience problems with coking. As illustrated in Fig. 4, materials located on the left side of the activity volcano will likely have high coverages of carbon, and thus may be more prone to coking, whereas materials on the right side with lower carbon binding energies may be more resistant to coking and show better performance under steam reforming conditions. A rough guide for this, the equilibrium line for CO^* decomposition to C^* , is plotted on the volcano in Fig. 8. Alloys that are close to or below this line will have a high driving force for the formation of atomic carbon, which is a precursor for the formation of graphitic carbon.

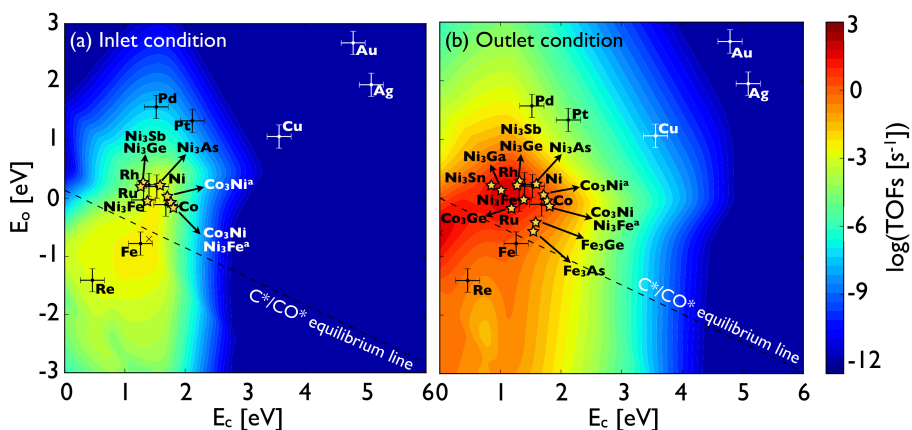


Figure 8 - Calculated turnover frequencies (TOFs) for CO production under industrial (a) inlet: $T = 638$ K, $P = 14.3$ bar, with a gas composition of 14.5% CH_4 , 83.1% H_2O , 0.1% CO , 0.4% N_2 and 1.9% H_2 (corresponding to 0.3% approach to equilibrium); and (b) outlet conditions: $T = 1066$ K, $P = 12.2$ bar, with a gas composition of 2.4% CH_4 , 65.8% H_2O , 6.5% CO , 0.3% N_2 and 25% H_2 (corresponding to 50% approach to equilibrium); for CH_4 steam reforming. A superscript "a" denotes AA type surface terminal of A_3B

alloy. The detailed structure of both terminals can be found Fig. S3 of the Supplementary material. Carbon equilibrium line is determined by the Gibbs free energy change of reaction $CO^* + * \leftrightarrow C^* + O^*$.

4. Conclusion

We have constructed a descriptor-based volcano rate plot for methane steam reforming that combines a microkinetic model with scaling relations across the periodic table while taking adsorbate-adsorbate interactions into account. The model predicts the reaction rates of transition metals and metal alloys for the CH₄ steam reforming reaction based on carbon and oxygen adsorption as the two descriptors. This approach allowed for a detailed description of the reaction mechanism for different catalytic surfaces under the given reaction conditions. In addition we have used the model to screen a large number of transition metal alloys with respect to their steam reforming activity. The combination with filters that consider stability and cost enables the screening for novel leads for active, stable, and low-cost steam reforming catalysts.

The methods outlined in this paper are very general, making their application possible for a wide range of reactions. Starting from data stored in the public online database *CatApp*, one can begin to understand very quickly what characteristics an optimal catalyst might have. The described framework also allows one to consider what effects might be expected due to changes in catalyst composition and reaction conditions. This is especially true given the ability of the model to provide insights into the expected reaction mechanisms for a given catalytic surface. Therefore, we suggest the presented method herein could become useful as a starting point in the search for technical catalysts in the future.

Acknowledgements

We acknowledge support from the U.S. Department of Energy Chemical Sciences, Geosciences and Biosciences Division under contract number DE-AC02-76SF00515, support from the National Basic Research Program of China (973 Program, No. 2012CB720500), the Natural Science Foundation of China (No. 21276077 and No. 21003046), the Fundamental Research Fund for Central Universities (No. WG1213011). Y.X. thanks the China Scholarship Council for funding her visit to SLAC National Accelerator Laboratory.

References

1. J.K. Nørskov, T. Bligaard, and J. Kleis: *Rate control and reaction engineering*. Science, **324**, 1655-1656 (2009)
2. M.P. Andersson, T. Bligaard, A. Kustov, K.E. Larsen, J. Greeley, T. Johannessen, C.H. Christensen, and J.K. Nørskov: *Toward computational screening in heterogeneous catalysis: Pareto-optimal methanation catalysts*. Journal of Catalysis, **239**, 501-506 (2006)

3. L.C. Grabow, F. Studt, F. Abild-Pedersen, V. Petzold, J. Kleis, T. Bligaard, and J.K. Nørskov: *Descriptor-based analysis applied to hcn synthesis from nh₃ and ch₄*. *Angewandte Chemie International Edition*, **50**, 4601-4605 (2011)
4. A.C. Lausche, J.S. Hummelshøj, F. Abild-Pedersen, F. Studt, and J.K. Nørskov: *Application of a new informatics tool in heterogeneous catalysis: Analysis of methanol dehydrogenation on transition metal catalysts for the production of anhydrous formaldehyde*. *Journal of Catalysis*, **291**, 133-137 (2012)
5. G. Jones, T. Bligaard, F. Abild-Pedersen, and J.K. Nørskov: *Using scaling relations to understand trends in the catalytic activity of transition metals*. *Journal of Physics-Condensed Matter*, **20**, - (2008)
6. F. Studt, F. Abild-Pedersen, T. Bligaard, R.Z. Sørensen, C.H. Christensen, and J.K. Nørskov: *Identification of non-precious metal alloy catalysts for selective hydrogenation of acetylene*. *Science*, **320**, 1320-1322 (2008)
7. J. Greeley and M. Mavrikakis: *Competitive paths for methanol decomposition on pt(111)*. *Journal of the American Chemical Society*, **126**, 3910-3919 (2004)
8. F. Studt, F. Abild-Pedersen, Q.X. Wu, A.D. Jensen, B. Temel, J.D. Grunwaldt, and J.K. Nørskov: *Co hydrogenation to methanol on cu-ni catalysts: Theory and experiment*. *Journal of Catalysis*, **293**, 51-60 (2012)
9. S. Linic, J. Jankowiak, and M.A. Barteau: *Selectivity driven design of bimetallic ethylene epoxidation catalysts from first principles*. *Journal of Catalysis*, **224**, 489-493 (2004)
10. J.K. Nørskov and T. Bligaard: *The catalyst genome*. *Angewandte Chemie International Edition*, **52**, 776 (2013)
11. A. Haryanto, S. Fernando, N. Murali, and S. Adhikari: *Current status of hydrogen production techniques by steam reforming of ethanol: A review*. *Energy & Fuels*, **19**, 2098-2106 (2005)
12. E. Kikuchi, S. Tanaka, Y. Yamazaki, and Y. Morita: *Steam reforming of hydrocarbons on noble metal catalysts (part 1)*. *Bull. Jpn. Pet. Inst.*, **16**, 95 (1974)
13. D. Qin and J. Lapszewicz: *Study of mixed steam and co₂ reforming of ch₄ to syngas on mgo-supported metals*. *Catalysis Today*, **21**, 551-560 (1994)
14. J.M. Wei and E. Iglesia: *Structural and mechanistic requirements for methane activation and chemical conversion on supported iridium clusters*. *Angewandte Chemie International Edition*, **43**, 3685-3688 (2004)
15. J.M. Wei and E. Iglesia: *Mechanism and site requirements for activation and chemical conversion of methane on supported pt clusters and turnover rate comparisons among noble metals*. *Journal of Physical Chemistry B*, **108**, 4094 (2004)
16. G. Jones, J.G. Jakobsen, S.S. Shim, J. Kleis, M.P. Andersson, J. Rossmeisl, F. Abild-Pedersen, T. Bligaard, S. Helveg, B. Hinnemann, J.R. Rostrup-Nielsen, I. Chorkendorff, J. Sehested, and J.K. Nørskov: *First principles calculations and experimental insight into methane steam reforming over transition metal catalysts*. *Journal of Catalysis*, **259**, 147-160 (2008)
17. J.R. Rostrup-Nielsen: *Sulphur-passivated nickel catalyst for carbon-free steam reforming of methane*. *Journal of Catalysis*, **85**, 31 (1984)

18. J.R. Rostrup-Nielsen: *Activity of nickel catalysts for steam reforming of hydrocarbons*. Journal of Catalysis, **31**, 173-199 (1973)
19. J.R. Rostrup-Nielsen and J.H.B. Hansen: *Co₂-reforming of methane over transition metals*. Journal of Catalysis, **144**, 38-49 (1993)
20. J. Sehested: *Four challenges for nickel steam-reforming catalysts*. Catalysis Today, **111**, 103-110 (2006)
21. E. Nikolla, J. Schwank, and S. Linic: *Comparative study of the kinetics of methane steam reforming on supported ni and sn/ni alloy catalysts: The impact of the formation of ni alloy on chemistry*. Journal of Catalysis, **263**, 220-227 (2009)
22. F. Besenbacher, I. Chorkendorff, B.S. Clausen, B. Hammer, A.M. Molenbroek, J.K. Nørskov, and I. Stensgaard: *Design of a surface alloy catalyst for steam reforming*. Science, **279**, 1913-1915 (1998)
23. Y.-H. Chin, D.L. King, H.-S. Roh, Y. Wang, and S.M. Heald: *Structure and reactivity investigations on supported bimetallic auni catalysts used for hydrocarbon steam reforming*. Journal of Catalysis, **244**, 153-162 (2006)
24. N.V. Parizotto, K.O. Rocha, S. Damyanova, F.B. Passos, D. Zanchet, C.M.P. Marques, and J.M.C. Bueno: *Alumina-supported ni catalysts modified with silver for the steam reforming of methane: Effect of ag on the control of coke formation*. Applied Catalysis a-General, **330**, 12-22 (2007)
25. Y. Guo, L. Thou, and H. Kameyama: *Steam reforming reactions over a metal-monolithic anodic alumina-supported ni catalyst with trace amounts of noble metal*. International Journal of Hydrogen Energy, **36**, 5321-5333 (2011)
26. D.L. Li, K. Nishida, Y.Y. Zhan, T. Shishido, Y. Oumi, T. Sano, and K. Takehira: *Sustainable ru-doped ni catalyst derived from hydrotalcite in propane reforming*. Applied Clay Science, **43**, 49-56 (2009)
27. H.S. Bengaard, J.K. Nørskov, J. Sehested, B.S. Clausen, L.P. Nielsen, A.M. Molenbroek, and J.R. Rostrup-Nielsen: *Steam reforming and graphite formation on ni catalysts*. Journal of Catalysis, **209**, 365-384 (2002)
28. S.G. Wang, X.Y. Liao, J. Hu, D.B. Cao, Y.W. Li, J.G. Wang, and H.J. Jiao: *Kinetic aspect of co₂ reforming of ch₄ on ni(111): A density functional theory calculation*. Surface Science, **601**, 1271-1284 (2007)
29. S.G. Wang, D.B. Cao, Y.W. Li, J.G. Wang, and H.J. Jiao: *Co₂ reforming of ch₄ on ni(111): A density functional theory calculation*. Journal of Physical Chemistry B, **110**, 9976-9983 (2006)
30. D.W. Blaylock, T. Ogura, W.H. Green, and G.J.O. Beran: *Computational investigation of thermochemistry and kinetics of steam methane reforming on ni(111) under realistic conditions*. The Journal of Physical Chemistry C, **113**, 4898-4908 (2009)
31. E. Iglesia and J.M. Wei: *Isotopic and kinetic assessment of the mechanism of reactions of ch₄ with co₂ or h₂o to form synthesis gas and carbon on nickel catalysts*. Journal of Catalysis, **224**, 370-383 (2004)
32. T. Bhattacharjee, O.R. Inderwildi, S.J. Jenkins, U. Riedel, and J. Warnatz: *Oxidation of hydrocarbons at surface defects: Unprecedented confirmation of the oxomethylidyne pathway on a stepped rh surface*. Journal of Physical Chemistry C, **112**, 8751-8753 (2008)

33. S. Shetty, A.P.J. Jansen, and R.A. van Santen: *Direct versus hydrogen-assisted co dissociation*. Journal of the American Chemical Society, **131**, 12874-+ (2009)
34. Y. Chen and D.G. Vlachos: *Density functional theory study of methane oxidation and reforming on pt(111) and pt(211)*. Industrial & Engineering Chemistry Research, **51**, 12244-12252 (2012)
35. O.R. Inderwildi, S.J. Jenkins, and D.A. King: *Mechanistic studies of hydrocarbon combustion and synthesis on noble metals*. Angewandte Chemie-International Edition, **47**, 5253-5255 (2008)
36. L.C. Grabow, B. Hvolbæk, and J.K. Nørskov: *Understanding trends in catalytic activity: The effect of adsorbate-adsorbate interactions for co oxidation over transition metals*. Topics in Catalysis, **53**, 298-310 (2010)
37. J.K. Nørskov, F. Abild-Pedersen, F. Studt, and T. Bligaard: *Density functional theory in surface chemistry and catalysis*. Proceedings of the National Academy of Sciences, **108**, 937-943 (2011)
38. N. Schumacher, A. Boisen, S. Dahl, A.A. Gokhale, S. Kandoi, L.C. Grabow, J.A. Dumesic, M. Mavrikakis, and I. Chorkendorff: *Trends in low-temperature water-gas shift reactivity on transition metals*. Journal of Catalysis, **229**, 265-275 (2005)
39. M. Neurock: *The microkinetics of heterogeneous catalysis*. By j. A. Dumesic, d. F. Rudd, l. M. Aparicio, j. E. Rekoske, and a. A. Treviño, acs professional reference book, american chemical society, washington, dc, 1993, 315 pp. Aiche Journal, **40**, 1085-1087 (1994)
40. F. Abild-Pedersen, J. Greeley, F. Studt, J. Rossmeisl, T.R. Munter, P.G. Moses, E. Skulason, T. Bligaard, and J.K. Nørskov: *Scaling properties of adsorption energies for hydrogen-containing molecules on transition-metal surfaces*. Physical Review Letters, **99**, 016105, 01615 (2007)
41. P. Ferrin, A.U. Nilekar, J. Greeley, M. Mavrikakis, and J. Rossmeisl: *Reactivity descriptors for direct methanol fuel cell anode catalysts*. Surface Science, **602**, 3424-3431 (2008)
42. G. Jones, F. Studt, F. Abild-Pedersen, J.K. Nørskov, and T. Bligaard: *Scaling relationships for adsorption energies of c2 hydrocarbons on transition metal surfaces*. Chemical Engineering Science, **66**, 6318-6323 (2011)
43. T. Bligaard, J.K. Nørskov, S. Dahl, J. Matthiesen, C.H. Christensen, and J. Sehested: *The brønsted-evans-polanyi relation and the volcano curve in heterogeneous catalysis*. Journal of Catalysis, **224**, 206-217 (2004)
44. A. Michaelides, Z.P. Liu, C.J. Zhang, A. Alavi, D.A. King, and P. Hu: *Identification of general linear relationships between activation energies and enthalpy changes for dissociation reactions at surfaces*. Journal of the American Chemical Society, **125**, 3704-3705 (2003)
45. V. Pallassana and M. Neurock: *Electronic factors governing ethylene hydrogenation and dehydrogenation activity of pseudomorphic pdml/re(0001), pdml/ru(0001), pd(111), and pdml/au(111) surfaces*. Journal of Catalysis, **191**, 301-317 (2000)
46. T. Khan, H. Falsig, S. Wang, W. Guo, S. Dahl, and T. Bligaard: *Parameterization of a model for adsorbate-adsorbate interactions*. Submitted,

47. A. C. Lausche, A. J. Medford, T. S. Khan, T. Bligaard, F. Abild-Pedersen, J. K. Nørskov, and F. Studt: *On the effect of adsorbate-adsorbate interactions for co methanation on transition metal surfaces*. Submitted,
48. H.F. Rase, *Chemical reactor design for process plants*, in *Chemical reactor design for process plants* 1900, Wiley & Sons: New York. p. 256.
49. J.K. Nørskov, T. Bligaard, A. Logadottir, S. Bahn, L.B. Hansen, M. Bollinger, H. Bengaard, B. Hammer, Z. Sljivancanin, M. Mavrikakis, Y. Xu, S. Dahl, and C.J.H. Jacobsen: *Universality in heterogeneous catalysis*. *Journal of Catalysis*, **209**, 275-278 (2002)
50. J.S. Hummelshøj, F. Abild-Pedersen, F. Studt, T. Bligaard, and J.K. Nørskov: *Catapp: A web application for surface chemistry and heterogeneous catalysis*. *Angewandte Chemie-International Edition*, **51**, 272-274 (2012)
51. M. Behrens, F. Studt, I. Kasatkin, S. Kühn, M. Hävecker, F. Abild-Pedersen, S. Zander, F. Girgsdies, P. Kurr, B.-L. Kniep, M. Tovar, R.W. Fischer, J.K. Nørskov, and R. Schlögl: *The active site of methanol synthesis over Cu/ZnO/Al₂O₃ industrial catalysts*. *Science*, **336**, 893-897 (2012)
52. B. Hammer, L.B. Hansen, and J.K. Nørskov: *Improved adsorption energetics within density-functional theory using revised Perdew-Burke-Ernzerhof functionals*. *Physical Review B*, **59**, 7413-7421 (1999)
53. G. Kresse and J. Furthmüller: *Efficiency of ab-initio total energy calculations for metals and semiconductors using a plane-wave basis set*. *Computational Materials Science*, **6**, 15-50 (1996)
54. in *CRC handbook of chemistry and physics*, D.R. Lide and R.C. Weast, Editors. 1987, CRC Press: Boca Raton, Florida.
55. D.W. Blaylock, Y.-A. Zhu, and W. Green: *Computational investigation of the thermochemistry and kinetics of steam methane reforming over a multi-faceted nickel catalyst*. *Topics in Catalysis*, **54**, 828-844 (2011)
56. S. Wang, V. Petzold, V. Tripkovic, J. Kleis, J.G. Howalt, E. Skulason, E.M. Fernandez, B. Hvolbæk, G. Jones, A. Toftelund, H. Falsig, M. Björketun, F. Studt, F. Abild-Pedersen, J. Rossmeisl, J.K. Nørskov, and T. Bligaard: *Universal transition state scaling relations for (de)hydrogenation over transition metals*. *Physical Chemistry Chemical Physics*, **13**, 20760-20765 (2011)
57. J.R. Kitchin, J.K. Nørskov, M.A. Barteau, and J.G. Chen: *Role of strain and ligand effects in the modification of the electronic and chemical properties of bimetallic surfaces*. *Physical Review Letters*, **93** (2004)
58. O.R. Inderwildi, S.J. Jenkins, and D.A. King: *An unexpected pathway for the catalytic oxidation of methylidyne on rh{111} as a route to syngas*. *Journal of the American Chemical Society*, **129**, 1751-1759 (2007)
59. Z.P. Liu and P. Hu: *General rules for predicting where a catalytic reaction should occur on metal surfaces: A density functional theory study of C-H and C-O bond breaking/making on flat, stepped, and kinked metal surfaces*. *Journal of the American Chemical Society*, **125**, 1958-1967 (2003)
60. L. Wang, D.L. Li, M. Koike, S. Koso, Y. Nakagawa, Y. Xu, and K. Tomishige: *Catalytic performance and characterization of Ni-Fe catalysts for the steam reforming of tar from biomass pyrolysis to synthesis gas*. *Applied Catalysis A-General*, **392**, 248-255 (2011)

61. A.C.W. Koh, L. Chen, W. Kee Leong, B.F.G. Johnson, T. Khimyak, and J. Lin:
Hydrogen or synthesis gas production via the partial oxidation of methane over supported nickel–cobalt catalysts. International Journal of Hydrogen Energy, **32**, 725-730 (2007)

Paper V

Study of the "Fast SCR"-like mechanism of H₂-assisted SCR of NO_x with ammonia over Ag/Al₂O₃

Dmitry E. Doronkin, Sebastian Fogel, Stefanie Tamm,
Louise Olsson, Tuhin Suvra Khan, Thomas Bligaard,
Pär Gabrielsson, Søren Dahl

Applied Catalysis B: Environmental **113–114**, 228–236 (2012)



Study of the “Fast SCR”-like mechanism of H₂-assisted SCR of NO_x with ammonia over Ag/Al₂O₃

Dmitry E. Doronkin^{a,*}, Sebastian Fogel^b, Stefanie Tamm^{c,d}, Louise Olsson^{c,d}, Tuhin Suvra Khan^e, Thomas Bligaard^f, Pär Gabrielsson^b, Søren Dahl^a

^a Center for Individual Nanoparticle Functionality (CINF), Department of Physics, Technical University of Denmark, Fysikvej 307, 2800 Kgs. Lyngby, Denmark

^b Haldor Topsøe A/S, Nymøllevej 55, 2800 Kgs. Lyngby, Denmark

^c Competence Center for Catalysis, Chalmers University of Technology, SE-412 96 Göteborg, Sweden

^d Chemical Reaction Engineering, Chalmers University of Technology, SE-412 96 Göteborg, Sweden

^e Center for Atomic-scale Materials Design (CAMD), Department of Physics, Technical University of Denmark, Fysikvej 307, 2800 Kgs. Lyngby, Denmark

^f SUNCAT Center for Interface Science & Catalysis, SLAC National Accelerator Laboratory, Menlo Park, CA 94025, USA

ARTICLE INFO

Article history:

Received 22 September 2011

Received in revised form

15 November 2011

Accepted 24 November 2011

Available online 3 December 2011

Keywords:

Ag/Al₂O₃

Alumina

NO_x SCR

Fast SCR

FTIR

ABSTRACT

It is shown that Ag/Al₂O₃ is a unique catalytic system for H₂-assisted selective catalytic reduction of NO_x by NH₃ (NH₃-SCR) with both Ag and alumina being necessary components of the catalyst. The ability of Ag/Al₂O₃ and pure Al₂O₃ to catalyse SCR of mixtures of NO and NO₂ by ammonia is demonstrated, the surface species occurring discussed, and a “Fast SCR”-like mechanism of the process is proposed. The possibility of catalyst surface blocking by adsorbed NO_x and the influence of hydrogen on desorption of NO_x were evaluated by FTIR and DFT calculations.

© 2011 Elsevier B.V. All rights reserved.

1. Introduction

Nitrogen oxides (NO_x) are the most challenging pollutants to address for light-duty diesel vehicles and sophisticated techniques like advanced fuel injection, exhaust gas recirculation (EGR), turbocharging, etc., are used by engine manufactures to reduce emissions. But NO_x removal by exhaust aftertreatment is still required due to stricter emission regulations and the trade off between fuel consumption and NO_x emission, i.e., the price for reducing fuel consumption and CO₂ emission by ~15% equals to ~50% increase in NO_x emissions [1].

Selective catalytic reduction (SCR) is the leading NO_x control technique with ammonia as a reductant. Commonly used catalysts are vanadia-based catalysts, Cu and Fe-containing zeolites. However, none of the systems demonstrates high thermal durability together with a good activity throughout a broad temperature region from 150 to 550 °C [1]. This fact explains the reason for the on-going research of novel catalytic systems for NH₃-SCR, which are supposed to be non-toxic, inexpensive and durable.

Alumina supported metals, such as Ag, In, Sn, etc., [2–5] are known to catalyse NO_x SCR by hydrocarbons under the conditions of lean-burn engine exhaust. The major drawback of these catalytic systems is their very poor activity at low temperatures. It has been found that addition of hydrogen to the gas feed can substantially improve the low-temperature activity of Ag/Al₂O₃ [6–8]. Interestingly, several groups have also demonstrated the possibility of Ag/Al₂O₃ to facilitate SCR of NO_x by ammonia or urea with co-feeding hydrogen, resulting in nearly 90% NO_x conversion at temperatures as low as 200 °C [9,10].

Hydrogen for this reaction can be produced on board of the vehicle by two means depending on the used reductant. The required amount of hydrogen can be produced in an on-board fuel reformer without the necessity to change the existing fuel infrastructure. This is convenient for hydrocarbon SCR systems utilizing Ag/Al₂O₃ catalysts and currently leads to fuel penalties from 5 to 10% [11,12] which might be improved by the optimisation of the system. For the NH₃ SCR applications hydrogen can be produced by cracking of part of the ammonia. Pure NH₃ required for this purpose can be stored on board in form of solid metal ammine salts [13]. The suggested system allows accurate and independent dosing of ammonia to the SCR catalyst and to the cracker where it can be decomposed to form the required hydrogen. Using ammonia for hydrogen storage has earlier been suggested for fuel

* Corresponding author. Tel.: +45 4525 3275.

E-mail addresses: dmdo@fysik.dtu.dk, dmitriy.doronkin@gmail.com (D.E. Doronkin).

cell applications but can also be applied for NO_x SCR applications [14,15].

There is no general agreement about the necessary concentration of hydrogen for the effective reduction of NO_x by ammonia over Ag/Al₂O₃. One can find H₂:NO_x ratios varying from 5 to 10 in the literature [9,10,16–18] which is a rather high value. However, Shimizu and Satsuma have demonstrated ever increasing NO_x reduction rate in the interval of H₂:NO_x ratios from 0 to 50 [17] which makes the choice of H₂ concentration a matter of finding the optimum between the amount of ammonia spent on hydrogen production and the SCR efficiency. We are considering a H₂:NO_x ratio 2.4 as an optimum in this work.

Hydrogen has also been considered as the only reductant in H₂-SCR of NO_x, however, currently available catalysts allow effective removal of NO_x only when using H₂:NO_x > 10 and such amount of hydrogen cannot be produced on board at an affordable price [19–21].

In this work we studied several catalysts: Ag supported on different carriers (γ-Al₂O₃, TiO₂ and ZrO₂), Sn and In supported on γ-Al₂O₃ and pure alumina under the conditions of H₂-assisted SCR of NO_x with NH₃. The aim of this study is to investigate the possibility of replacing traditional NO_x SCR catalysts by Ag/Al₂O₃ thus obtaining high catalyst activity even at low temperatures. Another goal of the study is to give insight to the mechanistic aspects of H₂-assisted NO_x SCR by ammonia.

2. Experimental

2.1. Catalyst preparation

Parent γ-alumina (Puralox SCFa-140, 59 ppm Fe₂O₃ content) was kindly provided by SASOL. Prior to its study as a catalyst it was calcined at 550 °C for 4 h in static air.

1%Ag/Al₂O₃, 3%Sn/Al₂O₃ and 3%In/Al₂O₃ were obtained by incipient wetness impregnation of parent γ-alumina by corresponding amounts of AgNO₃, SnCl₄·5H₂O and InCl₃·4H₂O (all from Sigma–Aldrich) solutions in deionised water. 1%Ag/TiO₂ and 1%Ag/ZrO₂ were obtained by incipient wetness impregnation of TiO₂ (anatase containing 10%SiO₂) and ZrO₂ (E10, Magnesium Elektron Ltd.) by the aqueous solution of AgNO₃. After impregnation all catalysts were dried at room temperature overnight and calcined at 550 °C for 4 h in static air.

The calcined catalysts were pressed, crushed and sieved to obtain the fraction 0.18–0.35 mm (mesh 80–mesh 45).

2.2. TEM measurements

TEM measurements were carried out in a TECNAI T20 transmission electron microscope equipped with an Oxford Instruments EDX detector. For the measurements the catalyst powder (in a dry form) was dispersed on a copper TEM grid covered with a lacey carbon film. Images were acquired using DigitalMicrograph from Gatan Inc.

2.3. Catalytic studies

The catalytic measurements were carried out in a fixed-bed quartz flow reactor (inner diameter = 4 mm) in a temperature programmed mode while the temperature was decreased from 400 °C to 150 °C with a rate 2 °C/min. The temperature was controlled using an Eurotherm 2416 temperature controller with a K-type thermocouple. 45 mg of catalyst was diluted with 100 mg of SiC (mesh 60) and placed on a quartz wool bed. The bed height was ~11 mm and the GHSV, calculated using the volume of the pure catalyst was ~110,000 h⁻¹. The gas composition normally contained 500 ppm NO, 520 ppm NH₃, 8.3% O₂, and 7% water balanced with

Ar. During some tests 1200 ppm of H₂ was added to the gas feed. The gas feed was mixed from 2000 ppm NO in Ar, 2000 ppm NH₃ in Ar, 4000 ppm H₂ in Ar (Air Liquide), oxygen and argon (AGA), dosed by individual mass flow controllers (UNIT Celerity). Water was dosed by an ISCO 100DM syringe pump through a heated capillary. Mixtures of NO and NO₂ were obtained by feeding NO and oxygen through a long capillary, giving NO_x with 26–47% NO₂. Reaction products were analysed by a Thermo Fisher Nicolet 6700 FTIR analyser, equipped with a gas cell (2 m optical pathlength). Gas capillaries were heated to ~130 °C and the FTIR gas cell to 165 °C to avoid condensation of water and formation of ammonium nitrate. To simplify experimental procedure we are not using CO₂ in the study as we have not observed CO₂ effect on the NO_x SCR by NH₃ during the preliminary experiments with Ag/Al₂O₃ catalysts.

Conversions were calculated using the following equations:

$$X_{\text{NO}_x} = 1 - \frac{C_{\text{NO}_x}^{\text{outlet}}}{C_{\text{NO}_x}^{\text{inlet}}} \quad (1)$$

where X_{NO_x} denotes total conversion of NO_x and $C_{\text{NO}_x}^{\text{inlet}}$ and $C_{\text{NO}_x}^{\text{outlet}}$ is the NO_x concentrations on the inlet and outlet of the reactor, where:

$$C_{\text{NO}_x} = C_{\text{NO}} + C_{\text{NO}_2} \quad (2)$$

NH₃ conversion (total), NH₃ conversion to NO_x (when no NO_x is fed) and NO conversion to NO₂ (when no NH₃ was fed) were calculated correspondingly:

$$X_{\text{NH}_3} = 1 - \frac{C_{\text{NH}_3}^{\text{outlet}}}{C_{\text{NH}_3}^{\text{inlet}}} \quad (3)$$

$$X_{\text{NH}_3 \rightarrow \text{NO}_x} = \frac{C_{\text{NO}_x}^{\text{outlet}}}{C_{\text{NH}_3}^{\text{inlet}}} \quad (4)$$

$$X_{\text{NO} \rightarrow \text{NO}_2} = \frac{C_{\text{NO}_2}^{\text{outlet}}}{C_{\text{NO}}^{\text{inlet}}} \quad (5)$$

and the ratio of converted NO to converted NO₂ in the experiments with NO and NO₂ mixtures:

$$\frac{C_{\text{NO}}^{\text{conv.}}}{C_{\text{NO}_2}^{\text{conv.}}} = \frac{C_{\text{NO}}^{\text{inlet}} - C_{\text{NO}}^{\text{outlet}}}{C_{\text{NO}_2}^{\text{inlet}} - C_{\text{NO}_2}^{\text{outlet}}} \quad (6)$$

NH₃:NO_x conversion ratio below 400 °C was always 1:0.95–1.05 for all tested catalysts, therefore we are presenting only NO_x conversion values in the discussion.

2.4. DRIFTS studies

In-situ diffuse reflectance infrared Fourier transform spectroscopy (DRIFTS) experiments were performed using a BioRad FTS 6000 FTIR spectrometer equipped with a high-temperature reaction cell (Harrick Scientific, Praying Mantis) with KBr windows. The temperature of the reaction cell was controlled with a K-type thermocouple connected to a Eurotherm 2416 temperature controller. Gases were introduced into the reaction cell via individual mass flow controllers (Bronkhorst Hi-Tech). The gas composition at the outlet of the DRIFTS cell was analysed by a mass spectrometer (Balzers QuadStar 420).

Each experiment was performed using approximately 100 mg of γ-Al₂O₃ powder, using new powder for each experiment. The powder was initially pretreated in a flow of 8% O₂ in Ar at 500 °C for 30 min, subsequently a background spectrum (60 scans, resolution 2 cm⁻¹ at 4000 cm⁻¹) was recorded in a flow of Ar. At 500 °C, 185 ppm NO₂, 315 ppm NO, 520 ppm NH₃ and 8.3% O₂ were added to the feed. Then the catalyst was cooled with a ramp rate of 10 °C/min in the reaction mixture to reaction temperature, where

the temperature is held for 10 min for stabilisation. Subsequently, NH_3 is removed from the feed gas mixture for 30 min and added again to it for 10 min. This procedure was repeated once. Thereafter, 1250 ppm H_2 were added for 10 min to the feed gas and, subsequently, NH_3 was removed again. The evolution of absorption bands in the spectra was followed using the kinetic mode (9 scans/spectrum, 6 spectra/min.) at a resolution of 2 cm^{-1} at 4000 cm^{-1} . The data are presented as absorbance, which is defined as the logarithm of the inverse reflectance ($\log 1/R$). All DRIFTS experiments were carried out using a total flow rate of 100 ml/min which corresponds to a space velocity of about $62,000\text{ h}^{-1}$.

2.5. DFT calculations

Plane wave DFT code DACAPO is used to calculate the adsorption energies and the gas phase energies of the adsorbates. Plane wave cutoff of 340.15 eV and density cutoff of 680 eV are used for the calculations. The core electrons are described by the Vanderbilt ultrasoft pseudopotential [22]. RBPE is used as the exchange correlation energy function [23]. Fermi population of the Kohn-Sham states is $k_B T = 0.1\text{ eV}$. The convergence limit is set as maximum change in force constant $f_{\text{max}} = 0.03\text{ eV}$.

The adsorption energies of O, NO, NO_2 and NO_3 are studied over six different transition metals (Ag, Cu, Pd, Pt, Rh, Ru) on both the (111) terrace and the (211) step surfaces. We use a 2×2 surface cell for O and NO for (111) terrace, 2×1 surface cell for O and NO for (211) step surface, 3×3 surface cell for NO_2 and NO_3 adsorption study on (111) terrace and the 3×1 surface cell for NO_2 and NO_3 adsorption study (211) step surfaces, with $8 \times 8 \times 1$ Monkhorst-Pack k -point sampling in the irreducible Brillouin zone for all the 2×2 surface cells, $8 \times 6 \times 1$ Monkhorst-Pack k -point sampling in the irreducible Brillouin zone for all the 2×1 surface cells and $4 \times 4 \times 1$ Monkhorst-Pack k -point sampling for both 3×3 and 3×1 surface cells. For all the (111) surfaces we use a four-layer slab where the two topmost layers are allowed to relax whereas for the (211) surfaces with 2×1 surface cell we use a slab model with twelve layers where the topmost six layers are allowed to relax and for (211) surfaces with 3×1 surface cell we use a slab model with nine layers where the topmost three layers are allowed to relax.

For the calculation of $\gamma\text{-Al}_2\text{O}_3$ and the adsorption of different species on $\gamma\text{-Al}_2\text{O}_3$ we also used the DACAPO code with a plane wave cutoff of 340.15 eV and a density cutoff of 680 eV . A $4 \times 4 \times 1$ Monkhorst-Pack k -point sampling in the irreducible Brillouin zone was used for $\gamma\text{-Al}_2\text{O}_3$. The $\gamma\text{-Al}_2\text{O}_3$ surface was modelled by a step on a nonspinel $\gamma\text{-Al}_2\text{O}_3$ structure which was derived bulk $\gamma\text{-Al}_2\text{O}_3$ model [24]. The cell parameters for the $\gamma\text{-Al}_2\text{O}_3$ step closed packed surface are $a = 8.0680\text{ \AA}$ and $b = 10.0092\text{ \AA}$ and $\alpha = \beta = \gamma = 90^\circ$. For the $\gamma\text{-Al}_2\text{O}_3$ surface the bottom two layers were fixed whereas the top three layers were allowed to relax.

In all the model surfaces, the neighboring slabs are separated by more than 10 \AA of vacuum.

NO_x and HNO_x adsorption energies were calculated relative to gas phase zero energy points of these species.

The energy minimum adsorption geometries used in the calculations are presented in the supplementary material.

3. Results and discussion

3.1. Unique activity of $\text{Ag}/\text{Al}_2\text{O}_3$ in H_2 -assisted NH_3 -de NO_x

NO_x conversions obtained over the prepared catalysts at 380°C tested under the conditions of SCR of NO_x with NH_3 , without and with H_2 in the exhaust, are given in Table 1. In the absence of H_2 all the catalysts are inert with respect to NO_x reduction or ammonia

Table 1

Studied catalysts and NO_x conversions obtained at 380°C without and with H_2 in the feed gas. Reaction conditions: 500 ppm NO, 520 ppm NH_3 , 8.3% O_2 , 7% H_2O in Ar, GHSV = $110,000\text{ h}^{-1}$.

Catalyst	Metal loading, wt%	Support BET surface area, m^2/g	NO_x conversion	
			0 ppm H_2	1200 ppm H_2
Al_2O_3	–	140	0	0
$\text{Ag}/\text{Al}_2\text{O}_3$	1	140	0	94
Ag/TiO_2	1	110	1.5	25
Ag/ZrO_2	1	14	0	0
$\text{Sn}/\text{Al}_2\text{O}_3$	3	140	0	0
$\text{In}/\text{Al}_2\text{O}_3$	3	140	0	10.5

oxidation at temperatures below 400°C . The hydrogen effect was observed only for $\text{Ag}/\text{Al}_2\text{O}_3$, Ag/TiO_2 and $\text{In}/\text{Al}_2\text{O}_3$ (Fig. 1). The former catalyst demonstrates extremely high performance with NO_x conversion exceeding 80% at 200°C at GHSV = $110,000\text{ h}^{-1}$. No more than 5 ppm N_2O was observed in the products. Ag/TiO_2 is much less active with maximum NO_x conversion of 25% at 380°C . The activity of $\text{In}/\text{Al}_2\text{O}_3$ below 400°C is only marginal. Therefore only $\text{Ag}/\text{Al}_2\text{O}_3$ may be considered for practical applications among the tested catalysts. Furthermore, it is evident that both silver and alumina are necessary components of the catalyst to obtain a high performance in de NO_x . Removal or change of each of these components lead to almost inactive catalysts. Therefore, it is likely that both silver and alumina take part in the catalytic cycle or the active site is positioned on the interface between Ag and Al_2O_3 .

3.1.1. TEM data on $\text{Ag}/\text{Al}_2\text{O}_3$ and Ag/TiO_2

In order to clarify if it is the catalyst morphology that determines the drastic difference in the SCR performance of $\text{Ag}/\text{Al}_2\text{O}_3$ and Ag/TiO_2 , TEM images of the samples were obtained. These micrographs are compared in Fig. 2. The choice of the catalysts in question is dictated by their common properties (Ag loading, BET surface area of the support, preparation technique), which is in contrast to their very different catalytic activity.

EDX shows the presence of $\sim 1\%$ Ag in the both depicted catalyst grains. However, we were unable to locate any metal particles with diameters larger than $2\text{--}3\text{ nm}$ in both catalyst samples. This confirms a high dispersion of Ag in both $\text{Ag}/\text{Al}_2\text{O}_3$ and Ag/TiO_2 .

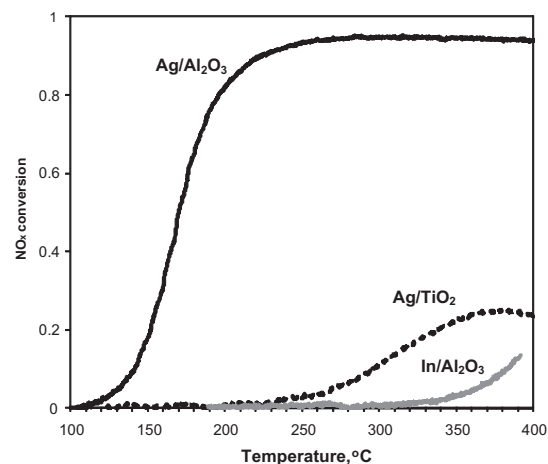


Fig. 1. NO_x conversion profiles obtained over $\text{Ag}/\text{Al}_2\text{O}_3$, Ag/TiO_2 and $\text{In}/\text{Al}_2\text{O}_3$. Reaction conditions: 500 ppm NO, 520 ppm NH_3 , 1200 ppm H_2 , 8.3% O_2 , 7% H_2O in Ar, GHSV = $110,000\text{ h}^{-1}$.

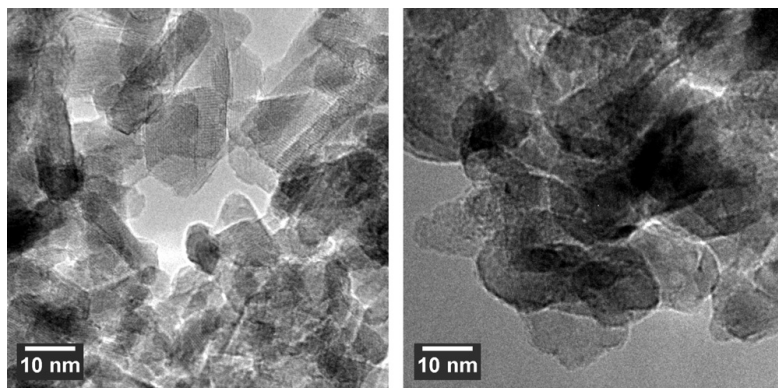


Fig. 2. TEM images of Ag/Al₂O₃ (left) and Ag/TiO₂ (right) calcined at 550 °C in air.

catalysts, which might be in the form of clusters of 4–8 Ag atoms as suggested by Kondratenko et al. [16]. Therefore the large difference in SCR activity of Ag/Al₂O₃ and Ag/TiO₂ is not due to a large difference in Ag dispersion.

3.2. Study of the mechanism of H₂-assisted NH₃-deNO_x

3.2.1. Experiments with Ag/Al₂O₃ where components of the feed are omitted

Studies of the mechanism of hydrogen-assisted NO_x SCR by NH₃ on Ag/Al₂O₃ were already performed before [16,17], where the attention was drawn to the state of silver. Our catalytic experiments show a uniqueness of the Ag/Al₂O₃ catalytic system, in which both components play a vital role.

To have a notion of the individual reactions occurring during NO_x SCR by NH₃ we consecutively run catalytic tests with one of the components absent in the feed.

According to the results obtained so far it is already clear that the removal of hydrogen leads to a completely inactive catalyst with regards to NH₃-deNO_x (Table 1) or ammonia oxidation. The concentration of all monitored gases remained constant during temperature ramping from 400 to 100 °C when no H₂ was in the feed. The same is true for the removal of oxygen from the feed – no NO reduction or NH₃ oxidation was observed without O₂.

When NH₃ was removed from the gas feed, a pronounced oxidation of NO to NO₂ starting from 100 °C was observed (Fig. 3, solid line). Together with that a very low NO_x to N₂ conversion (dotted line, max. 4%) was observed indicating that hydrogen normally acts not as the main reductant but as a co-reductant. When both ammonia and hydrogen were removed from the feed, no oxidation of NO to NO₂ was observed.

The latter observation agrees with the data obtained in [6,16]. As suggested in [6], hydrogen addition promotes oxidation of NO. However, we observed no oxidation of NO to NO₂ during the experiments with Ag/TiO₂ and Ag/ZrO₂ catalysts. This shows once again that not only Ag, but also the support plays an important role in the catalytic activity of Ag/Al₂O₃ which also agrees with the data on C₃H₈-SCR reported in [6].

The mechanism of O₂ activation by hydrogen has been suggested earlier [25,26] as follows. On the first step hydrogen dissociates on active Ag_n⁺ sites on alumina to form an acidic proton and hydride Ag_n–H. This hydride later reacts with oxygen to form a reactive oxidant, such as hydroperoxy radicals (HO₂), peroxide (O₂²⁻), or superoxide ions (O₂⁻) all of which later oxidise NO to NO₂.

When removing NO from the NO, NH₃, H₂, O₂ and H₂O containing feed, NH₃ oxidation to N₂ (Fig. 4, solid line) and to NO_x (Fig. 4, dotted line) occurs at temperatures higher than 200 °C. Comparison of the data in Fig. 3 and Fig. 4 suggests that NO oxidative activation starts at significantly lower temperature (corresponding to the NH₃-deNO_x light-off temperature) than NH₃ oxidative activation. Therefore it is more likely that oxidative activation of NO is an important step in the overall catalytic mechanism of NO_x SCR over Ag/Al₂O₃.

The data does not support a hypothesis of oxidative dehydrogenation of NH₃ (or NH₃-assisted NO decomposition) being the main catalysed step of H₂-assisted NH₃-deNO_x over Ag/Al₂O₃ [18]. Ag/Al₂O₃ rather participates in NO activation and possibly in the reaction of NH₃ with NO_x intermediates [16].

The hydrogen promoted oxidative activation of NO has been already reported by Satokawa et al. for NO_x SCR by C₃H₈ [6]. However in that study oxidative activation of NO was not enough to initiate SCR and activation of C₃H₈ by H₂ has been reported to be necessary which makes it different from SCR by NH₃.

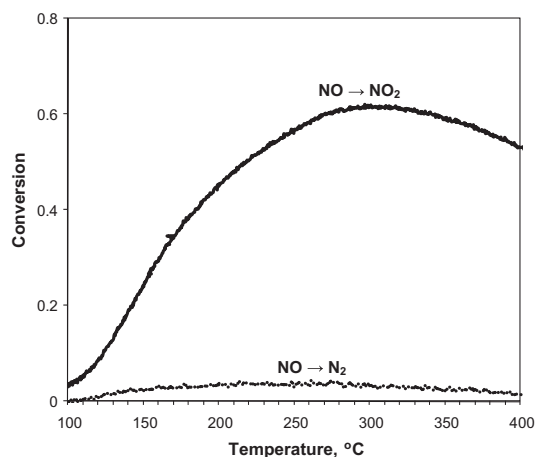


Fig. 3. NO conversion to NO₂ (solid line) and NO_x conversion to N₂ (dotted line) over Ag/Al₂O₃ without ammonia in the feed. Reaction conditions: 500 ppm NO, 1200 ppm H₂, 8.3% O₂, 7% H₂O in Ar, GHSV = 110,000 h⁻¹.

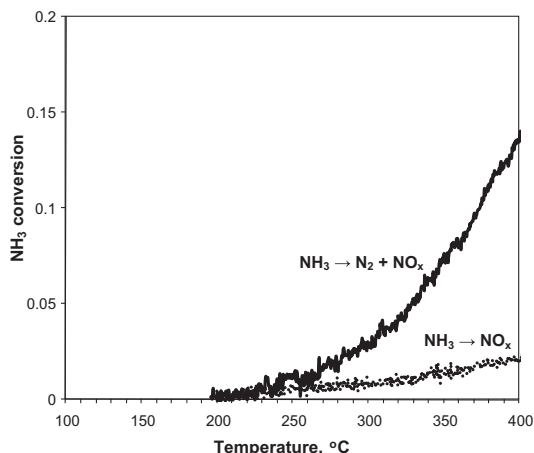


Fig. 4. Total NH_3 conversion (solid line) and NH_3 conversion to NO_x (dotted line) over $\text{Ag}/\text{Al}_2\text{O}_3$ with no NO in the feed. Reaction conditions: 520 ppm NH_3 , 1200 ppm H_2 , 8.3% O_2 , 7% H_2O in Ar, GHSV = 110,000 h^{-1} .

3.2.2. Experiments with feeding NO and NO_2 mixtures over $\text{Ag}/\text{Al}_2\text{O}_3$ and Ag/ZrO_2

After realizing that the hydrogen promoted oxidation of NO to NO_2 may be the first step in the H_2 -assisted NH_3 -de NO_x we decided to do catalytic tests with a feed containing a mixture of NO and NO_2 as NO_x . Since H_2 facilitates reversible NO - NO_2 transformation, undesirable for these experiments, no H_2 was co-fed.

Fig. 5 shows NO_x conversions to N_2 obtained over $\text{Ag}/\text{Al}_2\text{O}_3$ when a NO and NO_2 mixture is fed as NO_x (containing 26, 34 and 47% NO_2) and over Ag/ZrO_2 with 34% NO_2 in NO as NO_x . Surprisingly for all three cases we observe nearly equal, maximum 30%, NO_x conversion which changes only slightly with temperature. NH_3 conversion profiles follow the NO_x conversion profiles and they are therefore not shown. This observation allows us to conclude that oxidation of NO to NO_2 over $\text{Ag}/\text{Al}_2\text{O}_3$, at least, partially accounts

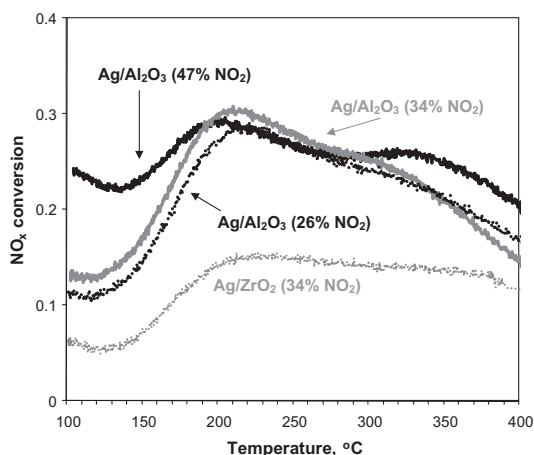


Fig. 5. NO_x conversion over $\text{Ag}/\text{Al}_2\text{O}_3$ and Ag/ZrO_2 without H_2 in the feed, when NO and NO_2 mixture is fed as NO_x (NO_2 content is specified, NO is the rest of 500 ppm NO_x). Conditions: 500 ppm NO_x , 520 ppm NH_3 , 8.3% O_2 , 7% H_2O in Ar, GHSV = 110,000 h^{-1} .

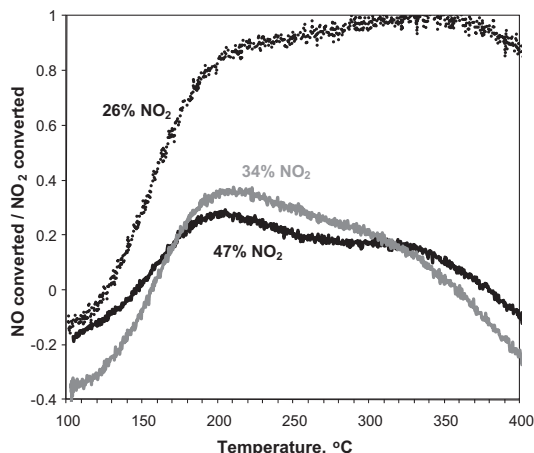


Fig. 6. Ratio of consumed NO to consumed NO_2 for simultaneous $\text{NO} + \text{NO}_2$ reduction by NH_3 over $\text{Ag}/\text{Al}_2\text{O}_3$. Reaction conditions: 500 ppm NO_x (NO_2 fraction is stated near the corresponding curves), 520 ppm NH_3 , 8.3% O_2 , 7% H_2O in Ar, GHSV = 110,000 h^{-1} .

for the activity of this catalyst in the NO_x SCR. This agrees with previous works, evidencing oxidation of NO to NO_2 involving H_2 [25] and supposing it to be crucial for low-temperature NO_x SCR by hydrocarbons [27].

Moreover, SCR of the NO and NO_2 mixture by NH_3 is not a unique feature of $\text{Ag}/\text{Al}_2\text{O}_3$ but was also observed for other supports though to a less extent, e.g. with 15% maximum NO_x conversion in the case of Ag/ZrO_2 (see Fig. 5, gray dotted line). Thus, metal oxides other than alumina can catalyse $\text{NO} + \text{NO}_2$ SCR by NH_3 but $\text{Ag}/\text{Al}_2\text{O}_3$ with H_2 co-feeding is required to oxidise NO at low temperatures. Therefore, we are focusing our study on $\text{Ag}/\text{Al}_2\text{O}_3$ catalysts and the corresponding alumina support.

The effect of increasing the NO_x SCR rate by feeding NO and NO_2 mixture has already been noticed for other catalytic systems including vanadia-based catalysts [28] and zeolites [29]. The effect is called “Fast-SCR” and characterised by a well-defined stoichiometry of $\text{NO}:\text{NO}_2$ being 1:1.

To check if the $\text{NO}:\text{NO}_2$ conversion without H_2 in the feed can be ascribed to “Fast SCR” [29], we calculated the ratio of consumed NO to consumed NO_2 (Fig. 6). In our case the ratio of consumed NO to consumed NO_2 changed with temperature from negative values (only NO_2 is consumed and a small amount of NO is produced from it) to positive values up to 1 in case of feeding 26% NO_2 (Fig. 6). Interestingly, the temperature at which NO starts to be consumed ($\sim 150^\circ\text{C}$) coincides with the onset temperature of H_2 -assisted SCR (Fig. 1). Therefore, we can suppose that parts of the mechanisms of both H_2 -assisted NO SCR by NH_3 and $\text{NO} + \text{NO}_2$ SCR by NH_3 are similar. But in case of $\text{NO} + \text{NO}_2$ SCR we observed a conversion limit at $\sim 30\%$, when almost 100% conversion is obtained in H_2 -assisted NO_x -SCR. This could be explained by blocking of the catalyst surface by adsorbed nitrate species [25]. The poisoning effect of surface nitrates for propane-SCR was observed in [26], where the authors also demonstrated the ability of hydrogen to effectively remove adsorbed nitrate species. Thus, introduction of hydrogen may facilitate not only NO to NO_2 conversion, but also regeneration of the catalyst surface, which removes the 30% conversion limit.

In general, the ratio of converted NO to converted NO_2 depends on the total amount of NO_2 in the feed and decreases with increase in NO_2 content. The higher the NO_2 content – the larger is the part of NO_2 in the NO_x that is converted to N_2 . Independent on this,

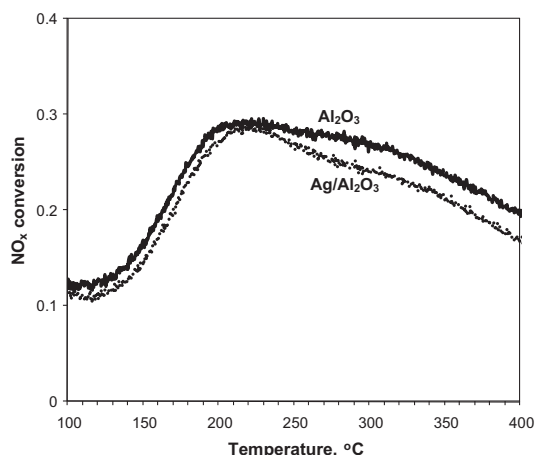


Fig. 7. NO_x conversion over Al_2O_3 (solid line) and $\text{Ag}/\text{Al}_2\text{O}_3$ (dotted line, for a comparison) without H_2 in the feed, when NO and NO_2 mixture is fed as NO_x . Reaction conditions: 500 ppm NO_x (37% NO_2), 520 ppm NH_3 , 8.3% O_2 , 7% H_2O in Ar, GHSV = 110,000 h^{-1} .

the ratio of converted NO_x to converted NH_3 was always 1:1 and maximum conversion remained constant at $\sim 30\%$.

3.2.3. Experiments with feeding NO and NO_2 mixtures over pure $\gamma\text{-Al}_2\text{O}_3$

In some of the papers on H_2 -assisted NO SCR by NH_3 , published earlier [16,17], alumina was considered only as a support for the active Ag nanoparticles. In this case, the properties of alumina could influence the catalyst activity indirectly by tuning the Ag particle size and distribution. In the following we test this assumption.

With or without hydrogen γ -alumina stays inactive under the experimental conditions of NO_x SCR by ammonia when NO is the only component of NO_x in the feed. This changes when NO_2 is introduced. Fig. 7 shows a comparison of NO_x (26% NO_2 of total NO_x at the reactor inlet) conversion by NH_3 obtained over pure Al_2O_3 (solid line) and $\text{Ag}/\text{Al}_2\text{O}_3$ (dotted line) with no H_2 in the feed. The profiles are almost identical indicating that presence of Ag in the catalyst is important only for the H_2 -assisted reaction. Taking into account the overall quantity of NO_2 , which can be produced from NO in presence of H_2 over $\text{Ag}/\text{Al}_2\text{O}_3$ (Fig. 3), it is evident that alumina can significantly contribute to the overall H_2 -assisted NO SCR mechanism. Thus, it cannot be neglected that alumina is an active part of the catalyst. Moreover the stoichiometry of $\text{NO} + \text{NO}_2$ SCR conversion over alumina follows the same trend as for the $\text{Ag}/\text{Al}_2\text{O}_3$ (Fig. 8), which may demonstrate the same mechanism is working in both cases. Running $\text{NO} + \text{NO}_2$ SCR with H_2 in the feed over pure Al_2O_3 yield almost the same NO_x conversion as as for the test without H_2 (Fig. 7, solid line).

Thus, the presence of Ag and H_2 is mostly important for oxidative activation of NO and possibly removal of adsorbed species blocking the catalyst surface. The reaction of NO and NH_3 with the obtained NO_2 can proceed further over pure Al_2O_3 yielding N_2 . This result agrees with the results of Lee et al. [30], who demonstrated the ability of pure alumina to catalyse the reduction of NO , activated over $\text{Ag}/\text{Al}_2\text{O}_3$, by partially oxidised hydrocarbons. At the same time, Meunier and Ross [31] observed the ability of pure alumina to run the propene SCR of NO_2 (but not of NO).

From the analysis of the stoichiometry of the $\text{NO} + \text{NO}_2$ SCR reaction (Figs. 6 and 8) it can be concluded that at temperatures lower than 150 °C only NO_2 reacts with NH_3 . The production of NO from

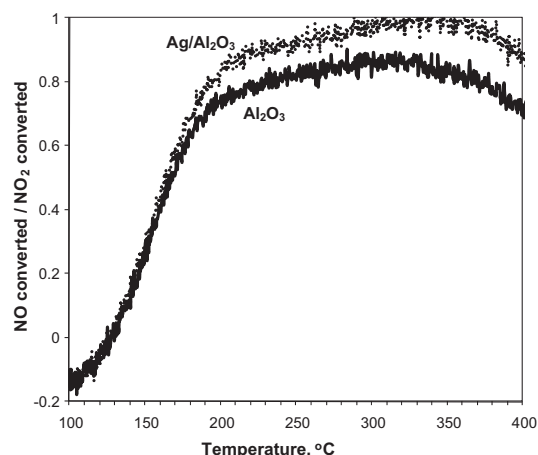
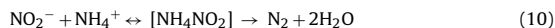


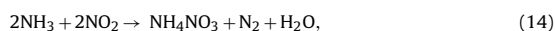
Fig. 8. Ratio of consumed NO to consumed NO_2 for $\text{NO} + \text{NO}_2$ simultaneous reduction by NH_3 over Al_2O_3 (solid line) and $\text{Ag}/\text{Al}_2\text{O}_3$ (dotted line, for a comparison). Reaction conditions: 500 ppm NO_x (26% NO_2), 520 ppm NH_3 , 8.3% O_2 , 7% H_2O in Ar, GHSV = 110,000 h^{-1} .

NO_2 can also be observed, which is thermodynamically not possible and is likely due to an uncomplete SCR reaction between NO_2 and NH_3 . Above 350 °C NO_2 decomposition to NO is thermodynamically favorable, and this may be a reason of decreasing apparent amount of consumed NO [32]. Only between 150 and 350 °C NO consumption is significant and almost equal to NO_2 consumption in the case of 26% NO_2 in NO_x feed. Based on the knowledge of the “Fast SCR” [29] the following reactions can be proposed:



According to the scheme, at temperatures higher than 150 °C reactions (7)–(11) take place yielding nitrogen and surface nitrate species. Disproportionation of adsorbed NO_2 (8), (9) was also suggested by DFT calculations earlier [33]. A small part of the surface nitrates is decomposed to N_2O (12), trace amount of which (<5 ppm) is observed in the reaction products at high temperatures. NO production from NO_2 (negative $\text{NO}_{\text{converted}}/\text{NO}_{2\text{converted}}$ ratio at $T < 150$ °C on Fig. 6) and the observation that the higher the NO_2 content – the larger is the part of NO_2 in the NO_x that is converted to N_2 in the NO/NO_2 experiments can be explained by reverse (13). NO reacts with surface nitrates according to (13) to form NO_2 and nitrite, which is readily decomposed to nitrogen (10). With that nitrates are partly removed from the catalyst surface and higher NO_x conversion is obtained.

With decreasing reaction temperature from 400 to 200 °C an increase in the NO_x conversion is observed. The effect is particularly evident for the 47% $\text{NO}_2 + \text{NO}$ mixture (Fig. 5, solid curve) and may be due to the formation of surface NH_4NO_3 . NH_4NO_3 formation is also consistent with decreased $\text{NO}_{\text{converted}}/\text{NO}_{2\text{converted}}$ ratio below 180 °C (Fig. 8) due to reaction stoichiometry:



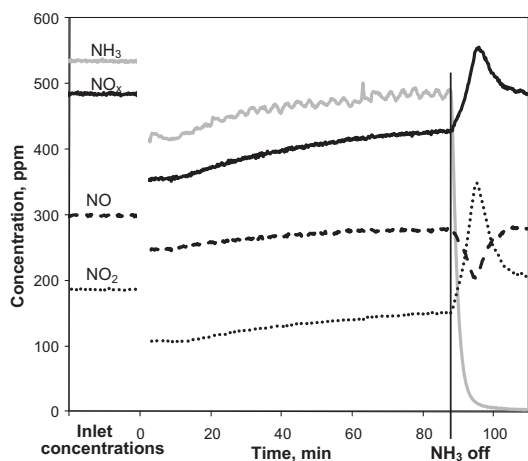


Fig. 9. Change of NO, NO₂ and NO_x concentrations after removing NH₃ from the feed. Catalyst: Al₂O₃. Reaction conditions: 500 ppm NO_x (37% NO₂), 520 ppm NH₃, 8.3% O₂, 7% H₂O in Ar, GHSV = 110,000 h⁻¹, temperature 210 °C.

which is, in fact, a combination of (7)+(8)+(9)+(10)+(11), but without (12) and (13), which are too slow at this temperature. It is also rather indicative of NH₄NO₃ formation that below 200 °C we do not observe N₂O evolution, while above this temperature its decomposition (12) yields N₂O. Therefore, below 200 °C nitrate formation and subsequent blocking the alumina surface limits NO_x conversion.

To check the reaction scheme during an Al₂O₃ activity test, temperature ramping was stopped at 500, 210 and 100 °C. After the concentrations of the outlet gas components were stabilised, NH₃ was switched off from the feed. Following the removal of NH₃ from the inlet gas at 500 and 100 °C the concentrations of NO and NO₂ equalled these concentrations at the reactor inlet (no reaction with adsorbed nitrates (13) was observed). However, the removal of NH₃ from the feed at 210 °C (Fig. 9) resulted in consumption of NO and release of NO₂. This is in agreement with NO consumption in the NO_x SCR over alumina, which takes place between 150 and 350 °C (Fig. 8). The ratio of evolved NO₂ to consumed NO was approximately 1.7. This ratio can be achieved by combination of the competing reactions (10), which gives no NO₂, reverse (9) and (8), which give 2 NO₂ molecules, and, of course (13), which initiates the NO consumption and yields 1 NO₂ molecule. Thus the mechanism of NO_x SCR by NH₃ over Al₂O₃ and Ag/Al₂O₃ could share most of the reaction steps with “Fast SCR”.

3.2.4. Surface species during NH₃-SCR over Al₂O₃

Diffuse reflectance infrared spectroscopy is a powerful tool to complement observations from catalytic experiments with observations of surface species. Fig. 10 shows the evolution of species on the Al₂O₃ surface, when switching off NH₃ from a feed containing NO, NO₂, NH₃ and O₂ at 150 °C and at 500 °C. Similar spectra were observed at 300 and 400 °C but not shown. The first spectra are taken in a feed containing NH₃ and the following spectra 5, 10, 15 and 25 min after the NH₃ was switched off. When all gases are present in the first spectra, bands at 1690, 1623, 1533, 1474, 1398, 1314 and 1236 cm⁻¹ can be distinguished at 150 °C. According to literature, the bands at 1623, 1533 and 1236 cm⁻¹ which are accompanied by bands at 3355, 3271 and 3173 cm⁻¹ (not shown) can be assigned to deformation vibrations and stretching vibrations of ammonia, respectively [34–37]. Bands at 1690 and 1474 cm⁻¹ have previously been assigned to deformation vibrations of NH₄⁺

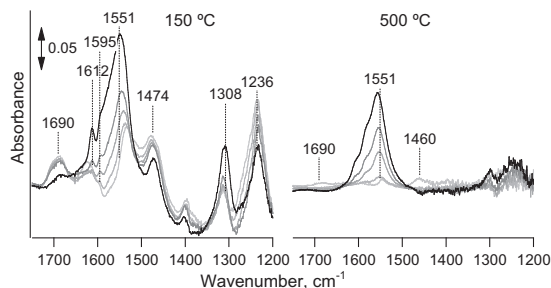


Fig. 10. Change in surface species after removing NH₃ for the first time from the feed over a fresh Al₂O₃ catalyst. Reaction conditions: 500 ppm NO_x (37% NO₂), 520 ppm NH₃, 8.3% O₂ in Ar. Spectra were taken from gray to black: with NH₃ in the feed, and 5, 10, 15 and 25 min after switching off NH₃.

or NH₃ [34,35,37]. At 500 °C all the bands are much smaller. But even there, mainly bands due to NH₃ or NH₄⁺ can be observed. Thus under NH₃-SCR conditions, mainly ammonia is adsorbed on Al₂O₃ and very little nitrates and nitrites are adsorbed. When turning off ammonia in the feed first the bands of adsorbed NH₃ at 1236, 1623, 3355, 3271 and 3173 cm⁻¹ decrease at 150 °C. Somewhat later, the NH₄⁺ bands at 1690 and 1474 cm⁻¹ start to decrease and two new bands at 1612 and 1585 cm⁻¹ grow. At the same time, the bands around 1551 and 1308 cm⁻¹ shift in wavenumber and increase. The shifts in wavenumber as well as the new bands are all caused by the stretching of the N=O bond of differently bound nitrate species [35–45] which start accumulating in the absence of NH₃. That the bands of adsorbed NH₃ diminish before the bands of adsorbed NH₄⁺ species start to decrease is in accordance with reaction (14). Switching back to SCR reaction conditions, the NH₃ and NH₄⁺ species start growing again at 150 °C while the nitrate species decrease but do not completely disappear, even in the presence of H₂ as shown by the first spectra in Fig. 11.

At 500 °C, the bands of adsorbed NH₄⁺ at 1690 and 1464 cm⁻¹ disappear previous to the bands of adsorbed NH₃ between 3355 and 3173 cm⁻¹ (not shown), while the nitrate band at about 1551 cm⁻¹ increases. The remaining nitrates may be regarded as inactive. However, whether the accumulation of these species reduce the

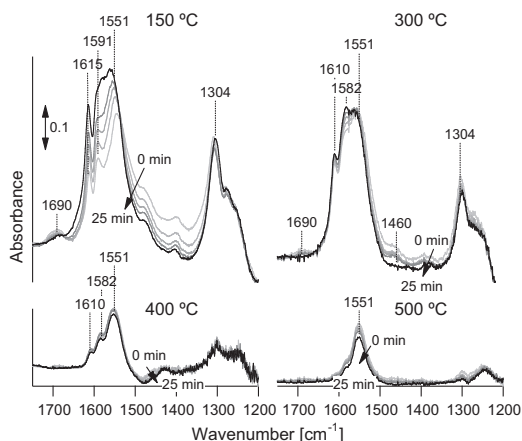


Fig. 11. Change in surface species after removing NH₃ from the hydrogen-containing feed over Al₂O₃. Reaction conditions: 500 ppm NO_x (37% NO₂), 520 ppm NH₃, 1250 ppm H₂, 8.3% O₂ in Ar. Spectra were taken from gray to black: with NH₃ in the feed, and 5, 10, 15 and 25 min after switching off NH₃.

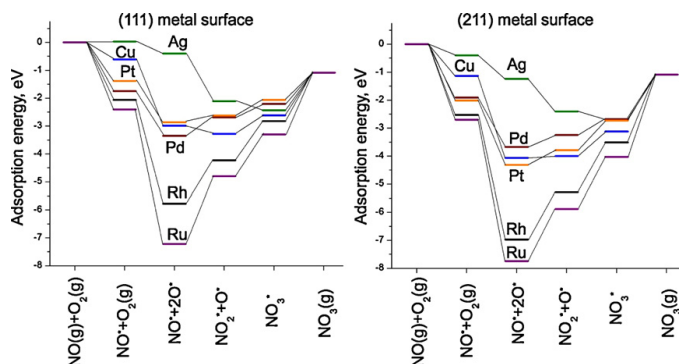


Fig. 12. Potential energy surface diagram for the formation of NO_x via the oxidation of NO over (111) and (211) surfaces of the selected transition metals.

activity for NO_x reduction and, thus, poison the surface or only act as spectator species, cannot be answered by the available data.

Fig. 11 shows, moreover, the evolution of bands when switching off NH_3 from a H_2 containing feed at different temperatures. At all temperatures, the spectra are dominated by nitrates with bands at 1551, around 1585, 1612 and around 1304 cm^{-1} . The amount of adsorbed species decreases with increasing temperature as indicated by fewer and smaller peaks at higher temperatures. When the ammonia is switched off from the feed containing H_2 at 150°C the bands assigned to NH_3 and NH_4^+ species on the surface decrease while the nitrate bands around 1615, 1585, 1551 and 1301 cm^{-1} increase. This evolution of the bands is similar to the case without H_2 in the feed. At 300°C , only the nitrate band at 1585 cm^{-1} increases, while the other nitrate bands are stable or decrease. At even higher temperatures, all NH_x bands are very tiny or hardly visible while all nitrate bands clearly decrease showing that the addition of H_2 to the feed has an influence on $\gamma\text{-Al}_2\text{O}_3$ without silver. For this observed effect of hydrogen at high temperatures (400 and 500°C) there are two reasonable explanations: hydrogen may either itself reduce the nitrates as observed by [26,31,46] on $\text{Ag}/\text{Al}_2\text{O}_3$ or it partially reduces some of the NO_2 to NO which in turn can reduce nitrates to nitrites (reaction (13)). Moreover, less new nitrates will be formed on the catalyst surface when the NO_2 concentration is decreased by partial reduction to NO.

3.3. DFT calculations

3.3.1. Oxidation of NO to NO_2 and NO_3 on the surface of transition metals

Fig. 12 shows the potential energy surface diagram for the absorption of NO and O_2 leading to NO_x , i.e., NO_2 and NO_3 calculated for 6 different transition metal catalysts Ag, Cu, Pd, Pt, Rh and Ru.

For all six different transition metal catalysts both the (111) terrace surface model and (211) step surface model were investigated and the results are similar for both surfaces. The diagram shows that among the transition metals studied the formation of NO_2 on (111) terraces is favorable for both Ag and Cu, whereas the formation of NO_3 is favorable only on Ag. On (211) step surface the formation of NO_2 and NO_3 via oxidation of NO is significantly favorable only on Ag. For other metals NO adsorption without oxidation to NO_x is preferred. That supports the idea of Ag being necessary catalyst component for the oxidation of NO to NO_x species as potentially first step of NO SCR.

3.3.2. Adsorption of NO_x and HNO_x on the step $\gamma\text{-Al}_2\text{O}_3$ surface

The model of the step on the $\gamma\text{-Al}_2\text{O}_3$ (representing uncoordinated Al sites) was used for calculations of NO_x adsorption energy as the most abundant surface of $\gamma\text{-Al}_2\text{O}_3$ crystals is the step surface [24]. It has been demonstrated by Mei et al. [33] that NO_3 adsorbs rather strongly on the $\gamma\text{-Al}_2\text{O}_3$ (100) and $\gamma\text{-Al}_2\text{O}_3$ (110) surfaces than compared to NO and NO_2 .

A clear decrease of concentration of surface nitrates has been observed by FTIR after addition of hydrogen at high temperatures (experiments at 400 and 500°C in the Section 3.2.4). Such removal of strongly bound nitrates which block the alumina surface can partly explain the positive effect of H_2 on the activity of $\text{Ag}/\text{Al}_2\text{O}_3$ catalysts in NO_x SCR.

Though authors of [33] have done extensive calculation for the adsorption of NO_x on $\gamma\text{-Al}_2\text{O}_3$ (100) and $\gamma\text{-Al}_2\text{O}_3$ (110) surfaces, however, no effect of H_2 on the stability of surface nitrates on $\gamma\text{-Al}_2\text{O}_3$ has been considered.

We have calculated the adsorption energy of NO_3 and HNO_3 on our model $\gamma\text{-Al}_2\text{O}_3$ step surface representing uncoordinated Al surface sites. Five different uncoordinated Al sites are present

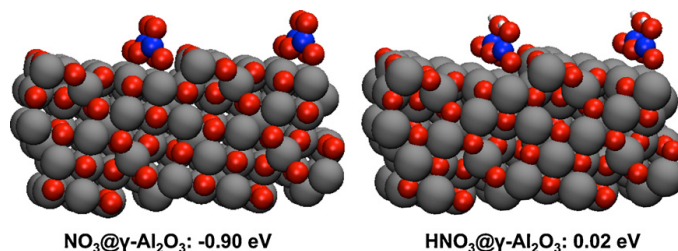


Fig. 13. NO_3 and HNO_3 adsorption geometries and adsorption energies on the model step closed packed gamma alumina surface. All the adsorption energies are given with the reference to the gas phase zero energy points of the respective species.

in our model alumina surface as derived from the bulk γ - Al_2O_3 geometry in [24]. These have all been used for the calculations, however, only the most energetically favorable (energy minimum among studied) adsorption geometries with two oxygen atoms of NO_3 and HNO_3 bridging with two Al sites of γ - Al_2O_3 are reported here. See supplementary information for more details on the used geometries.

The calculated adsorption energy of HNO_3 (Fig. 13) on the model surface of γ -alumina is considerably smaller than that of NO_3 (which agrees with [33]), which increases the probability of HNO_3 removal from the alumina surface compared to NO_3 in the absence of hydrogen. This supports the suggestion of H_2 facilitating removal of strongly bound NO_3 from the alumina.

The mechanism of reduction of adsorbed NO_x species by hydrogen with the formation of N_2 has been previously suggested for Pt/MgO– CeO_2 catalysts for H_2 -SCR of NO_x [20,21]. This mechanism includes dissociative adsorption of hydrogen on the metal nanoparticle, spillover of the formed atomic hydrogen on the support to the two neighboring NO_x species and their reduction with subsequent release of surface sites. However, this is not a major pathway of the SCR in our case because SCR in the absence of NH_3 is insignificant (Fig. 3, dotted line). Here we suggest that atomic hydrogen reacts rather with a single nitrate or nitrite group with subsequent release of HNO_x and adsorption sites on alumina. The evolved HNO_x can recombine with the formation of water and nitrogen oxides.

4. Conclusions

Ag supported on γ - Al_2O_3 is a very promising catalytic system which can be used for the removal of nitrogen oxides from the exhaust of diesel engines in the presence of H_2 . It is vital that both Ag and alumina are present in the catalyst formulation. The primary role of Ag is the H_2 -assisted oxidative activation of NO and the reaction of oxidised NO and NH_3 can proceed further on alumina. Hydrogen also facilitates removal of nitrates from the alumina surface, as supported by DRIFTS experiments and DFT calculation.

The studied catalysts facilitate $\text{NO} + \text{NO}_2$ mixture reduction without H_2 in the feed with the Al_2O_3 support defining the catalytic activity. Therefore, tuning the alumina support, not only the metal, is vital for obtaining active Ag/ Al_2O_3 catalyst.

Acknowledgements

This work was supported by grant 09-067233 from The Danish Council for Strategic Research. TEM images were acquired with the support of Center for Electron Nanoscopy (DTU CEN) and personally by Thomas W. Hansen. We acknowledge the supply of the commercial alumina for the study by the SASOL Germany.

The authors also wish to thank Dr. Alexander Yu. Stakheev and Dr. Jakob Weiland Høj for fruitful discussions.

Appendix A. Supplementary data

Supplementary data associated with this article can be found, in the online version, at doi:10.1016/j.apcatb.2011.11.042.

References

- [1] T.V. Johnson, Int. J. Engine Res. 10 (2009) 275–285.
- [2] S. Subramanian, R.J. Kudla, W. Chun, M. Chatth, Ind. Eng. Chem. Res. 32 (1993) 1805–1810.
- [3] T. Miyadera, Appl. Catal. B 2 (1993) 199–205.
- [4] G.E. Marnellos, E.A. Efthimiadis, I.A. Vasalos, Appl. Catal. B 48 (2004) 1–15.
- [5] Z.M. Liu, K.S. Oh, S.I. Woo, Catal. Lett. 106 (2006) 35–40.
- [6] S. Satokawa, J. Shibata, K. Shimizu, S. Atsushi, T. Hattori, Appl. Catal. B 42 (2003) 179–186.
- [7] R. Burch, J.P. Breen, C.J. Hill, B. Krutzsch, B. Konrad, E. Jobson, L. Cider, K. Eränen, F. Klingstedt, L.E. Lindfors, Top. Catal. 30–31 (2004) 19–25.
- [8] M. Richter, U. Bentrup, R. Eckelt, M. Schneider, M.M. Pohl, R. Fricke, Appl. Catal. B 51 (2004) 261–274.
- [9] M. Richter, R. Fricke, R. Eckelt, Catal. Lett. 94 (2004) 115–118.
- [10] K.-i. Shimizu, A. Satsuma, Appl. Catal. B 77 (2007) 202–205.
- [11] H. Kannisto, X. Karatzas, J. Edvardsson, L.J. Pettersson, H.H. Ingelsten, Appl. Catal. B 104 (2011) 74–83.
- [12] S. Bensaid, E.M. Borla, N. Russo, D. Fino, V. Specchia, Ind. Eng. Chem. Res. 49 (2010) 10323–10333.
- [13] T. Johannessen, H. Schmidt, US patent 2010/0021780 A1.
- [14] C.H. Christensen, R.Z. Sørensen, T. Johannessen, U.J. Quaaed, K. Honkala, T.D. Elmøe, R. Köhler, J.K. Nørskov, J. Mater. Chem. 15 (2005) 4106–4108.
- [15] A. Klerke, C.H. Christensen, J.K. Nørskov, T. Vegge, J. Mater. Chem. 18 (2008) 2304–2310.
- [16] V.A. Kondratenko, U. Bentrup, M. Richter, T.W. Hansen, E.V. Kondratenko, Appl. Catal. B 84 (2008) 497–504.
- [17] K.-i. Shimizu, A. Satsuma, J. Phys. Chem. C 111 (2007) 2259–2264.
- [18] E. Kondratenko, V. Kondratenko, M. Richter, R. Fricke, J. Catal. 239 (2006) 23–33.
- [19] P.G. Savva, C.N. Costa, Catal. Rev. – Sci. Eng. 53 (2011) 91–151.
- [20] C.N. Costa, A.M. Efsthathiou, J. Phys. Chem. C 111 (2007) 3010–3020.
- [21] P.G. Savva, A.M. Efsthathiou, J. Catal. 257 (2008) 324–333.
- [22] E. Ménéndez-Proupin, G. Gutiérrez, Phys. Rev. B 72 (2005) 35116–35119.
- [23] B. Hammer, L.B. Hansen, J.K. Nørskov, Phys. Rev. B 59 (1999) 7413–7421.
- [24] M. Digne, P. Sautet, P. Raybaud, P. Euzen, H. Toulhoat, J. Catal. 226 (2004) 54–68.
- [25] P. Sazama, L. Čapek, H. Drobná, Z. Sobalík, J. Dědeček, K. Arve, B. Wichterlová, J. Catal. 232 (2005) 302–317.
- [26] K.-i. Shimizu, J. Shibata, A. Satsuma, J. Catal. 239 (2006) 402–409.
- [27] V. Houel, P. Millington, R. Rajaram, A. Tsolakis, Appl. Catal. B 77 (2007) 29–34.
- [28] G. Madia, M. Koebel, M. Elsener, A. Wokaun, Ind. Eng. Chem. Res. 41 (2002) 3512–3517.
- [29] A. Grossale, I. Nova, E. Tronconi, D. Chatterjee, M. Weibel, J. Catal. 256 (2008) 312–322.
- [30] J.H. Lee, S.J. Schmieg, S.H. Oh, Appl. Catal. A 342 (2008) 78–86.
- [31] F.C. Meunier, J. Ross, Appl. Catal. B 24 (2000) 23–32.
- [32] J.G.M. Brandin, L.H. Andersson, C.U.I. Odenbrand, Acta Chem. Scand. 44 (1990) 784–788.
- [33] D. Mei, Q. Ge, J. Szanyi, C.H.F. Peden, J. Phys. Chem. C 113 (2009) 7779–7789.
- [34] A.A. Tsyganenko, D.V. Pozdnyakov, V.N. Filimonov, J. Mol. Struct. 29 (1975) 299–318.
- [35] J.B. Peri, J. Phys. Chem. 69 (1965) 231–239.
- [36] A.A. Davydov, Infrared Spectroscopy of Adsorbed Species on the Surface of Transition Metal Oxides, John Wiley & Sons, Chichester, New York, Brisbane, Toronto, Singapore, 1984.
- [37] G. Busca, H. Saussey, O. Saur, J.C. Lavalley, V. Lorenzelli, Appl. Catal. 14 (1985) 245–260.
- [38] A. Iglesias-Juez, A.B. Hungria, A. Martinez-Arias, A. Fuerte, M. Fernandez-Garcia, J.A. Anderson, J.C. Conesa, J. Soria, J. Catal. 217 (2003) 310–323.
- [39] S. Tamm, H.H. Ingelsten, M. Skoglundh, A.E.C. Palmqvist, J. Catal. 276 (2010) 402–411.
- [40] S. Tamm, H.H. Ingelsten, A.E.C. Palmqvist, J. Catal. 255 (2008) 304–312.
- [41] S. Kameoka, Y. Ukiu, T. Miyadera, Phys. Chem. Chem. Phys. 2 (2000) 367–372.
- [42] F.C. Meunier, J.P. Breen, V. Zuzaniuk, M. Olsson, J.R.H. Ross, J. Catal. 187 (1999) 493–505.
- [43] K.I. Hadjiivanov, Catal. Rev. Sci. Eng. 42 (2000) 71–144.
- [44] G.G. Ramis, G. Busca, V. Lorenzelli, P. Forzatti, Appl. Catal. 64 (1990) 243–257.
- [45] M. Schraml-Marth, A. Wokaun, A. Baiker, J. Catal. 138 (1992) 306–321.
- [46] H. Kannisto, H.H. Ingelsten, M. Skoglundh, Top. Catal. 52 (2009) 1817–1820.

Paper VI

Sulfur poisoning and regeneration of the $\text{Ag}/\gamma\text{-Al}_2\text{O}_3$ catalyst for H_2 -assisted SCR of NO_x by ammonia

Dmitry E. Doronkin, [Tuhin Suvra Khan](#), Thomas Bligaard, Sebastian Fogel, Pär Gabrielsson, Søren Dahl

Applied Catalysis B: Environmental **117–118**, 49–58 (2012)



Sulfur poisoning and regeneration of the Ag/ γ -Al₂O₃ catalyst for H₂-assisted SCR of NO_x by ammonia

Dmitry E. Doronkin^{a,*}, Tuhin Suvra Khan^b, Thomas Bligaard^c, Sebastian Fogel^{a,d}, Pär Gabriëlsson^d, Søren Dahl^a

^a Center for Individual Nanoparticle Functionality (CINF), Department of Physics, Technical University of Denmark, Fysikvej 307, 2800 Kgs. Lyngby, Denmark

^b Center of Atomic-scale Materials Design (CAMD), Department of Physics, Technical University of Denmark, Fysikvej 307, 2800 Kgs. Lyngby, Denmark

^c SUNCAT Center for Interface Science and Catalysis, SLAC National Accelerator Laboratory, Menlo Park, CA 94025, USA

^d Haldor Topsøe A/S, Nymøllevej 55, 2800 Kgs. Lyngby, Denmark

ARTICLE INFO

Article history:

Received 1 November 2011

Received in revised form

27 December 2011

Accepted 3 January 2012

Available online 9 January 2012

Keywords:

Ag/Al₂O₃

SO₂

NO_x SCR

Poisoning

Regeneration

ABSTRACT

Sulfur poisoning and regeneration mechanisms for a 2% Ag/ γ -Al₂O₃ catalyst for the H₂-assisted selective catalytic reduction of NO_x by NH₃ are investigated. The catalyst has medium sulfur tolerance at low temperatures, however a good capability of regeneration at 670 °C under lean conditions when H₂ is present. These heating conditions can easily be established during soot filter regeneration. Furthermore, two types of active sites could be identified with different regeneration capabilities, namely finely dispersed Ag and larger Ag nanoparticles. The most active sites are associated with the finely dispersed Ag. These sites are irreversibly poisoned and cannot be regenerated under driving conditions. On the other hand the larger Ag nanoparticles are reversibly poisoned by direct SO_x adsorption. The interpretation of the data is supported by DFT calculations.

© 2012 Elsevier B.V. All rights reserved.

1. Introduction

Selective catalytic reduction (SCR) is the leading NO_x control technique for diesel vehicles with ammonia used as a reductant. Commonly used catalysts are vanadia-based catalysts and Cu and Fe-containing zeolites. However, none of the systems demonstrate high thermal durability together with a good activity throughout the broad temperature region from 150 to 550 °C which is needed for vehicle applications [1]. Therefore, research of novel non-toxic, inexpensive and durable catalytic systems for NH₃-SCR is still an important focus area.

Recently two research groups suggested to use Ag/Al₂O₃, which is a well-known catalyst for NO_x SCR by hydrocarbons (HC-SCR), for SCR of NO_x by ammonia or urea with co-feeding hydrogen, resulting in nearly 90% NO_x conversion at temperatures as low as 200 °C [2,3]. Still, one of the major obstacles for the application of Ag/Al₂O₃ for NO_x SCR by ammonia is its rather poor sulfur tolerance [4]. A catalyst of 2% Ag/Al₂O₃ demonstrated a decrease in H₂-assisted NO_x conversion by urea from 50% to 30% after 20 h on stream in the presence of 50 ppm SO₂ at 250 °C. This is a rather good result

considering the very high GHSV = 380,000 h⁻¹ in the tests. However, the large amount of hydrogen (0.5%, 5:1 H₂:NO) used in this study is probably unacceptable for application in diesel vehicles because such a large consumption of hydrogen leads to a high “fuel penalty” [5].

A significant amount of data on sulfur tolerance of Ag/Al₂O₃ catalysts exists for NO_x SCR by hydrocarbons. Meunier and Ross [6] observed strong deactivation of a 1.2% Ag/Al₂O₃ catalyst for propene-SCR by 100 ppm SO₂ in the feed. It is noteworthy that the authors were able to recover most of the catalyst activity by treatment in 10% H₂/Ar at 650 °C or heating in the reaction mixture at 750 °C. Park and Boyer [7] compared the catalytic behavior of 2% and 8% Ag/Al₂O₃ catalysts in the presence of SO₂ and concluded that high Ag loadings may be preferential for making a sulfur tolerant catalyst. The authors demonstrated prominent activation of 8% Ag/Al₂O₃ by SO₂ in the feed and ascribed that to the formation of a very active silver sulfate phase.

When estimating the SO₂ tolerance of Ag/Al₂O₃ catalysts attention should be given also to the process temperature. Satokawa et al. [8] showed a clear dependence of the propane-SCR temperature on the deactivation degree with permanent catalyst deactivation at T < 500 °C and furthermore the ability to partially regenerate the catalyst by heating to 600 °C, even without removing low amounts (1 ppm) of SO₂ from the feed. Further studies [8] of sulfation-regeneration mechanisms included obtaining SO₂ TPD profiles and

* Corresponding author. Tel.: +45 4525 3275.

E-mail addresses: dmdo@fysik.dtu.dk, dmitriy.doronkin@gmail.com (D.E. Doronkin).

attribution of peaks to different types of adsorbed SO_2 , bound to Ag and alumina. The catalyst regeneration temperature was lower than any of the SO_2 desorption peaks, observed in the study, which did not allow drawing a clear conclusion about the deactivation and regeneration mechanisms.

Breen et al. [9] also demonstrated a drastic dependence of the catalyst degree of poisoning on the temperature of NO_x SCR by octane and toluene. The following was observed; at low temperatures ($<235^\circ\text{C}$) little deactivation, between 235 and 500°C – severe deactivation and at $T > 590^\circ\text{C}$ – activation due to a suppression of unselective oxidation of hydrocarbons. The low temperature sulfur tolerance was ascribed to low catalyst activity in SO_2 oxidation to SO_3 with the latter considered to be the main poisoning agent for Ag/ Al_2O_3 . The authors have evaluated a few regeneration options of which heating to 650°C in hydrogen-containing lean mixture showed promising results rather than regeneration under oxidizing conditions without H_2 . The fastest regeneration technique included heating the catalyst in a rich mixture containing CO and hydrogen.

The results of other research groups [10,11] agree with Breen's results in SO_2 oxidation to SO_3 by NO_2 being the major step in the sulfur poisoning of Ag/ Al_2O_3 catalysts. Partial regeneration of the catalyst was observed after heating to 600°C in a hydrocarbon-containing feed.

In this work we have attempted to reveal the Ag/ Al_2O_3 sulfation and regeneration mechanisms, which will allow us to develop an efficient regeneration strategy for the ammonia SCR catalyst in question. Special attention was given to the catalyst operation below 300°C , since for applications in light-duty diesel vehicles low temperatures are of great importance [10]. The suggested mechanism was supported by DFT calculations. A regeneration strategy using the high temperatures developed during Diesel Particulate Filter (DPF) regeneration in diesel cars was evaluated.

2. Experimental

2.1. Catalyst preparation

Parent γ -alumina (Puralox TH 100/150, $S_{\text{BET}} = 150 \text{ m}^2/\text{g}$) was kindly provided by SASOL. 1–3 wt.% Ag/ Al_2O_3 were obtained by incipient wetness impregnation of parent γ -alumina by AgNO_3 (Sigma–Aldrich) dissolved in deionized water. After impregnation the catalyst was dried at room temperature overnight and calcined at 550°C for 4 h in static air. The calcined catalyst was tableted, crushed and sieved to obtain a 0.18–0.35 mm fraction (mesh 80–mesh 45) used in the catalytic tests. A new batch of catalyst was sulfated and used to test every new regeneration recipe.

2.2. Determination of the specific surface area

The specific surface areas (S_{BET}) of the catalysts were measured by N_2 -adsorption with a Micromeritics Gemini instrument. Untreated catalysts were measured in powder form and for the catalysts after testing a 0.18–0.35 mm fraction of particles (as in catalytic tests) was used for the BET measurement.

2.3. Catalysis

Temperature-programmed activity tests were carried out in a fixed-bed flow reactor (quartz tube with 4 mm inner diameter) in a temperature programmed mode while the temperature was decreased from 400°C to 150°C with a rate of $2^\circ\text{C}/\text{min}$. Prior to the temperature ramp the catalyst was heated to 470°C for 30 min in the gas mixture used for the tests. The temperature was controlled using an Eurotherm 2408 temperature controller with a K-type thermocouple. 45 mg of catalyst was diluted with 100 mg of SiC (mesh 60) and placed on a quartz wool bed. The bed height

was $\sim 11 \text{ mm}$ and the GHSV, calculated using the volume of the pure catalyst was $\sim 110,000 \text{ h}^{-1}$. The gas composition normally contained 500 ppm NO , 520 ppm NH_3 , 1200 ppm of H_2 , 8.3% O_2 , and 7% water balanced with Ar. For sulfur poisoning tests 10 ppm SO_2 was admixed to the feed. Water was dosed by an ISCO 100DM syringe pump through a heated capillary. Reaction products were analyzed by a Thermo Fisher Nicolet 6700 FTIR analyzer, equipped with a 2 m gas cell. Gas capillaries were heated to $\sim 130^\circ\text{C}$ and the FTIR gas cell to 165°C to avoid condensation of water and formation of ammonium nitrate.

Conversions were calculated using the following equations:

$$X_{\text{NO}_x} = 1 - \frac{C_{\text{NO}_x}^{\text{outlet}}}{C_{\text{NO}_x}^{\text{inlet}}} \quad (1)$$

and

$$X_{\text{NH}_3} = 1 - \frac{C_{\text{NH}_3}^{\text{outlet}}}{C_{\text{NH}_3}^{\text{inlet}}} \quad (2)$$

where X_{NO_x} denotes the conversion of NO_x to N_2 and $C_{\text{NO}_x}^{\text{inlet}}$ and $C_{\text{NO}_x}^{\text{outlet}}$ are the NO_x concentrations at the inlet and outlet of the reactor respectively, where:

$$C_{\text{NO}_x} = C_{\text{NO}} + C_{\text{NO}_2} + C_{\text{N}_2\text{O}} \quad (3)$$

and $C_{\text{NH}_3}^{\text{inlet}}$ and $C_{\text{NH}_3}^{\text{outlet}}$ are NH_3 concentrations at the reactor inlet and outlet.

2.4. DFT calculations

The plane wave density functional theory (DFT) code DACAPO was used to calculate the adsorption energies and the gas phase energies of the adsorbates [12]. A plane wave cutoff of 340.15 eV and a density cutoff of 680 eV were used in the calculations. The core electrons were described by Vanderbilt ultrasoft pseudopotentials. The RBPE functional was used for describing the exchange correlation energy [13].

The adsorption energies of the SO_2 , SO_3 , and SO_4 species were studied over the Ag (111) terrace and (211) step surfaces, on a γ - Al_2O_3 model step surface, and two single atom Ag sites.

For the Ag (111) and (211) surfaces, we used a $4 \times 4 \times 1$ Monkhorst–Pack \mathbf{k} -point sampling in the irreducible Brillouin zone. We employed a 3×3 surface cell for the Ag (111) and 3×1 surface cell for the Ag (211) surfaces. For the (111) surface we used a four-layer slab where the two top-most layers were allowed to relax, whereas for the (211) surfaces we used a slab model with nine layers and the topmost three layers are allowed to relax. In all the model calculations, neighboring slabs were separated by more than 10 Å of vacuum.

For the calculation of γ - Al_2O_3 and the adsorption of different species on γ - Al_2O_3 we also used the DACAPO code with a plane wave cutoff of 340.15 eV and a density cutoff of 680 eV. A $4 \times 4 \times 1$ Monkhorst–Pack \mathbf{k} -point sampling in the irreducible Brillouin zone was used for γ - Al_2O_3 . The γ - Al_2O_3 surface was modeled by a step on a non-spinel γ - Al_2O_3 structure which was derived from bulk γ - Al_2O_3 model in [14]. The cell parameters for the γ - Al_2O_3 model step surface are $a = 8.0680 \text{ \AA}$ and $b = 10.0092 \text{ \AA}$ and $\alpha = \beta = \gamma = 90^\circ$. For the γ - Al_2O_3 surface the bottom two layers were fixed whereas the top-most three layers were allowed to relax. In all the model γ - Al_2O_3 surfaces, the neighboring slabs are separated by more than 10 Å of vacuum.

Single atom Ag sites were constructed by replacing one Al atom for Ag in the alumina step surface and by attaching one Ag atom to the γ - Al_2O_3 step (see Supplementary material for the geometries).

SO_x and HSO_x adsorption energies were calculated relative to gas phase energies of $\text{SO}_2(\text{g})$, $\text{O}_2(\text{g})$ and $\text{H}_2(\text{g})$.

For calculation of desorption temperatures for SO₂ and SO₃ we used the following procedure. Starting from the chemical equation:



where * is the free surface site and SO_x* is the adsorbed species. We can write down the ratio of occupied and free adsorption sites:

$$\begin{aligned} \frac{\theta_{\text{SO}_x}}{\theta^*} &= K_{\text{ads}} P_{\text{SO}_x} = \exp\left(-\frac{\Delta G_{\text{ads}}}{kT}\right) P_{\text{SO}_x} \\ &= \exp\left(\frac{-(\Delta G_{\text{ads}}^\ominus - kT \ln P_{\text{SO}_x})}{kT}\right) \end{aligned} \quad (6)$$

We assume that at the desorption temperature the numbers of occupied and free adsorption sites will equal ($\theta_{\text{SO}_x} = \theta^*$), which gives:

$$\Delta G_{\text{ads}}^\ominus - kT \ln P_{\text{SO}_x} = 0 \quad (7)$$

or

$$\Delta E_{\text{ads}} - \Delta \text{ZPE}_{\text{ads}} - T\Delta S_{\text{ads}} - kT \ln P_{\text{SO}_x} = 0 \quad (8)$$

We calculate the ZPE (zero point energy) and the entropy of the SO_x in their adsorbed state and so it is possible to calculate the desorption temperature for a given partial pressure of SO_x:

$$T = \frac{\Delta E_{\text{ads}}}{k \ln P_{\text{SO}_x} - \Delta S_{\text{gas}}} \quad (9)$$

The SO_x entropy and ZPE found for the γ -Al₂O₃ model surface were also used for the single Ag atom sites on the γ -Al₂O₃. Standard entropy values for SO₂ and SO₃ from [15] (neglecting entropy change with temperature) and a partial pressure of SO_x 4×10^{-7} bar (0.4 ppm in Ref. [9]) and partial pressure of O₂ is 0.07 bar [9] were used in the calculations.

3. Results and discussion

3.1. Catalyst choice: stability of Ag/Al₂O₃ and options for the regeneration

3.1.1. The catalyst choice

Temperature dependence of NO_x and NH₃ conversions for the fresh 1–3% Ag/Al₂O₃ catalysts is shown in Fig. 1a and b, respectively. 1% Ag/Al₂O₃ exhibits SCR onset at 130 °C reaching 80% NO_x conversion at 200 °C and leveling NO_x conversion at 90% at $T > 300$ °C. This is in agreement with previous studies [2]. 2% and 3% Ag/Al₂O₃ catalysts demonstrate SCR onset shifted by 7 °C to lower temperatures compared 1%, but lower maximum conversion and generally lower SCR activity at higher temperatures, unlike results of Shimizu and Satsuma [3]. The NH₃ conversion follows the NO_x conversion at $T < 270$ –300 °C. At higher temperature NH₃ becomes oxidized and the NH₃ conversion is higher than NO_x conversion. Thus, NH₃ oxidation plays some role in the decrease of high temperature NO_x conversion but this is not the main reason. The reason for observing conversion maxima for 2% and 3% Ag/Al₂O₃ catalysts at 200 °C with subsequent drop in NH₃ and NO_x conversions could be direct oxidation of H₂ by oxygen taking over. As it was shown earlier no NO and NH₃ is converted over an Ag/Al₂O₃ catalyst in the absence of H₂ [16]. Another possible reason is the lack of strong acid sites for NH₃ adsorption in the 2–3% Ag/Al₂O₃ catalysts which is demonstrated in [17].

Noteworthy, the tested catalysts demonstrate very high stability at temperature up to 700 °C which has also been shown in the number of papers on HC-SCR [3,9]. To further check the thermal stability of the 1% Ag/Al₂O₃ catalyst it was subjected to hydrothermal deactivation at 750 °C for 16 h. The activity of the obtained

catalyst is reported in Fig. 1a and b as gray dotted lines. The low-temperature conversion is only slightly shifted by 3 °C, whereas at $T > 300$ °C one may observe a decrease in NO_x and NH₃ conversions similar to that observed for catalysts with higher Ag loading. This may indicate sintering of Ag particles leading to the increased unselective oxidation of hydrogen. At the same time, the relatively small decrease in the catalyst specific surface area (S_{BET}) does not indicate any significant change in the alumina support (Table 1).

Contrary to the hydrothermal aging, sulfur poisoning of Ag/Al₂O₃ leads to significant catalyst deactivation. Preliminary experiments on the choice of sulfur poisoning temperature showed no catalyst deactivation with SO₂ in the feed at 500 °C and the most severe deactivation in the temperature range 200–300 °C in very good agreement with the earlier reported results for HC-SCR [8,9]. Therefore, preliminary SO₂ deactivation studies of 1–3% Ag/Al₂O₃ were performed at 200–227 °C and all the following deactivation–regeneration studies of 2% Ag/Al₂O₃ were done at 240–250 °C (Fig. 1c). For the comparison of regeneration methods the SO₂ poisoning was obtained by introducing 10 ppm SO₂ to the SCR feed for 4 h.

Catalytic performance of 1–3% Ag/Al₂O₃ in NO_x SCR after such sulfur treatment at 200–227 °C is shown in Fig. 1d. Lowering deactivation temperature from 250 °C to 200 °C leads to a very small shift of the low-temperature activity within 5 °C, therefore, the temperature difference is not the determining factor for the observed activity difference. 1% Ag/Al₂O₃ was poisoned to the highest degree, whereas higher Ag loading led to better sulfur tolerance with 3% Ag/Al₂O₃ showing the highest NO_x conversion at $T < 300$ °C. It should be noted that after exposure to SO₂ (and even after regeneration of 1% and 2% Ag/Al₂O₃ catalysts at 670 °C) the NH₃ conversion profiles coincided with the NO_x conversion profiles for all tested samples. That indicates quenching of NH₃ unselective oxidation over 1–3% Ag/Al₂O₃ by SO₂. Due to the similarity of NO_x and NH₃ conversion curves for the sulfated catalysts only NO_x conversions will be reported throughout the article.

Sulfation of 2 and 3% Ag/Al₂O₃ leads not only to a shift of the maximum NO_x conversion to higher temperatures but also to an increase to significantly higher values than demonstrated over the fresh catalysts. The shift of the maximum activity of 2% Ag/Al₂O₃ along with “activation” of the catalyst at 227 °C (near the conversion maximum of the fresh catalyst) and at 250 °C can be seen in Fig. 1c. Higher SO₂ exposure leads to a shift of the maximum NO_x conversion to higher temperatures along with deterioration of the low-temperature activity. The activity gain induced by sulfation has been observed earlier and attributed to the redistribution of Ag species [4]. However, as we have observed the decrease of unselective NH₃ oxidation after SO₂ exposure, we suppose the SO_x blocking of sites active in NH₃ and H₂ oxidation to play a major role in the increased NO_x conversion over 2 and 3% Ag/Al₂O₃ catalysts. At the same time SO₂ adsorption increases the alumina acidity which can also play the role for the SCR activity as discussed in a separate publication [17].

Several options for the catalyst regeneration under hydrocarbon (HC) SCR have been suggested in the literature. All of them include heating sulfated Ag/Al₂O₃ in different media – oxidizing [9], hydrogen (or hydrocarbon)-containing lean exhaust [6,8–10] or rich exhaust [6,9].

Heating sulfated 2% Ag/Al₂O₃ to 670 °C for 10 min in the NO_x SCR feed without hydrogen leads to a small 10 °C shift of T50% to lower temperatures (not shown). Therefore, regeneration of Ag/Al₂O₃ for NO_x SCR by NH₃ without co-feeding hydrogen is ineffective. Thus, regeneration at 670 °C in the reaction gas mixture was used to test the regeneration capability of 1–3% Ag/Al₂O₃ catalysts. Activity of the catalysts regenerated during 40 min is reported in Fig. 1e. All catalysts partially regained the low-temperature activity, however, the high-temperature activity of 3% Ag/Al₂O₃ was

Table 1
Specific surface areas of tested catalysts as measured by BET.

Catalyst	Treatment	S_{BET} (m ² /g)
1% Ag/Al ₂ O ₃	–	142
1% Ag/Al ₂ O ₃	Hydrothermal aging (750 °C, 16 h)	126
2% Ag/Al ₂ O ₃	Catalytic test (w/o deactivation)	130
2% Ag/Al ₂ O ₃	Sulfation and 10 min regen. @ 670 °C	129
2% Ag/Al ₂ O ₃	Sulfation and 80 min regen. @ 670 °C	113
2% Ag/Al ₂ O ₃	30 cycles of 1 h sulfation and 10 min regen. @ 670 °C, followed by heating to 950 °C	121
3% Ag/Al ₂ O ₃	–	141

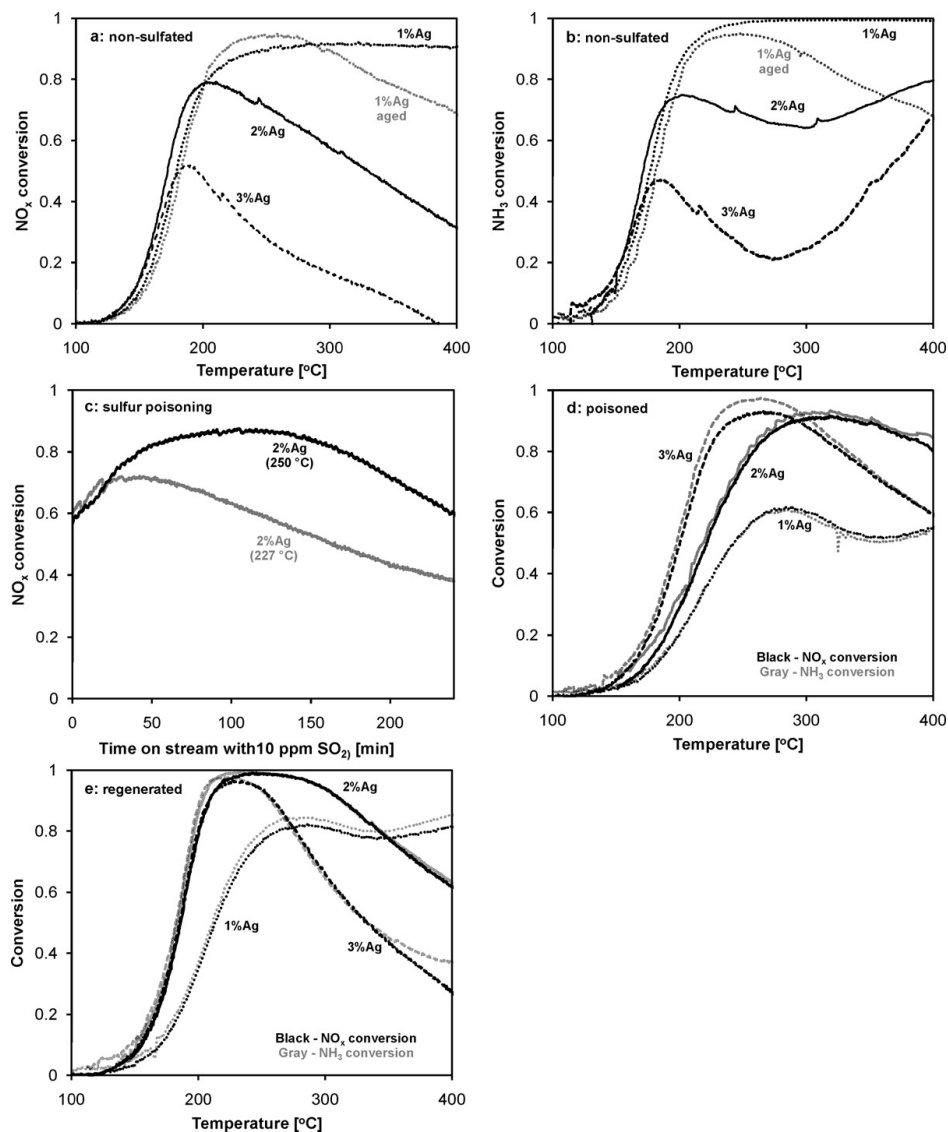


Fig. 1. NO_x (a) and NH₃ (b) conversion profiles obtained over fresh 1–3% Ag/Al₂O₃ (black) and hydrothermally aged 1% Ag/Al₂O₃ (gray dotted) catalysts. (c) Evolution of NO_x conversion at 227 and 250 °C over 2% Ag/Al₂O₃ with 10 ppm SO₂ in the feed. (d) NO_x and NH₃ conversion profiles obtained over sulfur poisoned 1–3% Ag/Al₂O₃ catalysts. (e) NO_x and NH₃ conversion profiles obtained over 1–3% Ag/Al₂O₃ catalysts after 40 min regeneration at 670 °C. Reaction conditions: 500 ppm NO, 520 ppm NH₃, 1200 ppm H₂, 8.3% O₂, 7% H₂O in Ar, GHSV = 110,000 h⁻¹.

decreased compared to the sulfated catalyst. At the same point this catalyst demonstrated a higher conversion of NH_3 compared to NO_x at $T > 350^\circ\text{C}$, indicating NH_3 oxidation. 2% $\text{Ag}/\text{Al}_2\text{O}_3$ showed the highest NO_x conversion throughout the whole temperature region and will, therefore, be used for the further study. For the simplicity in the text below and the following figures 2% $\text{Ag}/\text{Al}_2\text{O}_3$ will be referred as $\text{Ag}/\text{Al}_2\text{O}_3$.

3.1.2. Regeneration options

To simulate regeneration in rich exhaust the catalyst was heated to 670°C for 1 min with oxygen removed from the feed. The activity following from this rich regeneration is presented in Fig. 2a as a solid line. The profile is significantly shifted to lower temperatures compared to the non-regenerated sample. Another feature is the maximum NO_x conversion (96%), which is now higher than that of both the fresh and the non-regenerated catalysts. Still, regeneration under rich conditions did not allow regaining the low-temperature activity completely.

However, obtaining rich exhaust from diesel engine leads to high fuel consumption and is, therefore, undesirable. Thus, we have preferred relatively fast catalyst regeneration under lean conditions with co-feeding hydrogen. The NO_x conversion profile for $\text{Ag}/\text{Al}_2\text{O}_3$ regenerated 10 min at 670°C in the standard NO_x SCR feed (with hydrogen) is shown in Fig. 2a as a dashed line. The catalyst shows the same activity below 200°C as when regenerated under rich conditions and at higher temperatures even higher conversion (up to 100%). At the same time the surface area of the catalyst regenerated for 10 min is not deteriorated compared to the fresh catalyst (Table 1). This kind of regeneration is very easy to implement in diesel vehicles because it can coincide with regeneration of the DPF, which requires a similar heating strategy.

3.2. Influence of the regeneration time on the catalyst activity

Regeneration time is of high importance for automotive catalysts, as heating the catalyst requires a lot of energy, i.e. fuel to be spent. Influence of the regeneration time (for regeneration under lean conditions with co-feeding hydrogen) on the activity of the regenerated catalyst is shown in Fig. 2b. The value on the Y-axis is the shift of temperature for 50% NO_x conversion over the regenerated catalyst relative to the fresh catalyst:

$$T50\% \text{ shift} = T50\% \text{ regenerated} - T50\% \text{ fresh} \quad (10)$$

Zero at the timescale stands for non-regenerated catalyst. Heating to 670°C for 1 min leads to the shift of T50% by 24°C towards lower temperatures, which is already very good. Heating for 10 min allows us to get 6°C lower T50%, but further treatment at high temperatures does not lead to significant further activation of the catalyst. The best T50%, we could get by regenerating $\text{Ag}/\text{Al}_2\text{O}_3$, is 15°C higher than T50% of the fresh $\text{Ag}/\text{Al}_2\text{O}_3$. That result is obtained after 40 min of regeneration. Higher regeneration time does not yield better activity but causes loss of the catalyst surface area (Table 1) and is, therefore, undesirable. It is worth noting that we were not able to match the low-temperature activity of the fresh catalyst after regeneration.

3.3. Developing a deactivation–regeneration strategy to mimic automotive catalyst operating conditions

Typical lifecycle of an automotive light-duty $\text{Ag}/\text{Al}_2\text{O}_3$ NO_x SCR catalyst comprises normal driving, during which the catalyst operates at low temperatures $150\text{--}350^\circ\text{C}$ [10] and is poisoned by sulfur, and regeneration which optimally coincides with regeneration of the DPF. To be more precise, useful vehicle running time according to the modern Euro 5 and Euro 6 standards is 160,000 km [18], and typical intervals between DPF regenerations are 300–900 km

(with the modern Volvo D5 light-duty diesel engine as an example) [19], which gives a minimum of 160 catalyst regeneration cycles. Using average fuel consumption of this engine during urban driving (6.7 l/100 km with a manual gearbox), an average diesel fuel density approx. 850 g/l [20], and a maximum allowed sulfur content of 10 ppm in the diesel fuel [21], the total sulfur passed through the catalyst will amount to 91 g or 2.85 mol. Using available data on the volume of monolith catalyst for the mentioned engine (9 l) and the monolith density 2.5 g/in³ [10], the weight of the washcoat for an automotive catalyst (15% of the total) and the relative weight of the powder catalyst in the washcoat (80%) [22], we get a total of 0.47 g (14.7 mmol) sulfur per gram of powder catalyst during the vehicle lifetime. Therefore, the amount of sulfur per one deactivation cycle will be 83 $\mu\text{mol/g}$ of catalyst, assuming adsorption of all sulfur. In reality, however, not all sulfur will be adsorbed partly due to very high or low temperatures [9].

In our tests we have chosen the scheme involving catalyst poisoning with 10 ppm SO_2 at intermediate temperature of 240°C for 1 h which gives us a sulfur exposure before regeneration of 65 $\mu\text{mol/g}$ of catalyst, which is close to the theoretical maximum value calculated above. Thus, we will use this protocol as “worst case” scenario.

Fig. 3a and b shows two different ways of testing sulfur tolerance with the same total sulfur exposure (4 h with 10 ppm SO_2 , corresponds to 260 $\mu\text{mol/g}$ catalyst) and the same regeneration time, but split by four relatively small regeneration segments in the second case.

The comparison of the catalyst activity after these two tests is given in Fig. 3c. Evidently, the low-temperature activities of the two poisoned catalysts are identical. Different SCR activity at $T > 200^\circ\text{C}$ does not allow us to state that the regenerated catalyst activity observed in Fig. 3c represents “steady state” automotive catalyst activity in both cases. Further testing is needed to reveal “steady state” catalyst activity during sulfation–regeneration cycles.

3.4. Cycling deactivation–regeneration

In order to clarify if the catalyst will be further deactivated after several 1 h. SO_2 poisoning – 10 min regeneration cycles we have carried out 30 deactivation (at 240°C) – regeneration (at 670°C) cycles. Evolution of the NO_x and NH_3 conversions during the first 9 cycles of the experiment is shown in Fig. 4.

During the sulfation of the fresh catalyst (first 60 min) NO_x conversion steadily increases. During heating the catalyst to 670°C the NO_x conversion drops to slightly negative values. According to Eq. (1) in Section 2.3 this is due to a higher NO_x concentration at the reactor outlet than at the inlet. The latter is caused by oxidation of part of ammonia to NO_x at the regeneration temperature which can be seen by the higher conversion of NH_3 compared to NO_x at $T > 500^\circ\text{C}$. To prevent ammonia oxidation in the real life application it is possible to switch off ammonia supply during regeneration without compromising regeneration efficiency.

The NO_x conversion following regeneration is maximal (97%) after the first regeneration and decreases only a little (to 95%) with further regeneration cycles. However, sulfur poisoning of the regenerated sample leads to a decrease in the NO_x conversion at the end of each of the first deactivation cycles. This decrease in NO_x conversion could indicate that during each of these first regenerations the SO_x adsorbed during the preceding deactivation cycle is not completely removed from the catalyst surface. After seven sulfation–regeneration cycles NO_x conversion is stabilized, so each new testing cycle yields the same profile as the previous. Thus, further sulfation and regeneration do not change the catalyst performance.

Integration of the SO_2 signal measured by FTIR during 10th–20th cycles (they are all equal) gives the amount of SO_2 equal to the

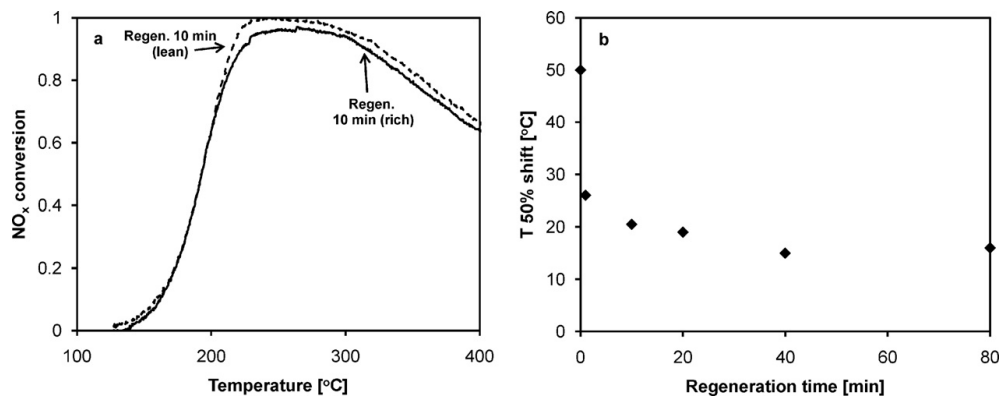


Fig. 2. (a) NO_x conversion profiles obtained over 2% Ag/Al₂O₃ after 10 min regeneration at 670 °C (dashed) and after 1 min regeneration at 670 °C in rich mixture (solid). Reaction conditions: 500 ppm NO, 520 ppm NH₃, 1200 ppm H₂, 8.3% O₂, 7% H₂O in Ar, GHSV = 110,000 h⁻¹. (b) Dependence of shift of temperature of 50% NO_x conversion on the regeneration time. The 0 corresponds to no regeneration.

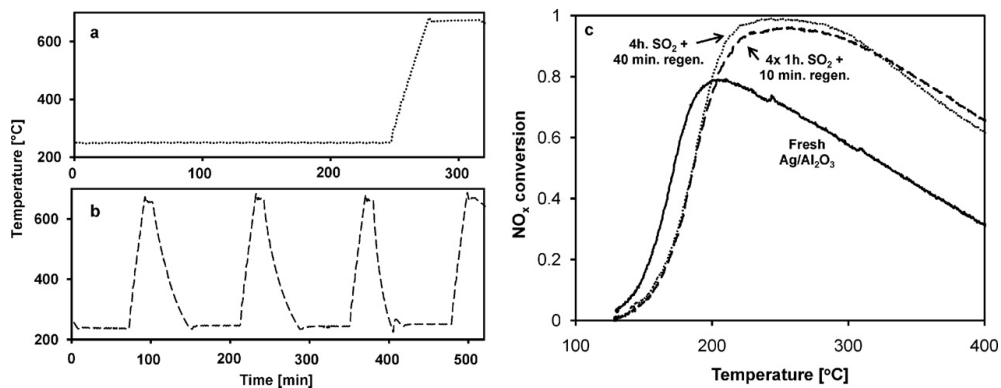


Fig. 3. (a) Temperature profile of 4 h sulfation – 40 min regeneration experiment. (b) Temperature profile of 4 × 1 h sulfation – 10 min regeneration experiment. (c) NO_x conversion profiles obtained over fresh 2% Ag/Al₂O₃ (solid line), 2% Ag/Al₂O₃ after 4 h with 10 ppm SO₂ at 240 °C and 40 min regeneration at 670 °C (dotted line), after 4 cycles 1 h with 10 ppm SO₂ at 240 °C and 10 min regeneration (dashed line).

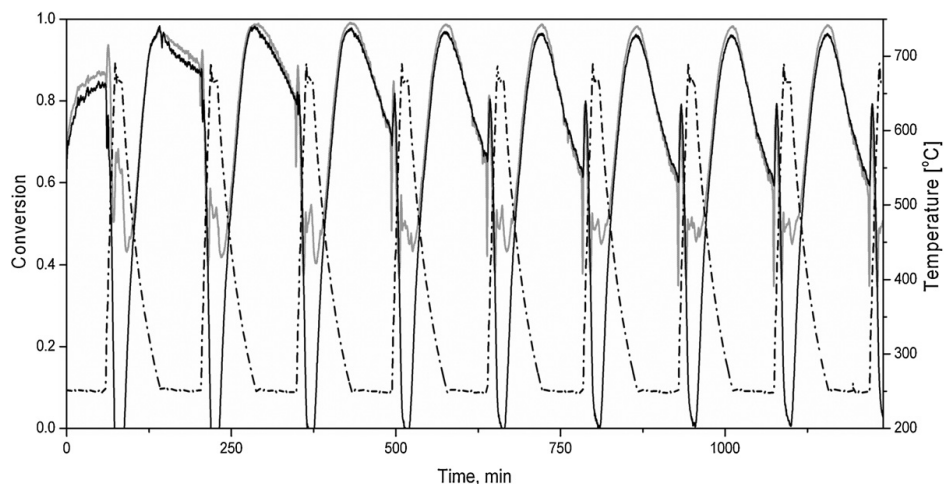


Fig. 4. Evolution of NO_x conversion with time for the first 9 cycles of the long-term stability test of 2% Ag/Al₂O₃. Reaction conditions: 500 ppm NO, 1200 ppm H₂, 8.3% O₂, 7% H₂O in Ar, GHSV = 110,000 h⁻¹. Sulfation with 10 ppm SO₂ for 1 h at 240 °C, regeneration for 10 min at 670 °C.

amount of SO_2 passed through the catalyst during these cycles. Therefore, using FTIR data we can estimate the amount of SO_2 , which was accumulated in the catalyst and not desorbed during the first regenerations to be 0.11 mmol/g catalyst.

Our data (not shown) suggests that the SO_2 poisoning effect is cumulative in the range of SO_2 concentrations 0.5–10 ppm, i.e. the catalyst deactivation degree depends only on total SO_2 exposure. Therefore, with the same SO_x exposure between DPF regenerations as in this study real catalyst performance will be high enough even in the end of a sulfation cycle before the next regeneration.

3.5. Mechanism of Ag/Al₂O₃ sulfation and regeneration

The results obtained in the previous Section 3.4 set the ground for a few conclusions regarding the sulfation and regeneration mechanisms for Ag/Al₂O₃ catalysts of hydrogen-assisted NO_x SCR by NH_3 .

First of all, some amount of SO_x is not desorbed after regeneration. This amount was estimated in the previous section and is reproducible. At the same time we cannot regenerate the full low-temperature activity of Ag/Al₂O₃, no matter if lean hydrogen-containing or rich mixtures were used for the regeneration. The SCR reaction onset for the sulfated and regenerated catalyst is always shifted to higher temperatures. Therefore, we suppose that a certain type of active sites exists (name it “Type I”), which stand for Ag/Al₂O₃ activity at low temperatures (<200 °C) that are irreversibly poisoned by SO_2 and cannot be regenerated using standard techniques. Taking into account the very low sulfur tolerance of low-loaded Ag/Al₂O₃ [6,7], we can attribute Type I active sites to highly dispersed silver e.g. $\text{Ag}^{\delta+}$ atoms or Ag^+ ions [23,24] (see Fig. 5).

SO_x adsorption on the alumina surface (where dispersed silver is localized) blocks these Type I active sites. SO_x can be adsorbed on single-atom Ag sites on the alumina as well as on the neighboring Al atoms. It is impossible to desorb SO_x from the alumina surface by heating the catalyst to 670 °C [25] and, therefore, Type I active sites could not be regenerated.

Another evidence of irreversibly poisoned active sites is the formation of excess of nitrogen dioxide over the fresh catalyst (Fig. 6b, solid line), a catalytic function which is irreversibly poisoned by SO_2 and cannot be regenerated (Fig. 6b, dotted line). Therefore, we also attribute the increased NO oxidation capacity to Type I active sites.

However, the possibility of regeneration of the most of the SCR activity of Ag/Al₂O₃ hints on the existence of “Type II” active sites. As they are more abundant in more SO_2 tolerant high-loaded Ag/Al₂O₃ [7] we attribute them to the surface of Ag nanoparticles. It has been shown that it is possible to desorb SO_2 from the Ag surface at temperatures near 600 °C [25]. Thus, we assume that sulfation and regeneration of these Type II active sites determines the SCR activity of Ag/Al₂O₃ with sulfur-containing fuel in diesel vehicles. According to the SCR mechanism suggested in [16] these Type II species are also capable of oxidizing NO to NO_2 which further reacts with NH_3 over alumina. However, Type II sites are less active which leads to the deficit of NO_2 and prevents observing it in the gas phase when NH_3 is present.

Our assumption about the existence and function of Type I active sites can be verified by the following. As follows from the SO_2 TPD profiles in Refs. [11,25], it is possible to desorb SO_x from alumina surface at ca. 1000 °C. Of course, the alumina will undergo partial restructuring at this temperature [26] accompanied by the formation of the α -Al₂O₃ phase, which will partially ruin the catalyst. However, this may help to test the principle.

The results of heating of sulfated Ag/Al₂O₃ to 950 °C in the SCR gas mixture with further immediate cooling are shown in Fig. 6a and b as dashed lines. By removing SO_x from the alumina surface (observed by FTIR) we were able to regain SCR onset at the same

temperature as for the fresh Ag/Al₂O₃ (Fig. 6a). At the same time we were able to regenerate excessive NO_2 production (Fig. 6b) which was impossible to get by any kind of regeneration at lower temperature. Still, the maximum activity of the catalyst was lower than that of the fresh catalyst resembling the activity of 3% Ag/Al₂O₃ (Fig. 1a). The specific surface area of the catalyst regenerated at 950 °C did not change significantly compared to the fresh sample (Table 1), therefore, it is rather sintering of Ag particles which caused a drop in the maximum activity. Thus, we consider possibility of regenerating low temperature activity as an evidence for the existence of several types of active sites in Ag/Al₂O₃ as was previously stated for HC-SCR Ag/Al₂O₃ catalysts [27].

The fact that SO_x irreversibly adsorbed on the alumina surface does not hinder that the SCR reaction can be explained if we assume that Ag species participate in the oxidation of NO to NO_2 and the alumina facilitates further reaction of NO , NO_2 and NH_3 according to the “Fast SCR” mechanism [28]. Since “Fast SCR” occurs over a number of acidic surfaces, sulfated alumina should catalyze SCR as well if SO_x -free Ag surface is left to oxidize NO .

3.6. Evaluation of the proposed sulfation and regeneration mechanism of Ag/Al₂O₃ by DFT

Adsorption energies of SO_2 , SO_3 , and SO_4 for the most energetically favorable adsorption geometries for different adsorption sites are summarized in Table 2 and the corresponding geometries for the γ -alumina model step surface are shown in Fig. 7. It should be noted that SO_x can be adsorbed on the γ -alumina in different configurations with similar energies and only the lowest energies (strongest adsorption) are shown. The DFT calculation shows that the SO_x adsorbs strongly on the step sites which is expected from the low coordination of these sites and the steric freedom available at the step sites [29–31]. At the same time the surface step is representative of small 1–3 nm nanoparticles containing mostly under-coordinated surface atoms [32].

Two trends can be identified from these values. First global trend is that all types of SO_x bind significantly stronger to the alumina surface than the metal surface. The adsorption sites also include single Ag sites at the alumina surface with Ag atom built in the surface substituting Al is binding SO_x most strongly (see Supplementary material for the exact site geometry). This can be explained by a thermodynamically unfavorable defect structure of this site. Secondly, the oxidation of SO_2 to SO_3 is thermodynamically favorable, with subsequent poisoning of the catalyst surface by the resulting SO_3 . This has been suggested in Ref. [9] and probably involves reaction with NO_2 [11]. SO_2 alone cannot be adsorbed on the studied metallic Ag surfaces under reaction conditions and SO_x can, thus, only poison the alumina support or single Ag sites on this surface.

The calculated desorption temperatures (Table 2) are low but the order, at which regeneration of Type II (Ag surface) and Type I (highly dispersed Ag on the alumina) occurs is in agreement with the mechanism of Ag/Al₂O₃ poisoning and regeneration suggested in Section 3.5. The difference between calculated and experimental desorption temperatures [11,25] might indicate the formation of bulk silver sulfate [7,33,34].

At the same time addition of hydrogen significantly enhances catalyst regeneration i.e. removal of SO_x which could be due to the formation of the correspondent HSO_x species with their subsequent desorption. Table 3 shows the energies of the HSO_x species in the gas phase and adsorbed on the most energetically favorable sites. According to the given numbers, the formation of HSO_x is highly favorable on Ag (2.11). As the adsorption energies of the HSO_x species with respect to the gas phase species H_2SO_3 (g) and H_2SO_4 (g) are very small they are easily desorbed. The formation of HSO_x is not favorable on the model γ -Al₂O₃ step surface and at the site with Ag built into the γ -Al₂O₃ model step surface. Thus,

Table 2
Adsorption energies and desorption temperatures of SO_x for the most energetically favorable adsorption geometries in case of different adsorption sites.

Type II (metallic Ag)				Type I (dispersed Ag)					
Ag (1 1 1)		Ag (2 1 1)		γ -Al ₂ O ₃		Ag built in the γ -Al ₂ O ₃ surface		Ag on the step of γ -Al ₂ O ₃	
E _{ads} (eV)	T _{des} (K)	E _{ads} (eV)	T _{des} (K)	E _{ads} (eV)	T _{des} (K)	E _{ads} (eV)	T _{des} (K)	E _{ads} (eV)	T _{des} (K)
SO ₂	Not adsorbed	–	81	–1.43	558	–2.06	791	–1.29	506
SO ₃	–1.61	390	458	–2.66	630	–3.34	781	–2.64	625
SO ₄	–2.65	454	597	–1.15	222	–1.77	331	–3.14	572

Table 3
Energies of HSO_x species in the gas phase and adsorbed on the most energetically favorable adsorption sites.

Energy ^a (eV)	HSO ₂	HSO ₃	H ₂ SO ₃	HSO ₄	H ₂ SO ₄
Gas phase	0.21	–0.75	–2.15	–1.48	–3.39
Adsorbed on γ -Al ₂ O ₃	Dissociates	–2.84	–2.18	–3.16	Dissociates
Adsorbed on Ag built in the γ -Al ₂ O ₃	Dissociates	–4.10	–3.38	–3.61	Dissociates
Adsorbed on Ag (2 1 1)	0.02	–2.56	–2.22	–3.94	–3.57

^a Energy of the HSO_x species is given with respect to SO₂ (g), O₂ (g) and H₂ (g).

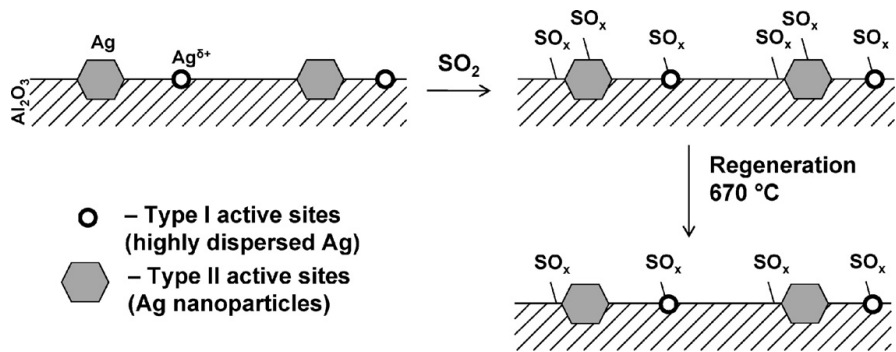


Fig. 5. The scheme of Ag/Al₂O₃ sulfation and regeneration.

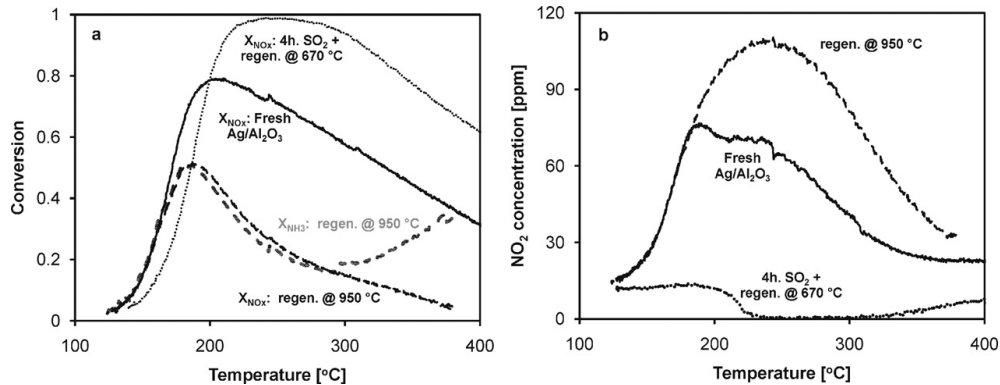


Fig. 6. (a) NO_x conversion profiles obtained over fresh 2% Ag/Al₂O₃ (solid line), 2% Ag/Al₂O₃ after 4 h with 10 ppm SO₂ at 240 °C, followed by 40 min regeneration at 670 °C (dotted line) and after additional regeneration at 950 °C (dashed line). (b) Temperature dependence of NO₂ concentration at the reactor outlet obtained over fresh 2% Ag/Al₂O₃ (solid line), 2% Ag/Al₂O₃ after 4 h with 10 ppm SO₂ at 240 °C, followed by 40 min regeneration at 670 °C (dotted line) and after additional regeneration at 950 °C (dashed line). Reaction conditions: 500 ppm NO, 520 ppm NH₃, 1200 ppm H₂, 8.3% O₂, 7% H₂O in Ar, GHSV = 110,000 h^{–1}.

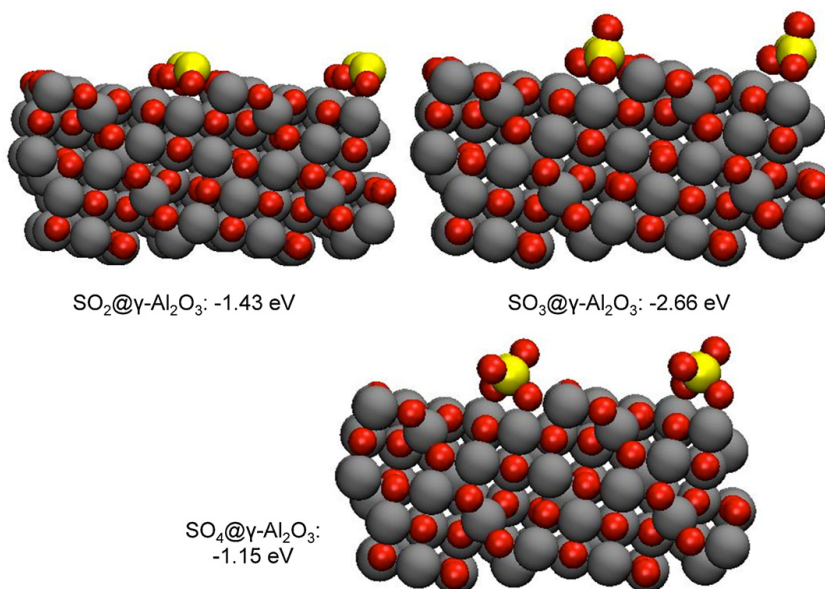


Fig. 7. The most energetically favorable adsorption geometries for adsorption of SO_2 , SO_3 , and SO_4 on the $\gamma\text{-Al}_2\text{O}_3$ model surface (with corresponding adsorption energies).

presence of H_2 will promote the desorption of SO_x species from the Ag (2 1 1) surface via formation of H_2SO_3 (g) and H_2SO_4 (g) but not for $\gamma\text{-Al}_2\text{O}_3$ surface and the single Ag sites on the $\gamma\text{-Al}_2\text{O}_3$ surface.

4. Conclusions

Sulfur tolerance and regeneration options of 2% Ag/ $\gamma\text{-Al}_2\text{O}_3$ catalyst for H_2 -assisted NO_x SCR by NH_3 have been tested. The catalyst has medium sulfur tolerance at low temperatures, however a good capability of regeneration. This regeneration should include heating to 650–700 °C for 10–20 min, provided the SCR gas feed is unchanged (ammonia may be removed) and hydrogen is co-fed. Regeneration of Ag/ Al_2O_3 without oxygen (rich mixture) leads to essentially the same effect, but requires less time.

Heating to 650–700 °C does not allow full regeneration of low-temperature activity and does not allow recovery of NO_2 formation over Ag/ Al_2O_3 in the course of SCR.

During the long-term tests with cycling poisoning–regeneration periods the catalyst activity is regenerated during each regeneration cycle, but at least for the first 6–7 cycles sulfur species are accumulated on the catalyst. Presumably, SO_x is removed from Ag, but not from the alumina surface during standard regeneration, which allows us to make a conclusion on the existence of different active sites in Ag/ Al_2O_3 , namely finely dispersed Ag ions and Ag nanoparticles.

Acknowledgement

This work was supported by the Danish Council for Strategic Research through grant 09-067233.

Appendix A. Supplementary data

Supplementary data associated with this article can be found, in the online version, at doi:10.1016/j.apcatb.2012.01.002.

References

- [1] T.V. Johnson, *Int. J. Engine Res.* 10 (2009) 275–285.
- [2] M. Richter, R. Fricke, R. Eckelt, *Catal. Lett.* 94 (2004) 115–118.
- [3] K.-I. Shimizu, A. Satsuma, *Appl. Catal. B* 77 (2007) 202–205.
- [4] A. Abe, N. Aoyama, S. Sumiya, N. Kakuta, K. Yoshida, *Catal. Lett.* 51 (1998) 5–9.
- [5] H. Kannisto, X. Karatzas, J. Edvardsson, L.J. Pettersson, H.H. Ingelsten, *Appl. Catal. B* 104 (2011) 74–83.
- [6] F.C. Meunier, J.R.H. Ross, *Appl. Catal. B* 24 (2000) 23–32.
- [7] P.W. Park, C.L. Boyer, *Appl. Catal. B* 59 (2005) 27–34.
- [8] S. Satokawa, K.-I. Yamaseki, H. Uchida, *Appl. Catal. B* 34 (2001) 299–306.
- [9] J.P. Breen, R. Burch, C. Hardacre, C.J. Hill, B. Krutzsch, B. Bandl-Konrad, E. Jobson, L. Cider, P.G. Blakeman, L.J. Peace, M.V. Twigg, M. Preis, M. Gottschling, *Appl. Catal. B* 70 (2007) 36–44.
- [10] F. Klingstedt, K. Eränen, L.-E. Lindfors, S. Andersson, L. Cider, C. Landberg, E. Jobson, L. Eriksson, T. Ilkenhans, D. Webster, *Top. Catal.* 30/31 (2004) 27–30.
- [11] Q. Ma, Y. Liu, H. He, J. Phys. Chem. A 112 (2008) 6630–6635.
- [12] B. Hammer, L.B. Hansen, J.K. Nørskov, *Phys. Rev. B* 59 (1999) 7413–7421.
- [13] E. Ménéndez-Proupin, G. Gutiérrez, *Phys. Rev. B* 72 (2005) 35116–35119.
- [14] M. Digne, P. Sautet, P. Raybaud, P. Euzen, H. Toulhoat, *J. Catal.* 226 (2004) 54–68.
- [15] M.W. Chase Jr., *NIST-JANAF Thermochemical Tables*, fourth edition, J. Phys. Chem. Ref. Data, Monograph 9, 1998, 1–1951.
- [16] D.E. Doronkin, S. Fogel, S. Tamm, L. Olsson, T.S. Khan, T. Bligaard, P. Gabrielson, S. Dahl, *Appl. Catal. B*, in press, doi:10.1016/j.apcatb.2011.11.042.
- [17] S. Fogel, D.E. Doronkin, P. Gabrielson, S. Dahl, Manuscript in preparation.
- [18] Regulation (EC) No. 715/2007 of the European Parliament and of the Council of 20 June 2007, Official Journal of the European Union, (29.6.2007), L 171/1–L 171/16.
- [19] VOLVO S80 Instruktionsbok Web Edition <http://esd.volvocars.com/site/owners-information/MY11/S80/PDF/S80.owners.manual.MY11.SE.tp11740.pdf> (accessed June 2011).
- [20] G.M. Wallace, *European Diesel Fuel – A Review of Changes in Product Quality 1986–1989*, Preprint Archive of the ACS Division of Fuel Chemistry 35 (4) (1990) 1080–1099.
- [21] Directive 2009/30/EC of the European Parliament and of the Council of 23 April 2009, Official Journal of the European Union, (5.6.2009), L 140/88–L 140/113.
- [22] L. Olsson, H. Sjövall, R.J. Blint, *Appl. Catal. B* 81 (2008) 203–217.
- [23] A. Sultana, M. Haneeda, T. Fujitani, H. Hamada, *Catal. Lett.* 114 (2007) 96–102.
- [24] K.-I. Shimizu, J.H.Y. Shibata, A. Satsuma, T. Hattori, *Appl. Catal. B* 30 (2001) 151–162.
- [25] Q. Wu, H. Gao, H. He, J. Phys. Chem. B 110 (2006) 8320–8324.
- [26] I. Levin, D. Brandon, *J. Am. Ceram. Soc.* 81 (1998) 1995–2012.

- [27] R. Burch, J.P. Breen, F.C. Meunier, *Appl. Catal. B* 39 (2002) 283–303.
- [28] T.C. Brüggemann, D.G. Vlachos, F.J. Keil, *J. Catal.* 283 (2011) 178–191.
- [29] B. Hammer, J.K. Nørskov, *Adv. Catal.* 45 (2000) 71–129.
- [30] B. Hammer, O.H. Nielsen, J.K. Nørskov, *Catal. Lett.* 46 (1997) 31–35.
- [31] Á. Logadóttir, J.K. Nørskov, *J. Catal.* 220 (2003) 273–279.
- [32] T.V.W. Janssens, B.S. Clausen, B. Hvolbæk, H. Falsig, C.H. Christensen, T. Bligaard, J.K. Nørskov, *Top. Catal.* 44 (2007) 15–26.
- [33] N. Jagtap, S.B. Umbarkar, P. Miquel, P. Granger, M.K. Dongare, *Appl. Catal. B* 90 (2009) 416–425.
- [34] B. Kartheuser, B.K. Hodnett, Alfredo Riva, G. Centi, H. Matralis, M. Ruwet, P. Grange, N. Passarini, *Ind. Eng. Chem. Res.* 30 (1991) 2105–2113.